Estudio numérico de la influenciade diferentes tipos de separadores en la emisión de gotas y en la pérdida de carga establecida en una torre de refrigeración

Proyecto fin de carrera

De

Ulrich Kling

Director: Dr. Antonio Sánchez Kaiser

Codirector: Dr. Blas Zamora Parra

Departamiento de Ingeniería Térmica y de Fluidos

Universidad Politécnica de Cartagena

Abril 2008

English version / *Versión inglesa*

Numerical Study of the Influence of different Types of Eliminators on the established Pressure Drop in the Interior of Cooling Towers

Final Degree Project

Of

Ulrich Kling

directed by

Dr. Antonio Sánchez Kaiser

Dr. Blas Zamora Parra

Departamiento de Ingeniería Térmica y de Fluidos

Universidad Politécnica de Cartagena

April 2008

für meine Eltern | para mis padres | for my parents

Acknowledgements

First, I owe thanks to *Prf. Dr. Eberhard Göde,* Head of the Institute of Fluid Mechanics and Hydraulic Machinery, University of Stuttgart, Germany, for the academic education I enjoyed in “his“ deparment and his contagious enthusiasm for hydraulic turbomachinery. Also, I have to thank him for giving me the possibility to carry out my diploma thesis in Spain.

Second, I would like to thank my director *Dr. Antonio Sánchez Kaiser* of the Technical University of Cartagena, Spain, for introducing me into the world of computational fluid dynamics, for his assistance, his helpful suggestions, his interest in my work, the opportunities given by him and last but not least for the patience with my “Teutonic“ Spanish.

Special thanks to my codirector *Dr. Blas Zamora Parra* of the Technical University of Cartagena, Spain, who was always “available“ for answering my questions, helping me with my doubts and putting up with my poor Spanish. I would like to thank him for inviting me to Spain to do my diploma thesis, too.

Table of contents

Table of figures

Index of tables

Symbols

Latin

A	Area
e_a	Approximate relative error
e_{ext}	Estimated extrapolated relative error
G_k	Production term of turbulent energy
h	Representative cell size
k	Turbulent kinetic energy
l	Length scale
p	Static pressure
p	Order of the method
r	Grid refinement factor
Re	*Reynold*s number
S_M	Source term in momentum conservation equation
U	Mean velocity
u	Velocity component in direction of x
u_τ	Friction velocity, $(\tau_\omega/\rho)^{1/2}$
u^+	Dimensionless near wall velocity, U/u_τ
v	Velocity component in direction of y
V_C	Control volume
x, y	Cartesian coordinates
y^+	Dimensionless wall distance, $\rho u_\tau y/\mu$

Greek

δ_{ij}	Kronecker delta
ε	Dissipation rate
μ	Dynamic viscosity
μ_t	Turbulent dynamic viscosity
ν	Kinematic viscosity
ρ	Density (of air)
τ_{ij}	Shear stress tensor

Indices (subscript)

i, j	Components of a vector or a matrix

1 Abstract

Cooling towers are used to cool down water, which, for example, is used in an industrial process. Ambient air enters the tower at the bottom and starts rising. At the same time the heated water is pulverized by means of sprinklers. Through the contact of the cold ambient air with the droplets of heated water the water gets cooled. The droplets fall to the ground where they are collected. The air continues rising to the top, where it leaves the tower.

The rising airflow carries small water droplets to the outside of the cooling tower. These drops can cause several problems. In countries with a cool climate, like in Northern Europe, the water leaving the cooling tower wets the surroundings of the tower, which can damage nearby infrastructures through icing.

In countries having a warmer climate the danger is of a total different type: Inside the cooling towers the conditions of high temperature and humidity are excellent for pathogens, especially the *Legionella pneumophila*, to spread. This pathogen causes the legionnaires' disease and is spread by means of water droplets smaller than 5µm, which are respirable by human beings.

The heaviest outbreak of the legionnaires' disease, with more than 800 infected persons, took place in Murcia, Spain (2001). It was caused by a cooling tower situated on top of a hospital in an urban area.

To avoid the dispersion of water droplets so-called eliminators are installed in the cooling towers. They are positioned above the sprinklers to prevent very small water droplets from leaving the inside of the cooling tower. The eliminators have a special shaped geometry and force the airflow to follow their shape. Through this fast alternation of direction the water droplets cannot succeed the airflow and impact on the eliminators from where they fall back to the ground of the cooling tower.

Not only is it important for the environment that no water leaves the tower, but also for the accurate operation of the tower itself. All water leaving the tower has to be replaced by new one to assure that the tower yields his full performance.

The disadvantage of installing drift eliminators is an increased pressure loss of the airflow. This pressure loss influences the output of the cooling tower. A high pressure loss contributes to a lower flow rate of air or a higher engine power of the ventilators, depending on the type of cooling tower. It is obvious that with less air the cooling performance of the cooling tower decreases or the operating costs for a better fan system increase.

1.1 Background

The European Parliament and Council states in his directive 2002/91/EC of December 2002 that the building sector accounts 40% of the EU energy requirements and is still expanding, leading to even higher energy consumption and more emissions of carbon dioxide.

Water cooled refrigerant systems feature lower energy consumption than air cooled refrigerant systems with no losses in cooling performance, due to their lower condensening pressure. In accordance with Spanish law (CTE (Código Técnico de la Edificación / construction permit) HS4) water cooled refrigerant systems must be outfitted with recovery installations. The most common installation is the cooling tower.

After several outbreaks of the Legionnaires' disease, see above, some local Spanish governments restrict the installation of cooling towers and dry coolers are used to replace them. This context leads to increasing energy consumption and carbon dioxide emissions.

Therefore the Spanish government requires a comparative study for the selection of the air conditioning system for certain new buildings (thermal load higher than 70 kW, useful area greater than 1000 m^2) involving heat rejecting systems.

The Technical University of Cartagena (UPCT), Spain, in cooperation with the Miguel Hernández University of Elche (UMH), Spain, contributes to improving the energy efficiency of centralized air conditioning systems of buildings by developing a research project. In this project they carry out an analysis focusing on energy, economical and environmental aspects of the associated heat rejection systems.

One point, on which lays the focus of this project of the UPCT, is the analysis of the theoretical fundamentals and of the experimental implementation of the drift measurements, in order to characterise the cooling towers' drift and to estimate the efficacy of improvements of their design (drift eliminators).

The present work is embedded in the above named research project of the UPCT.

1.2 Objectives

The objective of the present project is a numerical simulation of the airflow inside a cooling tower, with special interest in the drift eliminators. It is especially dealt with the pressure loss generated by the eliminators, and the resulting changes in the airflow. The simulation is carried out with the commercial code FLUENT v6.2 using the finite- volumes method.

The project consists of several different parts, which can be described as follows:

- Study of literature to find sources concerning drift eliminators and presenting experimental data. Important is the completeness of the provided data, that is to say, entire characterization of the eliminators' geometry, velocity of the

introduced airflow (or introduced mass flow), exact description of the experiment set- up, measured pressure losses, etc.

- The second part of the project is the construction phase. The virtual reproduction of the eliminator geometries found in the literature and grid creation for the following simulations. An estimation of the uncertainty of the numerical results and the attempt to find a solution, which does not depend on the grid size.
- Introduction of different velocity of the airflow and examination of the results with respect to the pressure loss. Analysis of the airflow and its behaviour passing through the eliminators.
- Comparison of the different types of eliminators in reference to their pressure loss, as well as with the experimental data found in the literature.

Finally, the present work is considered as the starting point for the optimization of the drift eliminator shapes as part of the research project of the UPCT. It should provide a model based on experimental data to forecast the behaviour for new eliminator shapes during the optimization process before constructing any prototype for experiments.

1.3 Phases of project

The project starts with a review of the literature focusing on cooling towers, especially on executed experiments regarding drift eliminators. Then virtual models of the eliminator geometries are built and different types of grids, using GAMBIT v2.0.4, are established. The grids differ in their cell size, which leads to grids with very big cells and others with very small ones. Thus, it is possible to estimate the uncertainty of the numerical solution.

After choosing a suitable grid a comparison of the obtained results by the numerical solution with the ones from the experimental data follows. The interest is turned on the pressure loss and the behaviour of the airflow.

Actually, the phases of the project could be sectioned like:

1. Review of the literature concerning experimental data on drift eliminators
2. Creation of virtual models of the given geometries
3. Establishing different grids
4. Evaluate the uncertainty of the numerical solution by examining the results of the different grids
5. Introduction of different velocities of the airflow in the virtual model
6. Examination of the results and the flow itself

7. Interpreting and displaying of the different flow phenomena
8. Comparison of the results with experimental data

2 State – of – the – art

2.1 Cooling towers

Cooling towers are used to transfer process waste heat to the environment. They use either evaporation to cool the working fluid to the wet- bulb air temperature (wet cooling towers) or only air to cool the working fluid to the dry- bulb air temperature (dry cooling towers).

But the way they cool is not the only way to categorize them. Other distinctions are their application (for industrial or air conditioning purposes), airflow generating methods (natural or mechanical draft) and the air- to- water flow (counter or cross flow).

The present work is on drift eliminators, which are installed in wet cooling towers. Thus, a short orientation on wet cooling towers and drift eliminators is given.

2.1.1 Basics

As already mentioned, wet cooling towers use evaporation to cool the working fluid. For that purpose water is pulverized and, by getting in contact with the (cold) air, a part of it is evaporated. But the evaporation revokes the non- evaporated part of the water heat and cools it thereby.

The act of evaporation is underlain by the *Clausius- Clapeyron* relation:

$$\ln\left(\frac{P_2}{P_1}\right) = -\frac{\Delta H_{vap}}{R}\left(\frac{1}{T_2} - \frac{1}{T_1}\right) \tag{2.1}$$

In this equation P_1 and P_2 are the vapor pressures at temperatures T_1 and T_2, ΔH_{vap} is the enthalpy of vaporization, and R is the universal gas constant. Indeed, this equilibrium is true for only closed systems, but the rate of evaporation in open systems is related to the vapor pressure found in closed systems.

The water is not only cooled by evaporation, but also by convection of the hot water with the cold air. The most important mathematical ansatz for convection is:

$$q = kAdT \tag{2.2}$$

Where q is the heat transferred per time unit, A is the heat transfer area of the unit, k is the convective heat transfer coefficient and dT is the temperature difference between the surface and the bulk fluid.

2.1.2 Function of a cooling tower

In this section the functional principle of wet cooling tower is briefly expressed and displayed in Figure 2.1.

The hot working fluid (normally water) is dropped by a water distribution system above special fillings. The task of the fillings is to maximise the surface of the working fluid to provide an area as big as possible for the heat exchange with the (cold) airflow. In the fillings the water transfers the main part of its heat to the airflow. After crossing the fillings the water is recollected by a water basin and fed to the industrial process, where it gets heated again.

Contrariwise, the air enters the cooling tower at the bottom, then flows through the fillings and gets heated by the water, absorbs evaporated water and collects small droplets. When passing through the eliminators, the droplets get caught by them. Outside of the tower one can see a plume formed by air borne water vapor.

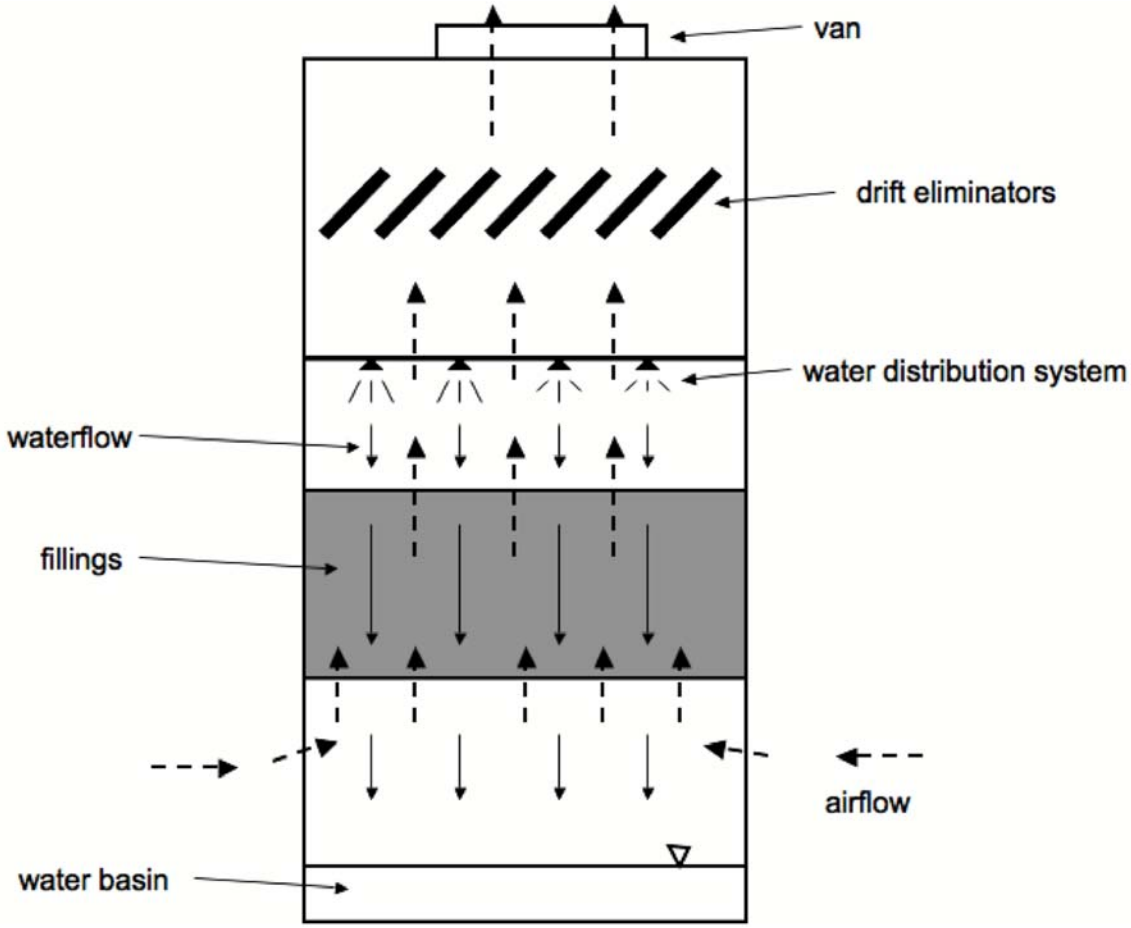

Figure 2.1: Schematic diagram of a cooling tower

The amount of water that is carried to the outside of the tower by the air has to be replaced by new water.

2.1.3 Drift eliminators

As already mentioned, the mission of the eliminators is to prevent water droplets from escaping the cooling tower. This is implemented by the shape of the eliminators. They deflect the airflow in such a way that the water droplets cannot follow due to their idleness and are forced to impact on the eliminators. Thereby a film of water is formed on the eliminators. Bigger droplets are created by the accumulation of water, which fall back into the interior of the cooling tower. Now, they are too heavy to be borne by the air. This way, good eliminators reach an effectiveness of 0,002% that means only 0,002% of the water, which is circulating in the process, gets lost to the environment. Figure 2.2 shows a schematic diagram of drift eliminators, Figure 2.3 a photograph.

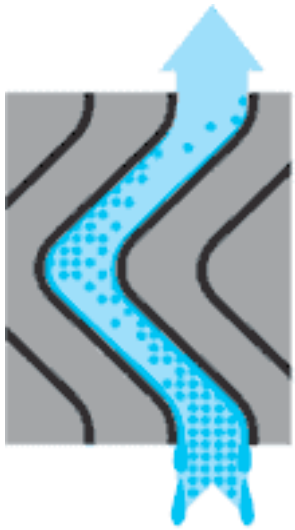

Figure 2.2: Schematic diagram of drift eliminators

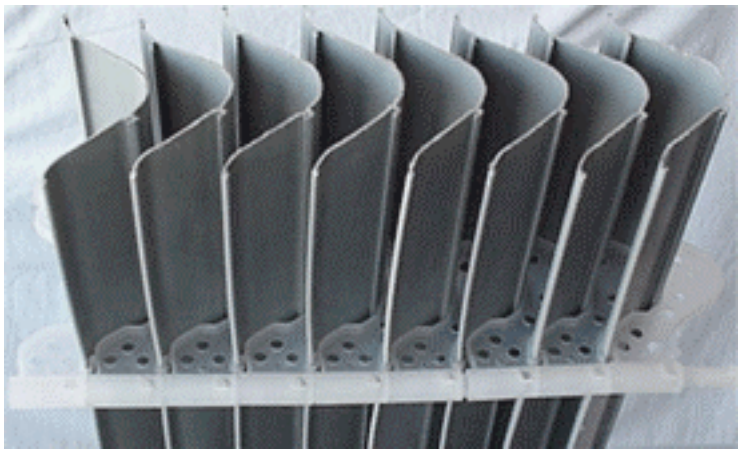

Figure 2.3: Photograph of drift eliminators

However, the eliminators increase the pressure loss of the system by deflecting the air. Thereby the van power, by mechanical draft cooling towers, has to be increased. That leads to higher operation costs of the tower. In natural draft cooling towers, a higher pressure loss leads to a lower flow of air and thus to a lower performance of the tower. Therefore it is very important to have well designed eliminators.

2.2 Literature on cooling towers

There can be found several authors in the literature, who investigated cooling towers in general or drift eliminators in particular. However, there are not many published research papers related to experiments with drift eliminators. Since this work wants to be the basis for further numerical studies and an optimization progress, experimental data on eliminators is fundamental. Although, some other topics regarding cooling towers are introduced in this chapter, the focus had to be turned on vital data for this project.

The number of publications of numerical simulations regarding cooling towers has increased in recent years due to availability of computer resources.

2.2.1 Experimental data on cooling towers in the literature

2.2.1.1 Cooling towers in general

S. R. Hanna and S. D. Swisher (1972) presented a method to calculate the size of cooling towers plumes. They considered the potential effects of the latent heat for the initial buoyancy effects. Also, they considered the height of the tower to be an important factor for the calculation. [1]

M. W. Golay, W. J. Glantschig and F. R. Best (1985) compared some measurements to determine the drift of cooling towers. The interet of their study study was evaluating the capability of the different methods to measure the water droplet distribution, droplet mass flux and gas velocity. The result was that the tested instruments vary widely in their possibilities, some were better for heavy load and others for low load. The major source of error was believed to be found in the relative humidity of the gas stream. [2]

K. E. Haman and S. P. Malinowski (1988) examined the plumes of cooling towers by means of aircrafts to compare the observations with a plume model. They provided images describing the plume size as well as they stated some observed plume- plume and plume-environment interactions indicating an evident dynamic influence of the plume on the ambient atmosphere. [3]

A. K. M. Mohiuddin and K. Kant (1995) discussed in their work a detailed methodology for the thermal design of cooling towers. They described typical geometries of cooling tower packings, water distribution systems and fan design for a mechanical draught cooling tower. [4]

T. Michioka, A. Sato, T. Kanzaki and K. Sada (2006) executed wind tunnel experiments for predicting a visible plume region from a wet cooling tower. The diffusion of water vapor and heat emitted from a cooling tower were estimated by adding a tracer gas. They predicted the time- average visible plume region based on the instantaneous concentration. To confirm their results and the developed model, they compared them with observations at a real cooling tower. [5]

2.2.1.2 Drift Eliminators

A. Martin and F. R. Barber (1977) executed measurements in the inside of several cooling towers using water sensitive papers. They exposed the papers at various tower levels, under the eliminators, over the eliminators and high in the towers. Thus, they provided a droplet distribution at each level and eliminator removal efficiencies. Furthermore they gave an exact description of the eliminator types, which they examined. [6]

One of the most important sources for the present work is the research paper published by P. M. Foster, M. I. Williams and R. J. Winter (1974). They made theoretical and experimental investigations for two types of drift eliminators, which were the Ratcliff lath eliminator (double louvre type) and the asbesto- cement eliminator. The theoretical part was a simulation of the trajectories of different sized droplets. In the experimental part they examined the eliminators' performance by means of photographs, see Figure 2.4.

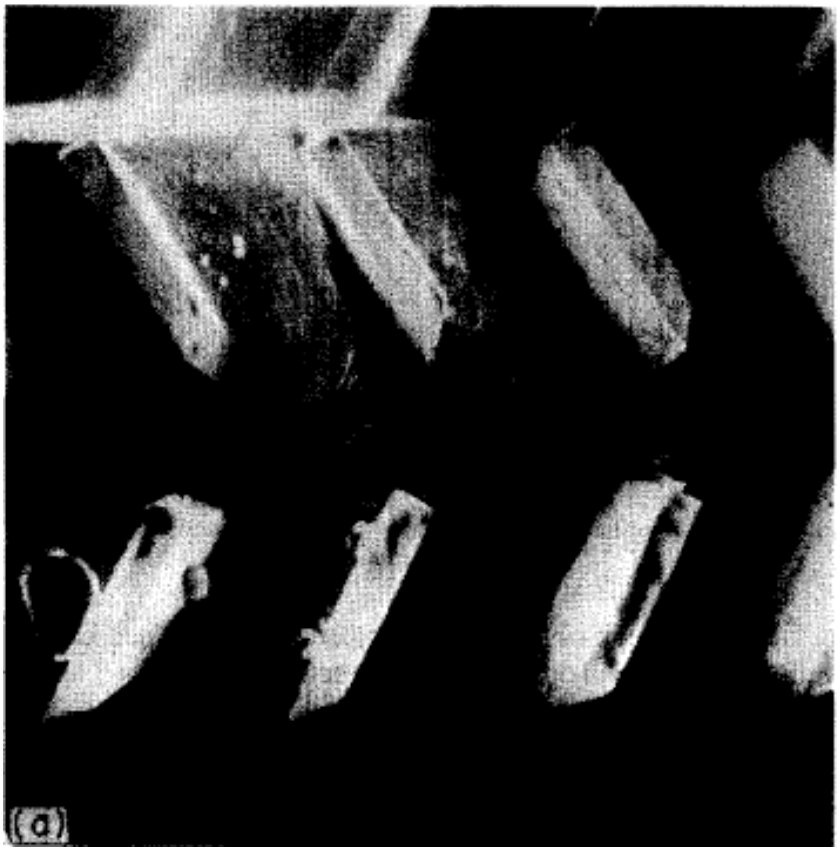

Figure 2.4: Photograph of drift eliminators by P. M. Foster, M. I. Williams and R. J. Winter

They also provided a detailed description of the drift eliminators' geometries as well as a reproduction of their experiments. [7]

Another important publication was made by J. Chan and M. Golay (1977). Their work was very similar to the work of P. M. Foster et al. (1974). They did a theoretical and experimental examination of different designed drift eliminators, however, not the same ones as P. M. Foster et al. Figure 2.5 shows a schematic diagram of their experiment set- up.

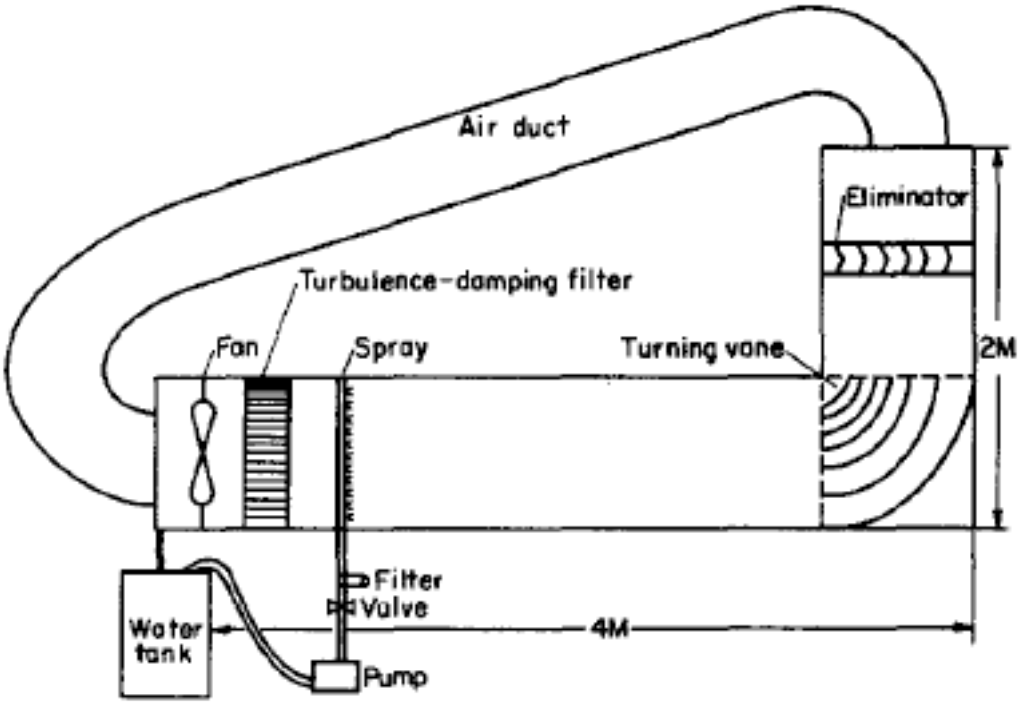

Figure 2.5: Schematic diagram of experiment set- up of J. Chan and M. Golay

For the examination of the droplet distribution they developed a new technique using laser light scattering. [8]

B. R. Gardner and H. J. Lowe (1974) presented a study on environmental problems of natural draught cooling towers. They engaged two types of drift eliminators: The so-called double-louvre type and the asbesto- cement type, which are exactly the same types as those studied in the work of P. M. Foster et al., see above. They stated an exact description of the shape of the eliminators and the pressure loss of them for different velocities. Furthermore they gave observations on how the drift of a cooling tower influenced on the environment and the level of wetting. [9]

A recent work of A. K. M. Mohiuddin (2005) is about flow visualization and drift eliminators characteristics. Three types of drift eliminators were discussed; wooden drift eliminators, asbesto- cement drift eliminators and cellular type drift eliminators. The experimental set- up is shown in Figure 2.6. The expertise was that the pressure loss and the drift loss strongly

depend on the air flow rate and the number of stages of eliminators. Also it could be shown that the flow pattern inside the test tower was similar at various flow rates.

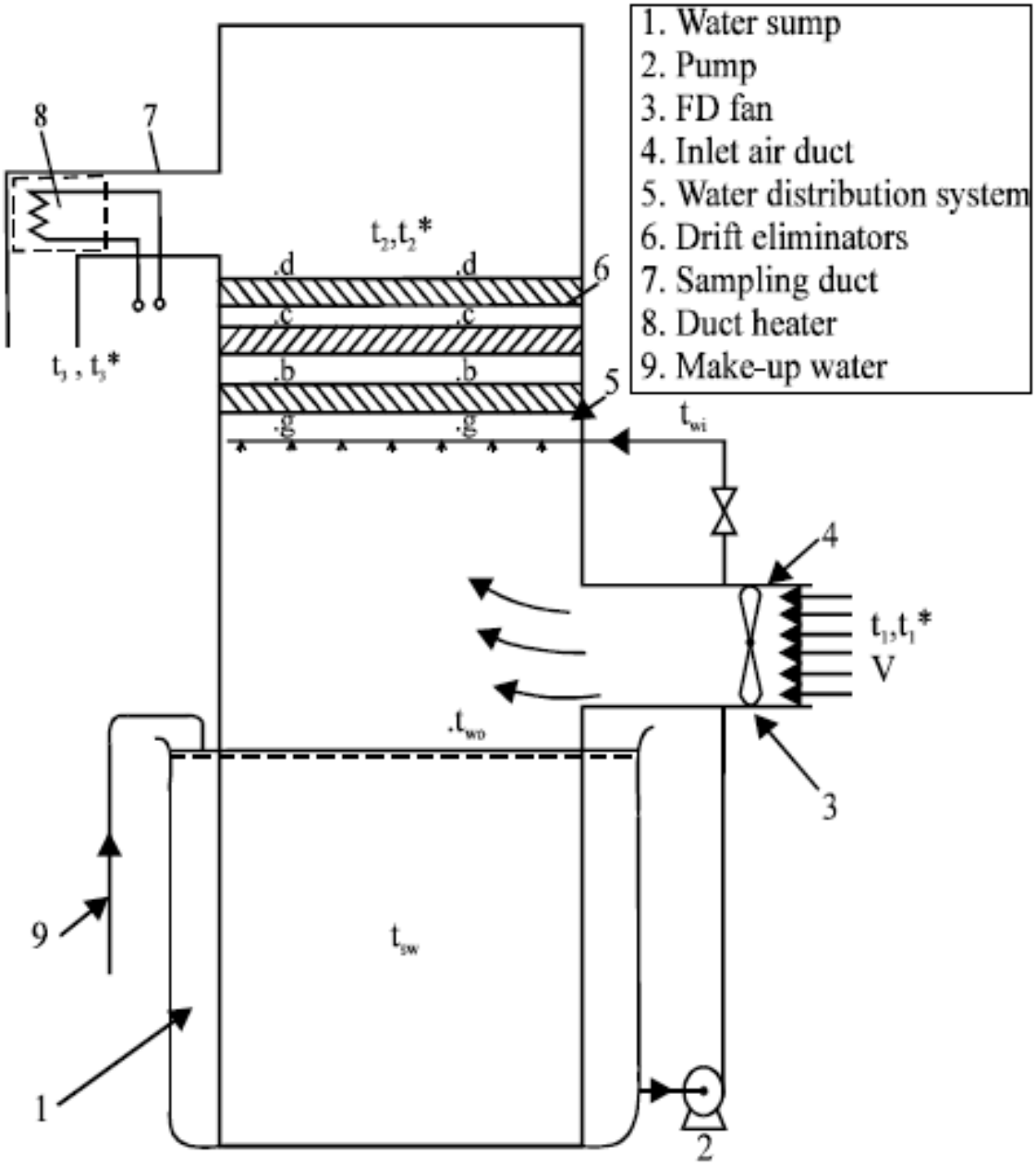

Figure 2.6: Schematic diagram of experiment set- up of A. K. M. Mohiuddin

Unlike in the above mentioned papers, in this paper an exact description of the geometries of the eliminator shapes was missing. [10]

2.2.2 Numerical simulations of cooling towers in the literature

2.2.2.1 Cooling towers in general

R. Al- Waked and M. Behnia (2007) presented a work on performance- enhancing of cooling towers. They established a numerical study of the effect of windbreak walls on the output of

cooling towers. They could show that installing walls at certain point of a cooling tower was able to increase the performance of them. [11]

A numerical study of a single and two interacting plumes was discussed by M. R. Mokhtarzadeh- Dehghan, C. S. König and A. G. Robins (2006). The simulation was validated with results from a small- scale wind tunnel experiment. They were primarily interested in improving the understanding of plume interaction to contribute to the estimation of pollutant dispersion. [12]

R. N. Meroney (2006) published a very detailed paper on a CFD study of cooling tower drift. He compared his obtained results with an experiment of 1977, the chalk point dye tracer experiment. He calculated plume rise, surface concentrations, plume centerline concentrations and surface drift deposition. [13]

S.P. Fisenko, A. I. Petruchik and A. D. Solodukhin (2001) presented a mathematical model of the performance of a cooling tower. The model described the self- consistent evaporative cooling of falling droplets and water films. The model shown very good agreement with experimental data. [14]

2.2.2.2 Drift Eliminators

A numerical simulation concerning drift eliminators can be found in the publication of J. Chan and M. W. Golay (1977), which was mentioned above. With the same eliminator types they made numerical simulations. Thus, the geometry of one of them was slightly more complicated than the others; they had problems with the simulation due to the limitations of the calculation method in describing turbulence. As an example Figure 2.7 shows a result of a calculation of one eliminator type.

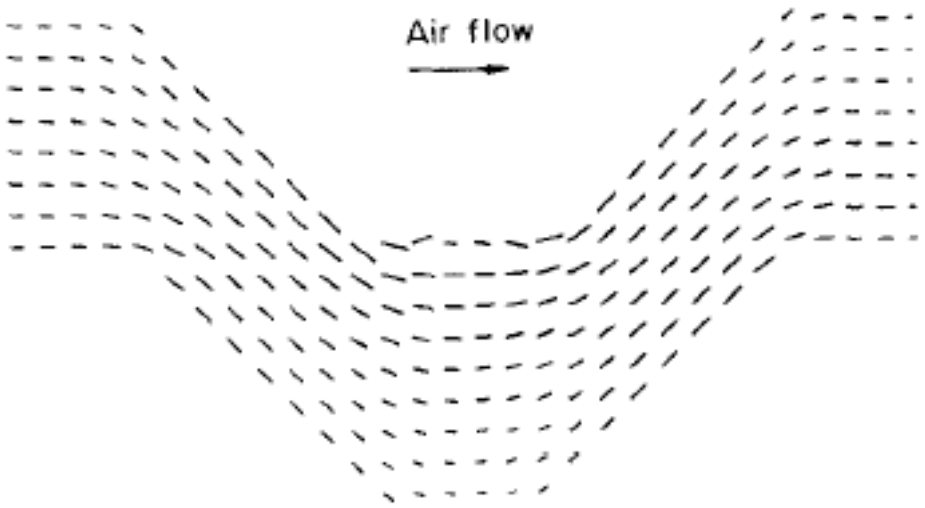

Figure 2.7: Calculated velocity distribution of air flow by J. Chan and M. W. Golay

Also, they calculated droplet trajectories; Figure 2.8 shows the same type of drift eliminator with calculated trajectories of droplets of a given size.

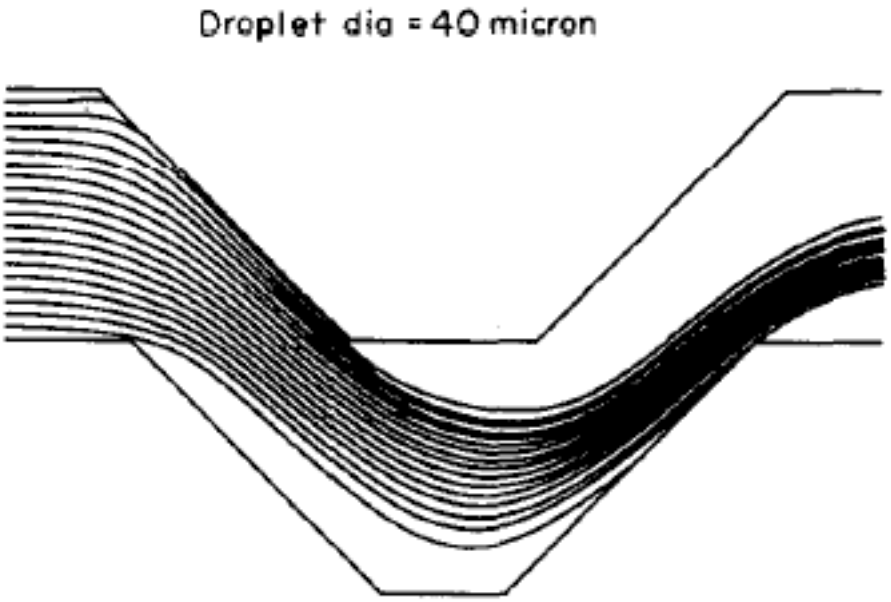

Figure 2.8: Calculated droplet trajectories by J. Chan and M. W. Golay

Figure 2.9 shows the eliminator shape which could not be calculated. Thus, they always calculated only one pair of eliminators, or two walls of eliminators, one can see that numerical simulations were quite restricted in the past (and are still). [8]

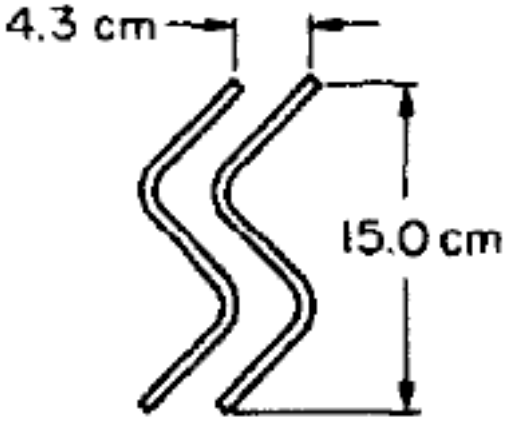

Figure 2.9: Eliminator geometry which could not be simulated by J. Chan and M. W

The second part of the work of P. M. Foster, M. I. Williams and R. J. Winter (1974), which is already mentioned above, was a numerical simulation of drift eliminators, too. Like J. Chan and M. W. Golay, they calculated trajectories for droplets of different diameters. But unlike their researching colleagues, they chose other boundaries for their simulation to include entire

eliminators, see Figure 2.10. However, they did not calculate the pressure losses of the two types of eliminators. [7]

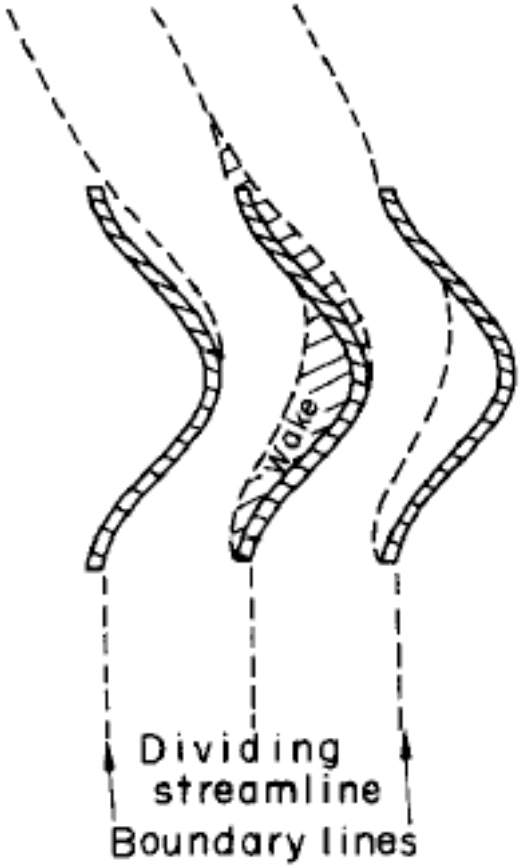

Figure 2.10: Boundaries for simulation of P. M. Foster, M. I. Williams and R. J. Winter

2.3 A brief introduction to computational fluid dynamics

In the sections on the literary sources on cooling towers the method of computational fluid dynamics (CFD) has already been mentioned. Now, in this section a short introduction is given, and also some expressions used in association with CFD are explained.

In the 17th century the base of experimental fluid mechanics were established in France and England. Later, in the 18th and 19th centuries a gradually development of the theory of fluid mechanics took place. From this, a further theoretical, as well as an experimental development of fluid mechanics, followed for a great part of the 20th century.

With the appearance of modern computers and of accurate numerical algorithms, the way of studying and using fluid mechanics has changed. A new branch was created: Computational Fluid Dynamics. Nowadays, CFD is one of the most powerful tools in engineering and his importance equals that of experiments.

In general a flow is characterised by three fundamental principles:

1. Mass conservation (continuity equation)
2. *Newton*' s second law of motion (*Navier- Stokes* equations)
3. Energy conservation (energy equation)

These three physical principles can be expressed as mathematical equations, in the most general way as differential or integral equations. These equations are the starting point for the CFD method. CFD replaces the partial derivatives or integrals by discretised algebraic equations, which can be solved by means of modern computers. By the solving process a discrete series of numbers is obtained, which represents the physical magnitudes of the fluid dynamic problem. Figure 2.11 shows a schematic diagram of the solution process of a problem using CFD.

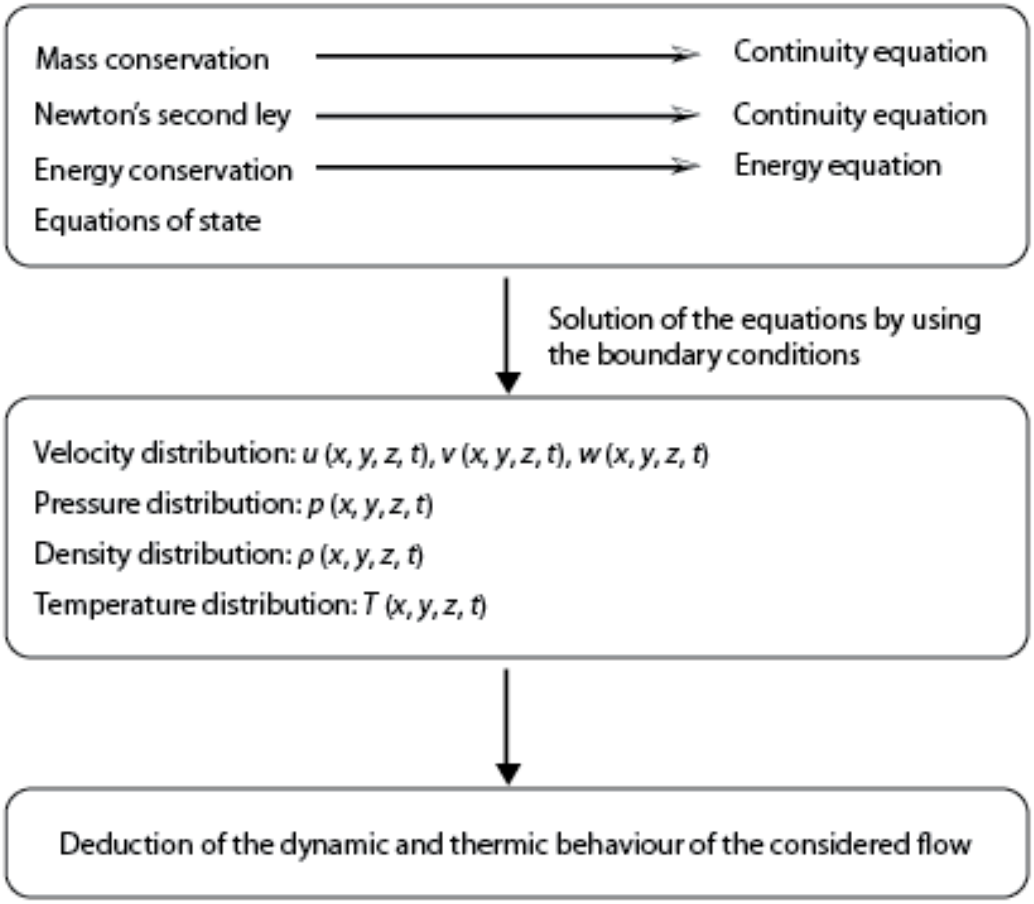

Figure 2.11: Schematic diagram of problem solving process by means of CFD

Nowadays CFD plays an important role in mechanical engineering. Due to its broad application range it can be used to simulate the most different fluid mechanical problems, such as weather forecasts, turbine machinery, engines, metal smelting processes, ocean currents, river flows, areodynamical problems, blood flows in human bodies, etc.

Due to the great complexity of the solution of fluid mechanical problems, computational fluid dynamics methods could not compete with experimental techniques. However, the rise in performance of modern computers led to an increasing interest in CFD in the industry. The advantages of CFD over experiments are:

- Reduction of costs and time for new devices to be constructed
- Possibility to simulate flows and situations beyond experimental range
- Possibility to simulate systems under dangerous conditions
- Very detailed solution

However, a disadvantage which cannot be denied is that Computational fluid dynamics are still based on models. Thus, the power of today's computer is still insufficient to solve the governing equations of a flow within a reasonable time; and models are used to give an approach to the exact solution. These models are only empirical. Nevertheless, CFD have turned into an excellent engineering tool which user must aware of how the used models work and must question if the obtained results are "reasonable".

3 Creation of the virtual model

This chapter turns the attention to the definition and construction of the virtual model of the eliminators, which is the domain for the numerical study. Afterwards the domain is divided into cells or finite volumes, which form the grid. On this grid the method of finite volumes is applied to solve the equations, which express the behaviour of the problem. This technique is known as Computational Fluid Dynamics (CFD).

The solution of the problem by means of CFD depends strongly on the cell size of the grid. With an increasing number of cells the accuracy of the solution is assumed to increase. But this leads to an uneven longer calculation period and higher deployment of hardware resources. Therefore in chapter five a review of errors and uncertainties is presented and a study of the uncertainty of the grid is executed. There is also an intent to determine the accuracy of the solution in dependence on the grid refinement.

3.1 Analysis of experimental data on drift eliminators in the literature

To be able to evaluate the results of the numerical simulation, a good documented experimental base of data on drift eliminators was needed. For a valid simulation the following information was required:

- Exact description of the drift eliminators shape (engineering drawing)
- Pressure losses and details on where they were measured
- Velocities of the introduced air
- Density (and temperature) of the air
- Dimensions of the experimental setup

As written in paragraph 2.2.2, only five sources could be found providing information on drift eliminators. Furthermore all of them lacked a piece or several pieces of the above requested information.

Thus in [10] no exact description of the eliminators was given, and so cannot be used for the simulation. The same happens to [8], there was no exact description of the eliminators. But the pressure drop in Torr and units of velocity head was quoted.

Only in [7] and [9] a roughly sufficient illustration of the eliminators was given, and since both works dealt with the same eliminators they completed each other. Also in [9] three different air velocities were stated with the according pressure losses in units of velocity head. Hence, the pressure losses were only displayed in units of velocity head, so without knowing

the density of the air the pressure loss in Pascal could not be calculated. Then, the only magnitude lacking was the density of the air. Therefore, in order to use a typical value for the simulation, the density of the values of pressure drop stated in [8] was calculated. See Figure 3.1, which shows the stated values.

Type of eliminator	Air speed (m/s)	Calculated value (Torr)	Measured value (Torr)	Accuracy of measurement
Sinus	1.5	0.02868 (2.82)*	0.03054 (3.00)	13%
	2.5	0.06546 (2.32)	0.06279 (2.23)	11%
Three-segment	1.5	0.03482 (3.43)	0.03734 (3.68)	12%
	2.4	0.07663 (2.72)	0.08119 (2.88)	11%
Zig-zag	1.5	—	0.07424 (7.31)	8%
	2.3	—	0.16079 (5.70)	6%

Figure 3.1: Stated table of pressure losses in [8]

The units of velocity head (*uvh*) are defined as follows (*Bernoulli's* principle):

$$uvh = \frac{\Delta P}{\frac{1}{2}\rho V^2} \tag{3.1}$$

Where ΔP is the pressured drop, V the velocity and ρ the density.

Resolving the equation for ρ:

$$\rho = \frac{\Delta P}{\frac{1}{2}V^2 uhv} \tag{3.2}$$

Inserting the values from Figure 3.1 for the sinus eliminator, an air speed of 1,5 m s^{-1} and with 1 Torr ≈ 133,322 Pa follows:

$$\rho = \frac{(0{,}03054 Torr \bullet 133{,}322 \frac{Pa}{Torr})}{\frac{(3{,}00)}{2}(1{,}5 \frac{m}{s})^2} \tag{3.3}$$

$$\rho = 1{,}206 \frac{kg}{m^3} \tag{3.4}$$

The outcome of the same eliminator type but with a speed of 2,5 m s^{-1} and a pressure loss of 0,06279 m s^{-1} is:

$$\rho = \frac{(0{,}06279 Torr \bullet 133{,}322 \frac{Pa}{Torr})}{\frac{(2{,}23)}{2}(2{,}5 \frac{m}{s})^2} \tag{3.5}$$

$$\rho = 1{,}201 \frac{kg}{m^3} \tag{3.6}$$

As one can see there is almost no difference in the density of the air at these velocities. In the latter simulation a value of 1,206 kg m^{-3} is applied.

Solving equation (3.1) for the pressure drop ΔP leads to:

$$\Delta P = \frac{1}{2} \rho V^2 uhv \tag{3.7}$$

By inserting the calculated density value of equation (3.6) and the air velocities and pressure losses, in units of velocity heads, stated in [9], the pressure losses in Pa can be calculated for each eliminator type. In Table 3.1 the values for the wooden lath eliminator are shown, and in Table 3.2 for the asbesto- cement eliminator.

Table 3.1: Calculated pressure drops for wooden lath eliminator

Velocity stated in [9] [m s^{-1}]	Units of velocity head stated in [9]	Calculated pressure drop [Pa]
0,91	2,9	1,463
1,52	2,9	4,063
2,13	2,9	7,963

Table 3.2: Calculated pressure drops for asbesto- cement eliminator

Velocity stated in [9] [m s^{-1}]	Units of velocity head stated in [9]	Calculated pressure drop [Pa]
0,94	3,4	1,831
1,58	3,4	5,120
2,23	3,4	10,153

In [9] the values of the velocities are stated in *feet per second* (ft s^{-1}), for example in the case of the wooden lath eliminator the values are: 3, 5, and 7 ft s^{-1}. The values for the velocities in the two tables above are rather peculiar due to the conversion in *metre per second* (m s^{-1}). In any case, the values of the velocities in m s^{-1} were used for the simulations.

Furthermore, Table 3.3 displays an extract from the properties of air. It can be seen that air with a density of 1,205 kg m^{-3} has a viscosity of 15,11 x 10^{-6} m^2 s^{-1}. This value was used in the simulation for the viscosity.

Table 3.3: Extract of air properties

Temperature [°C]	Density [kg m^{-3}]	Viscosity [m^2 s^{-1}]
0	1,293	13,30 x 10-6
20	1,205	15,11 x 10-6
40	1,127	16,97 x 10-6

With the viscosity, the velocities and the characteristic length, it was possible to calculate the *Reynolds* number for the different cases so as to decide if the flow (or flows) is (are) turbulent or laminar. The Reynolds number is defined as:

$$\mathrm{Re} = \frac{v\,L}{\nu} \tag{3.8}$$

Where L is the characteristic length, v the flow velocity and ν the kinematic viscosity.

The distance between two single eliminator shapes is chosen as characteristic length. In the case of the wooden lath eliminator this distance is 76 mm and for the asbesto- cement eliminator it is 57 mm. Table 3.4 displays the calculated *Reynolds* numbers for the two geometries and the different velocities. As criterion the critical *Reynolds* number of 2300 for a pipe flow was chosen. That means for a *Reynolds* number below 2300 the flow was considered to be laminar and for a value above the flow was turbulent.

Table 3.4: Calculated Reynolds numbers for the two geometries

-	Wooden lath eliminator	Asbesto- cement eliminator
Reynolds numbers	4577 (0,91 m s^{-1})	3546 (0,94 m s^{-1})
	7665 (1,52 m s^{-1})	5960 (1,58 m s^{-1})
	10713 (2,13 m s^{-1})	8412 (2.23 m s^{-1})

All values are bigger than the critical *Reynolds* number. Although the first Reynolds number for the asbesto- cement eliminator is relatively close to the critical value, the flow was considered to be turbulent in all cases.

In [7] an adequate description of the experimental set- up was stated. The most important fact is that the experiments were executed in a test tower with a square base area of 1,22 m side length and that under the eliminators was a free space of 1 m. With this dimensions the domain of the simulation was built. Figure 3.2 shows the schematic experimental setup of [7].

Finally Table 3.5 is a conclusion which of the above mentioned literary sources provides important data for the simulation. An < X > implies that the information was used for the simulation. < O > that the literary source possesses the information, but it was not used for this work and < - > that the analogical information was not mentioned.

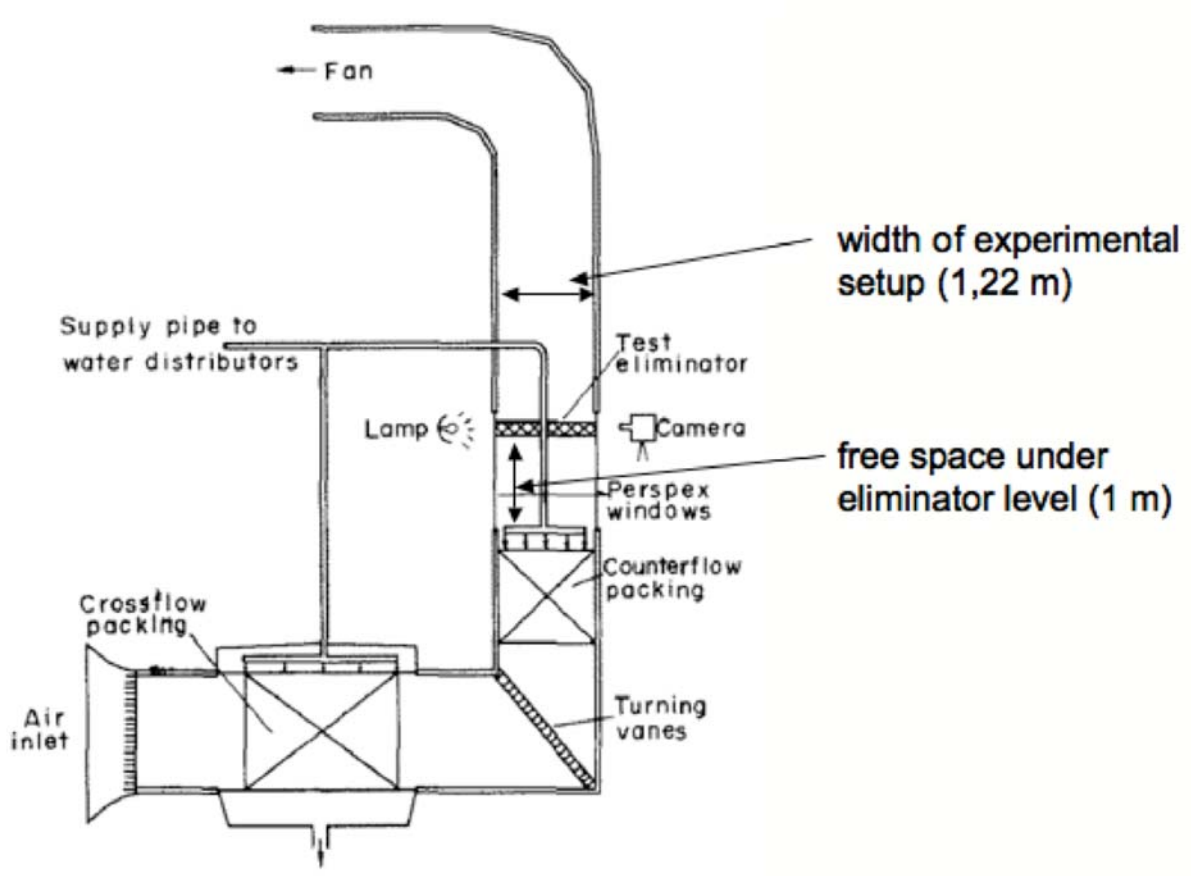

Figure 3.2: Schematic diagram of experimental set- up displayed in [7]

Table 3.5: Available information in the literature (< **X** > = available and used in simulation, < **O** > = available but not used in simulation, < **-** > = not available)

Source of literature	**[6]**	**[7]**	**[8]**	**[9]**	**[10]**
Eliminator geometry	**-**	**X**	**-**	**X**	**-**
Pressure loss	**-**	**-**	**O**	**X**	**O**
Velocity	**-**	**O**	**O**	**X**	**O**
Density	**-**	**-**	**X**	**-**	**-**
Experimental set- up	**-**	**X**	**O**	**O**	**O**

With the provided information it was possible to carry out the simulation. However, some of the details were missing. For example, in [9] there is not stated where the observed pressure losses were measured, and the description of the eliminator geometry in [7] and [9] was incomplete, which is shown in Figure 3.3.

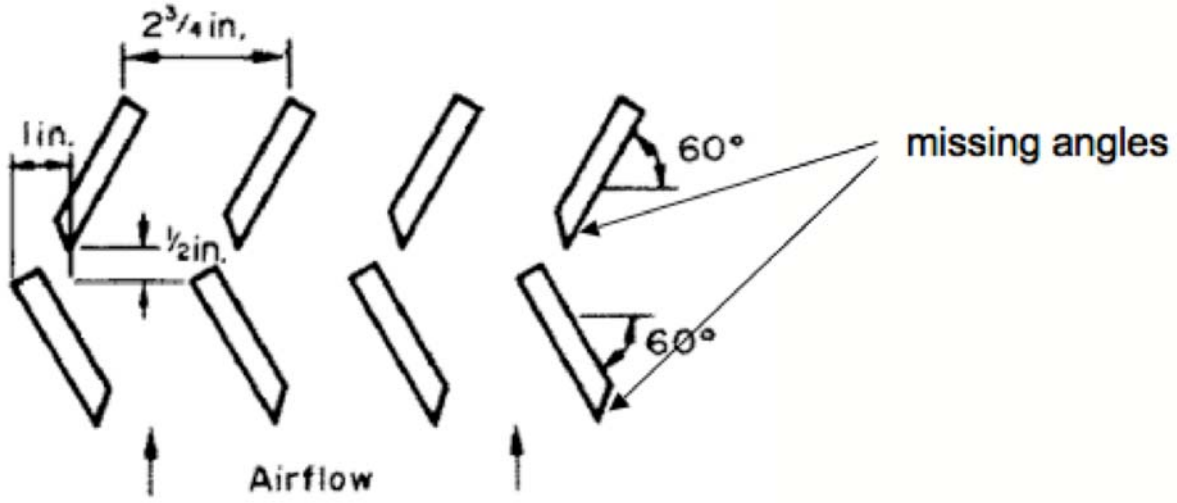

Figure 3.3: Cutout of eliminator geometry with missing angles stated in [7]

3.2 Creation of eliminator geometry in GAMBIT

3.2.1 Introduction to GAMBIT

For the calculation of a fluid mechanics' problem by means of computational fluid dynamics, the virtual domain of the problem has to be divided in small subdomains. The subdomains consist of either hexahedrons and tetrahedrons in 3D domains or tetragons, and triangles in cases of domains in 2D. The subdomains form the grid or mesh on which the simulation is applied. There are different types of grids depending on the distribution of the cells. Figure 3.4 shows a so-called structured grid (due to the regularity of the cells) and Figure 3.5 an unstructured one. The choice of grid depends on different criterions, such as the geometry and characteristics of the problem, but also eminently on the solver method. Since in this work the method of finite volumes is applied, both types of grids can be used.

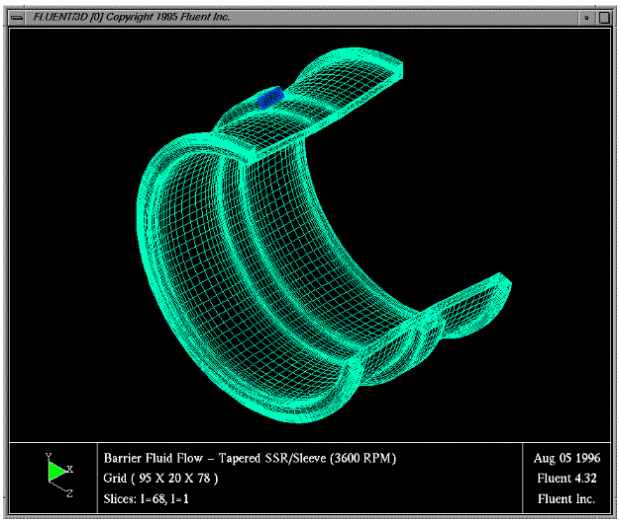

Figure 3.4: Example for structured grid

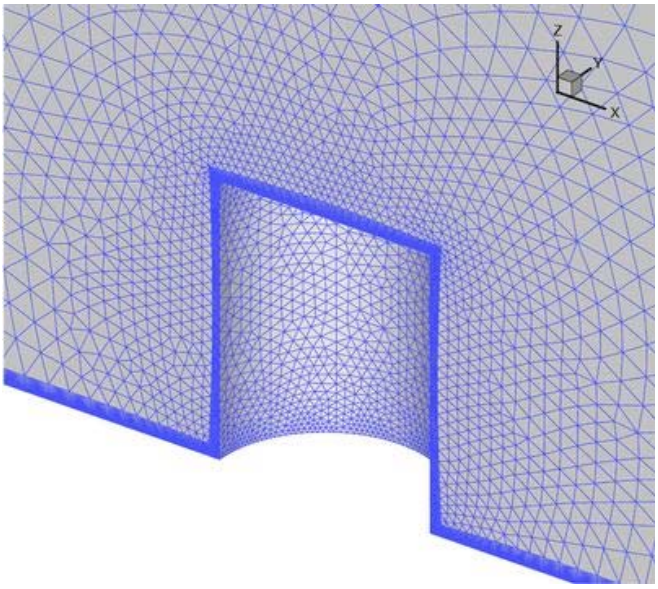

Figure 3.5: Example for unstructured grid

The simulation in this work was executed with the FLUENT code provided by the ANSYS Company. There is GAMBIT, which is the software of FLUENT for grid generation. With Gambit it is possible to:

- create geometries (2D and 3D)
- generate structured and unstructured grids
- define boundary conditions

3.2.2 Eliminator geometry

In the two literary sources, which were used for the simulations in this work, two different types of eliminators were considered. There was the wooden lath (or double- louvre type) eliminator and the asbesto- cement eliminator type. A virtual model had to be built for each one of them.

First of all it was important to decide if the simulation needed to be calculated in a 3D domain or if a 2D domain would be sufficient. This question strongly depends on the geometry of the problem. Since the two types of drift eliminators studied in the present work have a special shaped cross section and do not alter their shape in the third direction of space, a 2D domain was considered to be sufficient.

Figure 3.6 shows detail drawings of the wooden lath eliminator, and Figure 3.7 of the asbesto-cement eliminator stated in [7] and [9]. From these drawings the eliminator geometries were constructed in Gambit.

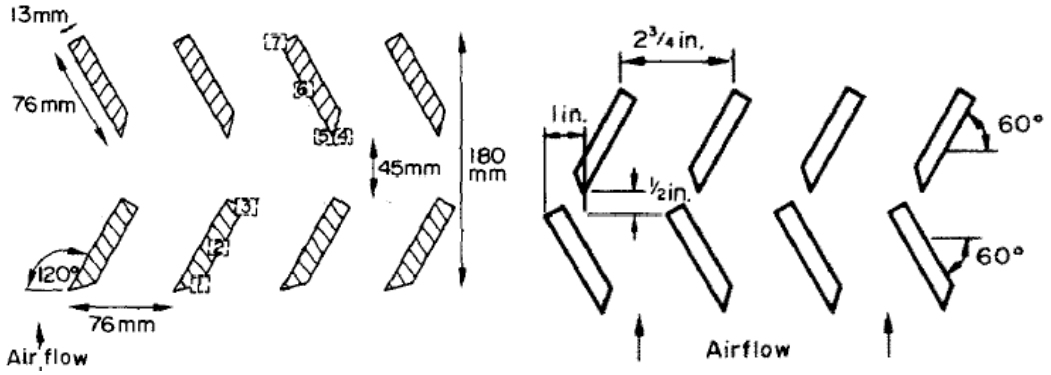

Figure 3.6: Detail drawings of the wooden lath eliminator geometry, left: stated in [7], right: stated in [9]

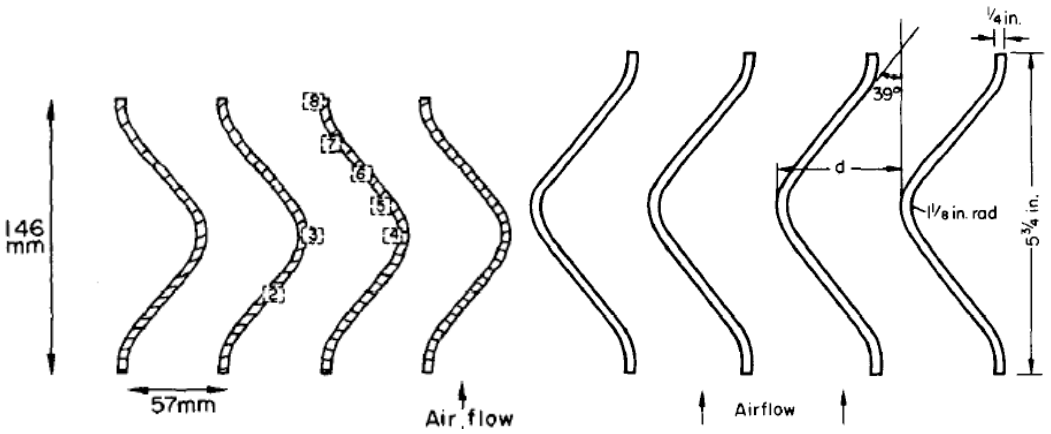

Figure 3.7: Detail drawings of the asbesto- cement eliminator geometry, left: stated in [7], right: stated in [9]

Figure 3.8 displays the in GAMBIT generated geometry of a single wooden lath eliminator. In comparison Figure 3.9 shows the geometry of the same type of eliminator posted in [7].

Figure 3.8: Geometry of wooden lath eliminator stated in [7]

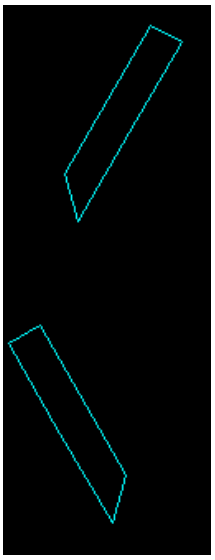

Figure 3.9: Geometry of wooden lath eliminator generated in GAMBIT

The missing angles, see 3.2, are supposed to be 45°. As one can see the generated eliminator geometry and the one given by the literature agree.

Also, the geometry of the asbesto- cement eliminator type was constructed in GAMBIT. See Figure 3.10, which shows the geometry posted in the literature, and Figure 3.11 displaying the geometry generated in Gambit.

Figure 3.10: Geometry of asbesto- cement eliminator stated in [7]

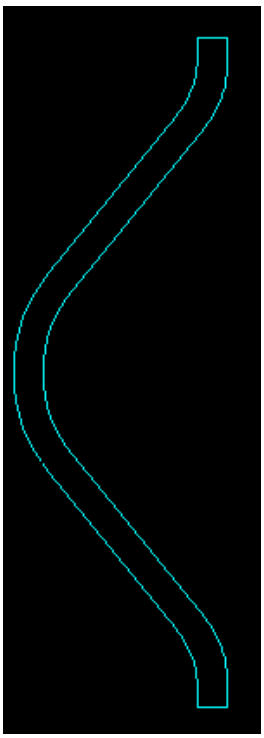

Figure 3.11: Geometry of asbesto- cement eliminator generated in GAMBIT

Hence, in [7] the dimensions of the experimental setup were mentioned, and there was an attempt to adopt these dimensions in the computational domain. Actually, only two measures were of importance. They have already been mentioned. It was the base area of the experimental setup, which was a square of 1,22 m side length. Thus, it was decided to build the geometry only in 2D, and only one side of the square was needed. This context results in a

width of the problem geometry of 1,22 m. The other measure was the free space under eliminator level of 1 m length. Therefore the computational domain has also a free space of 1 m below the eliminators, where the airflow enters the domain later (inlet). There is also a free space above the eliminators, but in [7] there were no dimensions stated. Because of that it was decided to keep a free space of 1 m length, too. In this way the possibility is given to see how the airflow develops after passing through the eliminators. After this 1 m the air leaves the computational domain (outlet).

In each case of the two different eliminator types the width of 1,22 m could not be maintained, due to the distances between the single eliminator laths. Therefore the width is changed and the domain is bulged at the eliminator level, see Figure 3.12 for the wooden lath eliminator and Figure 3.13 for the asbesto- cement type.

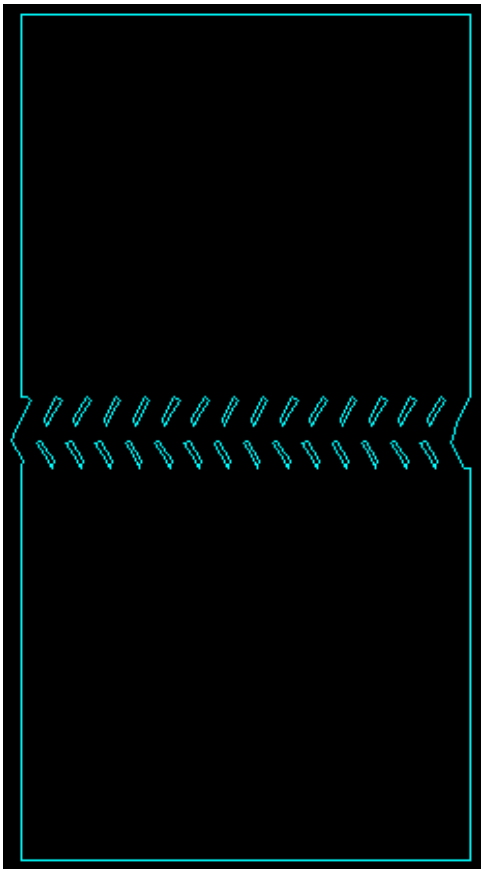

Figure 3.12: Whole computational domain of wooden lath eliminators generated in GAMBIT

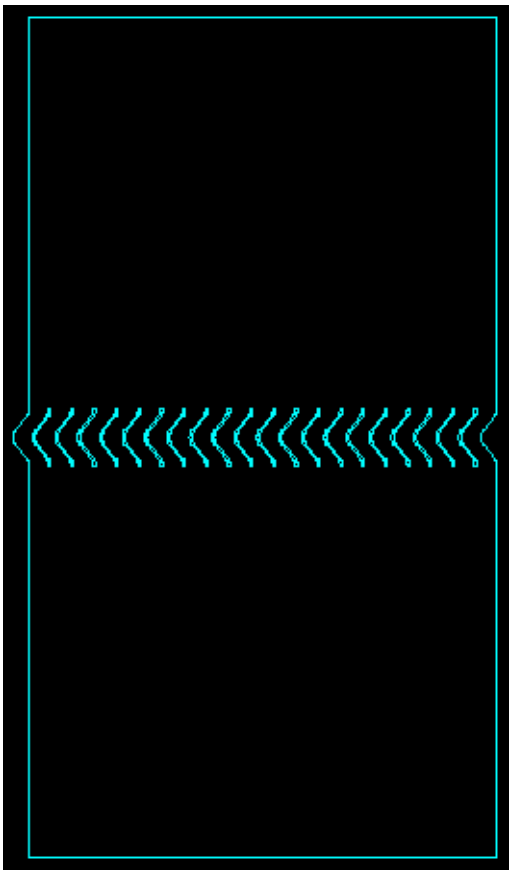

Figure 3.13: Whole computational domain of asbesto- cement eliminators generated in GAMBIT

The changes result in a new width of 1,15 m for the wooden eliminator type and 1,19 m in the case of the asbesto- cement eliminators. The bulging was applied in order to receive a constant airflow, so as to have the same eliminator shapes over the whole width of the domain. The inlet and the outlet have the same length, providing the continuity of the velocity.

On these two computational domains grids were built. Although, there were built several grids for each geometry, see chapter 5, here only one example is displayed. All grids consisted of three different parts: the inlet area, the eliminator area, and the outlet area. The inlet and the outlet area were meshed with an unstructured coarse grid to keep the number of cells small. They were very similar for each grid. In the eliminator area the eliminator shapes were situated with an additional zone below and above the eliminators. The eliminator area contained the bigger part of the cells. The reason therefore was that especially in this area the flow is of high interest. In order to evaluate the flow just before entering and leaving the eliminators, two zones of 5 cm height below and above of them were added to the eliminator area. Figure 3.14 shows an example for one grid for the wooden lath eliminator. The different zones are marked.

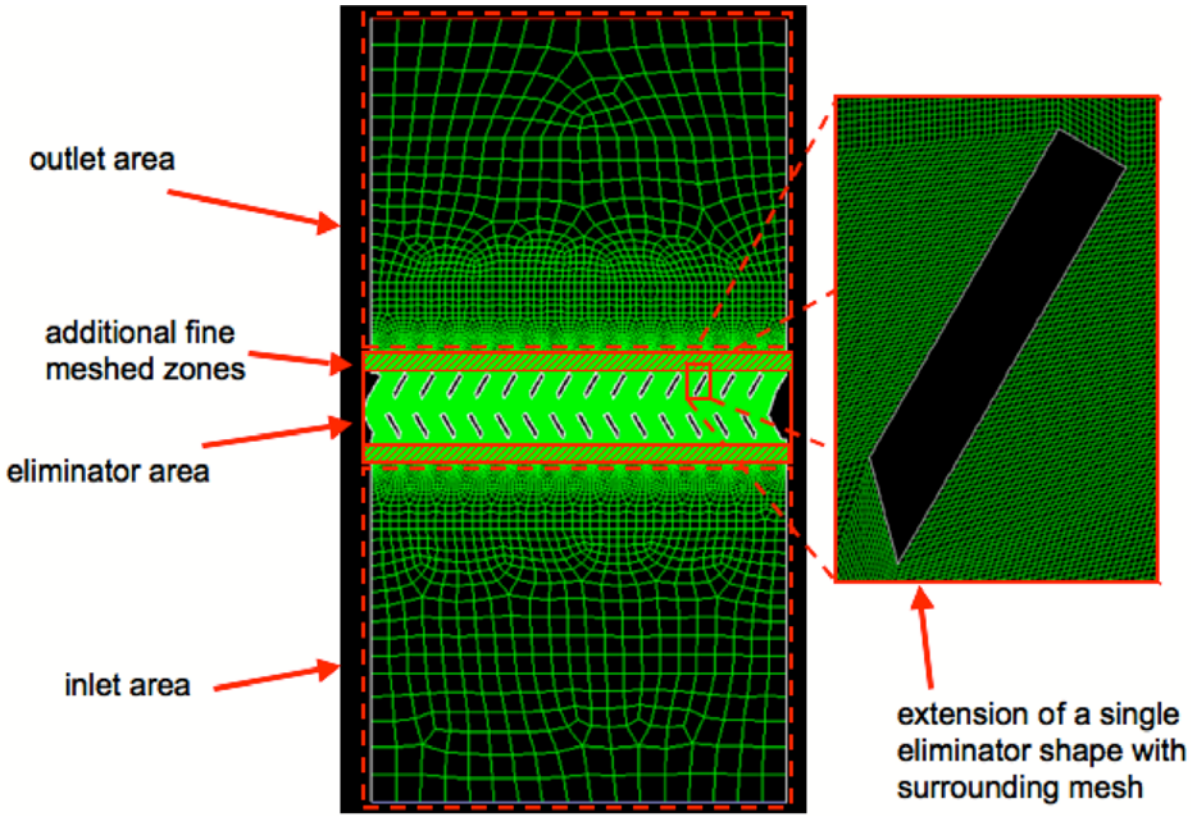

Figure 3.14: Example for one grid created in GAMBIT with different zones

4 Mathematical model and numerical simulation in FLUENT

In this chapter a short introduction to FLUENT, the fluid dynamics program, which is used in this work for all flow simulations, is given first. Then, the equations determining the behaviour of a steady, incompressible flow in their differential form are discussed. Afterwards, the different algorithms are presented, which are used in FLUENT for the simulation to solve the obtained system of equations, as well as the boundary conditions. Models to define the physical properties of the flow and applied criteria to evaluate the convergence are also introduced.

4.1 Introduction to FLUENT

FlUENT is a computational code, written in the computer language C and used to calculate and simulate miscellaneous types of fluid flows by using the finite volume method. It is developed and distributed by the FLUENT Inc. Company.

FLUENT is able to simulate two- or three- dimensional geometries in a wide range of flow problems varying from steady or unsteady, compressible or incompressible, turbulent or laminar flows to combustion, heat transfer, two- phase flows and chemical reactions. By means of the simulations of FLUENT it is possible to construct new machines, forecast the functioning of technical installations, design energy generation processes as well as production processes, etc. It is used in the aircraft and automobile industry, architecture, etc.

In FLUENT are several programs available, but in this work only the mesh and geometry generation software GAMBIT and FLUENT itself are used. GAMBIT is the so- called preprocessor, which is used to build and discretise the computational domain, see section 3.2. With FLUENT the geometry and grid, built in GAMBIT, are interpreted, the properties of the problem are introduced, and the calculation of the problem is executed (processing). Finally, by means of FLUENT the results are displayed and analysed (postprocessing).

Once, a grid is imported into FLUENT, the characteristics of the physical problem to be solved have to be inserted. FLUENT offers several models, depending on the considered flow problem. The following can be chosen: If the energy equation is solved, if the laminar or turbulent (with several alternatives) equations are solved, if a multiphase flow is simulated, if heat radiation is considered, and if the flow is compressible or incompressible. Also, the boundary conditions have to be specified. In fact they are predetermined by the geometry built in GAMBIT, but in FLUENT these conditions can be quantified, for example: Velocity of

the flow at the inlet of the computational domain, or roughness of the established walls. Furthermore the properties of the flow medium(s) can be adjusted.

The next step is the specification of the numerical solution of the problem. Therefore several discretisation schemes are available in FLUENT. Based on the truncation error of the Taylor series there are first, second and third order schemes available. Furthermore, FLUENT provides several methods of pressure- velocity coupling (SIMPLE, SIMPLEC and Piso). After determining the solver properties the calculation can be started.

Finally, the gained results of the calculation can be "postprocessed", i. e. expressed and displayed, with FLUENT. The variables of interest of the problem, such as velocity, pressure, density, etc, are presented. With this final step of postprocessing, the numerical simulation can be regarded as completed.

In the following sections the methods applied in FLUENT to execute this work are described in detail.

4.2 Mathematical model of the problem

4.2.1 Governing equations (*Navier- Stokes* equations)

Now, the equations that govern the behavior of a two- dimensional flow are introduced.

- Mass conservation equation

$$\frac{\partial \rho}{\partial t} + \nabla\left(\rho \vec{u}\right) = 0 \tag{4.1}$$

- Momentum conservation equations

$$\rho \frac{Du}{Dt} = -\frac{\partial p}{\partial x} + \nabla\left(\mu \nabla u\right) + S_{Mx} \tag{4.2}$$

$$\rho \frac{Dv}{Dt} = -\frac{\partial p}{\partial y} + \nabla\left(\mu \nabla v\right) + S_{My} \tag{4.3}$$

Since only the pressure drop of the eliminators is examined the energy equation is not needed. Furthermore, only a steady flow is considered, which results in a constant value for the density and no alternation of the velocity with time. With the introduction of the Newtonian fluid model, which expresses the shear stresses as components of the velocity gradient, a system of three equations and three unknowns is obtained. This equation system could be solved by applying suitable boundary conditions.

Considering the form of the equation above (4.1 to 4.3) a similar structure can be observed. Introducing a generic variable ϕ in these equations and keeping in mind that the regarded flow is steady and incompressible; the following expression can be set up:

$$\nabla(\rho\phi\vec{u}) = \nabla(\Gamma\nabla\phi) + S_\phi \tag{4.4}$$

Equation (4.4) is the equation for the transport of the variable ϕ, representing different phenomena of transport (convection and diffusion (with Γ = diffusion coefficient)). The equation is the origin for the finite volumes method. By making ϕ equal to *1*, *u*, *v* and selecting suitable values for Γ and S_ϕ , it is possible to obtain the mass conservation equation and/or the momentum conservation equations. The finite volumes method is developed by integrating of equation (4.4) over a control volume V_c , obtaining:

$$\int_{V_c} \nabla(\rho\phi\vec{u})dV = \int_{V_c} \nabla(\Gamma\nabla\phi)dV + \int_{V_c} S_\phi dV \tag{4.5}$$

By applying Gauss's divergence theorem on the term on the left side of the equal sign (convective term) and on the first term on the right side (diffusion term), the equation (4.5) can be transformed. In general for an arbitrary vector $\vec{a}$ is:

$$\int_{V_c} \nabla\vec{a}dV = \int_{S_c} \vec{n}\vec{a}dA \tag{4.6}$$

Implemented on equation (4.5) one obtains:

$$\int_{S_c} \vec{n}(\rho\phi\vec{u})dA = \int_{S_c} \vec{n}(\Gamma\nabla\phi)dA + \int_{V_c} S_\phi dV \tag{4.7}$$

The convective term on the left side of the equal sign expresses the flow of the component of ϕ in the direction of the normal vector. It represents the disappearance of ϕ in the fluid element due to convection.

The diffusion term (first term on the right side of the equal sign) represents the progression of ϕ in the fluid due to diffusion. The last term of the equation stands for the increase of ϕ regarding associated sources of other phenomena.

Note that the present work is only dealing with a two- dimensional airflow. Therefore the control volume V_c has actually two dimensions (area) and the areas obtained by the divergence theorem one dimension (line).

4.2.2 Turbulence

Since in this project a turbulent flow is examined, the turbulence has to be calculated as well. In general, turbulent flows are defined over fluctuating velocity fields. The fluctuations cause other magnitudes, such as momentum, energy, etc., to fluctuate, too. Thus the fluctuations are small but of high frequency, the computational afford to calculate them in practical engineering equations is too high. Therefore the governing equation can be manipulated by removing the small scales. The result is an altered set of equations, whose calculation is less extensive. However, the modified equations contain new unknown variables and turbulence models have to be introduced to compute these new unknowns.

In FLUENT a number of turbulence models are existent, but in this work only the standard *k*- ε turbulence model is used.

There are two different methods to alter the Navier- Stokes equations to avoid direct calculation of small scale turbulence. The methods are *Reynolds*- averaging and filtering. The two methods introduce additional terms to the governing equations, which are to be modeled to obtain a solution for the unknowns. In connexion with the standard *k*- ε model the *Reynolds*- averaging is used in FLUENT.

Using Reynolds averaging means that the solution variables in the exact Navier- Stokes equation are decomposed into the average and fluctuating components. For the velocity components this can be expressed as:

$$u_i = \overline{u}_i + u_i' \tag{4.8}$$

where $\overline{u_i}$ and u_i' are the mean and fluctuating velocity components. For other scalar quantities:

$$\phi = \overline{\phi} + \phi' \tag{4.9}$$

where ϕ is a scalar, such as pressure, and $\overline{\phi}$ and ϕ' are the mean and fluctuating components. Inserting these forms into the mass and momentum conservation equations leads to the ensemble- averaged momentum equations, in Cartesian tensor form (and dropping the overbar on the mean velocity, $\overline{u}$) expressed as:

$$\frac{\partial}{\partial x_i}\left(\rho u_i\right) = 0 \tag{4.10}$$

$$\frac{\partial}{\partial x_j}\left(\rho u_i u_j\right) = -\frac{\partial p}{\partial x_i} + \frac{\partial}{\partial x_j}\left[\mu\left(\frac{\partial u_i}{\partial x_j} + \frac{\partial u_j}{\partial x_i} - \frac{2}{3}\delta_{ij}\frac{\partial u}{\partial x}\right)\right] + \frac{\partial}{\partial x_j}\left(-\rho\overline{u_i' u_j'}\right) \tag{4.11}$$

These equations are called the *Reynolds*- averaged *Navier- Stokes* (RANS) equations. They are of the same form as the *Navier- Stokes* equations. However, additional terms appear which represent the effects of turbulence. These *Reynolds*- stresses, $-\rho\overline{u_i' u_j'}$, have to be modeled in order to "close" the equation (4.11).

To model the *Reynolds*- stresses, in FLUENT the Bossinesq approach is used for the *k*- ε model. The Bossinesq approach relates the *Reynolds*- stresses to the mean velocity gradients:

$$-\rho\overline{u_i' u_j'} = \mu_t\left(\frac{\partial u_i}{\partial x_j} + \frac{\partial u_j}{\partial x_i}\right) - \frac{2}{3}\left(\rho k + \mu_t\frac{\partial u_k}{\partial x_k}\right)\delta_{ij} \tag{4.12}$$

The great advantage of this approach is the low computational effort associated with the computation of the turbulent viscosity, μ_t. In case of the *k*- ε model two additional transport equations have to be solved, one for the turbulence energy *k*, and another for the turbulence dissipation rate ε. μ_t is calculated as a function of *k* and ε. The disadvantage of the Bossinesq approach is that it considers μ_t as an isotropic scalar quantity, which is not true.

The kinetic energy, *k*, and its dissipation rate, ε, are obtained from the following transport equations:

$$\frac{\partial}{\partial x_i}(\rho k u_i) = \frac{\partial}{\partial x_j}\left[\left(\mu + \frac{\mu_t}{\sigma_k}\right)\frac{\partial k}{\partial x_j}\right] + G_k - \rho\varepsilon \tag{4.13}$$

$$\frac{\partial}{\partial x_i}\left(\rho\varepsilon u_i\right) = \frac{\partial}{\partial x_j}\left[\left(\mu + \frac{\mu_t}{\sigma_\varepsilon}\right)\frac{\partial \varepsilon}{\partial x_j}\right] + C_{1\varepsilon}\frac{\varepsilon}{k}G_k - C_{2\varepsilon}\rho\frac{\varepsilon^2}{k} \tag{4.14}$$

where the turbulent viscosity μ_t is

$$\mu_t = \rho C_\mu \frac{k^2}{\varepsilon} \qquad \text{with } C_\mu = const. \tag{4.15}$$

The generation of turbulence kinetic energy due to the mean velocity gradients, G_k, is defined as:

$$G_k = -\rho\overline{u_i' u_j'}\frac{\partial u_j}{\partial x_i} \tag{4.16}$$

The scalars $C_{1\varepsilon}$, $C_{2\varepsilon}$, C_μ, σ_k, and σ_ε are constants with the following values:

$$C_{1\varepsilon} = 1{,}44, \quad C_{2\varepsilon} = 1{,}92, \quad C_\mu = 0{,}09, \quad \sigma_k = 1{,}0, \quad \sigma_\varepsilon = 1{,}3 \tag{4.17}$$

These values are the default values provided by FLUENT. They were determined with air and water experiments and work properly for a wide range of problems.

4.3 Near- wall treatment

Walls affect turbulent flows significantly. The mean velocity field is affected by the no- slip condition, which has to be satisfied at the wall. But also, walls have an impact on turbulence in non- trivial ways. Close- by the wall, viscous damping reduces the tangential velocity fluctuations, while the normal fluctuations are reduced by kinematic blocking. However, beyond the near wall region, the large gradients in the mean velocity lead to rapid "production" of turbulent energy and consequently turbulence is increased.

The near- wall modeling has a major influence on the accuracy of numerical simulation, due to the fact that walls are the main sources for turbulence and vorticity. An accurate representation of wall regions is the key to predict wall- bounded turbulent flows. In this work the behaviour of the flow passing through the eliminator shapes is considered to be the main source for the pressure drop. Therefore, the treatment of the walls is considered to be key for obtaining exact numerical solutions from the simulations.

The near- wall region can be divided into three distinct layers. The closest one to the wall is called the "viscous sublayer", the flow is almost laminar. The opposite of this layer is fully-turbulent layer, where turbulence plays the major rule. Between these two sublayers is the third one, where the effects of the turbulent and the viscous sublayer have the same importance.

Traditionally, there are two different approaches to model the near- wall region. In one of them the inner, viscous sublayer is not resolved. Instead, so-called "wall functions" are applied. These functions are semi- empirical formulas. With these formulations the area between the wall and the turbulent sublayer is totally bridged. In this approach, the viscous sublayer is not considered.

The other approach regards the viscous sublayer as well as the other sublayers. This is achieved by modifying the turbulence model and a mesh fine enough in the near- wall region. It is called the "near- wall modeling" approach.

It is obvious that wall functions decrease the computational effort. But it is inadequate in cases where low- Reynolds- number effects dominate the flow domain.

In FLUENT, in conjunction with the *k*- ε model, it is possible to use both approaches. In the present work wall functions and enhanced wall treatment (as near- wall modeling approach) are applied.

FLUENT recommends the use of the different wall treatments depending on the value of y^+, which is defined as

$$y^+ \equiv \frac{\rho u_\tau y}{\mu} \tag{4.18}$$

where ρ is the density, μ the dynamic viscosity, and u_τ is the friction velocity, defined as

$$u_\tau = \sqrt{\frac{\tau_\omega}{\rho}} \tag{4.19}$$

where τ_ω is the shear force of the wall.

FLUENT suggests the use of wall functions for coarse grids, in which all wall- adjacent cell centroids are situated in the log- law layer. That means that the value of y^+ is $30 < y^+ < 300$. If the laminar sublayer is to be resolved by means of enhanced wall treatment, the grid has to be sufficiently fine, so that $y^+ = 1$ for the wall- adjacent cells. However, a higher value is acceptable, as long as it is in the viscous sublayer ($y^+ < 4$ to 5).

In FLUENT, the application either of walls function or enhanced wall treatment depends on the value of y^+. In turn, y^+ depends strongly on the cell size near the wall.

4.3.1 Wall functions

The standard wall functions in FLUENT are defined as:

- Momentum

  The law of the wall for the mean velocity yields is

$$U^* = \frac{1}{\kappa}\ln(Ey^*) \tag{4.20}$$

  where

$$U^* \equiv \frac{U_P C_\mu^{1/4} k_P^{1/2}}{\tau_\omega / \rho} \tag{4.21}$$

$$y^* \equiv \frac{\rho C_\mu^{1/4} k_P^{1/2} y_P}{\mu} \tag{4.22}$$

and κ = von Kármán constant (= 0,4187)

E = empirical constant (= 9,793)

U_P = mean velocity of the fluid at point P

k_P = turbulence kinetic energy at point P

y_P = distance from point P to the wall

μ = dynamic viscosity of the fluid

The logarithmic law for mean velocity is known to be valid for $30 < y^* < 300$. In FLUENT this law is applied when $y^* > 11{,}225$.

- Turbulence

  In the k- ε model, the k equation is solved over the whole domain, also for the wall- adjacent cells. At the wall it is imperative that:

$$\frac{\partial k}{\partial n} = 0 \tag{4.23}$$

  where n is the local coordinate normal to the wall.

  The production of kinetic energy, G_k, and its dissipation rate, ε, at the wall-bordering cells, which are considered to be the source terms in the k equation, are calculated by means of the local equilibrium hypothesis. Hence, the production of k and its dissipation rate are believed to be equal in the wall-bordering control volume.

  From this it follows that k can be calculated from

$$G_k \approx \tau_\omega \frac{\partial U}{\partial y} = \tau_\omega \frac{\tau_\omega}{\kappa \rho C_\mu^{1/4} k_P^{1/2} y_P} \tag{4.24}$$

  and ε follows from

$$\varepsilon_P = \frac{C_\mu^{3/4} k_P^{3/2}}{\kappa y_P} \tag{4.25}$$

The ε is not solved at the wall- bordering cell, instead equation (4.25) is used.

4.3.2 Enhanced wall treatment

Enhanced wall treatment is a method, with which the near- wall regions are modeled. It is a combination of a two- layer model and enhanced wall functions. If the mesh close to the wall is fine enough to be able to resolve the laminar sublayer, then the enhanced wall treatment is equal to the traditional two- layer zonal model (see below). But, the near- wall mesh increases the computational effort by being sufficiently fine. The best way is to have a near- wall formulation for coarse meshes and another one for fine meshes.

FLUENT can combine the two- layer model with enhanced wall functions to achieve the goal of having a near- wall approach and at the same time be able to use coarse meshes without significantly reducing the accuracy.

- Two- layer model for enhanced wall treatment

  In the near- wall model of FLUENT the near- wall region, which is affected by viscosity, is totally resolved. The two –layer approach is used to specify ε and the turbulent viscosity in the cells situated close to the wall. In this approach the domain is divided into either viscosity affected or fully turbulent regions. The border between these two regions is determined by a wall- distance- based, turbulent *Reynolds* number, Re_y, which is:

$$\mathrm{Re}_y \equiv \frac{\rho y \sqrt{k}}{\mu} \tag{4.26}$$

  where y is the normal distance from the wall to the cell centres. FLUENT interprets y as the distance to the nearest wall:

$$y \equiv \min_{\vec{r}_\omega \in \Gamma_\omega} \left\| \vec{r} - \vec{r}_\omega \right\| \tag{4.27}$$

  where $\vec{r}$ is the position vector at the field point, and $\vec{r}_\omega$ is the position vector on the wall boundary. Γ_ω is the union of all involved wall boundaries. By this interpretation, it is possible to define y uniquely in flow domains of complex shapes involving several walls. Also, in this way y is defined independently of the used mesh topology, and is definable even on structured grids.

  In the fully turbulent regions the k- ε model is employed.

  In the viscosity- affected near- wall region, the *Wolfstein* one- equation model is applied. This one- equation- model retains the momentum conservation and

the *k*- equation, but a new expression for the turbulent viscosity, μ_t, is established:

$$\mu_{t,2layer} = \rho C_\mu l_\mu \sqrt{k} \tag{4.28}$$

where the length scale l_μ is calculated from:

$$l_\mu = yC_l^*\left(1 - e^{-\mathrm{Re}_y/A_\mu}\right) \tag{4.29}$$

The above described two- layer formulation for the turbulent viscosity is a part of the enhanced wall treatment. In this formulation the two- layer definition is slightly mixed with the following high- *Reynolds*- number μ_t definition from the outer region:

$$\mu_{t,enh} = \lambda_\varepsilon \mu_t + (1 - \lambda_\varepsilon)\lambda_{t,2layer} \tag{4.30}$$

where is μ_t the high- *Reynolds*- number definition. A bleeding function, λ_ε, is defined in such a way that it is unity far from walls and is zero very far from walls. It is expressed as follows:

$$\lambda_\varepsilon = \frac{1}{2}\left[1 + \tanh\left(\frac{\mathrm{Re}_y - R_y^*}{A}\right)\right] \tag{4.31}$$

A is a constant that determines the width of the bleeding function. By defining a width so that the value of λ_ε is within 1% of its far- field value given a variation of ΔRe_y, the result is

$$A = \frac{\left|\Delta \mathrm{Re}_y\right|}{\tanh(0{,}98)} \tag{4.32}$$

Typical values for ΔRe_y are chosen between 5% and 20% of Re_y^*. The main purpose of the bleeding function λ_ε is to prevent solution convergence from being impeded when the *k*- ε solution in the outer layer does not match with the two- layer formulation.

The field ε is calculated from

$$\varepsilon = \frac{k^{3/2}}{l_\varepsilon} \tag{4.33}$$

The length scales l_ε of equation (5.33) is computed from

$$l_\varepsilon = yC_l^*\left(1 - e^{-\mathrm{Re}_y/A_\varepsilon}\right) \tag{4.34}$$

The constants in the length scales equations (5.29) and (5.30) are defined as:

$$C_l^* = \kappa C_\mu^{-3/4}, \quad A_\mu = 70, \quad A_\varepsilon = 2C_l^* \tag{4.35}$$

- Enhanced wall functions

To provide a method which is able to be extended throughout the near- wall region it is necessary to formulate the law- of- the- wall as a single law valid for the whole wall region. Therefore FLUENT blends linear (laminar) and logarithmic (turbulent) laws- of- the- wall using the following function:

$$u^+ = e^{\Gamma} u_{lam}^+ + e^{1/\Gamma} u_{turb}^+ \tag{4.36}$$

where the blending function is defined as:

$$\Gamma = -\frac{a(y^+)^4}{1 + by^+} \tag{4.37}$$

with a = 0,01 and b = 5.

Similarly, the general equation for the derivative $\frac{du^+}{dy^+}$ is

$$\frac{du^+}{dy^+} = e^{\Gamma} \frac{du_{lam}^+}{dy^+} + e^{1/\Gamma} \frac{du_{turb}^+}{dy^+} \tag{4.38}$$

This formulation enables the easy modification and extension of the fully turbulent law. In this way, other effects, such as pressure gradients or variable

properties can be taken into account. By applying this approach, the asymptotic behaviour for large and small values of y^+, as well as reasonable representation of velocity profiles for values of y^+ inside the wall buffer zone, is guaranteed ($3 < y^+ < 10$).

4.4 Simulation hypothesis

This paragraph is on schemata and algorithms used by FLUENT to discretise, linearise and solve the above introduced system of equations, integrated on the computational domain.

4.4.1 Numerical schema, segregated solver

In FLUENT it is possible to choose between two different numerical methods to solve the obtained equation system. The methods are the segregated and the coupled solver. In both solvers the used finite volume method consists of the following steps:

- Dividing of the computational domain into discrete control volumes due to the associated grid
- Integrating the governing equations over the individual control volumes to build a system of algebraic equations for the discretised unknowns (velocity, pressure)
- Linearising the discretised equations and solving the resulting equation system to obtain the values of the unknowns of the problem

The two different solvers use a similar process of discretisation (finite volumes), but the applied approximation to linearise and solve the problem is different. In the present work only the segregated solver is used. Therefore an introduction to this solver is given.

The segregated solver resolves the governing equations sequentially or, as the name implies, segregated. Hence, the governing equations are non- linear and coupled, they have to be solved iteratively to obtain a converged numerical solution. All iterations consist of several steps:

1. Updating of the properties of the flow referring to the current solution (for the first iteration these values agree with the initial values)
2. Simultaneous solution of the velocity components of the momentum conservation equations applying the updated value of the pressure and the mass fluxes of the control volume borders. In this way the velocity field is updated.
3. When the obtained velocity field values of the previous step are not adequate for the mass conservation equation for each control volume a pressure correction (e. g. Poisson) for the mass conservation equation is derived. Also, the momentum conservation equations are linearised. This correction is used to obtain the corrected velocity fields, pressure and mass fluxes, until the mass conservation equation is met.

4. The values of the current solution are used to solve equations of additional scalars, for example turbulent quantities and energy, if necessary.
5. Checking for the convergence of the equations. If the process has converged no further iterations are executed. Otherwise a new iteration is started until the desired convergence is reached.

Figure 4.1 shows the steps 1 to 5 in a shorter and more concise form.

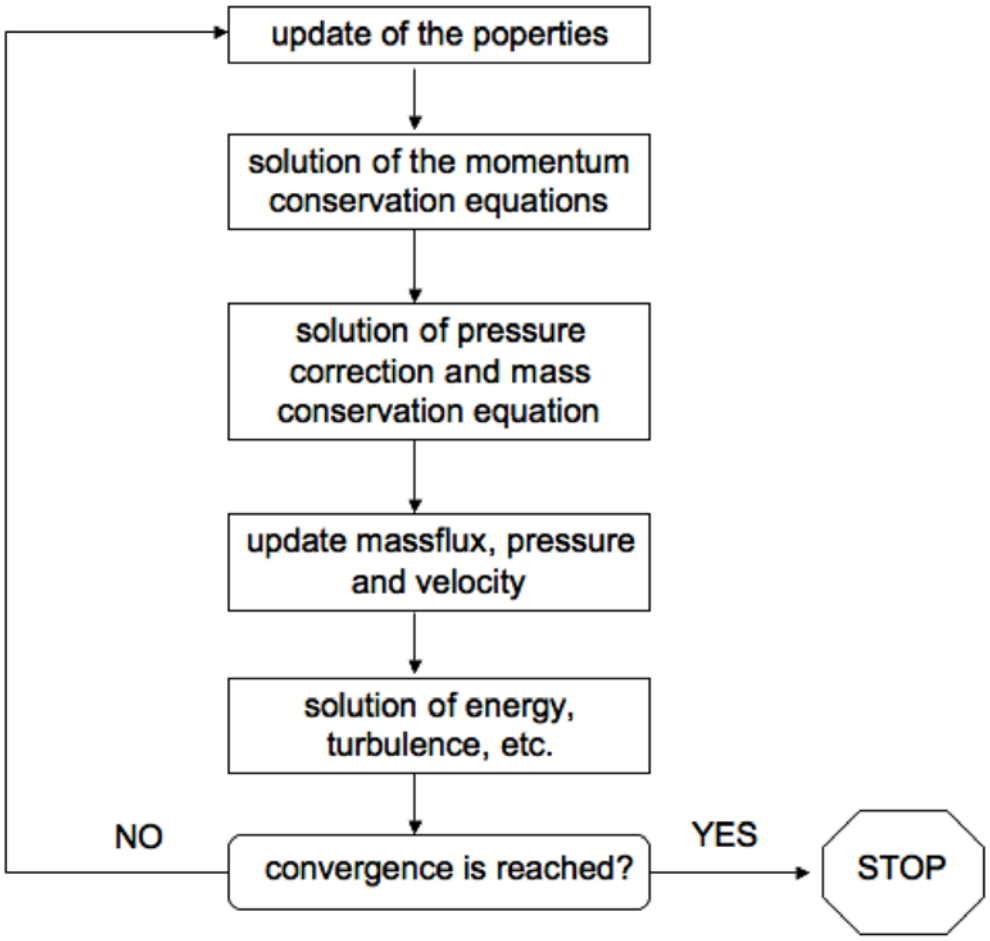

Figure 4.1: Schema of segregated solver

4.4.2 Linearisation

Irregardless of the method applied to solve the problem, the discretised equations have to be linearised to obtain an equations system for the dependent variables in each cell of the computational domain. The linearised equation system can be solved to obtain the values of the mentioned variables.

Depending on the way of linearisation one can obtain an implicit or explicit formulation of the problem. These expressions mean the following:

- *Implicit formulation*: For one unknown variable of the problem a value is calculated in each cell, using a relation. This relation includes the known values of this variable as well as the known values of the variable in other cells. These values are not known a

priori. Ergo, each unknown appears in more than one equation of the system and these equations have to be solved simultaneously to obtain the values of all unknowns.

- *Explicit formulation*: For one unknown of the problem, the value of this unknown in each cell is calculated by using a relation which only includes the known values of the unknown in other cells. Ergo, each unknown appears only in one equation of the system. These equations can be solved for each cell irrespective of all other cells.

The segregated solver linearises the discretised governing equation by applying the implicit formulation with respect to the dependent variable of the equation. Thereby it is possible to form a linear equation system with one equation for each cell of the computational domain. To solve the obtained equation system the Gauss- Seidel- method in combination with an algebraic multigrid method (AMG) is used. For example, the *x* component of the momentum conservation equation is linearised to obtain a system of equations, in which the *u* component of the velocity vector is the unknown variable. The simultaneous solution of this equation system, applying the algebraic multigrid method, makes way to receive the current value of the component *u* of the velocity field.

In short, the segregated solver solves all unknown values of all cells at the same time for one variable (the pressure, for example). Afterwards, it solves the next variable considering all cells at the same time, again in a successive way, until a solution is obtained for all variables. The segregated solver does not allow to work with an explicit formulation of the problem.

4.4.3 Schemes of interpolation and discretisation

FLUENT applies the finite volume method to convert the governing equations of a flow into algebraic ones, which can be solved numerically. This method consists of integrating the governing equation over each control volume (cell), resulting in a discrete equation system, which represents the conservation of the flowing magnitudes of each control volume.

When discretising the transport equation (4.4) for a steady case obtained by means of the finite volume method and for a triangle shaped control volume, as displayed in Figure 4.2, one receives:

$$\sum_{f}^{N} \rho_f \vec{u}_f \phi_f \vec{A}_f = \sum_{f}^{N} \Gamma_\phi (\nabla \phi)_n \vec{A}_f + S_\phi V \tag{4.39}$$

where N is the number of faces enclosing the cell, ϕ_f is the value of convected through face f, $\rho_f \vec{u}_f \vec{A}_f$ is the mass flux through the face f, $\vec{A}_f$ is the area of the face f, $(\nabla\phi)_n$ is the magnitude of $\nabla\phi$ in normal direction of the face f and V is the volume of the cell.

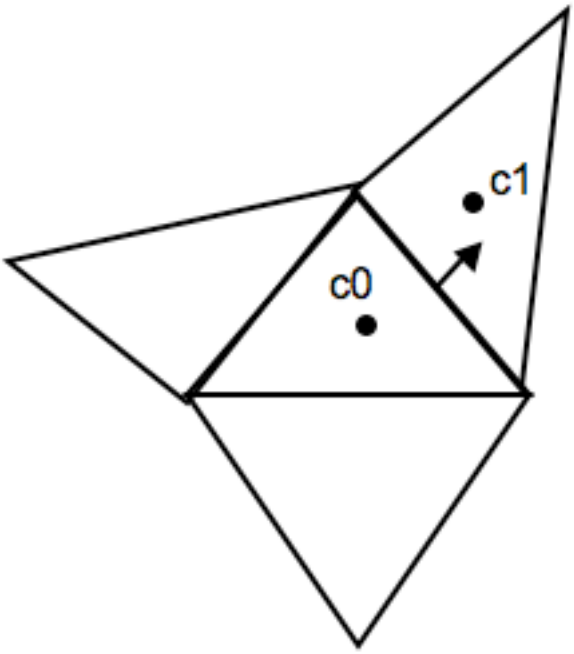

Figure 4.2: Scheme of finite volume method

FLUENT saves the discrete values of the variable ϕ by default in the center of the cells (c0 and c1 in Figure 4.2). However, the values of ϕ_f are needed. These values are obtained by interpolation of the values of the cell centers by a scheme, which is called *upwind*.

With an *upwind* scheme, it is possible to obtain the values of ϕ_f from the values of the upstream cells in the normal direction of the face vector. There are different types of *upwind* schemes available in FLUENT (first order *upwind* scheme, second order *upwind* scheme, exponential law and QUICK). In the present work only the second order *upwind* scheme is used.

Using a second order scheme means that the values of variables in the cells' faces are obtained by applying a multidimensional linear reconstruction approach. In this approach, a higher- order of precision is reached at cell faces by applying a Taylor series expansion of the cell centered solution about the cell centroid. Hence, with a second order upwind scheme the value of ϕ in the face *f* is computed by using the following expression:

$$\phi_f = \phi + \nabla\phi\Delta\vec{r} \tag{4.40}$$

where ϕ and $\nabla\phi$ are the values in the centre of the cell and the gradient with reference to the upstream cell, and $\Delta\vec{r}$ is the displacement vector from the upstream cell to the face centroid. This formulation requires to determine the gradient of $\nabla\phi$ in each cell. This is accomplished with the theorem of divergence, which is expressed in discrete form as:

$$\nabla\phi = \frac{1}{V}\sum \bar{\phi}_f \vec{A} \tag{4.41}$$

The summation is over all faces belonging to the cell. $\bar{\phi}_f$ is the calculated average value of cell and the neighbouring cell with the same face. There are different ways to compute it. A cell based gradient evaluation and a node based one. Here the cell based form is used, where $\bar{\phi}_f$ is the arithmetic average at the neighbouring cell centres, ϕ_{c0} and ϕ_{c1}:

$$\bar{\phi}_f = \frac{\phi_{c0} + \phi_{c1}}{2} \tag{4.42}$$

FLUENT uses interpolation schemes to discretise the momentum and mass conservation equations. For the segregated solver the interpolation scheme is based on the momentum and mass conservation equation in their integral form.

$$\oint \rho \vec{u} d\vec{A} = 0 \tag{4.43}$$

$$\oint \rho \vec{u}\vec{u} d\vec{A} = -\oint pI d\vec{A} + \oint \bar{\bar{\tau}} d\vec{A} + \int_V \vec{F} dV \tag{4.44}$$

where I is the identity matrix, $\bar{\bar{\tau}}$ the stress tensor, and $\vec{F}$ the force vector.

With the same procedure as mentioned above, it is possible to discretise the momentum conservation equation. For instance for the x component of this equation (with u as the component of the velocity in direction of x) the following expression is obtained:

$$a_P u = \sum a_{nb} u_{nb} + \sum p_f A \hat{i} + S \tag{4.45}$$

If the pressure field and the mass fluxes through the faces are known, equation (4.45) can be solved by applying the discretisation methods named above, obtaining the velocity field. However, the pressure field and the face mass fluxes are not known a priori, but are a part of the solution. With the storage of the values of the pressure field and discretisation of the pressure gradient term very important matters are connected, which are now considered.

In FLUENT pressure and velocity are stored in the cell centres by using a co- located scheme. But for solving the equation (4.45) the values of the pressure of the face between cell c0 and c1, as shown in Figure 4.2, are needed. Therefore, it is necessary to apply an interpolation scheme, which allows to obtain the values of the pressure at the faces from the cell values.

- Pressure interpolation scheme

  In this work a second order scheme is used to interpolate the pressure. It calculates the pressure in a face in the same way as an *upwind* scheme. This scheme provides a higher accuracy than other schemes offered by FLUENT (default scheme, linear scheme). But it can also cause problems when a grid of poor quality is used. In cases with discontinuous pressure gradients this scheme should not be used, but this does not apply to the present work.

The discretisation of the mass conservation equation (4.43) is achieved by integration over the control volume. The result is the following expression:

$$\sum_{f}^{N_{faces}} J_f A_f = 0 \tag{4.46}$$

where J_f is the mass flux through face *f*, ρu_n .

In order to continue with the process, the values of the face velocities, $\vec{u}_n$, have to be connected with the stored velocities of the cell centres. However, linear interpolation between the face velocities and the velocity in the cell centres leads to unphysical checker- boarding of pressure. To avoid that, FLUENT does not interpolate the velocities linearly. Instead momentum- weighted averaging, with weighted factors based on the a_p coefficients of equation (4.45), is applied. Thus the mass face flux J_f may be written as:

$$J_f = \rho_f \frac{a_{p,c0} u_{n,c0} + a_{p,c1} u_{n,c1}}{a_{p,c0} + a_{p,c1}} + d_f((p_{c0} + (\nabla p)_{c0} \vec{r}_0) - (p_{c1} + (\nabla p)_{c1} \vec{r}_1)) = \hat{J}_f + d_f(p_{c0} - p_{c1}) \tag{4.47}$$

where p_{c0}, p_{c1} and $u_{n,c0}$, $u_{n,c1}$ are the pressures and normal velocities within the cells on the two sides of the face *f*, and $\hat{J}_f$ contains the influence of the velocities in these cells. The term of d_f is a function of $\overline{a}_P$, which is the average of momentum equation coefficients a_P for the cells connected with the face *f*.

4.3.3.1 Density interpolation schemes

For compressible flows, FLUENT uses upwind interpolation of density at the cells. There are several interpolation schemes available. Since in this work an incompressible flow is examineded an interpolation of the density is not applied. In fact FLUENT calculates the density for incompressible flows by means of arithmetic averaging.

4.3.3.1 Pressure velocity coupling

By altering equation (4.45), a further condition for the pressure can be added and pressure velocity coupling is achieved. FLUENT provides five different possibilities of pressure velocity coupling. However, in the present work only the SIMPLE algorithm is employed.

The SIMPLE algorithm uses a relation between the velocity and the pressure correction to accomplish the mass conservation equation and to obtain the pressure field. By means of a guessed pressure field *p** the momentum conservation equation can be solved, and the mass flux J_f^* over the face *f* is obtained by:

$$J_f^* = \hat{J}_f^* + d_f(p_{c0}^* - p_{c1}^*) \tag{4.48}$$

Equation (4.48) does not satisfy the mass conservation equation. Therefore a correction, $J_f^{|}$, has to be added to the face flux J_f^*, in such a way that corrected mass flux, J_f

$$J_f = J_f^* + J_f^{|} \tag{4.49}$$

satisfies the mass conservation equation. The SIMPLE algorithm assumes the above mentioned correction as:

$$J_f^{|} = d_f(p_{c0}^{|} - p_{c1}^{|}) \tag{4.50}$$

where $p^{|}$ is the pressure correction in the cell.

The SIMPLE algorithm inserts the correction equations, (4.49) and (4.50), into the discrete mass conservation equation, (4.46), in order to obtain a discrete equation for the corrected cell pressure value.

$$a_P p^{|} = \sum_{nb} a_{nb} p_{nb}^{|} + b \tag{4.51}$$

where *b* represents the net flow rate into the cell. It is given by

$$b = \sum_{f}^{N_{faces}} J_f^* A_f \tag{4.52}$$

The pressure correction equation, (4.51), can be solved applying the algebraic multigrid (AMG) method. Once a solution is obtained the pressure in the cells and the mass flow rate over the faces can be corrected using the following expressions:

$$p = p^{*} + \alpha_p p' \tag{4.53}$$

$$J_f = J_f^{*} + d_f (p'_{c0} - p'_{c1}) \tag{4.54}$$

where α_p is the under- relaxation factor for the pressure. Now, with the new corrected face flow, J_f, the discrete mass conservation equation can be satisfied identically for each iteration.

4.5 Boundary conditions

Boundary conditions are the applied conditions at the limits or boundaries of the computational domain. They are necessary to be able to close the system of the governing equations and solve the concerning problem.

There are many different types of boundary conditions available in FLUENT. But, in the present work only three different types are used and therefore introduced: *Velocity inlet*, *pressure outlet* and *wall*.

- *Velocity inlet*: Is used to define the velocity, and other scalar properties, in the entrance zones of the flow. In this work several velocities are introduced to the computational domain.
- *Pressure outlet*: Is used to define the static pressure of the flow at outflow zones (together with other scalar variables, in case of backflow). In the present work the static pressure is chosen as 0 Pa for all calculations.
- *Wall*: Is applied to introduce the boundary condition associated with a solid surface or wall. It is possible to specify properties, such as heat transfer, roughness, etc. For this work the default values of FLUENT are retained.

4.6 Iterative convergence

As already mentioned, the governing equations of the flow are solved by means of an iterative calculation. During the process of iteration to obtain a solution of the problem, it is very important to control that the algorithm converges to a final solution, because it is possible that the FLUENT code does not converge, or even does not stabilise in one value, and iterates in an infinite way.

4.6.1 Residuals

The residuals are one of the most important tools to control the convergence during the iterative calculation. In general, they represent the difference of values of the variables to solve between two iterations. When a code converges, these differences incline to reduce and stabilise in a very "small" value. In an ideal case the differences become zero, but the computers of today own only a finite accuracy. Nowadays, magnitude drops of 10^{-6} (simple-precision) and 10^{-12} (double- precision) with respect to the initial values are reached.

Depending on the applied solver, FLUENT defines the residuals in a different way. As a segregated solver is used for this project, the definition of the residuals for this type of solver is stated now.

After the process of equation discretisation, the conservation equation for a general variable ϕ at a cell P can be expressed as followed:

$$a_p \phi_p = \sum_{nb} a_{nb} \phi_{nb} + b \tag{4.55}$$

where a_P is the central coefficient of the cell P, a_{nb} are the coefficients of the neighbouring cells, and b is the contribution of the constant part of the source term S_C ($S = S_C + S_P \phi$).

Consequently, equation (4.55) can be written as:

$$aP = \sum_{nb} a_{nb} - S_P \tag{4.56}$$

The residual R^{ϕ} calculated by the segregated solver is the sum of the differences of the terms in equation (4.55) for all cells P of the computational domain. This value is also named "unnamed" residual. It may be expressed as:

$$R^{\phi} = \sum_{cells\, P} \left| \sum_{nb} a_{nb} \phi_{nb} + b - a_P \phi_P \right| \tag{4.57}$$

In general, it is difficult to evaluate the convergence based on the obtained results of equation (4.57) without scaling, because it is difficult to know, a priori, which value of the residuals can be an acceptable to consider the code to be converged. To solve these problems, the "scaled" residuals are applied, which are defined as:

$$R^{\phi} = \frac{\sum_{cells\,P} \left| \sum_{nb} a_{nb}\phi_{nb} + b - a_P\phi_P \right|}{\sum_{cells\,P} \left| a_P\phi_P \right|} \tag{4.58}$$

in the momentum equations the dominator term $a_P\phi_P$ is repalced by $a_P v_P$ to obtain the residuals where v_p is the magnitude of the velocity at cell P.

For the mass conservation equation the "unscaled" residuals are defined as:

$$R^C = \sum_{cells\,P} \left| rate\ of\ \ mass\ creation\ in\ cell\ P \right| \tag{4.59}$$

Whilst the "scaled" residuals are obtained by:

$$\frac{R^C_{iteration\,N}}{R^C_{iteration\,5}} \tag{4.60}$$

Where the dominator is the largest absolute value of the continuity residual of the first five iterations.

4.6.2 Convergation criteria

Judging convergence cannot be achieved by a universal method. Convergence criteria which work for one kind of calculation can be misleading in another. Therefore, to evaluate the convergence process of a calculation a combination of different criteria is considered. First of all it is essential to monitor the residuals of the iteration process. Furthermore, the behaviour of a magnitude of interest (pressure, for example) has to be regarded, too. Finally, the global mass balance has to be satisfied.

Now the mentioned criteria are described explicitly.

- *Scaled residuals*: The default convergence criterion used by FLUENT for the scaled residuals is suitable for most problems. To satisfy it, the scaled residuals, defined by equation (4.27) or (4.29), have to decrease to 10^{-3} for all equations.
- *Magnitude of interest*: A magnitude of interest, such as pressure, is observed during the calculation process in a certain point. Considering the two computational domains for the two different types of eliminators, the point is situated just above the eliminators. During the convergence process the magnitude of interest should stabilise in a certain value.

The value of the magnitude of interest in the certain point is evaluated by a FLUENT offered report type. There are several types available, but only the area-weighted average type is applied. The area- weighted average of a quantity is calculated by dividing the summation of the product of the chosen field variable and facet area by the total surface of the area:

$$\frac{1}{A}\int \phi dA = \frac{1}{A}\sum_{i=1}^{n} \phi_i |A_i| \tag{4.30}$$

- *Global mass balance*: Should be satisfied by an error of only 10^{-16} kg/s at the end of the iteration process. That means that the value of the mass flow entering the computational domain through the inlet has to be equal to the mass flow leaving through the outlet (for an incompressible flow).

These three criteria have to be completed for a calculation to be considered as "converged".

4.7 Resume

In this short sector all the above models and the method applied in FLUENT for the calculations of this work are summarised in some tables, in order to give a review. Table 4.1 displays the used models, Table 4.2 the solver properties. The used interpolation and discretization schemes are stated in Table 4.3. Finally, Table 5.4 shows the under- relaxation factors.

Table 4.1: Used Models

Mass conservation equation	two dimensional, steady state
Momentum conservation equation	two dimensional, steady state
Turbulence model	k- ε
Wall models	Enhanced wall treatment, wall functions

Table 4.2: Properties of the applied solver

Solver	Segregated
Formulation	Implicit
Gradient evaluation	Cell- based
Velocity formulation	Absolute
Domain dimension	Two dimensional
Time dependence	Steady

Table 4.3: Used interpolation and discretization schemes

Pressure	Second order upwind
Pressure- velocity coupling	SIMPLE
Momentum equation	Second order upwind
Turbulence kinetic energy	Second order upwind
Turbulence dissipation rate	Second order upwind

Table 4.4: Under- relaxation factors

Pressure	0,3
Density	1
Body forces	1
Momentum	0,7
Turbulence kinetic energy	0,8
Turbulence dissipation rate	0,8
Turbulent viscosity	1

5 Errors and uncertainty

This chapter presents the methodology of estimating the numerical uncertainty and the results obtained by applying it on the computational domain of this work. Also, another method of determining the independence of the solution of the grid size is introduced dealing with the value of y^+. Finally, the two methods are compared.

5.1 Introduction

It is obvious that computational fluid dynamics (CFD) is of high interest for companies working on the mechanical engineering sector. Compared to experiments, its low costs and its versatile application makes it very attractive for such companies. However, one must not forget that in CFD different types of models are used. Making decisions on wrong calculated CFD results may, in some cases, only lead to loss of time and money, but it could also cause collapses and break downs of structures and machines.

Therefore it is very important to bear in mind that numerical simulations involve uncertainties. In experimental examinations it is a widespread method to estimate the uncertainty of the obtained results. In CFD the uncertainty of the simulation should be considered, too.

For that reason the criterions of influence on the uncertainties of numerical studies and the obtained results were executed. There was an intent to follow the example of the experimental estimation of uncertainties. The two most relevant publications of guides estimating the incertitude were made by the *American Institute of Aeronautics and Astronautics* (AIAA) in 1998 and the *European Research Community on Fluids, Turbulence and Combustion* (ERCOFTAC) in 2000.

In the above paragraphs the subjects of error and uncertainty are brought up. According to [15] a small definition is given:

- Error is defined as the difference between an observed or calculated value and the true value. The so-called systematic or bias errors are connected with consistent or repeatable sources or, if truly random, they are connected with random fluctuations, which tend to have a *Gaussian* distribution. Considering numerical simulations executed on today's computers only systematic or bias errors will appear.
- Uncertainty is defined as the percentage or estimated amount of an observed or calculated value that differs from the true one. There are three sources of uncertainty in a simulation:

1. *Input uncertainty*: results from poor defined parameters
2. *Model uncertainty*: results from alternative model formulations, structure or implementation
3. *Numerical uncertainty*: results from influences of discretization and iterative convergence errors, it is the only uncertainty that cannot be eliminated

5.2 Verification and validation

Knowing that uncertainty is an inherent aspect of numerical simulation, methods are needed to quantify the level of confidence on the obtained results. The following nomenclature is applied by the AIAA (1999) and Oberkampf and Trucano (2002) and is largely accepted:

- Verification: Process which determines the reliability whether the implemented model corresponds to the conceptual model
- Validation: Is the determination whether the implemented model corresponds to and explains some phenomena in the real world

5.2.1 Verification

The process of verification implies the quantification of the errors. It is supposed that program errors (“bugs“) and errors introduced by the user can be disregarded. But the rounding errors, iterative convergence errors and discretization errors have to be estimated.

- Rounding errors can be evaluated by comparing the obtained results of CFD using different precision levels of the computer. This task must not be realized due to using the maximum precision available of the solver provided by the FLUENT code (2ddp, 2 dimensional double precision).
- Iterative convergence errors can be quantified by investigating the effects of the systematic variation of truncation of all residuals.
- Discretization errors are quantified by a systematic refinement of the grid. There exists a methodology of refinement, which allows to carry out a study of the grid and estimate the numerical uncertainty.

5.2.2 Validation

The process of validation is an attempt to quantify the uncertainty of the associated CFD model. On the one hand this is achieved by studying the numerical uncertainty and on the other hand by comparing the obtained numerical results with experimental data. In the present work only experimental data of other authors can be used to evaluate the numerical results, see 3.1.

5.3 Methodology for estimation of numerical uncertainty

5.3.1 Introduction

Before applying a grid convergence study, some particular activities are supposed to be completed, related with code verification. With the expression “verification“ it is meant that the computer code is able to solve a system of non- linear coupled partial differential equations with a properly posed set of initial and/or boundary conditions. Furthermore, the code must approach the exact solution to these equations when sufficiently fine grid resolution is given. In addition iterative convergence has to be achieved with at least three orders of magnitude decrease in correctly normalized residuals for each equation solved over the whole computational domain. This is one of the matters which is analysed with FLUENT later on.

The following method was introduced by C. J. Freitas et al. [17] and it is the proposal of the *Computational Fluid Dynamics Technical Committe* of the *American Society of Mechanical Engineers* (ASME) and of the *American Institute of Aeronautics and Astronautics* (AIAA) to quantify the numerical uncertainty associated with a numerical simulation. The methodology consists of five steps.

- Step 1

  A representative cell, mesh or grid size h is defined. The following is defined for three- dimensional, structured, geometrically similar grids:

  $$h = (\Delta x_{\max} \cdot \Delta y_{\max} \cdot \Delta z_{\max})^{1/3} \tag{5.1}$$

  for unstructured grids:

  $$h = \left(\frac{1}{N} \sum_{i=1}^{N} \Delta V_i \right)^{1/3} \tag{5.2}$$

  with:

  Δx_{max} as the maximum distance of the representative cell in x- direction
  Δy_{max} as the maximum distance of the representative cell in y- direction
  Δz_{max} as the maximum distance of the representative cell in z- direction
  ΔV_i as the volume f the i^{th} cell
  N as the total cell number of the computational domain

- Step 2

  With three significantly different sets of grid resolutions, preferably integer factors of each other, simulations have to be run and key variables that are important to the objective of the simulation determined. Here the variable ϕ is introduced as an example. The refinement factor

$$r = h_{coarse} / h_{fine} \tag{5.3}$$

should be greater than 1,3.

This value of 1,3 is based on experience. The refinement is required to be done systematically and geometrically similar cells are to be preferred.

- Step 3

With three different grids, described by the subscripted numbers of 1, 2 and 3. The grids have to meet the following requirement: $h_1 < h_2 < h_3$. The factors of refinement can be calculated as follows:

$$r_{21} = \frac{h_2}{h_1} \quad \text{(connecting the smallest grid with the medium one)} \tag{5.4}$$

$$r_{32} = \frac{h_3}{h_2} \quad \text{(connecting the biggest grid with the medium one)} \tag{5.5}$$

With these factors one can calculate the apparent (or observed) order, p, of the method:

$$p = \frac{1}{\ln r_{21}} \cdot \left(\ln \left| \frac{\varepsilon 32}{\varepsilon 21} \right| + q(p) \right) \tag{5.6}$$

$$q(p) = \ln \left(\frac{r_{21}^p - s}{r_{32}^p - s} \right) \tag{5.7}$$

$$s = 1 \cdot sign \left(\frac{\varepsilon_{32}}{\varepsilon_{21}} \right) \tag{5.8}$$

where $\varepsilon_{32} = \phi_3 - \phi_2$ and $\varepsilon_{21} = \phi_2 - \phi_1$, and ϕ_k denotes the simulation value of the variable on the k^{th} grid. r = *constant* for $q(p) = 0$. This is a set of three equations, which can be solved using fixed- point iteration, with an initial guess to the first of $q = 0$, for example.

At least four grids are required to demonstrate that the observed order of p is constant for a simulation series. It all depends on the used initial grid resolution and where the predicted value of ϕ lies as a function of the grid resolution.

- Step 4

  Calculation of extrapolated values from the equations

$$\phi_{ext}^{21} = \frac{\left(r_{21}^{p}\phi_1 - \phi_2\right)}{\left(r_{21}^{p} - 1\right)} \tag{5.9}$$

$$\phi_{ext}^{32} = \frac{\left(r_{32}^{p}\phi_2 - \phi_3\right)}{\left(r_{32}^{p} - 1\right)} \tag{5.10}$$

- Step 5

  With *p*, the apparent order of the method, one can calculate the following error estimates:

  Approximate relative error:

$$e_a^{21} = \left|\frac{\phi_1 - \phi_2}{\phi_1}\right| \tag{5.11}$$

$$e_a^{32} = \left|\frac{\phi_2 - \phi_3}{\phi_2}\right| \tag{5.12}$$

  Estimated extrapolated relative error:

$$e_{ext}^{21} = \left|\frac{\phi_{ext}^{21} - \phi_1}{\phi_{ext}^{21}}\right| \tag{5.13}$$

$$e_{ext}^{32} = \left|\frac{\phi_{ext}^{32} - \phi_2}{\phi_{ext}^{32}}\right| \tag{5.14}$$

  With the equations stated above, it is possible to calculate the *Grid Convergence Index, GCI*:

$$GCI_{fine} = \frac{Fs \cdot e_a^{21}}{r_{21}^{p} - 1} \tag{5.15}$$

$$GCI_{coarse} = \frac{Fs \cdot e_a^{32}}{r_{32}^{p} - 1} \tag{5.16}$$

where *Fs* is a safety factor. At the beginning Roache chose a value of *Fs = 3* (1993). But later the value was improved for three grid studies by a more conservative one: *Fs = 1,25* (Roache (1998)). Roache obtained this value by empirical studies and it roughly correlates with the definition of uncertainty *U* used by Coleman and Stern (1997). It implies that using a value of 1,25 leads to a *GCI* with 95% confidence interval.

If the order of the method, *p*, is less than "1" a value of $p = 1$ can be used to obtain an error band as well. However, this is not necessary and the *GCI* with the original order of the method is the most conservative approach.

5.3.2 Study of the grid sensibility

The goal of the grid sensibility study is to determine the influence of the alignment of the nodes and/or the size of the cells on the results of the numerical simulation. Hence, it is possible to evaluate the accuracy of the results calculated with a certain mesh bearing in mind the mesh size and consequently the computational effort.

In order to implement the study of grid sensibility it is necessary to choose the zone or zones inside the computational domain which have the biggest influence on the flow. That is to say, the zones of the domain where the major gradient of the flowing magnitudes may occur. Thus, in these zones the cell sizes play an important role on the later obtained results and the sensibility study has to be applied there.

In the present work, the zone of the computational domain where the eliminators are situated is regarded for the uncertainty methodology, because examining the behaviour of the flow when passing through the eliminators is the main objective.

The uncertainty study is applied different times on the two geometries of eliminators, each time with different considerations. First, the eliminator area where the eliminators are situated is considered, regarding the eliminators as the main source of pressure loss in the computational domain. In this case the cells are very small, so that values of y^+ close to the magnitude of one are reached. Therefore the approach of the enhanced wall treatment is used for the wall nearby cells.

Figure 5.1 shows the entire computational domain for the wooden lath eliminator again, with the marked eliminator area and an extension for one single eliminator. Figure 5.2 shows the same for the asbesto- cement eliminator type.

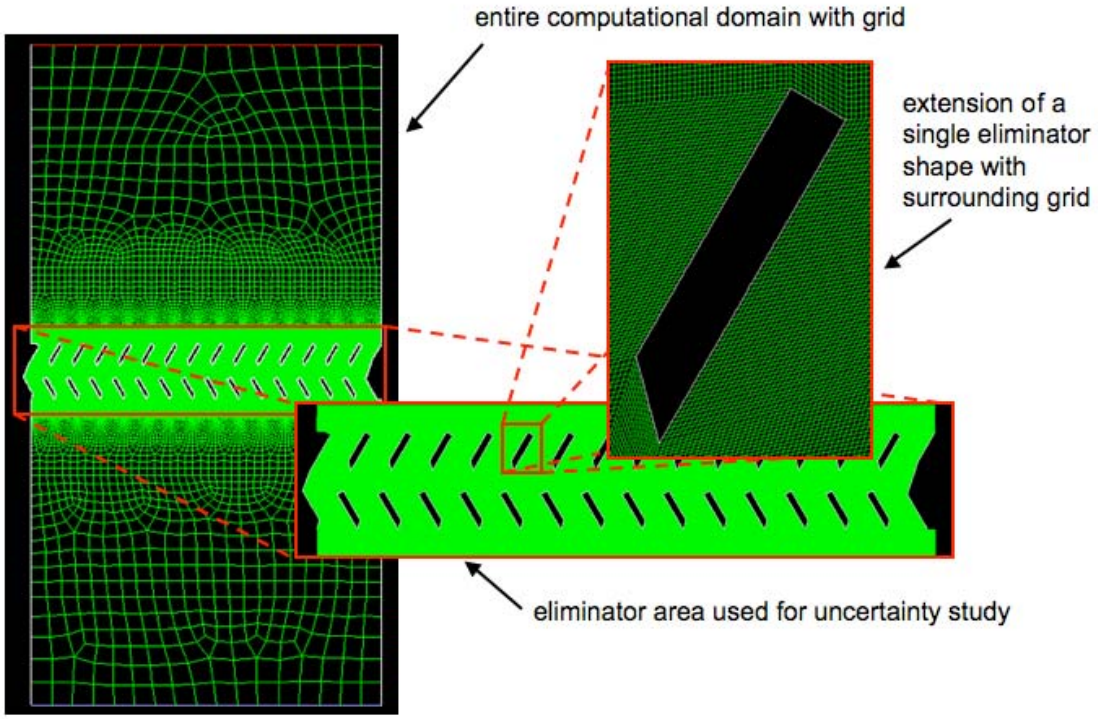

Figure 5.1: Computational domain of wooden lath eliminator with marked eliminator area

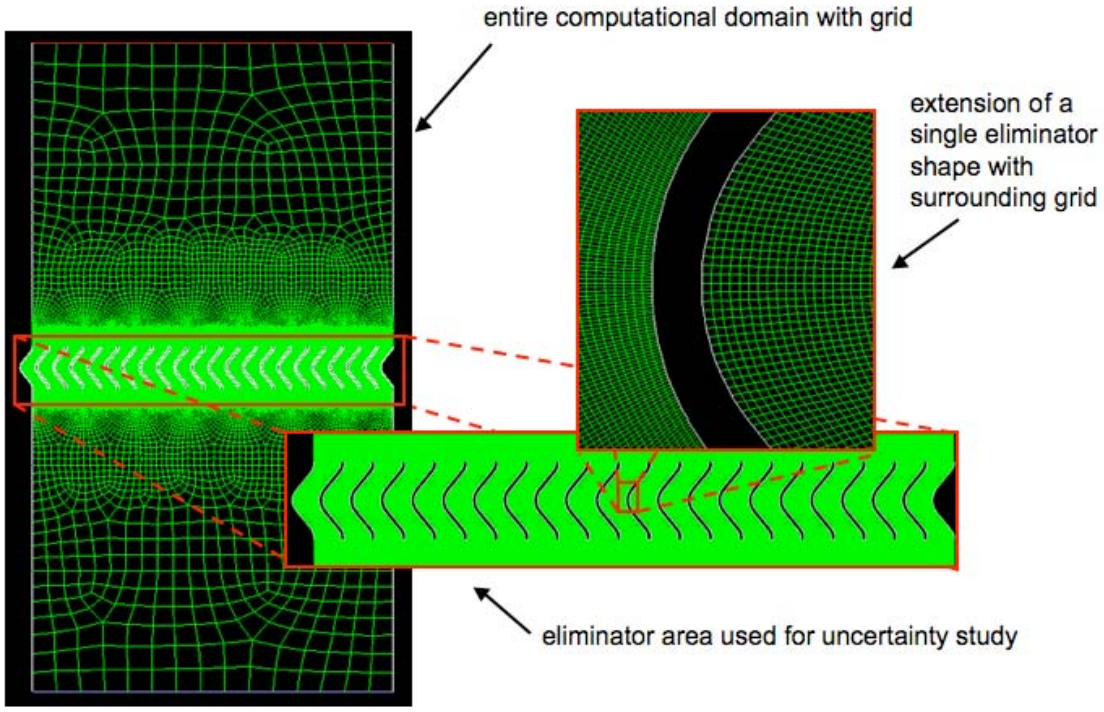

Figure 5.2: Computational domain of asbesto- cement eliminator with marked eliminator area

Second, the study is applied by only regarding the wall adjacent cells, exactly, only the cells within a distance of 0,5 cm to the eliminator walls. This is motivated by the consideration that the actual main influences of the flow are the boundary layers around each single eliminator shape. In this case, the enhanced wall treatment is also used to model the near wall behaviour of the flow.

The wall adjacent cells, which are used for the second uncertainty study, are displayed in Figure 5.3 for the wooden lath eliminator, and in Figure 5.4 for the asbesto- cement eliminators geometry. In both figures the used cells are coloured red.

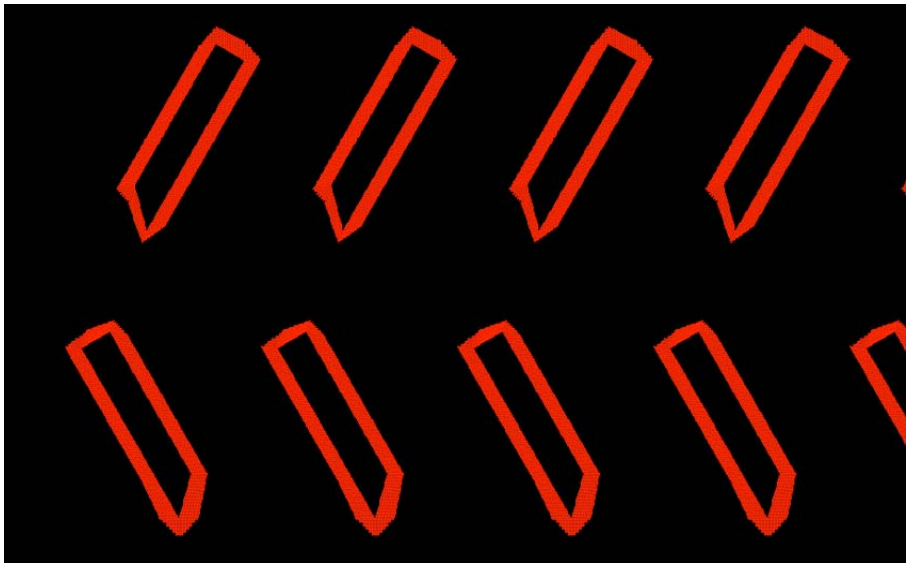

Figure 5.3: Wall adjacent cells of the wooden lath eliminator used for the uncertainty study

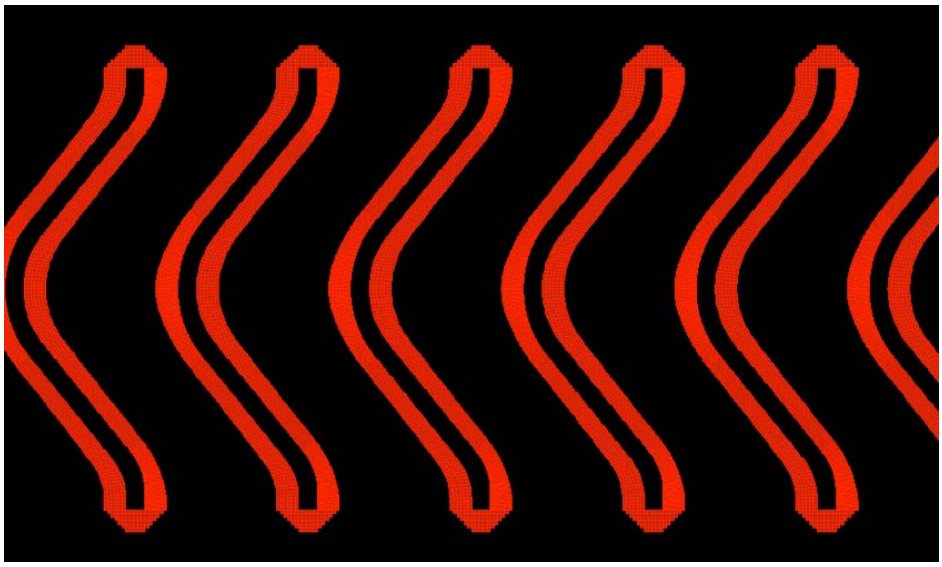

Figure 5.4: Wall adjacent cells of the asbesto- cement eliminator used for the uncertainty study

The methodology is applied a third and last time for the two different geometries. This time with coarser grids. Thus, there are fewer cells and consequently the value of y^+ is around the magnitude of thirty or beyond, wall functions are used for the near wall approach. This consideration is encouraged by the thought of decreasing the number of cells significantly to make the computational effort as small as possible.

Two reference cases have been employed for carrying out this grid sensibility study, each one corresponding to the two basic eliminator geometries analysed. Inlet velocities of 1,52 m s^{-1} and 1,58 m s^{-1} have respectively been considered for each reference case. The pressure loss induced by the eliminators has been taken as reference variable for analysing the results obtained of the grid sensibility study. Taking into account that a relative pressure of zero has

been imposed at the outlet section in all cases and that the pressure loss and the average pressure at the inlet section of the domain are coincident.

In the next sections the used meshes for three applications of the methodology are described.

5.3.2.1 Sensibility study considering eliminator area using enhanced wall treatment

In this section the grids and results for the uncertainty study considering the eliminator area and using enhanced wall treatment are described.

A set of different grids has to be built, according to the criterion of the methodology of section 5.3.1. That is to say, the specific cell size *h* of a grid must be at least 1,3 times bigger than that of the next finer grid, see formula (5.3).

$$r = \frac{h_{coarse}}{h_{fine}} \leq 1,3 \tag{5.17}$$

With the definition of the specific cell size *h* of formula (5.2) and for a two- dimensional case, it follows:

$$\left(\frac{\sum \Delta V_i}{N_{coarse}}\right)^{1/2} = 1,3\left(\frac{\sum \Delta V_j}{N_{fine}}\right)^{1/2} \tag{5.18}$$

Thus, the volume (in the present case, the volume is an area) of the computational domain is constant for each grid, formula (5.18) may be written as:

$$\sqrt{N_{fine}} = 1,3\sqrt{N_{coarse}} \rightarrow N_{fine} = 1,7\,N_{coarse} \tag{5.19}$$

This means that the number of cells of each finer grid is 1,7 times greater than that of previous coarser grid.

Now, several grids are built by applying the correlation of (5.19). Because, by using the minimum value of $h_{coarse}/h_{fine}=1,3$ more grids can be built and the computational effort can be limited. The objective is to build the coarsest mesh with around 90000 cells. This leads to the next finer grids with 152000, 257000, etc. It is obvious that the mentioned exact number for a grid, for example 90000, cannot be accomplished. The true number of cells may differ. For example, the number of cells for the grid for the wooden lath eliminator, which is supposed to have 90000 cells, has 85269.

Now, the grids, their properties and the results for the wooden lath eliminator are presented first.

5.3.2.1.1 Wooden lath eliminator

In order to get a satisfactory Grid Convergence Index (*GCI*), successive grid refinement was carried out and the study applied. Six grids were created and considered with a number of cells varying from 85269 to 1486781. It should be kept in mind that these values correspond to the number of cells in the considered influence area of this case, which is the eliminator area. The main characteristics of the grids and the obtained pressure losses are presented in Table 5.1.

Table 5.1: Properties of grids for the wooden lath eliminator

Grid number [-]	Cell number [-]	Average cell area [m^2]	Representative cell size *h* [-]	Average inlet pressure [Pa]
6	85269	3,48E-06	0,001865747	5,5264
5	152589	1,95E-06	0,001394856	5,4769
4	280341	1,06E-06	0,001028854	5,4214
3	496734	5,97E-07	0,00077287	5,3734
2	866069	3,43E-07	0,000585303	5,3184
1	1486781	2,00E-07	0,000446699	5,3060

In table 5.2 the results of the grid sensibility study, as it has been previously defined, are presented. The refinement factors ($r_{coarse/centre}$, $r_{centre/fine}$), the relations between the solutions of the calculations ($\varepsilon_{coarse/centre}$, $\varepsilon_{centre/fine}$), the approximate relative error ($e_a^{centre/fine}$) and the Grid Convergence Index ($GCI_{centre/fine}$) have been presented for each set of grids as representative parameters for broaching this type of sensibility studies.

Table 5.2: Results of the uncertainty study for the wooden lath eliminator, considering only the eliminator zone and using enhanced wall treatment.

Set of grid	6 – 5 – 4	5 – 4 – 3	4 – 3 – 2	3 – 2 – 1
$r_{coarse/centre}$ [-]	1,34	1,36	1,33	1,32
$r_{centre/fine}$ [-]	1,36	1,33	1,32	1,31
$\varepsilon_{coarse/centre}$ [-]	0,0496	0,0555	0,0480	0,0550
$\varepsilon_{centre/fine}$ [-]	0,0555	0,0480	0,0550	0,0124
p	-0,23	0,28	-0,58	5,31
$e_a^{centre\,/\,fine}$ [%]	1,02	0,89	1,03	0,87
$GCI_{centre/fine}$ [%]	-19,28	13,50	-8,67	0,09

The refinement factors are all around 1,3, due to the idea explained above. The order of the method p is almost constant, it is only changing between -0,58 in the third set of grids and 0,28 in the second one. Only the last set breaks ranks and the values of p are much bigger than one.

The *GCI* seems to oscillate. The last value of the *GCI*, 0,09% can be accepted as more than sufficiently small. However, the two finest grids need a lot of computational resources. The last grid was only built to see if the value of the *GCI* kept falling.

The approximate error resulted to be very small for all sets and the values can be considered as more as satisfying.

As can be seen in Table 5.2 some values for the order of the method, p, are negative. This results in a negative value for the Grid Convergence Index, *GCI*, as well. In the introduction of uncertainty methodology in section 5.3.1 the possibility is described to insert the value of one for the order of the method, p, if it is $p < 1$. However, it is not said if this could be done as well if the order of the method, p, was negative, $p < 0$. However, it is supposed to be possible, too. Due to results of order of the method, p, in Table 4.2, Table 4.3 states the results again with replaced original values of p with $p = 1$.

Table 5.3: Results of the uncertainty study for the wooden lath eliminator, considering only the eliminator zone, using enhanced wall treatment and inserting $p = 1$.

Set of grid	6 – 5 – 4	5 – 4 – 3	4 – 3 – 2
p	1,00	1,00	1,00
$e_a^{centre/fine}$ [%]	1,02	0,89	1,03
$GCI_{centre/fine}$ [%]	3,59	3,37	4,03

Now, the *GCI* is around 3,5- 4% for all sets of grids and all values for the *GCI* are acceptable. But the original values should not be forgotten, as they are the more conservative approaches.

In this case it is considered that grid 3 would be the best choice for further calculations. The value of the *GCI* may be higher for grid 3 than for grid 1, but the calculated pressure values only deviate 1,25% from each other. The great advantage of grid 3 over the other two finer grids is the relatively low computational effort needed for the calculations.

5.3.2.1.2 Asbesto- cement eliminator

Table 5.4 shows the properties of the meshes built for the uncertainty study for the asbesto-cement eliminator geometry. The coarsest grid possesses 90000 cells (only eliminator area), such as the coarsest grid of the wooden lath eliminator. Also, to satisfy the criterion of the uncertainty study the next finer grid must have a 1,7 times greater number of cells, etc. In the case of this geometry only five grids are built, with a cell number of the finest grid of 844000. The result including the finest grid is already satisfying. However, the computational effort for the finest grid is extensive by now. Table 5.5 shows the result of the study for the asbesto-cement eliminator.

Table 5.4: Properties of grids for the asbesto- cement eliminator

Grid number [-]	Cell number [-]	Average cell area [m^2]	Representative cell size h [-]	Average inlet pressure [Pa]
5	90000	3,12E-06	0,001765203	2,8142
4	152000	1,62E-06	0,001273513	2,7708
3	257000	9,53E-07	0,000976189	2,9214
2	476000	5,50E-07	0,00074162	3,1072
1	844000	3,22E-07	0,000567222	3,0169

Table 5.5: Results of the uncertainty study for the asbesto- cement eliminator, considering only the eliminator zone and using enhanced wall treatment.

Set of grid	5 – 4 – 3	4 – 3 – 2	3 – 2 – 1
$r_{coarse/centre}$ [-]	1,37	1,30	1,32
$r_{centre/fine}$ [-]	1,30	1,32	1,31
$\varepsilon_{coarse/centre}$ [-]	0,043	-0,151	-0,186
$\varepsilon_{centre/fine}$ [-]	-0,151	-0,186	0,090
p	-4,46	-0,65	2,65
$e_a^{centre/fine}$ [%]	5,15	5,97	2,99
$GCI_{centre/fine}$ [%]	-9,27	-45,39	3,62

Only for the last set of grids an acceptable value of the *GCI* is calculated. The others are too high and even negative. The order of the method, *p*, can not be regarded as constant, but the value seems to increase from step to step.

For two of the sets of grids the order of the method, *p*, is negative. Therefore the results are stated in Table 5.6 again with a value of $p = 1$.

Table 5.6: Results of the uncertainty study for the asbesto- cement eliminator, considering only the eliminator zone, using enhanced wall treatment and inserting $p = 1$.

Set of grid	5 – 4 – 3	4 – 3 – 2
p	1,00	1,00
$e_a^{centre/fine}$ [%]	5,15	5,97
$GCI_{centre/fine}$ [%]	21,16	23,63

Changing the original value of *p* to $p = 1$ results in positive values for the *GCI*. However, the values are, with around 20%, very big and not very satisfying.

In this case the best grid for further considerations may also be the grid with around 500000 cells (grid 2), because of the little deviation to the finest grid (≈ 0,09 Pa) and the less computational effort.

5.3.2.2 Sensibility study considering near- wall cells using enhanced wall treatment

As already mentioned, the idea of only regarding the near- wall cells for the uncertainty study is that near- wall boundary layers are considered to be the main impact on the flow and the pressure drop.

In FLUENT there exists the possibility to adapt grids. The magnitude on which the cells are adapted can be chosen. For example, the cells are adapted to a certain value of y^+. That means that the volume or area of the wall touching cells is changed in such a way that the required value is met (Remember, all magnitudes depend on the cell sizes). Also, in FLUENT it is possible to adapt a certain number of wall adjacent rows. This possibility is used in the present case. All cells within a 0,5 cm distance to the single eliminator shape walls are adapted. See Figure 5.3 above for the wooden lath eliminator and 5.4 for the asbesto- cement eliminator. The value of 0,5 cm is derived by trying on the one hand to consider as much as possible of the wall-near cells and on the other hand to keep the computational effort small.

The adaptation process in FLUENT divides the existent cells in four smaller cells, see Figure 5.5. That means the refinement factors for the uncertainty study are $r_{coarse/fine} = 2$. In the following two small sections the results for the study only considering the wall adjacent cells are presented. Again, first for the wooden lath eliminator and for the asbesto- cement eliminator.

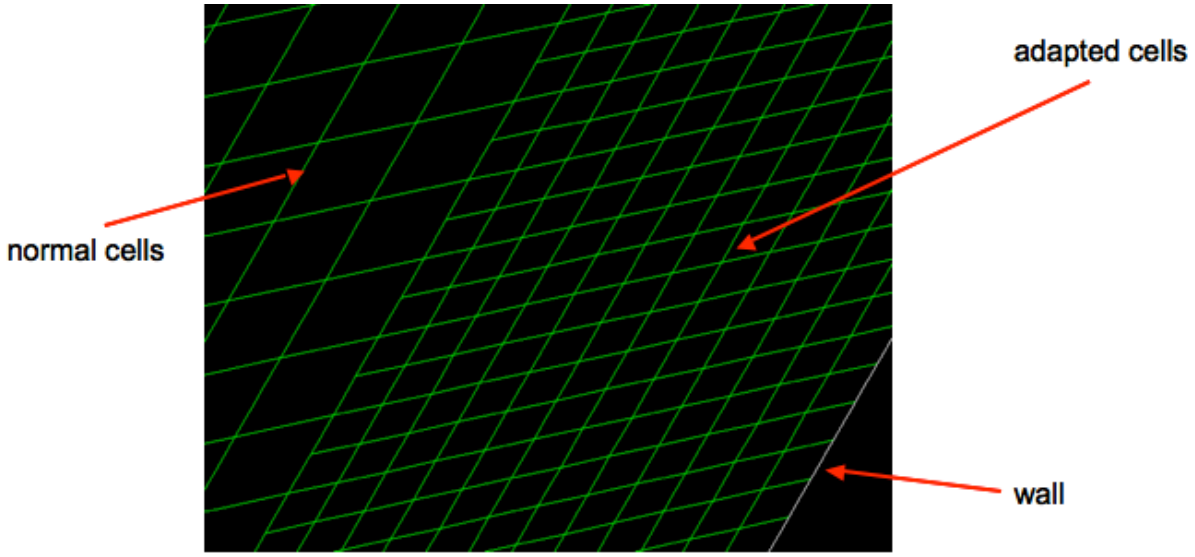

Figure 5.5: Grid adaptation in FLUENT

5.3.2.2.1 Wooden lath eliminator

The meshes used for this uncertainty study are some of the same grids used in the study considering the entire eliminator area. That is to say, the grids with 85269, 152589, 280341 and 496743 cells in the eliminator area. Now, of course only the first rows of the near wall cells are regarded. And on the other hand two new grids are added, which are first rows adaptation of the grids with 280341 and 496743 cells. In the grid with 280341 cells in the

eliminator area in the near- wall distance of 0,5 cm, which is considered for the study, six rows of cells are adapted, resulting in new twelve adapted rows. In case of the grid with 496743 cells in the eliminator zone the first eight rows are adapted, leading to new sixteen adapted rows.

Table 5.7 displays the properties of the different grids used. The grid number refers to the numbers assigned to the grids in section 5.3.2.1. The new introduced numbers “3a“ and “4a“ indicate the adapted meshes

Table 5.7: Properties of grids and adapted grids for the wooden lath eliminator

Grid number [-]	Cell number [-]	First rows cell number	Average cell area [m^2]	Representative cell size *h* [-]	Average inlet pressure [Pa]
6	85269	10814	3,20E-06	0,001788854	5,5264
5	152589	18382	1,80E-06	0,001341641	5,4769
4	280341	29420	9,67E-07	0,000983362	5,4214
4a	368601	118398	2,42E-07	0,000491681	5,3785
3	496734	52266	5,48E-07	0,00074027	5,3734
3a	653532	210022	1,37E-07	0,000370135	5,2843
2	866069	96758	3,18E-07	0,000563915	5,3184
1	1486781	161828	1,84E-07	0,00042945	5,3060

Due to the adaptation process the refinement factor for grid 4 and the adapted grid 4a is r_{44a} = 2. Hence, the refinement factor including the next finer grid, which is grid 3, is r_{34a} = 1,51. However, the resulting representative cell size of grid 4a is almost the same as of grid 1, the refinement factor r_{14a} = 1,15. Thus, the criterion of the uncertainty methodology is not satisfied. Therefore the uncertainty study is applied on different sets of grids, for example 4 – 3 – 4a and 3 – 2 – 3a, where partly the same grids are used and overlap. Table 5.8 displays the results for the study.

The row of grid number 1 is shaded grey because it is not used for the following study. Thus, the representative cell size *h* of this grid is similar to the ones of grid number 3a and 4a. The refinement factors are r_{13a} = 1,16 and r_{4a1} = 1,15 and consequently not adequate for the uncertainty methodology.

Table 5.8: Results of the uncertainty study for the wooden lath eliminator, considering only cells within a distance of 0,5cm to the wall and using enhanced wall treatment.

Set of grid	6 – 5 – 4	5 – 4 – 3	4 – 3 – 2	4 – 3 – 4a	3 – 2 – 3a
$r_{coarse/centre}$ [-]	1,33	1,36	1,33	1,33	1,31
$r_{centre/fine}$ [-]	1,36	1,33	1,31	1,51	1,52
$\varepsilon_{coarse/centre}$ [-]	0,0496	0,0555	0,0480	0,0480	0,0549
$\varepsilon_{centre/fine}$ [-]	0,0555	0,0480	0,0550	-0,0051	0,0341
p	-0,12	0,18	-0,64	7,68	1,64
$e_a^{centre/fine}$ [%]	1,02	0,89	1,03	0,09	0,65
$GCI_{centre/fine}$ [%]	-35,43	21,12	-8,09	0,01	0,81

The values of the first three sets of grids are, of course, similar to the values of the uncertainty study regarding the eliminator zone, because of a slight change of the refinement factors. The values for the *GCI* for the sets of grids using the grids with adapted first rows are very satisfying. For the set 4 – 3 – 4a a value of 0,01% is calculated, but for the next set of grid using even finer grids the *GCI* is slightly increased again.

Some of the values for the order of the method, *p*, of table 5.8 are negative. They can be replaced with $p = 1$ as in the previous section. The result is denoted in Table 5.9.

Table 5.9: Results of the uncertainty study for the wooden lath eliminator, considering only cells within a distance of 0,5cm to the wall, using enhanced wall treatment and inserting $p = 1$.

Set of grid	6 – 5 – 4	5 – 4 – 3	4 – 3 – 2
p	1,00	1,00	1,00
$e_a^{centre/fine}$ [%]	1,02	0,89	1,03
$GCI_{centre/fine}$ [%]	3,51	3,40	4,13

With the changed p all values of the *GCI* can be considered to be small enough. They are all around 3,50- 4%.

With the grid 4a a grid is found, which on the one hand is accessible due to its relatively small number of cells, and on the other hand has a very small value of *GCI*.

5.3.2.2.2 Asbesto- cement eliminator

For the asbesto- cement eliminator geometry the proceeding applied is the same that is used for the wooden lath eliminator. This means that for the uncertainty study of only the near-wall cells the grids used are the same grids as those in the study of the entire eliminator area. Furthermore two additional meshes are built by adapting the first rows of the meshes with 257920 and 494480 cells in the eliminator zone. In the case of the mesh with 257920 cells the first five rows are adapted, which results in new ten first rows. In the mesh with 494480 cells the first seven rows are adapted, leading to new fourteen first rows. Table 5.10 shows the grid properties used for the study.

Table 5.10: Properties of grids and adapted grids for the asbesto- cement eliminator

Grid number [-]	Cell number [-]	First rows cell number [-]	Average cell area [m^2]	Representative cell size *h* [-]	Average inlet pressure [Pa]
5	88032	21304	2,96E-06	0,001788854	2,8142
4	168729	29680	1,57E-06	0,001341641	2,7708
3	286681	48450	9,22E-07	0,000983362	2,9214
3a	432031	194220	2,31E-07	0,000480104	3,1065
2	494480	88396	5,22E-07	0,00074027	3,1072
2a	759668	354172	1,31E-07	0,000361248	2,8664
1	846855	148014	3,08E-07	0,000554977	3,0169

As well as for the wooden lath eliminator, the refinement factor r_{13a} = 1,16 does not fit the methodology criterion. Therefore different overlapping sets of grids are used (3 – 2 – 3a, 2 – 1 – 2a). Table 5.11 displays the results for the uncertainty study for the grids of Table 5.10.

Table 5.11: Results of the uncertainty study for the asbesto- cement eliminator, considering only cells within a distance of 0,5 cm to the wall and using enhanced wall treatment.

Set of grid	5 – 4 – 3	4 – 3 – 2	3 – 2 – 3a	2 – 1 – 2a
$r_{coarse/centre}$ [-]	1,37	1,30	1,33	1,30
$r_{centre/fine}$ [-]	1,30	1,33	1,50	1,54
$\varepsilon_{coarse/centre}$ [-]	0,0434	-0,1506	-0,1858	0,0903
$\varepsilon_{centre/fine}$ [-]	-0,1506	-0,1858	0,0007	0,1588
p	-4,49	-0,52	19,61	-0,19
$e_a^{centre/fine}$ [%]	5,15	5,97	0,02	5,56
$GCI_{centre/fine}$ [%]	-9,24	-54,25	9,31E-06	-87,95

It attracts the attention that the Grid Convergence Index reaches a positive value only one time. However, this value, for the set of grids 3 – 2 – 3a, is almost zero. But for the next set of grids, 2 – 1 – 2a, where the representative cell size is smaller a value of -87,95% is calculated for the *GCI*. Also, the approximate error is around 5% for all grids, only for the set 2 – 1 – 2a it is almost zero.

The negative values of the order of the method, *p*, are changed again to $p = 1$. The result is shown in Table 5.12.

Table 5.12: Results of the uncertainty study for the asbesto- cement eliminator, considering only cells within a distance of 0,5cm to the wall, using enhanced wall treatment and inserting $p = 1$.

Set of grid	5 – 4 – 3	4 – 3 – 2	2 – 1 – 2a
p	1,00	1,00	1,00
$e_a^{centre/fine}$ [%]	5,15	5,97	5,56
$GCI_{centre/fine}$ [%]	21,13	22,72	12,95

The new value of *p* turns the value of the *GCI* positive. However, the values continue to be high. Only for the set 2 – 1 – 2a the value is in an acceptable range.

Here, the grid 3a would be the best choice for further calculations, regarding the *GCI* and the computational effort.

5.3.2.3 Sensibility study considering eliminator area using wall functions

In the case of these studies the built grids are much coarser than in the studies using enhanced wall treatment. FLUENTS' guidelines declare to use wall functions for values of y^+ around 30 to 500. Therefore the finest grids of the uncertainty study for the two geometries must have a value of y^+ about 30. The following coarser meshes have to complete the criterion of the methodology regarding the refinement factor $r_{coarse/fine} \geq 1{,}3$. As in section 5.3.2.1 only the eliminator zone is considered.

As can be seen above for the uncertainty studies using enhanced wall treatment, in order to reach small values of uncertainty the cell number of the grids has to be increased very much. Therefore the uncertainty methodology is applied on grids with relative big cells in order to decrease the computational effort.

In the next sections the results of the study are presented, again in the same sequence: First the wooden lath eliminator, then the asbesto- cement eliminator.

5.3.2.3.1 Wooden lath eliminator

For this study four grids are built. Their properties can be seen in Table 5.13. The numeration is orientated at the grids of the two previous studies, in which the grids are finer. Therefore the finest mesh has now number "7" (the coarsest mesh in the studies with enhanced wall treatment has number 6).

Table 5.13: Properties of coarse grids for the wooden lath eliminator

Grid number [-]	Cell number [-]	Average cell area [m^2]	Representative cell size *h* [-]	Average inlet pressure [Pa]
10	1444	2,05E-04	0,014317821	5,5985
9	6616	4,50E-05	0,006708204	6,1393
8	11405	2,61E-05	0,005107935	5,9968
7	35400	8,39E-06	0,002896550	5,7125

The following Table 5.14 shows the results for the study. Now, some refinement factors are around the value of two and are therefore more than adequate for the methodology.

Table 5.14: Results of the uncertainty study for the wooden lath eliminator, considering only the eliminator zone and using wall functions.

Set of grid	10 – 9 – 8	9 – 8 – 7
$r_{coarse/centre}$ [-]	2,12	1,31
$r_{centre/fine}$ [-]	1,31	1,76
$\varepsilon_{coarse/centre}$ [-]	-0,5408	0,1426
$\varepsilon_{centre/fine}$ [-]	0,1426	0,2843
p	2,10	0,10
$e_a^{centre/fine}$ [%]	2,38	4,98
$GCI_{centre/fine}$ [%]	3,84	103,38

For the first set of grid the approximate relative error is 2,38% less than the half of the value for the second set of grids. The error is pretty small, as well as for the second set of grids. However, only the *GCI* for the first set results is small. For the second set the *GCI* is beyond 100%.

For the second set of grid the order of the method, *p*, can be changed with the value of $p = 1$. The new result is stated in Table 5.15.

Table 5.15: Results of the uncertainty study for the wooden lath eliminator, considering only the eliminator zone cells, using wall functions and inserting $p = 1$.

Set of grid	9 – 8 – 7
p	1,00
$e_a^{centre/fine}$ [%]	4,98
$GCI_{centre/fine}$ [%]	8,15

With p = 1the *GCI* can be reduced from 103,38% to 8,15%, which carries still a great uncertainty.

The best grid choice may be grid 8. In cases with coarse grids, the computational effort is irrelevant. The decision must be taken by considering only the *GCI*.

5.3.2.3.2 Asbesto- cement eliminator

As well as for the wooden lath eliminator, four grids are built for the study. The numeration is again orientated at the grids of the uncertainty study using enhanced wall treatment. Now, the finest mesh has number "6" (the coarsest mesh in the studies above is grid 5). In Table 5.16 the properties of the grids are displayed. Table 5.17 shows the results.

Table 5.16: Properties of coarse grids for the asbesto- cement eliminator

Grid number [-]	Cell number [-]	Average cell area [m^2]	Representative cell size *h* [-]	Average inlet pressure [Pa]
9	4176	6,69E-05	0,008179242	3,7202
8	12496	2,22E-05	0,004711688	3,4258
7	33847	8,16E-06	0,002856326	3,0161
6	78340	3,49E-06	0,001868154	2,9938

Table 5.17: Results of the uncertainty study for the asbesto- cement eliminator, considering only the eliminator zone and using wall functions.

Set of grid	9 – 8 – 7	8 – 7 – 6
$r_{coarse/centre}$ [-]	1,74	1,65
$r_{centre/fine}$ [-]	1,65	1,53
$\varepsilon_{coarse/centre}$ [-]	0,2944	0,4097
$\varepsilon_{centre/fine}$ [-]	0,4097	0,0223
p	-0,82	5,74
$e_a^{centre/fine}$ [%]	13,58	0,75
$GCI_{centre/fine}$ [%]	-50,68	0,09

For the second set of grids the approximate relative error and the *GCI* is very small. But for the first set these values are even higher.

The set of grid 9 – 8 – 7 has a negative value for the order of the method, *p*. Therefore Table 5.18 shows the result again with $p = 1$.

Table 5.18: Results of the uncertainty study for the asbesto- eliminator, considering only the eliminator zone cells, using wall functions and inserting $p = 1$.

Set of grid	9 – 8 – 7
p	1,00
$e_a^{centre/fine}$ [%]	13,58
$GCI_{centre/fine}$ [%]	26,14

Also, with a changed value for p the *GCI* is with 26,14% too high.

Of the four tested grids, grid 6 should be considered for further calculations.

5.4 Study of grids considering the value of y^+

Another method to determine the dependence of the calculated solution from the grid size is to evaluate the results obtained by different grids and the value of y^+. As already mentioned the boundary layers of the flow seem to have the main impact on the behaviour of the flow and the resulting pressure drop. FLUENT recommends to use the different wall approaches, wall functions and enhanced wall treatment in the present work, from the value of y^+. To reach a small value of y^+ a fine grid has to be built and vice versa for big values of y^+ a coarse grid has to be built. In these considerations it is supposed that the cells are distributed evenly, meaning that a grid with very small wall- touching cells has also relative small cells in regions without wall contact.

With this idea it is possible to create various grids and evaluate the solution, that is to say the variable which is of interest. In the present work, as for the previous sections of uncertainty studies, the pressure is of interest. With a decreasing value of y^+, and the grid getting finer, the solution converges in a certain value. That means that by keeping decreasing the cell size the obtained value does not change.

This new introduced method is applied on several grids. On the one hand the grids are known from the uncertainty studies of the previous sections, and on the other hand some new grids are built and added. As already said several times, the near wall approach of enhanced wall treatment is, actually, only recommended for small values of y^+. However, in this study enhanced wall treatment is used for the entire spectrum of grids to use the same approach for all grids.

In the following section 5.4.1 the results for the y^+ study for the wooden lath eliminator are presented and in section 5.4.2 for the asbesto- cement eliminator.

5.4.1 Study of y^+ for the wooden lath eliminator

In Table 5.19 the properties of all grids used are displayed. In the table the cell numbers of the grid, the value of y^+, and the calculated pressure at the inlet surface are written. Obviously, the inlet pressure is the same pressure that is used in the uncertainty studies. In these cases enhanced wall treatment is used for all calculations. The cell number refers again only to the eliminator area, since in this study that section of the computational domain is considered to be the most important one.

In the column “Grid number for uncertainty studies“ the numbers are stated, with which the grids are described for the uncertainty studies. Some grids are not used for the uncertainty study. They are marked with an “X“ and a number to numerate them, for example: X1.

Table 5.19: Properties of grids used for the study of y^+ with enhanced wall treatment

Number of cells [-]	Grid number for uncertainty studies [-]	Value of y^+ [-]	Average inlet pressure [Pa]
1444	10	80,38	5,5985
6616	9	46,82	6,1393
11405	8	27,99	5,9968
35400	7	20,94	5,7125
85269	6	9,98	5,5264
152589	5	7,82	5,4769
280341	4	5,98	5,4214
320670	X3	4,07	5,3256
368601	4a	3,12	5,3785
378330	X2	3,03	5,3297
471400	X1	2,00	5,2784
496734	3	4,61	5,3734
653532	3a	2,37	5,2843
866069	2	3,61	5,3184
1486781	1	2,78	5,3060

Now, by means of Table 5.19 a diagram can be created. The *x*- axis is for the values of y^+ and the *y*- axis for the pressure values. Furthermore, the x- axis is in logarithmic scale. See Figure 5.6.

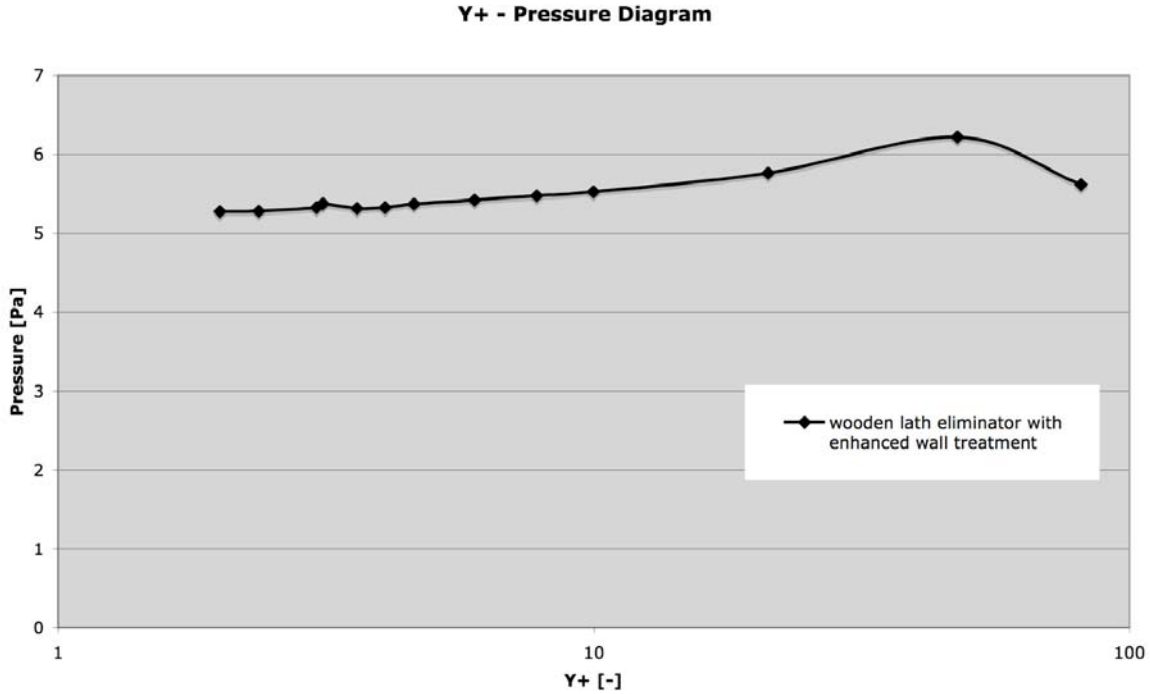

Figure 5.6: y^+ - pressure diagram for wooden lath eliminator using enhanced wall treatment

It can be seen that for a value of $y^+ \approx 7$ the solution stabilises. This means that for a refinement of the grid beyond a value of y^+ of seven the solution does not (considerably) change. Due to the smallest value of y^+ grid X1 is chosen as the best grid of the study.

5.4.2 Study of y^+ for the asbesto- cement eliminator

In Table 5.20 the properties of the used grids are stated. As well as for the wooden lath eliminator the exact cell number of the eliminator area, the number of the grid for the uncertainty studies, the value of y^+, and the average pressure at the inlet are given. Also, enhanced wall treatment is used for the calculations.

Table 5.20: Properties of grids used for the study of y^+ with enhanced wall treatment

Number of cells [-]	Grid number for uncertainty studies [-]	Value of y^+ [-]	Average inlet pressure [Pa]
4176	9	80,77	3,7202
12496	8	41,66	3,4258
33847	7	25,50	3,0161
78340	6	25,74	2,9938
88032	5	13,99	2,8142
168729	4	10,29	2,7708
257920	X3	5,38	3,1979
286681	3	7,83	2,9214
322432	X2	2,94	2,9447
394880	X1	2,75	2,7513
432031	3a	3,73	3,1065
494480	2	5,76	3,1072
759668	2a	2,84	2,8581
846855	1	4,36	3,0169

With the values of Table 5.20 it is possible again to construct a diagram as in the previous section, with an *x*- axis in logarithmic scale. See Figure 5.7.

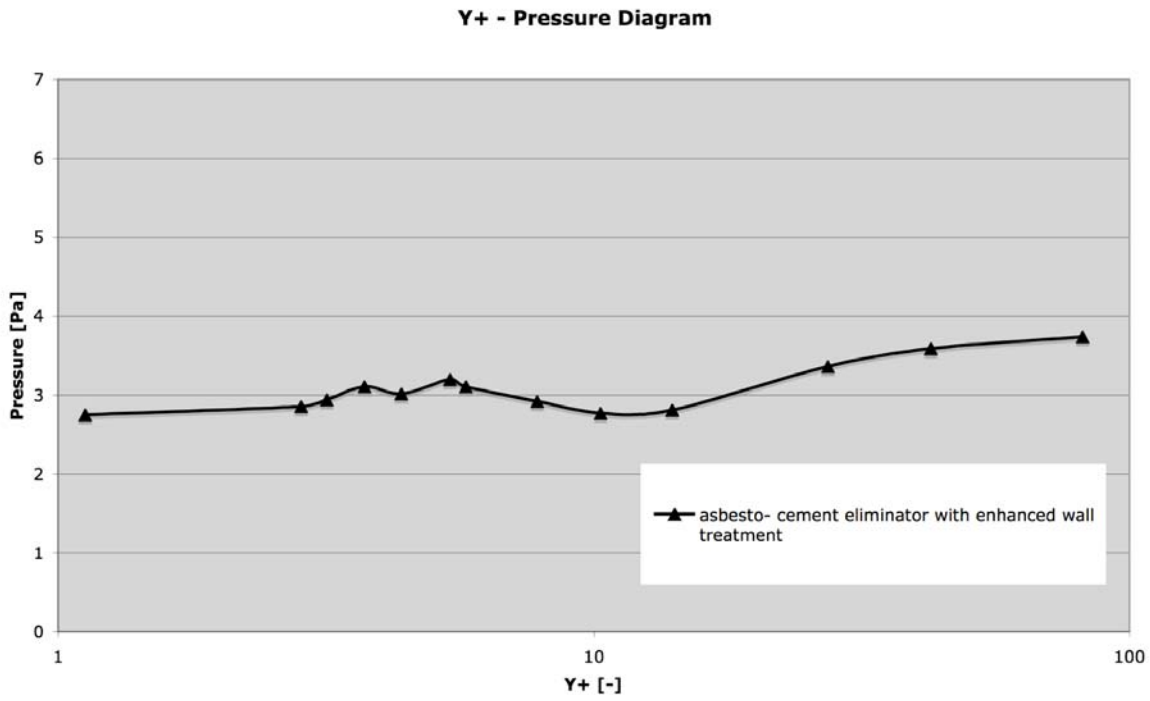

Figure 5.7: y^+ - pressure diagram for asbesto- cement eliminator using enhanced wall treatment

In Figure 5.7 the pressure stabilises in a value for a value of y^+ around seven. However, the convergence process is not as obvious as for the wooden lath eliminator. The values are oscillating. However, because of the grid size already reached (about 900000 cells) and the satisfying result of the uncertainty study considering the entire eliminator area, the possibility of building finer grids is excluded.

In this case, as well as for the wooden lath eliminator, the grid with the smallest value of y^+ is considered to be the best grid to choose. The grid is named grid X1.

5.5 Discussion

In this short section the results of the uncertainty studies and the y^+ study are discussed and compared. Again, first for the wooden lath eliminator and then for the asbesto- cement eliminator.

5.5.1 Wooden lath eliminator

With the results of the uncertainty studies considering the entire eliminator area using enhanced wall treatment some error bands can be calculated. The most interesting error band is the one using the *GCI* value of the last set of grids. The inlet pressure was computed as 5,3060 Pa with the *GCI* of 0,09% this results in a possible deviation of ± 0,0048 Pa. Due to the great cell number of the two last grids, the grid with a cell number of 500000 is preferred. Therefore an error band can be calculated, too. Using the value of *GCI* for the set of grids of 5 – 4 – 3 and p = 1, which is 3,37% (with original p = 0,28: *GCI* = 13,50%). Then the error

band is ± 0,1811 Pa of the calculated pressure 5,3734 Pa of grid 3. For the original value of p an error band of ± 0,7254 Pa can be calculated.

Moreover, for the uncertainty studies considering the first rows of the nearby wall cells error bands can be calculated. For the set of grids 4 – 3 – 4a, with a *GCI* of 0,01%, the error band is ± 5,38E-04 Pa of the calculated pressure 5,3785 Pa. For the other set 3 – 2 – 3a the calculated pressure is 5,2843 Pa, *GCI* is 0,81%, and the error band is ± 0,0428 Pa.

For the last uncertainty study using wall functions the error band for the first set of grids is ± 0,2303 Pa (calculated pressure is 5,9968 Pa, *GCI* is 0,81%). For the second grid the *GCI* is 103,38% therefore no error band is denoted. With p = 1 calculated *GCI* is 8,15%, but the difference between these two values is considered to be too big to make sense. However, for the second grid an acceptable value for the *GCI* is calculated, and the numerical solution seems to be converging. It can be seen that the differences from the values calculated using enhanced wall treatment are extensive.

From the y^+ study it can be reasoned that calculations using grids with similar values of y^+ compute similar results. For example, grids X1 and 3a. Grid X1 has 471400 cells, a value of 2,00 for y^+ and the pressure is 5,2784 Pa. Grid 3a has 653532 cells, a value of 2,37 for y^+ and the pressure is 5,2843 Pa.

In comparison to the study using the uncertainty methodology and the y^+ study, it seems that the set of grids in which the single grids have a value of y^+ bigger than five, have a big value for the *GCI*. This is consistent with the recommendation of the FLUENT guidelines is to use enhanced wall treatment in cases where the value of y^+ is smaller than five. Unfortunately, this circumstance leads to a great number of cells for the given problem.

Comparing only the uncertainty study for the eliminator area with enhanced wall treatment and the y^+ study, the values of the *GCI* and y^+ turn out to be connected. In the present work the grids are built in such way that the refinement factors for the uncertainty methodology are almost constant ($r_{coarse/centre}$ = 1,3, $r_{centre/fine}$ = 1,3). Therefore, the only factor affecting the methodology is the relation of the calculated solution for the different grids, $\varepsilon_{coarse/centre}$ and $\varepsilon_{centre/fine}$. For meshes 6, 5, 4, and 3 the pressure decreases almost linearly: 5,5264 (grid 6) to 5,4769 (grid 5) to 5,4214 (grid 4) to 5,3734 (grid 3). Also, the values of y^+ decrease almost linearly: 9,98 (grid 6) to 7,82 (grid 5) to 5,98 (grid 4) to 4,61 (grid 3). For the finer grids the linear decrease stops for the values of pressure and y^+.

5.5.2 Asbesto- cement eliminator

Error bands can be calculated for the different uncertainty studies. For the study considering the eliminator area and using enhanced wall treatment the error band, for the set of grids 3 – 2 – 1, is ± 0,1092 Pa (calculated pressure is 3,0169 Pa, *GCI* is 3,62%). For the other two sets the order of the method, p, is negative. For a value of p = 1, for the set 4 – 3 – 2, the error

band is ± 0,7343 Pa of the pressure 3,1072 Pa (*GCI* is 23,63%). That means an extensive deviation.

The study considering only the first rows does not necessarily lead to a small value of the *GCI* in case of the asbesto- –cement eliminator. However, for the set of grids 3 – 2 – 3a the smallest value of the *GCI* is calculated of all studies: 9,31E-06. That value leads to an error band, which is nearly ± 0 Pa (calculated value: ± 2,89E-07). But, for the set of grids 2 – 1 – 2a, with grids that are supposed to have smaller cells, the value is -87,95%. Using a value of p =1 leads to an error band of ± 0,3712 Pa (calculated pressure is 2,8664 Pa, *GCI* is 12,95%). This is a big difference in comparison with the error band of the set 3 – 2 – 3a, and a great increase.

In the last uncertainty study using wall functions the set of grids 8 – 7 – 6 has a very small value for the *GCI* of 0,09%. This leads to the calculated pressure for the grid 6 of 2,9938 Pa to an error band of ± 0,0027 Pa. The reason why for this set of grids the *GCI* is small whereas for the other set (9 – 8 – 7) it is considerably higher (26,14% for p = 1) may lie in the similar values of y^+ for the two grids 6 (y^+ = 25,74) and 7 (y^+ = 25,50) and in the great gap between the grids 7 and 8 (y^+ = 41,66). But the recommendation of FLUENT is to use wall functions for values of y^+ bigger than 30.

The study of y^+ for the asbesto- cement eliminator is not as clear as for the wooden lath eliminator. The pressure seems to oscillate around the value of 3 Pa for the different grids. Regarding Figure 4.7 in the part of a value of y^+ smaller than three, the pressure still appears to decrease. However, no further examinations with finer grids, and values of y^+ smaller than one are executed due to the computational effort and the good result of the uncertainty study for the entire eliminator area with enhanced wall treatment.

5.5.3 Grid choice for further calculations

As a result of each study a grid is chosen, which is regarded as the best for further calculations. In this section the properties of the chosen grids are displayed once again and it is discussed which one(s) is (are) considered to be the best for further calculations.

Table 5.21 shows the chosen grids and their properties for the wooden lath eliminator and Table 5.22 the same for the asbesto- cement eliminator.

Table 5.21: Chosen grids of each type of grid study, wooden lath eliminator

Type of Study	Grid number [-]	Number of cells [-]	*GCI* [%]	Value of y^+ [-]	Average inlet pressure [Pa]
Eliminator area, enhanced wall treatment	3	496734	13,50 *(3,37 for p = 1)*	4,61	5,3734
First row cells, enhanced wall treatment	4a	368601	0,01	3,12	5,3785
Eliminator area, wall functions	6	11405	3,84	27,99	5,9968
Study of y^+	X1	471400	-	2,00	5,2784

Table 5.22: Chosen grids of each type of grid study, asbesto- cement eliminator

Type of Study	Grid number [-]	Number of cells [-]	*GCI* [%]	Value of y^+ [-]	Average inlet pressure [Pa]
Eliminator area, enhanced wall treatment	2	496734	-45,39 *(23,63 for p = 1)*	5,76	3,1072
First row cells, enhanced wall treatment	3a	432032	9,31E-06	3,73	3,1065
Eliminator area, wall functions	8	78340	0,09	41,66	2,9938
Study of y^+	X1	394880	-	2,75	2,7513

Comparing the results for the study of the eliminator area using enhanced wall treatment with those in the study of the first row cells and enhanced wall treatment, it can be said that it is not clear which of these studies provides the best results. The chosen meshes calculate almost the same inlet pressure. But the values of the *GCI* for both cases vary for both geometries. For the study regarding the first row cells, the *GCI* is very small, almost zero. Therefore, it seems that considering only the wall near cells is not appropriate, because great parts of the grid do not change by the adaptation process. However, the adaptation process leads to high refinement factors and consequently to a small value of the *GCI*.

Also, in the present work the uncertainty study does not seem to be the suitable form to judge the behaviour of the grids. In no case the order of the method was calculated constant. In

many cases it was smaller than 1 or even negative. In many cases small values for the *GCI* could only be calculated with high computational effort.

The grids chosen from the study of the value of y^+ have the smallest value of y^+ and it can be seen that the calculated inlet pressure is around 0,1 Pa (wooden lath eliminator ≈ 1,9 %, asbesto- cement eliminator ≈ 3,9 %) smaller than for the two uncertainty studies. Thus, FLUENT recommends to use enhanced wall treatment with values of y^+ as small as possible. It is supposed that the grids of the y^+ study are the best grids of the finer meshes. Therefore, on the one hand these grids, the grids called X1, are chosen for further calculations.

On the other hand the chosen coarser grids for both geometries are also considered for further calculations. This decision is based on the consideration that the fine grids have already reached the computational manageable size. That means if the computational domain has to be enlarged to include more parts of the cooling tower or if a third dimension is added, the cell number will multiply and easily reach numbers beyond 1000000. The computational effort will be too high.

However, the calculated inlet pressures for the coarse meshes is higher than for the chosen finer meshes “X1“. Especially for the wooden lath eliminator the deviation is relatively high, 13,6 % (8,0 % asbesto- cement eliminator). However, the two coarser grids are chosen and examined in the following chapters, as well as the two chosen finer grids.

From now on the chosen grids X1 will be referred to as the “fine grids“ and the selected grids with wall functions (wooden lath eliminator: grid 6, asbesto- cement eliminator: grid 8) as “coarse grids“.

6 Comparison with experiments

Now, the numerical results are compared with the results of experiments found in the literature. Thus, in this work especially the pressure loss is of high interest, the aim is to compare the pressure losses of the different eliminators found in the literature with the calculated values. Since only three different values of pressure losses are found the comparison is relatively simple.

The only problem is that in the literary source used for the comparison it is not stated where the pressure losses are measured. It is supposed that the values are average values of several metering points. But it is not said, for example, in which distance to the eliminators the pressure losses are measured.

Table 6.1 states again the values of the pressure losses and the different velocities found in the literature for the wooden lath eliminator and Table 6.2 does the same for the asbesto- cement eliminator.

Table 6.1: Pressure losses for the velocities found in the literature for the wooden lath eliminator

Air velocity (m s-1)	Pressure loss (Pa)
0,91	1,463
1,52	4,063
2,13	7,963

Table 6.2: Pressure losses for the velocities found in the literature for the asbesto- cement eliminator

Air velocity (m s-1)	Pressure loss (Pa)
0,94	1,831
1,58	5,120
2,23	10,153

Since the values of the pressure drops in the literature are only figures and not curves or different tables, average values for the pressures are taken from the numerical results. Therefore, the surfaces, introduced in the computational domain, see chapter 7, are once again used. As in the literature it is not stated where the pressure drop is measured, the question of where the values are taken from the computational domain for the comparison must be made.

In this work there is an attempt to evaluate only the pressure drop of the eliminators. Therefore the two surfaces next to the eliminators are chosen and the difference of the pressure values between them is considered to be the pressure drop. Figure 6.1 shows where the surfaces are situated for the wooden lath eliminators and Figure 6.2 for the asbesto-cement eliminator. The used surfaces are coloured red.

In the case of the wooden lath eliminators the distances are 35 mm from the surfaces to the eliminators and in case of the asbesto- cement eliminators 27 mm.

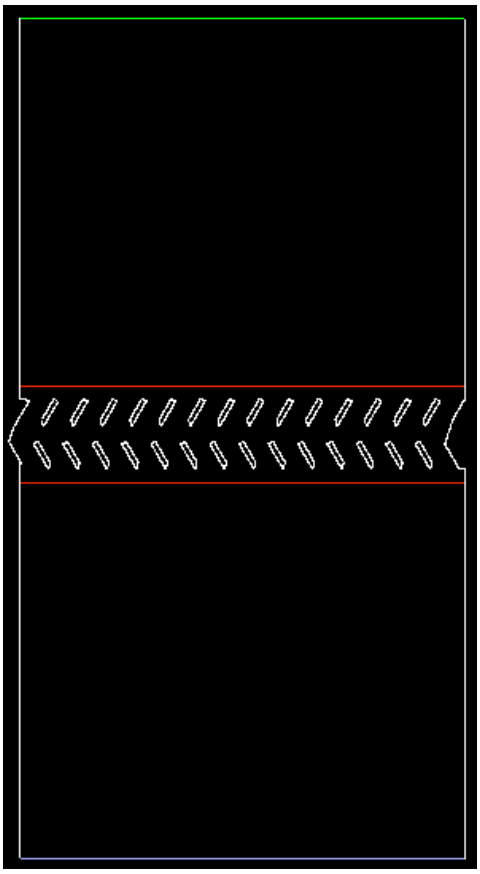

Figure 6.1: Computational domain of wooden lath eliminator with used surfaces

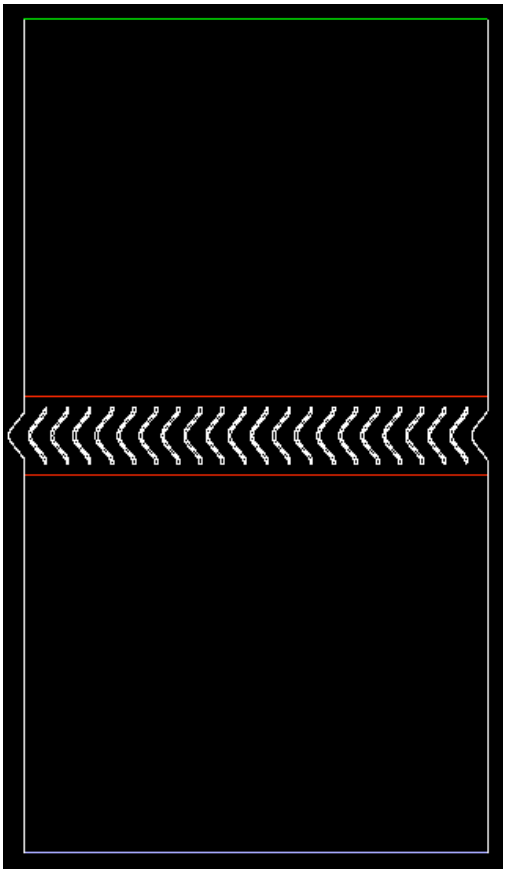

Figure 6.2: Computational domain of asbesto- cement eliminator with used surfaces

The average pressure values of all cells being crossed by these surfaces are taken. Table 6.3 shows these values for the wooden lath using the fine grid for the calculation and Table 6.4 using the coarse grid. Table 6.5 shows the calculated pressure losses for the asbesto- cement eliminator with the fine grid and table 6.6 with the coarse grid.

Table 6.3: Calculated pressure losses for the three different velocities for the wooden lath eliminator with fine grid

Air velocity [m s^{-1}]	Pressure value surface below eliminators, p_1 [Pa]	Pressure value surface above eliminators, p_2 [Pa]	Resulting pressure drop, $p_1 - p_2$ [Pa]
0,91	1,8871	0,3838	1,5033
1,52	5,2378	1,1153	4,1225
2,13	10,3074	2,2601	8,0473

Table 6.4: Calculated pressure losses for the three different velocities for the wooden lath eliminator with coarse grid

Air velocity [m s^{-1}]	Pressure value surface below eliminators, p_1 [Pa]	Pressure value surface above eliminators, p_2 [Pa]	Resulting pressure drop, $p_1 - p_2$ [Pa]
0,91	2,0933	0,4121	1,6812
1,52	5,6905	1,2079	4,4826
2,13	10,9169	2,4187	8,4982

Table 6.5: Calculated pressure losses for the three different velocities for the asbesto- cement eliminator with fine grid

Air velocity [m s^{-1}]	Pressure value surface below eliminators, p_1 [Pa]	Pressure value surface above eliminators, p_2 [Pa]	Resulting pressure drop, $p_1 - p_2$ [Pa]
0,94	1,1602	0,1478	1,0124
1,58	2,8525	0,2334	2,6191
2,23	5,2288	0,3182	4,9106

Table 6.6: Calculated pressure losses for the three different velocities for the asbesto- cement eliminator with coarse grid

Air velocity [m s^{-1}]	Pressure value surface below eliminators, p_1 [Pa]	Pressure value surface above eliminators, p_2 [Pa]	Resulting pressure drop, $p_1 - p_2$ [Pa]
0,94	1,2035	0,0790	1,1245
1,58	2,9073	0,1867	2,7206
2,23	5,2282	0,3295	4,8987

By means of the different values, diagrams can be created using the difference of the pressure values of the surfaces below and above the eliminators and also displaying the experimental results. Figure 6.3 displays the diagram for the wooden lath eliminator and Figure 6.4 for the asbesto- cement eliminator type.

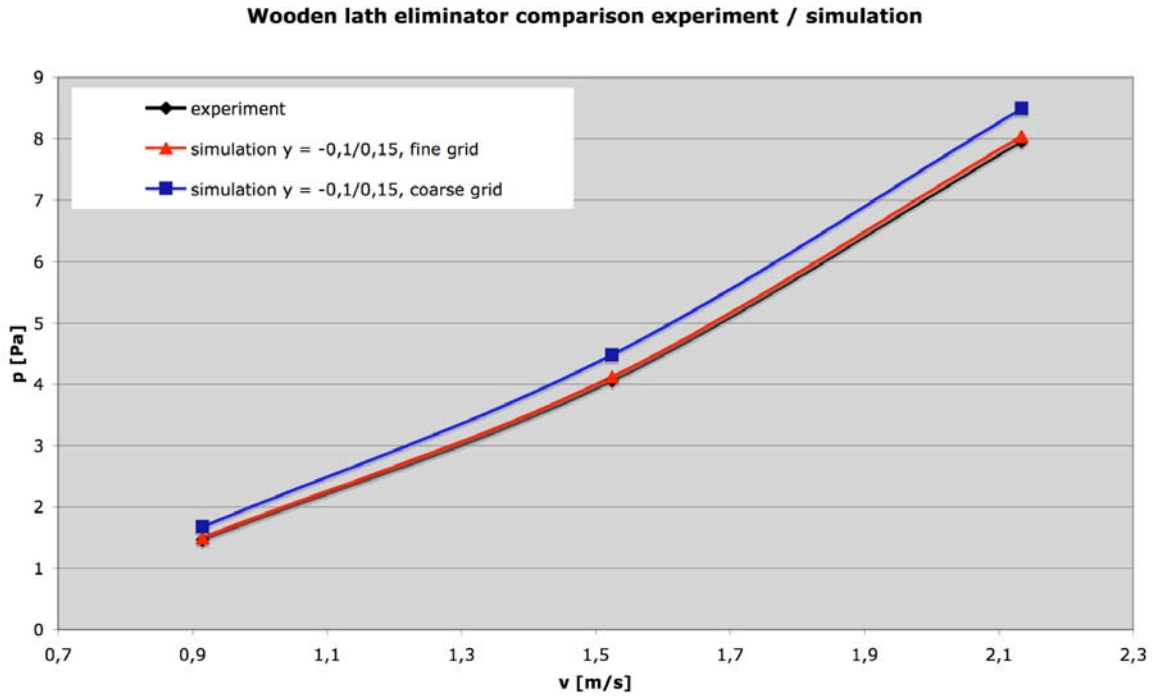

Figure 6.3: Comparison experiment / simulation for the wooden lath eliminator

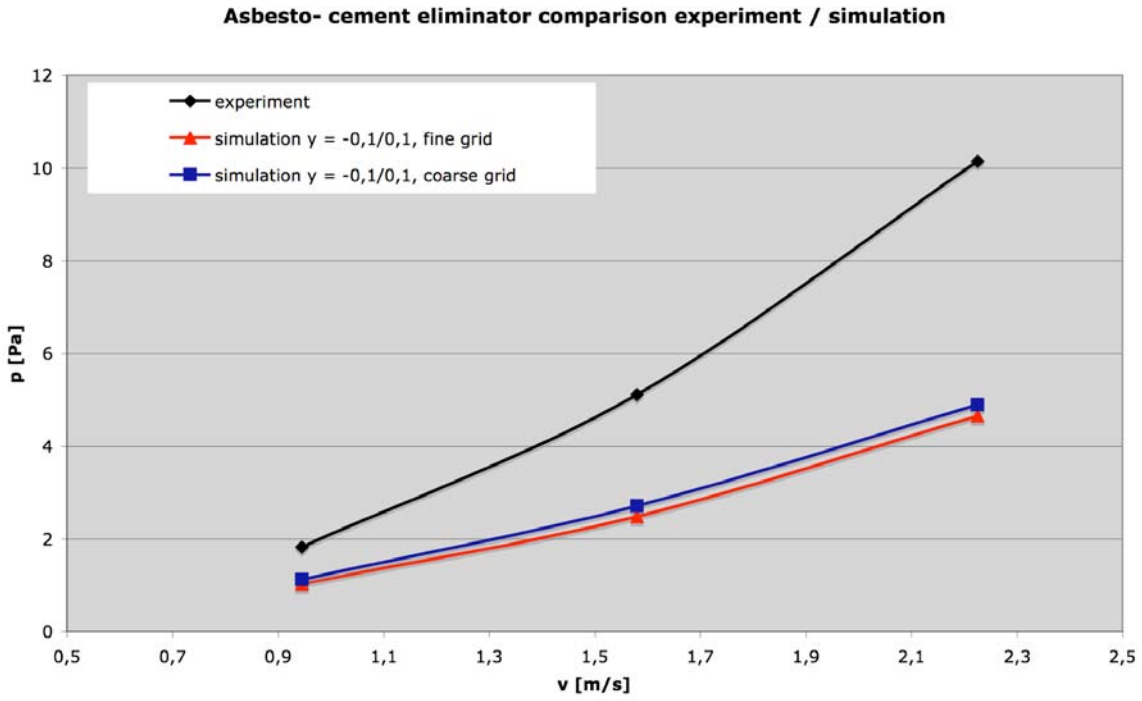

Figure 6.4: Comparison experiment / simulation for the asbesto- cement eliminator

For the wooden lath eliminator the experimental and numerical values for the pressure drop are almost the same. For the fine grid there is a deviation of 2,68% of the experimental result from the numerical one for a velocity of 0,91 m s^{-1}. For a velocity of 1,52 m s^{-1} the deviation

is 1,44% and for 2,13 m s^{-1} the deviation is 1,05%. With the coarse grid the deviation is higher, for a velocity of 0,91 m s^{-1} it is 14,91%. For the next bigger velocity of 1,52 m s^{-1} the deviation is 10,33%, and for the highest velocity of 2,13 m s^{-1} it is 6,72%. In both cases the deviations decrease with increasing velocity.

For the asbesto- cement eliminator the numerical results deviate very much from the experimental ones in comparison with the wooden lath eliminator. For the fine mesh and a velocity of 0,94 m s^{-1} the deviation of the experimental result from the numerical one is 44,71%. For the second velocity of 1,58 m s^{-1} the deviation is 48,85%, and for 2,23 m s^{-1} it is 51,63%. The deviations for the coarse grid are: 38,59% (0,94 m s^{-1}), 46,86% (1,58 m s^{-1}) and 51,75 (2,23 m s^{-1}). For both grids the deviations are very big and compared to the wooden lath eliminator the deviation does not decrease with increasing velocity.

7 Numerical Results

In this chapter the results of the simulations are discussed, regarding the two different types of eliminators, pressure and velocity fields and stream lines. This is the so-called postprocessing part of the work, see section 5.1.

The chapter is divided into two equal parts, one for the wooden lath eliminator and the other for the asbesto- cement eliminator type. Simulations were executed for the three different velocities found for each eliminator type in the literary sources, 0,91 m s^{-1}, 1,52 m s^{-1}, and 2,13 m s^{-1} for the wooden lath and 0,94 m s^{-1}, 1,58 m s^{-1}, and 2,23 m s^{-1} for the asbesto-cement eliminator. See section 3.1. The calculations were applied on the two grids, the fine and the coarse one, chosen for each geometry. However, the calculation results of the fine grids are more detailed, due to the bigger number of cells. In the following sections they are used to describe the appearing flow phenomena.

The results of the fine and coarse grids are compared in the short section of 7.4.

7.1 Wooden lath eliminator

For the inlet velocity of 1,52 m s^{-1} the calculated results are examined and described in more detail. Thus there are no bigger changes in the behaviour of the flow, the results of the other velocities are displayed in a shorter form. With the velocity of 1,52 m s^{-1} the uncertainty and y^+ studies are executed, therefore it is chosen for the detailed description.

Figure 7.1 displays the pressure field for the whole computational domain for the velocity of 1,52 m s^{-1}.The first thing that attracts attention is that the pressure on the right side of the computational domain is higher than on the left side. Especially directly at the eliminators on the right side the pressure is greater than on the other side. The cause of the different pressures on both sides lies most likely in the shape of the eliminators.

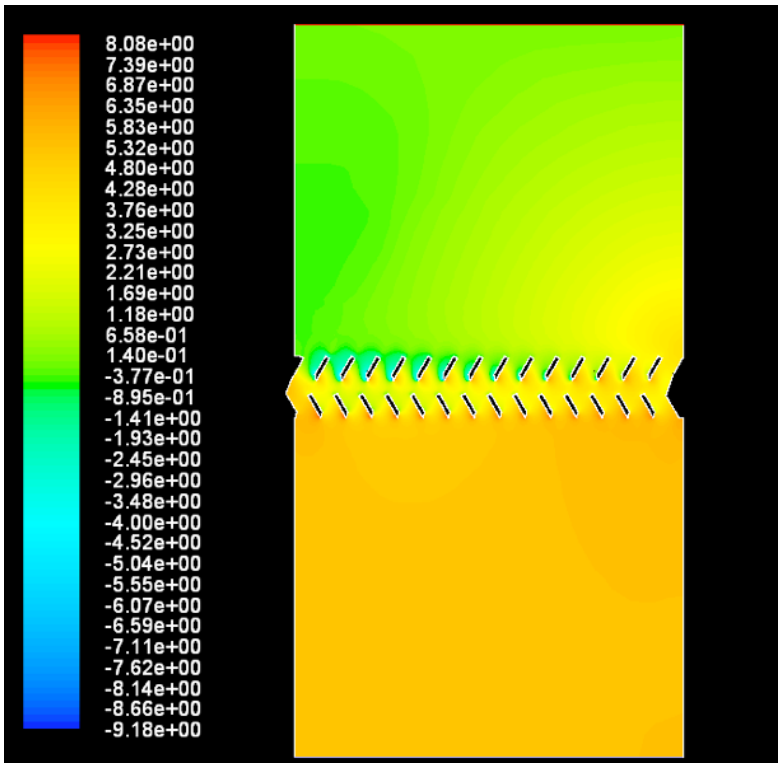

Figure 7.1: Static pressure field for wooden lath eliminator for a velocity of 1,52 m s^{-1} (Pa)

Due to the different distribution of the pressure on the sides the velocity distribution is not consistent either. Figure 7.2 shows the computational domain again, this time the velocity field is displayed. For the velocity the distribution is contrariwise as for the pressure. This means that now on the left side of the computational domain between the next eliminator shape to the wall and the wall the velocity is eminently higher. On the other side the velocity has the lowest value for the entire domain.

Furthermore it can be seen that changing the computational domain to fit the shape of the eliminators influences the flow. Almost half of the left side of the domain is colored blue, which means a very low velocity. It can be seen how this part is influenced by the wall shape at the eliminator level.

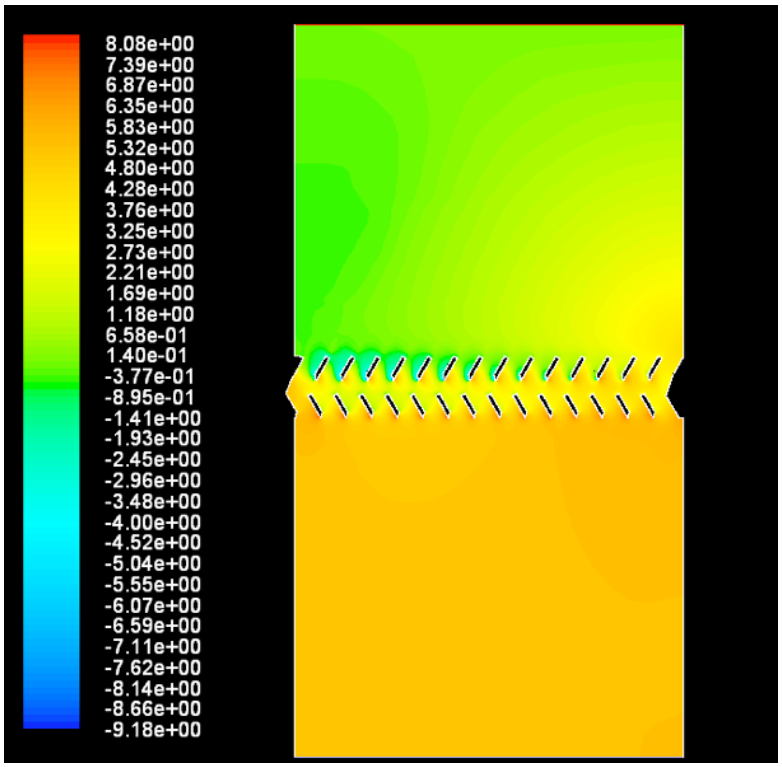

Figure 7.2: Velocity field for wooden lath eliminator for a velocity of 1,52 m s^{-1} (m s^{-1})

Figure 7.3 displays an aperture of the two eliminators next to the wall on the left and the two next to the right wall. The velocity is displayed, this time in form of small vectors. On the left side the biggest velocity of the entire domain is calculated, it is around 3,64 m s^{-1}. As above stated, the velocity at the inlet is 1,52 m s^{-1}. This means that the velocity more than reduplicates in comparison with the inlet. On the other side, very near to the wall, the velocity is almost zero (around 4E-4 m s^{-1}) and it appears to form a vortex in the near- wall region.

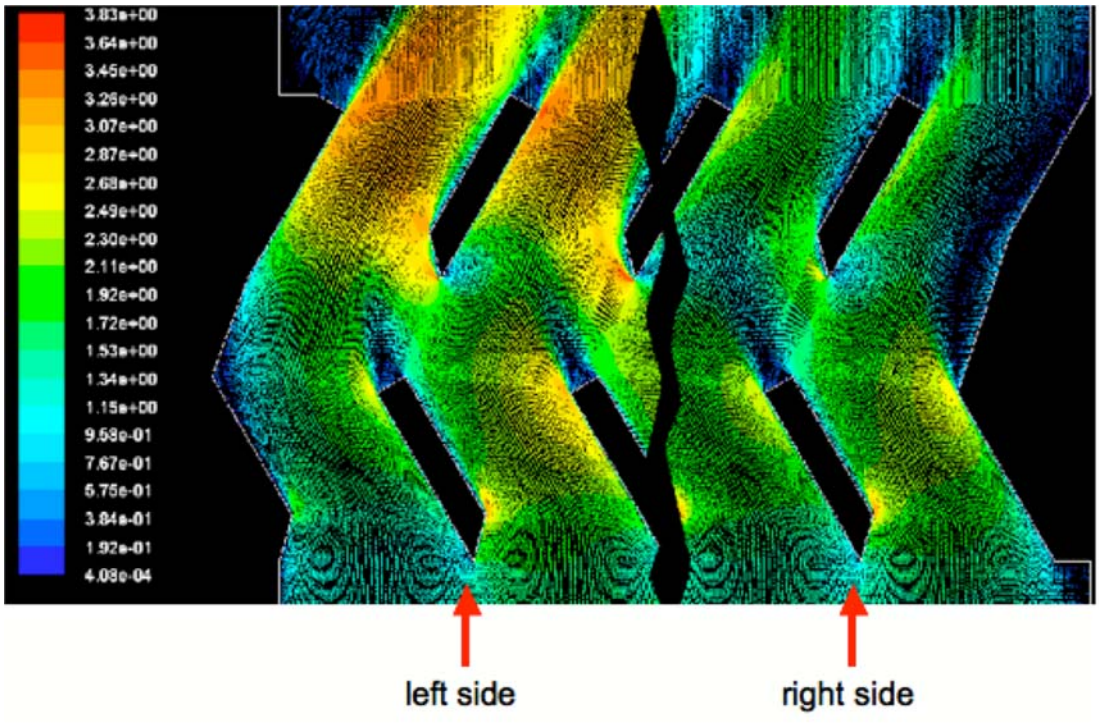

Figure 7.3: Comparison of the velocity, left and right side of computational domain (m s^{-1})

A closer examination of the eliminator shapes reveals that vortexes are formed, too. Especially when leaving the eliminators, vortexes are created by the airflow. In Figure 7.4 one of these vortexes is shown. Also, around the cone points of the eliminators shapes the flow is highly deflected. This is shown in Figure 7.5.

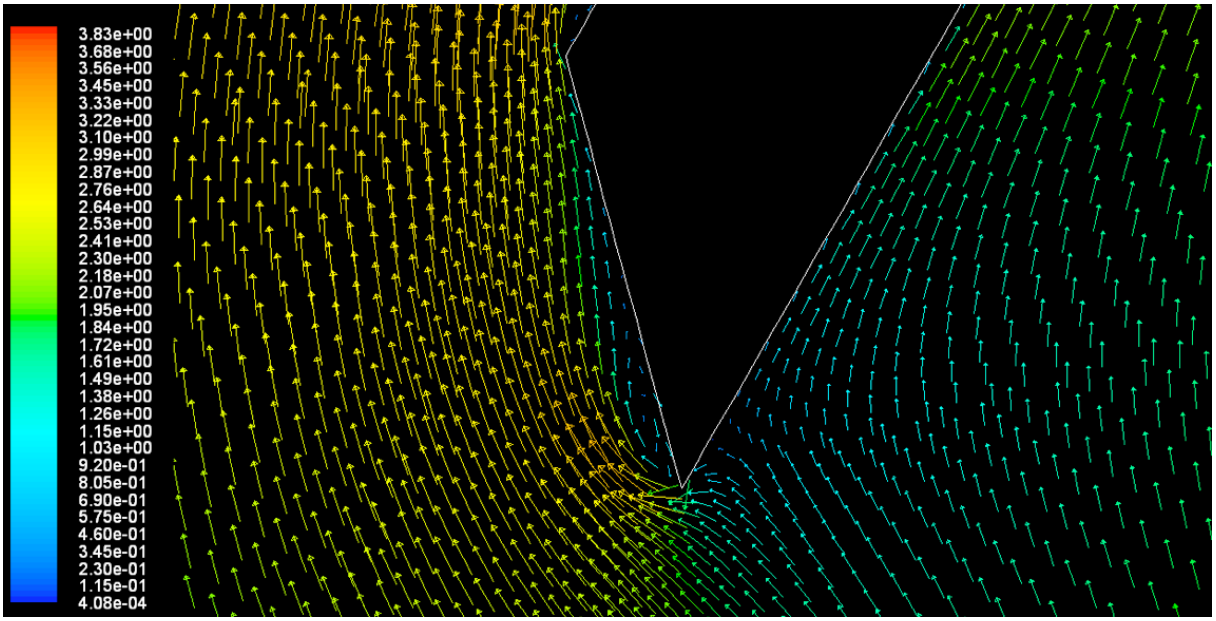

Figure 7.4: Formed vortex of the flow at leaving the eliminators (m s^{-1})

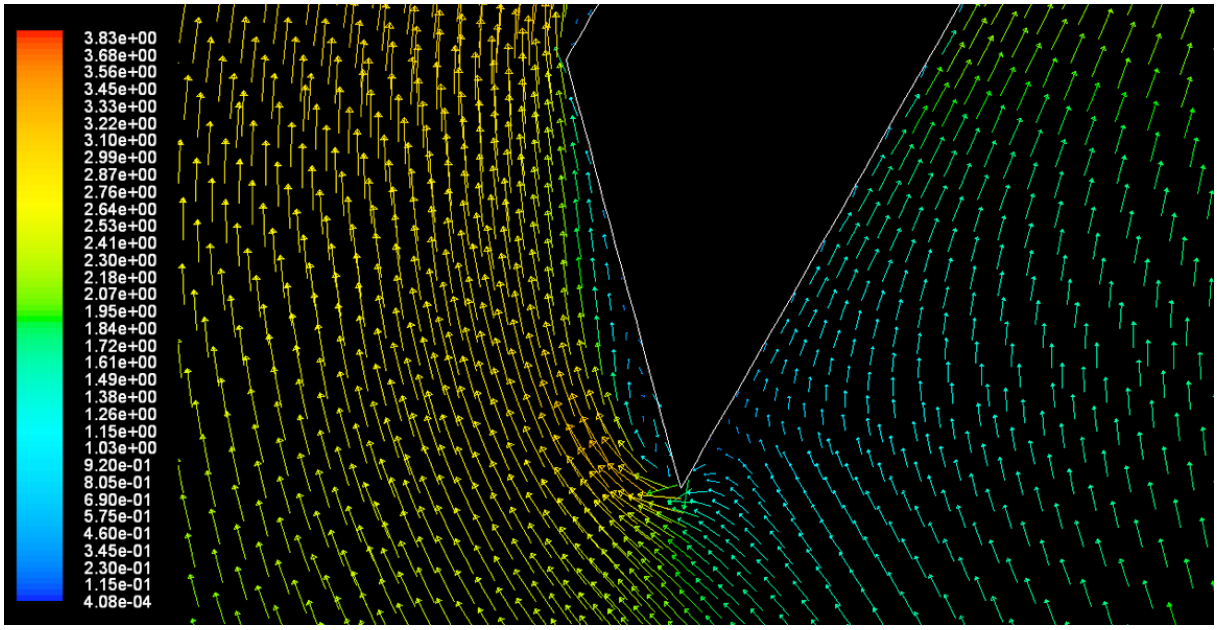

Figure 7.5: Aperture of cone point of single eliminator shape (m s^{-1})

For the other examined velocities the pressure and velocity fields are displayed. One can see that the distributions are almost the same. That is to say that there are no great changes in the behaviour of the flow, only the magnitude of the pressure and the velocity changes. There are no new big vortexes created by the increase (or decrease) of the velocity.

Figure 7.6 and Figure 7.7 display the pressure and the velocity field of the computational domain for a velocity of 0,91 m s^{-1}. Figure 7.8 and 7.9 do the same for a velocity of 2,13 m s^{-1}. As can be seen the pressure fields are similar to each otheras well as the velocity fields.

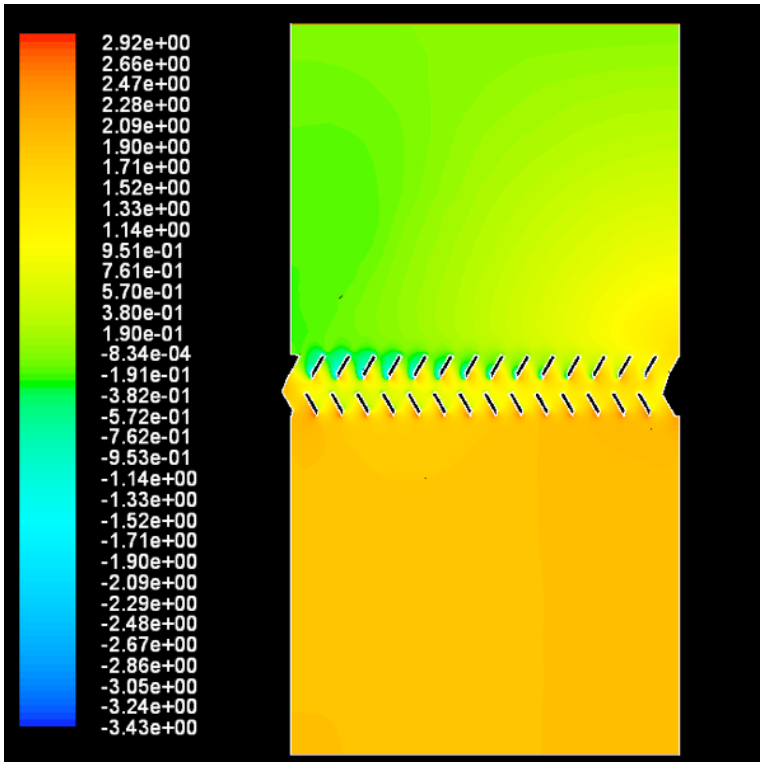

Figure 7.6: Pressure field for an inlet velocity of 0,91 m s^{-1}, wooden lath eliminator (Pa)

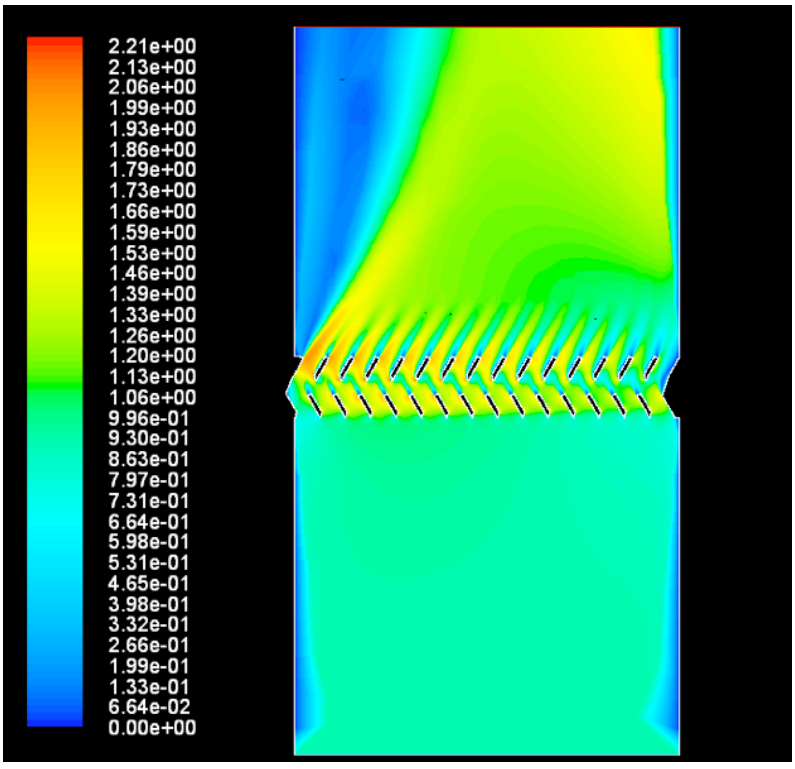

Figure 7.7: Velocity field for an inlet velocity of 0,91 m s^{-1}, wooden lath eliminator (m s^{-1})

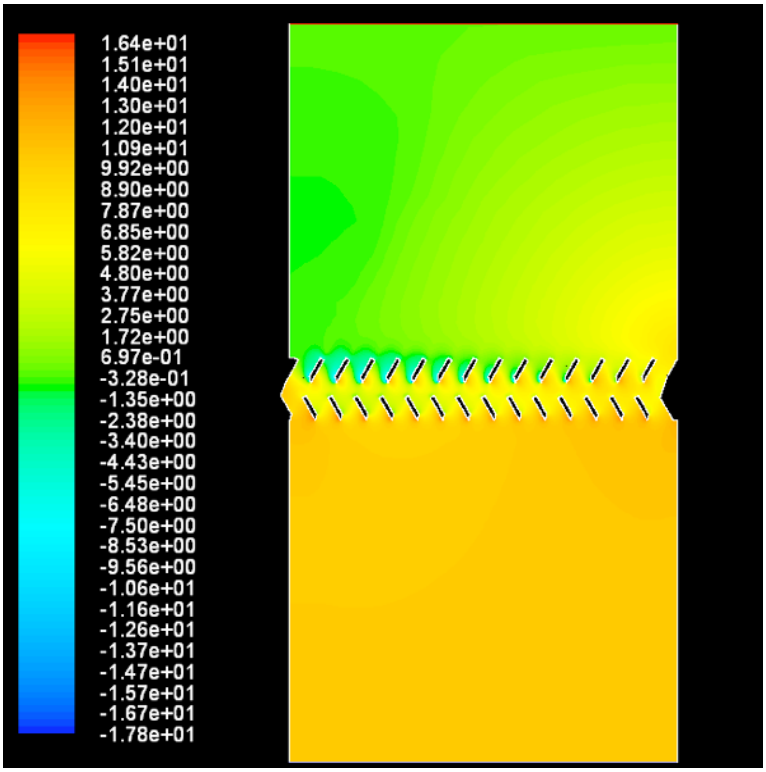

Figure 7.8: Pressure field for an inlet velocity of 2,13 m s^{-1}, wooden lath eliminator (Pa)

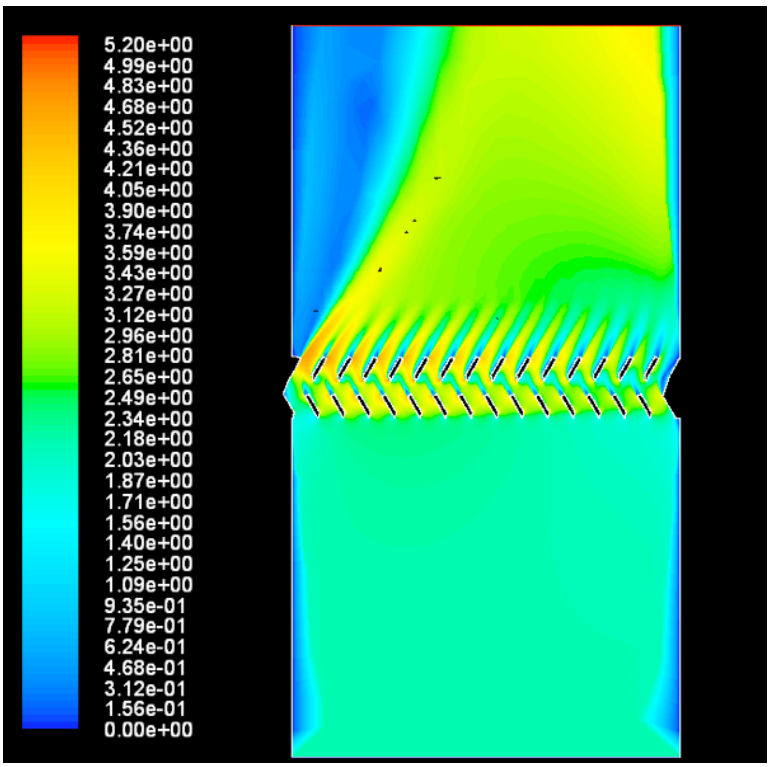

Figure 7.9: Velocity field for an inlet velocity of 2,13 m s^{-1}, wooden lath eliminator (m s^{-1})

Another possibility to display the flow is by means of stream lines. These lines are tangent to the vectors of the velocity of the flowing fluid. Thus, one can evaluate how the fluid flows through the geometry. Figure 7.10 shows the computational domain with some stream lines.

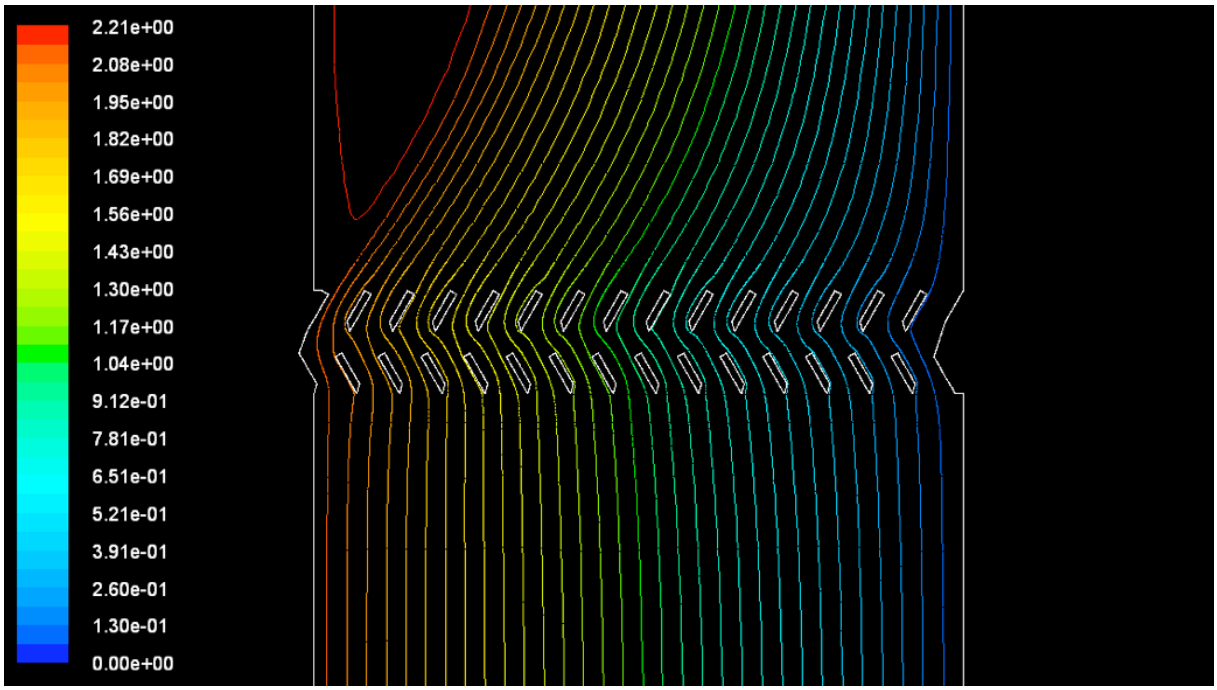

Figure 7.10: Streamlines for wooden lath eliminator (kg s^{-1})

In Figure 7.10 it can be seen how the fluid passes through the eliminators. At the eliminator level, the stream lines are deflected by the eliminator shapes.

In the following sections the results are examined by using a diagram of the pressure and the velocity. Therefore the computational domain is divided by means of several surfaces. In these surfaces the different values of the pressure and velocity of the single grid cells are taken to create the diagrams. Figure 7.11 displays the computational domain with the different lines. The vertical lines are chosen in such a way that they do not cross the eliminators shapes.

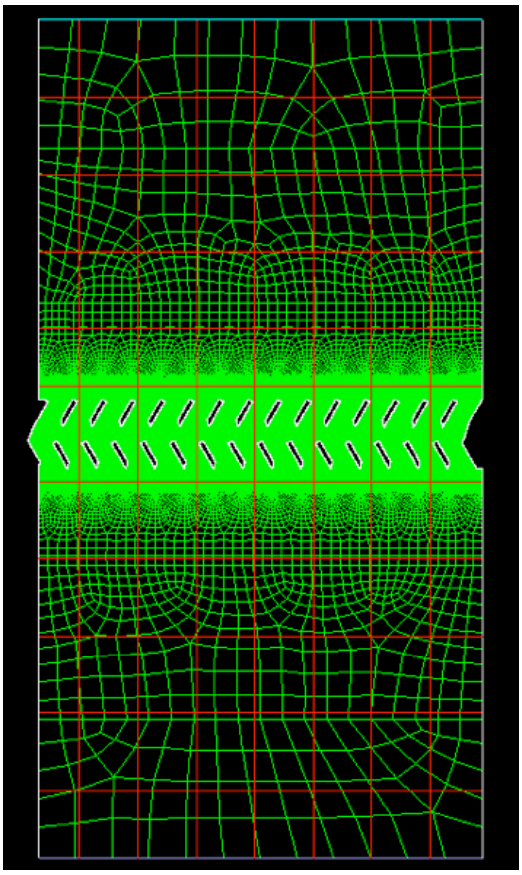

Figure 7.11: Computational domain of wooden lath eliminator with used grid and lines

The following figures are for the velocity of 1,52 m s^{-1}. Figure 7.12 displays the values of the pressure for the different surfaces. The lines around the value of zero are the surfaces which are situated above the eliminators. The other lines around the value of five are the surfaces below the eliminators. The two green lines are the two surfaces which are the closest ones to the eliminators. One line before and the other after the eliminators. Due to the influence of the eliminators these two lines are waved. What has already been mentioned above can also be seen here: On the right side of the domain the pressure is higher than on the left side. Above all, immediately after the eliminators the pressure is very high on the right side. However, with increasing height the pressure decreases. Also, the diagram shows the values of the *y*-coordinate in the caption.

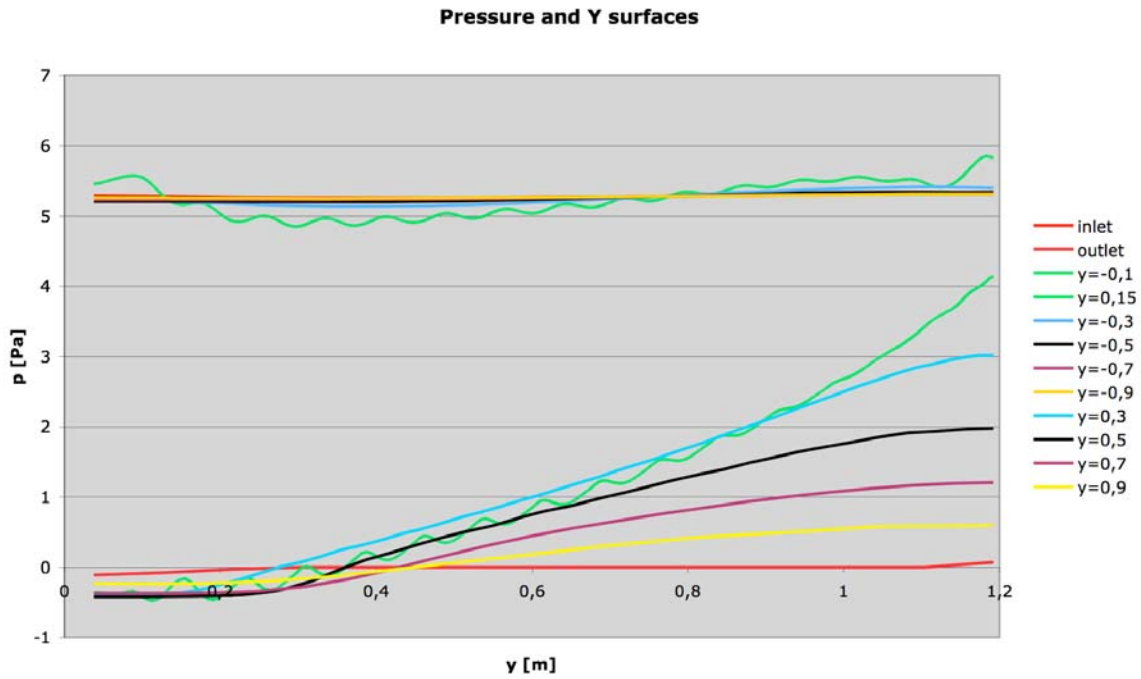

Figure 7.12: Diagram for the different *y* surfaces regarding pressure

Figure 7.13 shows the same for the vertical surfaces. In the caption are again the coordinates of the different surfaces are again shown. At the *x*- coordinate of around -1 the flow enters the domain (inlet). At the *x*- coordinate of around zero the flow passes through the eliminators. Therefore the lines are curved there.

The green line shows the pressure curve on the right side of the domain. There it can be seen that the pressure on that side is the highest of the entire domain, too.

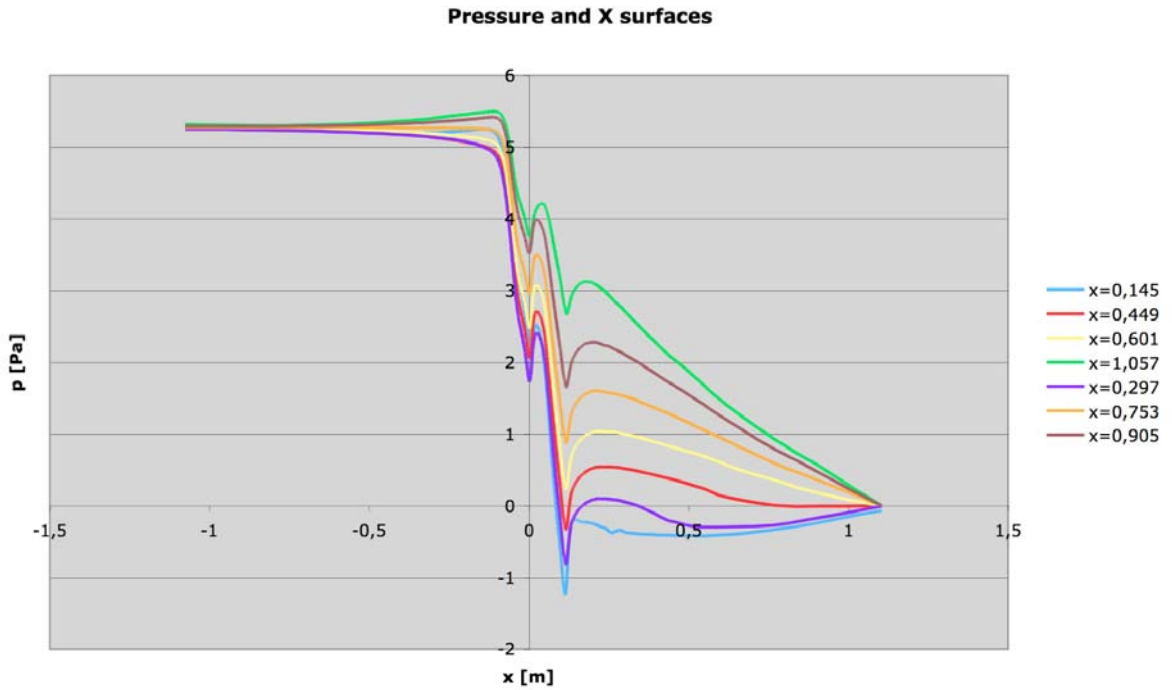

Figure 7.13: Diagram for the different *x* surfaces regarding pressure

For the velocity the same procedure can be made as for the pressure. That is to say display the values of the velocity in the different surfaces. Figure 7.14 shows the velocity for the inlet, outlet and the two surfaces next to the eliminators. The velocities for the *x*- surfaces is displayed in Figure 7.15.

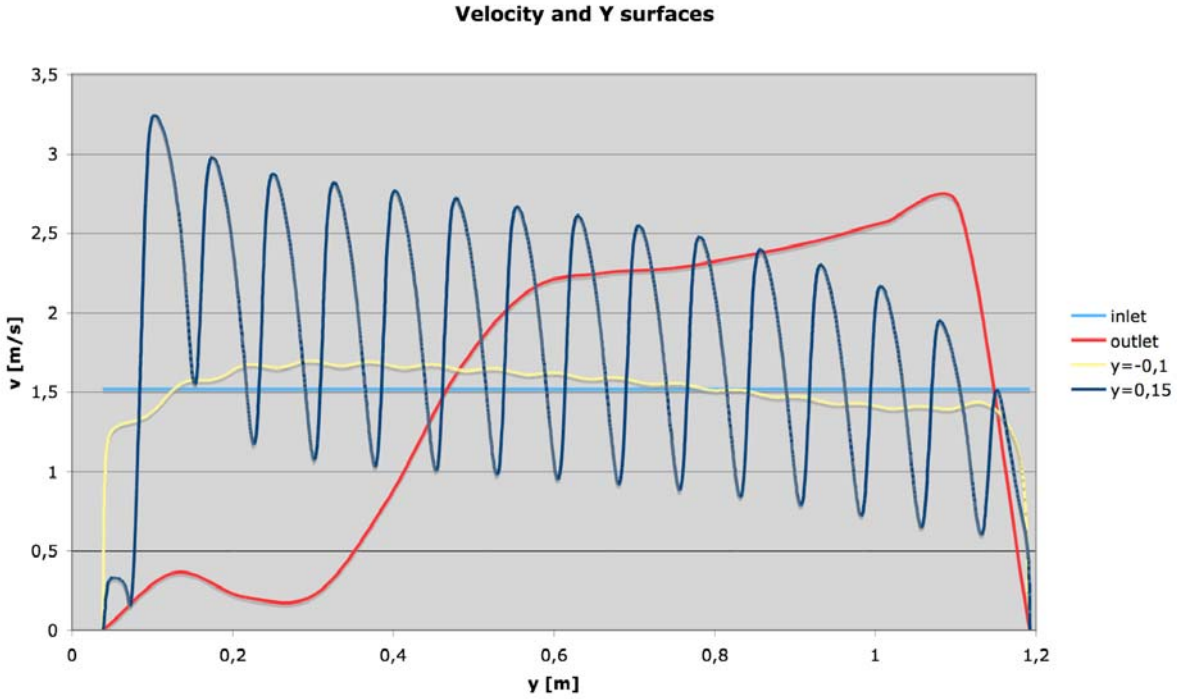

Figure 7.14: Diagram for *y* surfaces regarding velocity

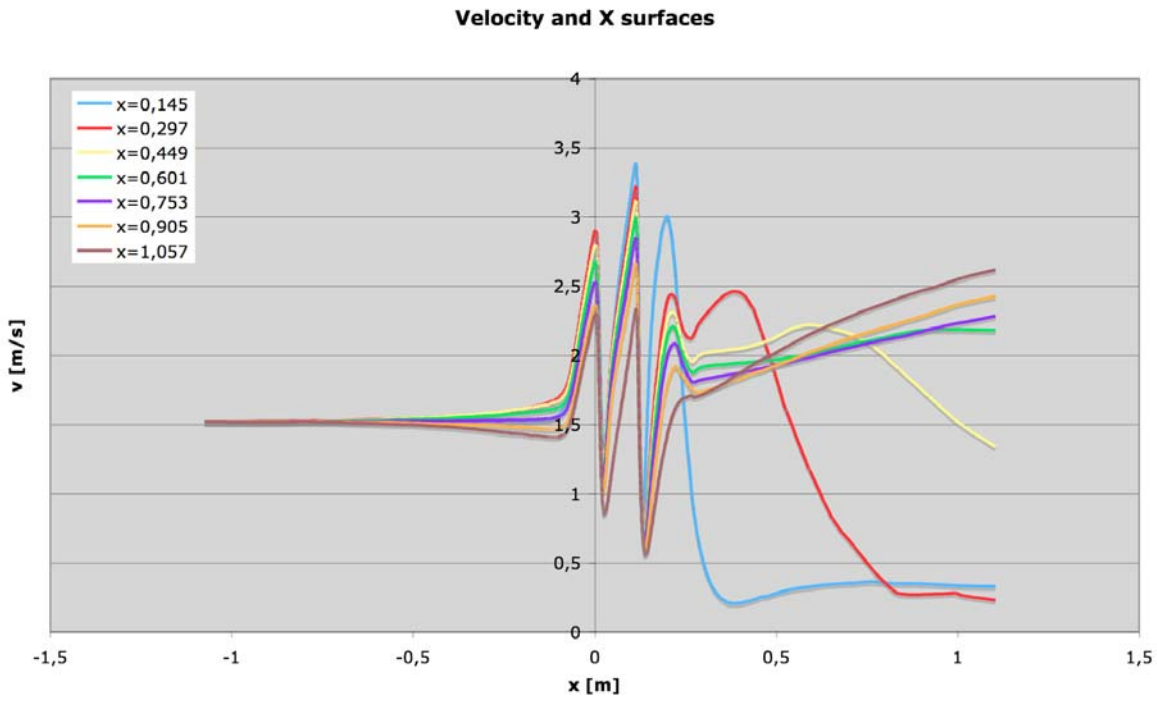

Figure 7.15: Diagram for the different *x* surfaces regarding velocity

In these two diagrams it can be seen again that on the right side the pressure is higher and on the left one the velocity is. Also, one sees how the eliminator shapes influence the velocity. The surface y = 0,15 m is waved, for each eliminator shape there is one wave trough.

Because of the similarity of behaviour of the flow for the three different velocities diagrams regarding the different surfaces and the other two velocities are not displayed.

The most important intuition of the examination is the influence of the eliminators on the pressure and the velocity. Due to their shape they appear to increase the pressure on one side and to decrease it on the other.

7.2 Asbesto- cement eliminator

As well as for the wooden lath eliminator, the results of the simulation are examined in detail for the velocity of 1,58 m s^{-1}, which is the velocity of the uncertainty and y^+ study. The other two velocities found in the literature, 0,94 m s^{-1} and 2,23 m s^{-1}, are regarded in a shorter form.

Figure 7.16 displays the pressure field of the entire computational domain for the asbesto-cement eliminators. The pressure is distributed almost uniformly. The entire domain is coloured yellow, which means a pressure of around 2,4 Pa. Only in the upper side the pressure is slightly lower. As a matter of course the pressure must be lower above eliminator level due to the pressure drop the eliminators provoke.

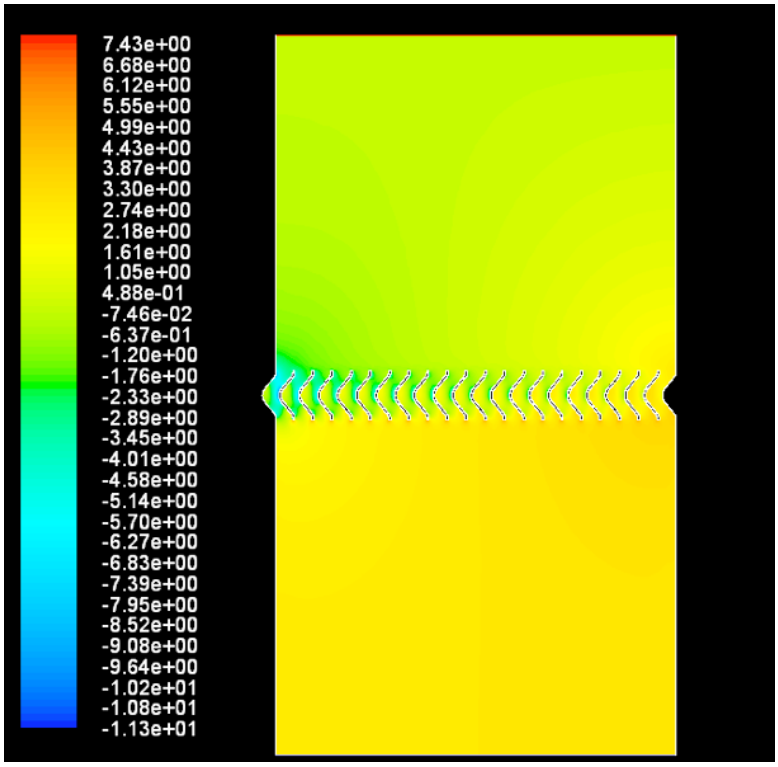

Figure 7.16: Static pressure field for asbesto- cement eliminator for a velocity of 1,58 m s^{-1} (Pa)

The same can be seen in Figure 7.17, which shows the entire domain, this time for the velocity field. In almost the entire domain the flow has the same velocity. However, this can be expected due to the mass conservation equation. The flow does not behave like the flow in the wooden lath domain and the velocity is not much higher on one side.

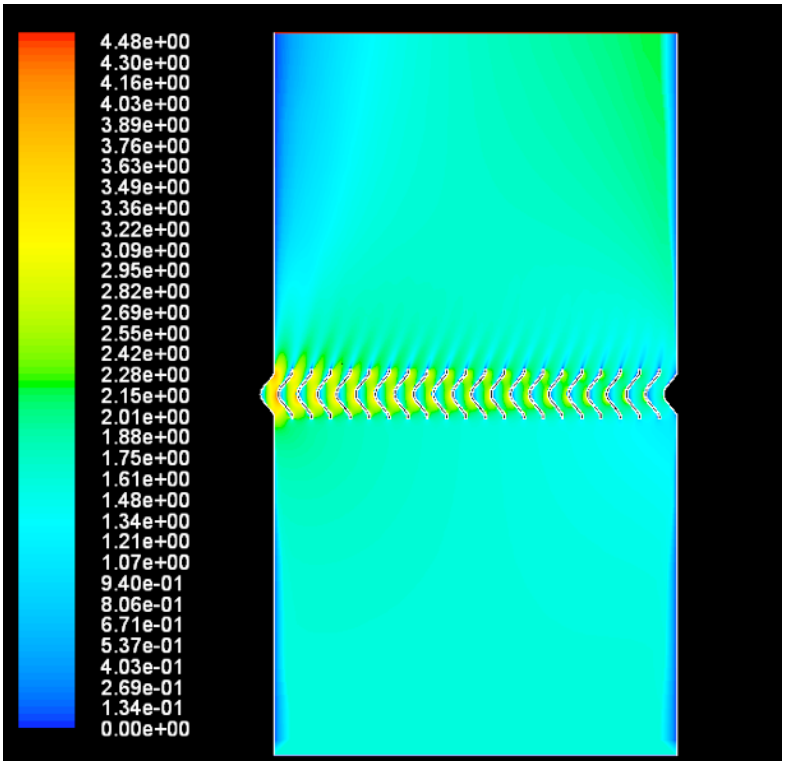

Figure 7.17: Velocity field for asbesto- cement eliminator for a velocity of 1,58 m s^{-1} (m s^{-1})

Only in the eliminators it can be seen that on the left side the velocity is higher than on the right side. The yellow colour stands for a higher velocity. On the left side, between the eliminator shape next to the wall and the wall, is a small region where the velocity is around 3 m s^{-1}. Between the next shapes this region is reducing and on the right side the yellow region is disappeared.

Now, the design is changed and the velocity is displayed in the form of different vectors. Figure 7.18 faces the left and the right side of the domain, as in Figure 7.3 for the wooden lath eliminator. There is a difference in the velocity between the left and the right side of about 2 m s^{-1}. But compared with the wooden lath eliminator after the eliminators, this difference clears.

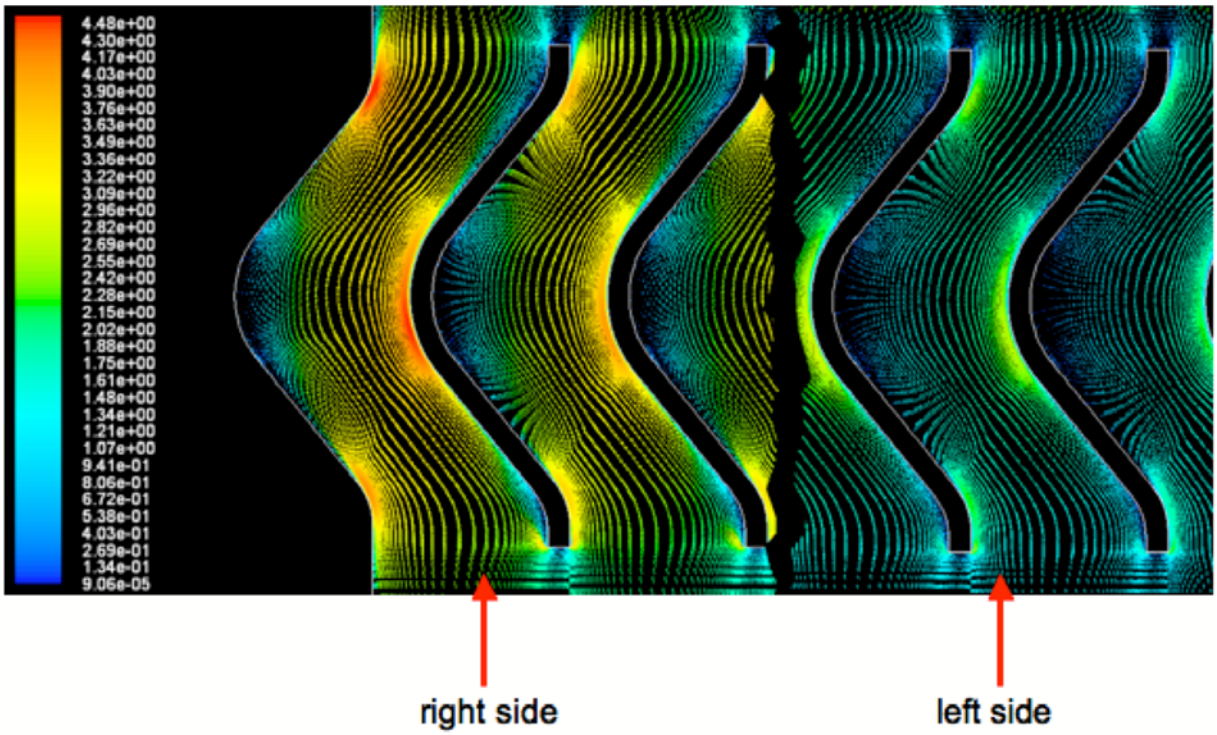

Figure 7.18: Comparison of the velocity, left and right side of computational domain (m s^{-1})

Considering a single eliminator “duct“ one can see that on one side the flow is accelerated and on the other side of the indentation an eddy “water“ is formed, which means the flow does not appear to move there. A vortex is formed. This is shown in Figure 7.19.

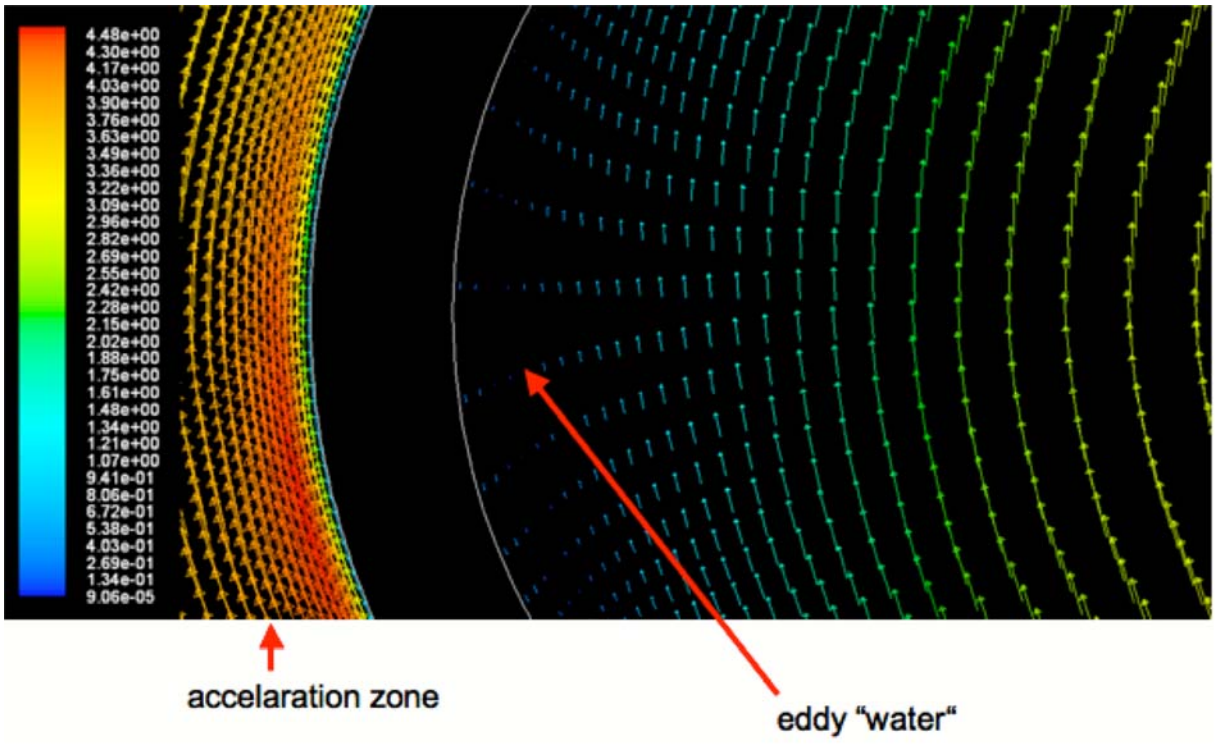

Figure 7.19: Vortex and acceleration zone formed in eliminator duct (m s^{-1})

As well as for the wooden lath eliminator, the computational domain can be displayed regarding the stream function of the flow. This is shown in Figure 7.20. The flowing fluid is deflected by the eliminator shapes and the stream functions are curved.

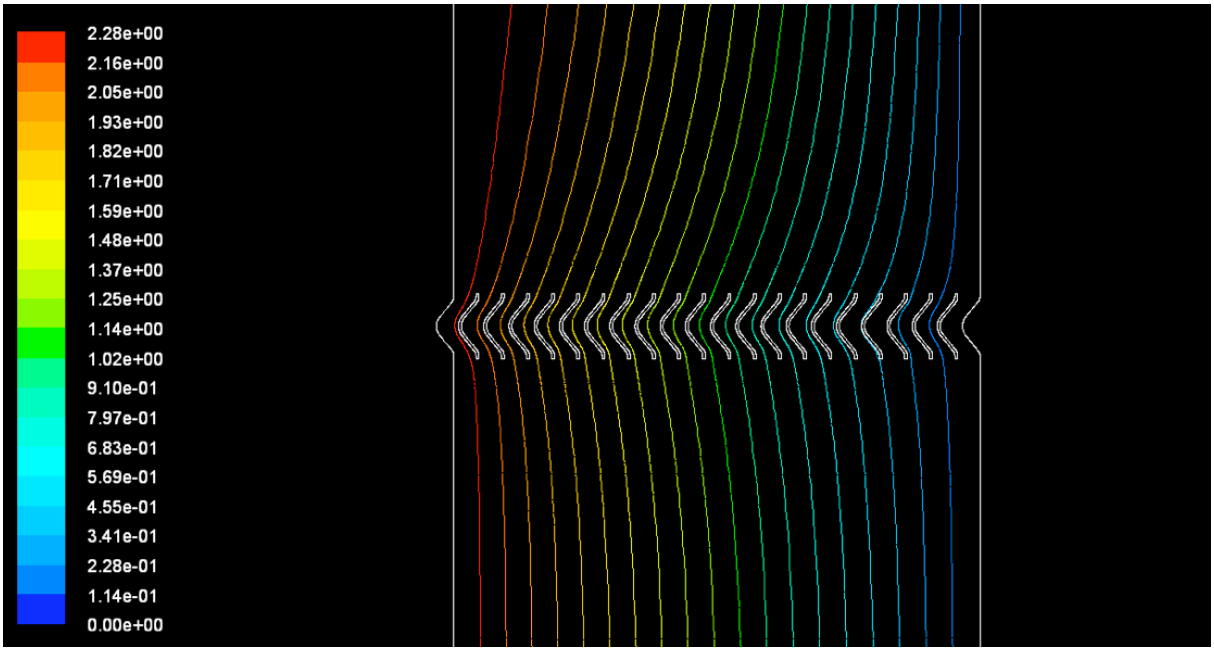

Figure 7.20: Streamlines for asbesto- cement eliminator (kg s^{-1})

For the two other velocities found in the literature calculations are executed, too. However, as in the case of the wooden lath eliminator, there is no big difference in the behaviour of the flow. Therefore the results for the other velocities are presented in a short form, like for the wooden lath eliminator.

Figure 7.21 displays the pressure field for the entire computational domain for an inlet velocity of 0,94 m s^{-1} and Figure 7.22 the velocity field for the same inlet velocity.

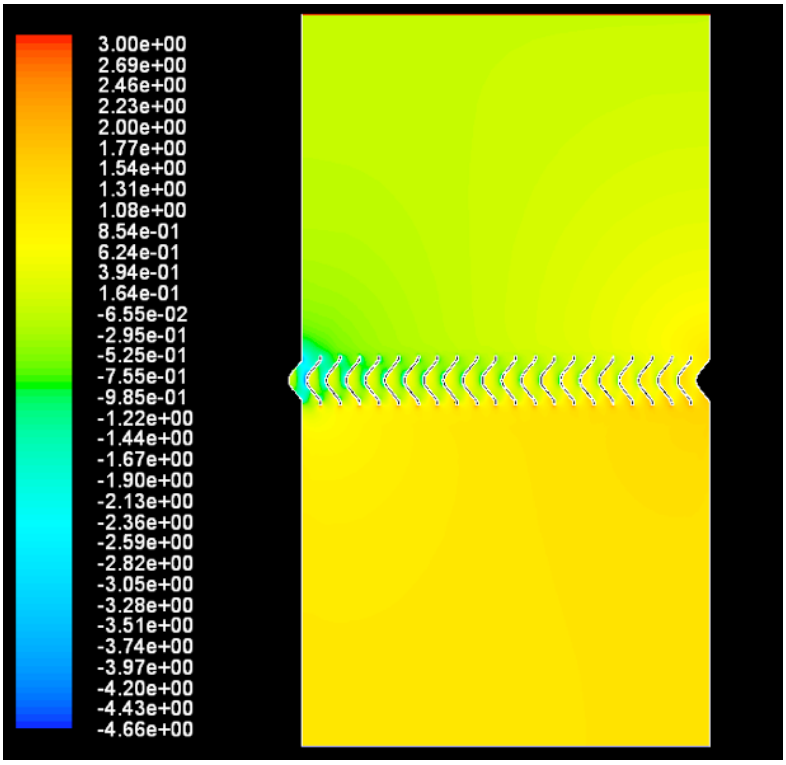

Figure 7.21: Pressure field for an inlet velocity of 0,94 m s^{-1}, asbesto- cement eliminator (Pa)

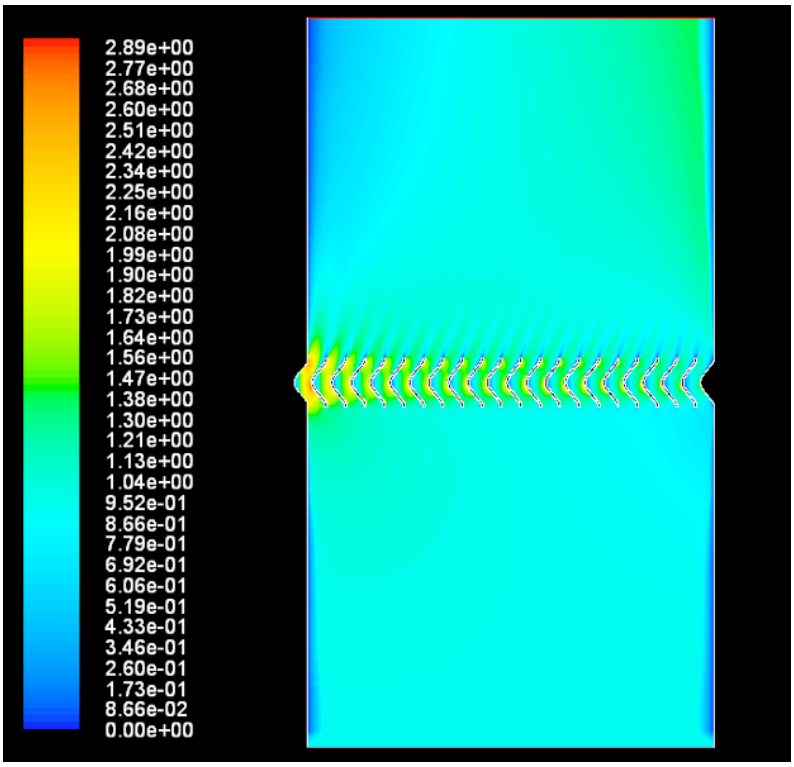

Figure 7.22: Velocity field for an inlet velocity of 0,94 m s^{-1}, asbesto- cement eliminator (m s^{-1})

The third velocity examined is 2,23 m s^{-1}. For this velocity Figure 7.23 shows the pressure field and Figure 7.24 the velocity field.

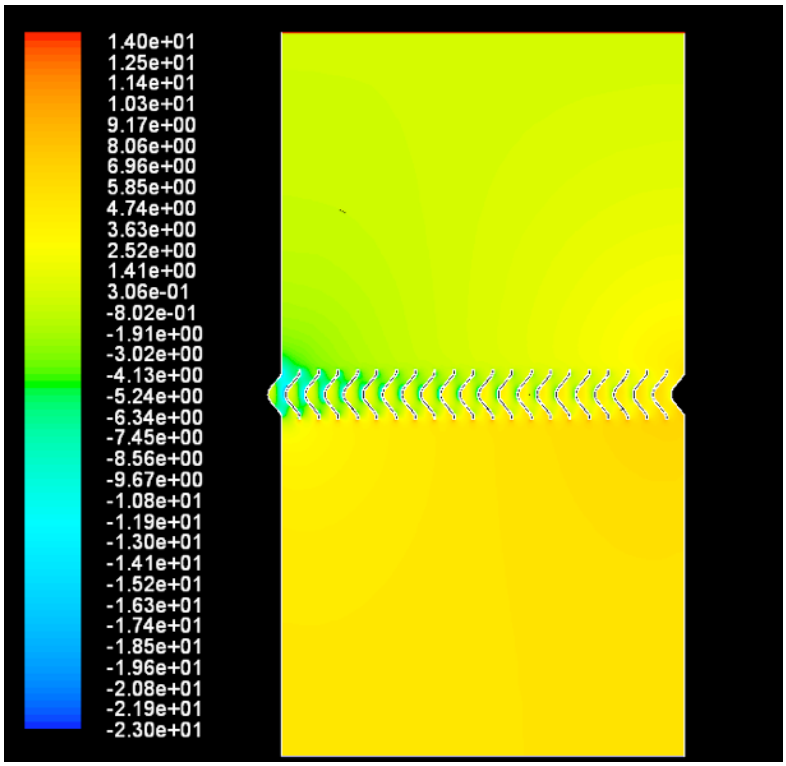

Figure 7.23: Pressure field for an inlet velocity of 2,23 m s^{-1}, asbesto- cement eliminator (Pa)

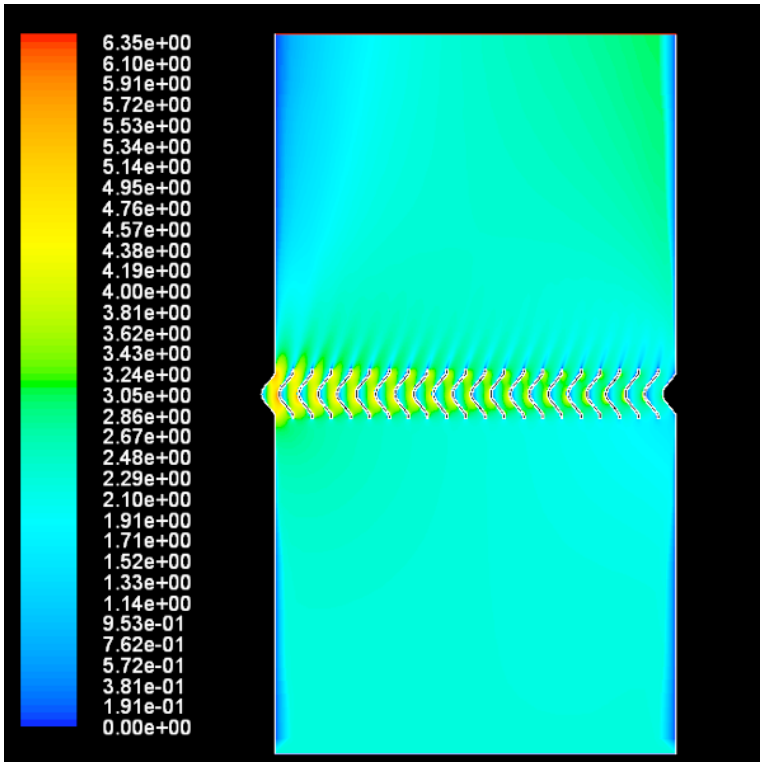

Figure 7.24: Velocity field for an inlet velocity of 2,23 m s^{-1}, asbesto- cement eliminator (m s^{-1})

Regarding the pressure and the velocity fields for the other two inlet velocities, it can be seen that there is no great change in the behaviour of the flow. On the left side the velocity is higher than on the right side. After passing the eliminators this inequality balances.

Now, several vertical and horizontal surfaces are introduced to the computational domain. In these surfaces the velocity and pressure is examined, like in the case of the wooden lath eliminator. Figure 7.25 shows the computational domain with the grid and the different surfaces. The *x*- surfaces are chosen in such a way that they do not cross the walls of the eliminator shapes.

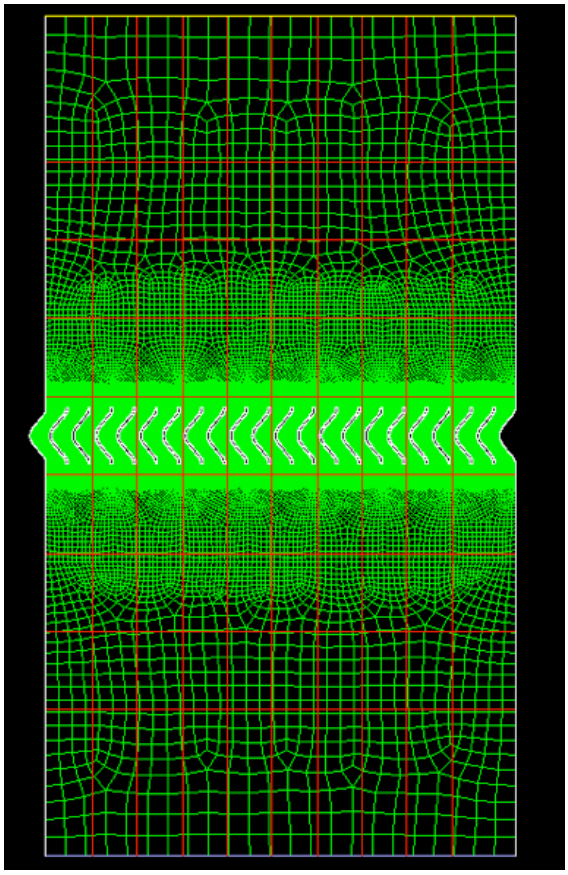

Figure 7.25: Computational domain of asbesto- cement eliminator with used grid and lines

In Figure 7.26 the pressure for the different *y* surfaces is displayed, for an inlet velocity of 1,58 m s^{-1}. The lines around the value of 0 Pa represent the surfaces above the eliminator level. The others around the value of 2,5 Pa are the surfaces the flow crosses before passing through the eliminators.

It can be seen, as described above, that by passing the eliminators the pressure on the right side increases and on the left side decreases (violet line). The yellow line represents the surface just below the eliminators. It is waved. Each wave represents a single eliminator shape. The lines above the eliminators balance with increasing value of *y*.

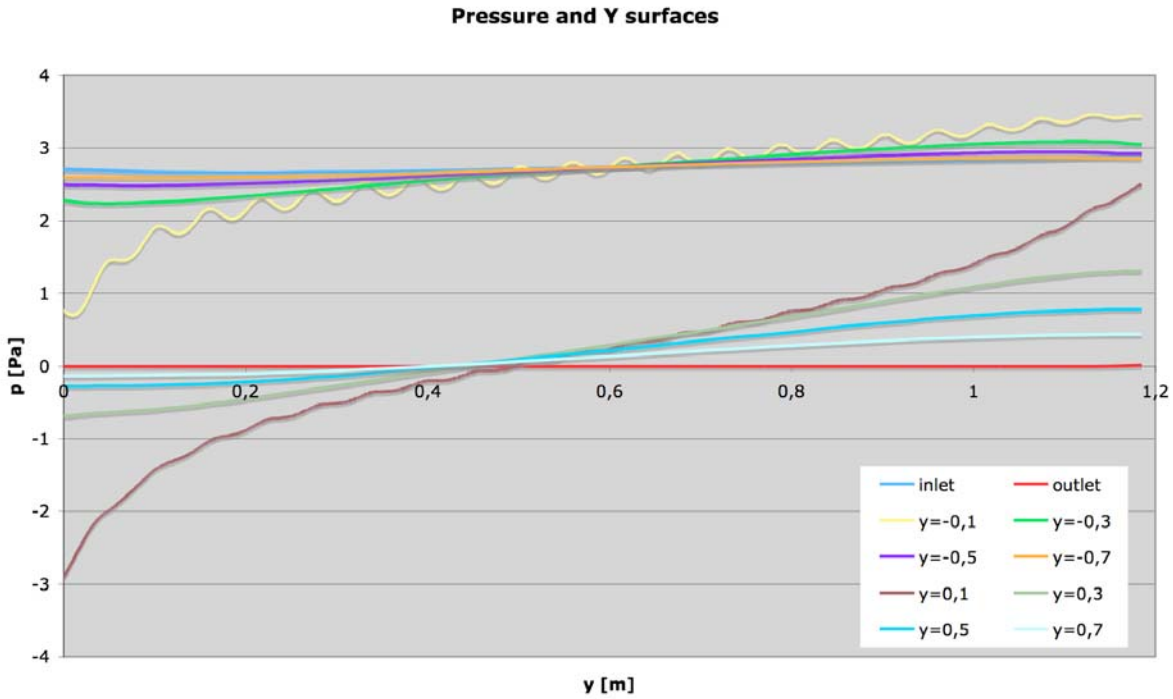

Figure 7.26: Diagram for the different *y* surfaces regarding pressure

Figure 7.27 shows the distribution of the pressure for the *x*- surfaces. On the left side, for an *x* value of -1 m, the inlet is situated. At the value of around 0 the flow passes through the eliminators. The right side of the diagram corresponds to the outlet.

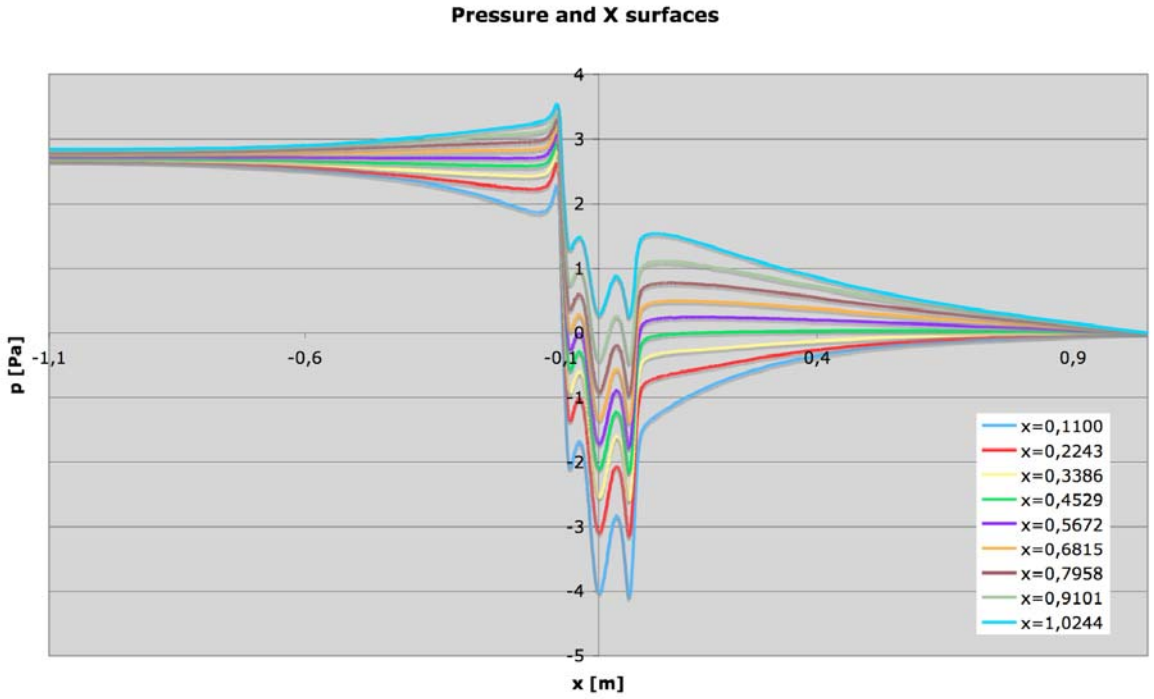

Figure 7.27: Diagram for the different *x* surfaces regarding pressure

The same procedure can be done with the velocity. That is to say, the different surfaces regard the values of the velocity. Figure 7.28 shows the distributions of the velocity for the *y*- surfaces of the inlet, outlet and the surfaces next to the eliminators.

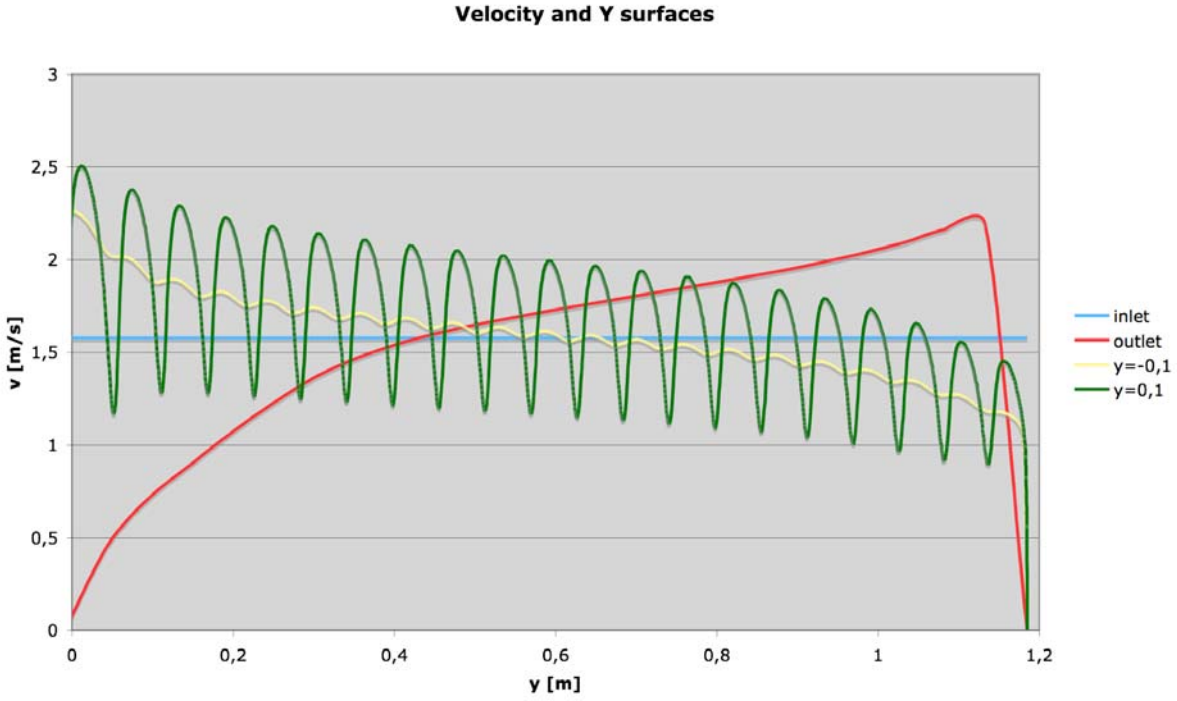

Figure 7.28: Diagram for *y* surfaces regarding velocity

Figure 7.29 shows the distribution of the velocity for the different *x*- surfaces. Due to the different magnitude of the velocity on the two sides of the domain the blue line is the next one to the left wall. Also, Figure 7.28 is almost the mirror- inverted diagram of Figure 7.27 regarding the pressure in the *x*- surfaces.

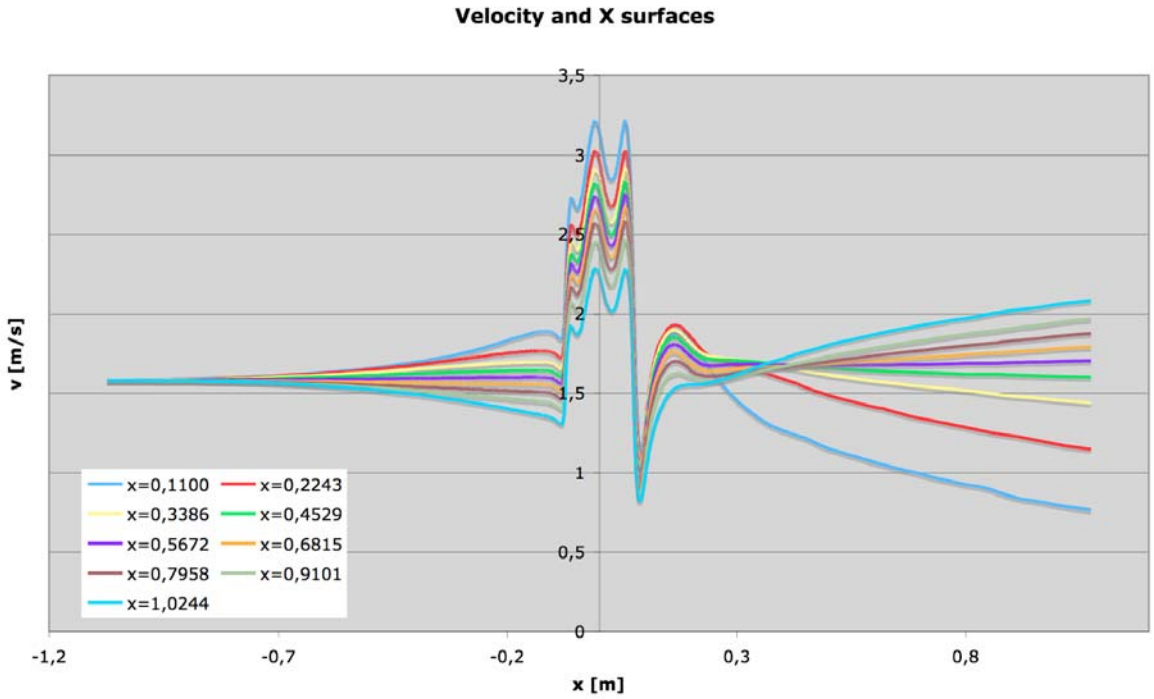

Figure 7.29: Diagram for the different *x* surfaces regarding velocity

7.3 Discussion of results

For both geometries it is calculated that the velocity is bigger on the left side. This is probable because of the shape of the eliminators. The two geometries are bent to the left, this may cause that the air be conducted to the left side, too.

The ratio of the velocity of the two sides is approximately equal for the two different geometries. That is to say that the velocity on the left side is around two times bigger than on the right one. However, in the wooden lath eliminator geometry the velocity influences the entire region above the eliminators. The velocity is around 2 m s^{-1} in a big part of this area. But in case of the asbesto- cement eliminator the velocity balances after the flow has passed through the eliminators. The velocity of the flow is around 1,5 m s^{-1} before entering the eliminators (such as the inlet velocity) and after the eliminators, too.

In the case of the wooden lath geometry another big part of the area above the eliminators is influenced by the modification of the wall to fit the eliminators. There is a nose on the left side, which causes a separation of the flow. Due to this separation a big part of the region above the eliminator has a velocity of 0,7 m s^{-1}. Also, the eliminator shapes form a “lee“ and therefore in the areas behind the shapes the flow has a velocity of approximately 0,5 m s^{-1}. Especially beyond the lower eliminators the flow is very deflected.

In the asbesto- cement eliminator geometry such a lee is not formed. The reason may lie in the different thickness of the eliminator shapes. They are much thinner in case of the asbesto-cement geometry.

7.4 Comparison of the numerical results of the fine and coarse grid

In this section the results for the fine and coarse grids are compared. It can be said that there are no big changes in the behaviour of the flow for the two geometries. That means in the simulations with the coarse grids no “new“ vortexes or other phenomena appear.

7.4.1 Wooden lath eliminator

In this section the results for the wooden lath eliminator for the two grids are compared.

Figure 7.30 displays the comparison of the pressure field of the two grids for an inlet air velocity of 1,52 m s^{-1} . On the left side the results for the fine grid and on the right side for the coarse one are shown.

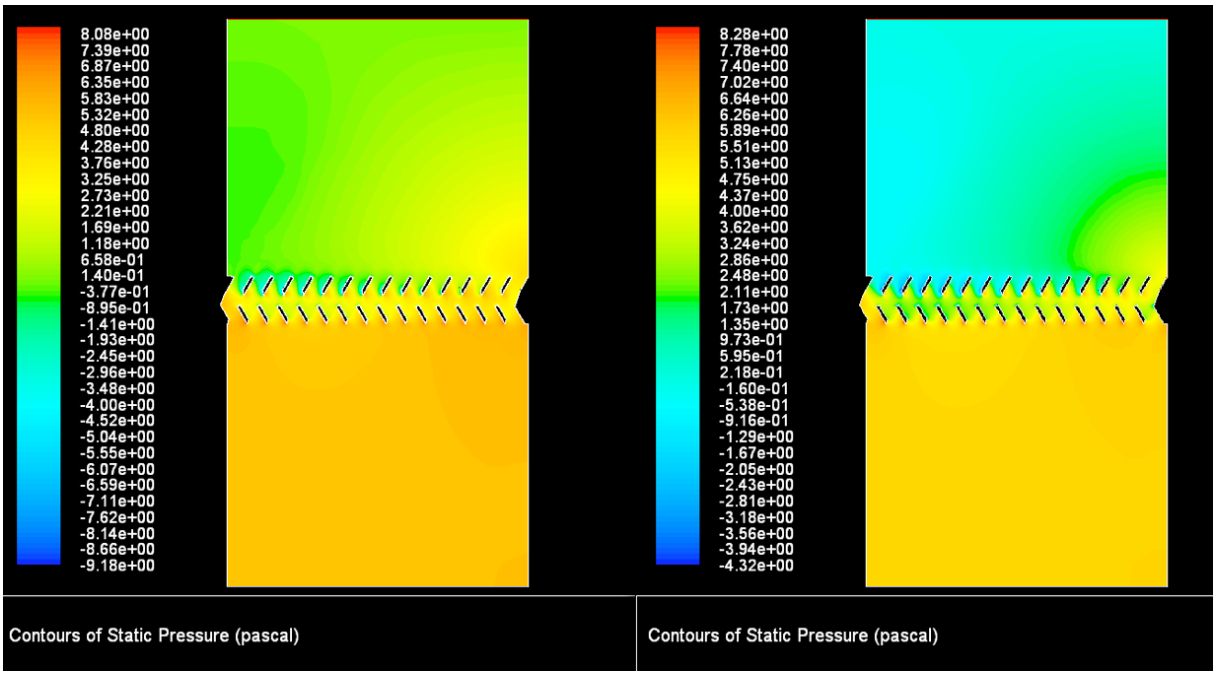

Figure 7.30: Comparison of the pressure field of the fine and coarse grids for the wooden lath eliminator for a velocity of 1,52 m s^{-1} (left: fine, right: coarse)

As seen in chapter 5 the coarse grid calculates the pressure higher than the finer one (average inlet pressure fine grid: 5, 2784 Pa, average inlet pressure coarse grid: 5,9968 Pa). Therefore the entire pressure field is calculated higher for the coarse grid. Through the different colours the difference seems to be very big between the two grids. However, when focusing on the colour scale it can be seen that the difference is the same as for the inlet pressures.

Figure 7.31 displays the velocity field for the same velocity of 1,52 m s^{-1}.

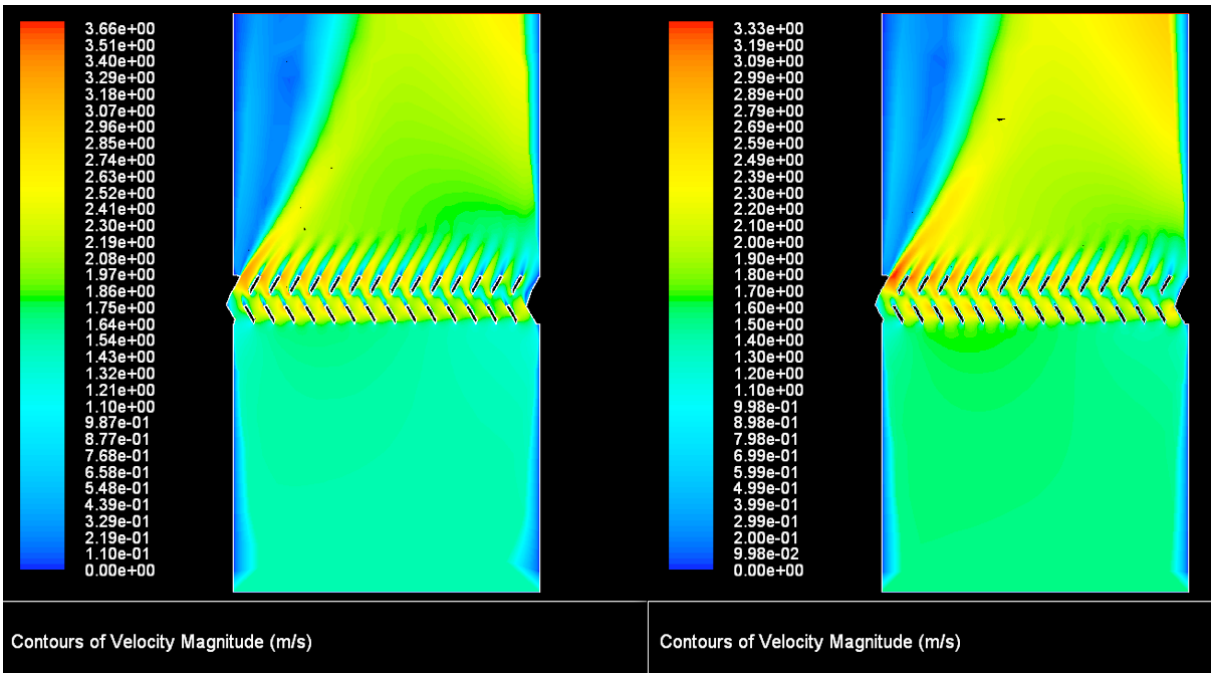

Figure 7.31: Comparison of the velocity field of the fine and coarse grids for the wooden lath eliminator for a velocity of 1,52 m s^{-1} (left: fine, right: coarse)

The velocity fields for the two grids are very similar, but this was expected because the velocity has to fulfill the mass conservation equation.

Figures 7.32 and 7.33 display the comparisons of the pressure distributions for the other two inlet velocities. The velocity distributions are not shown either, because they are very similar.

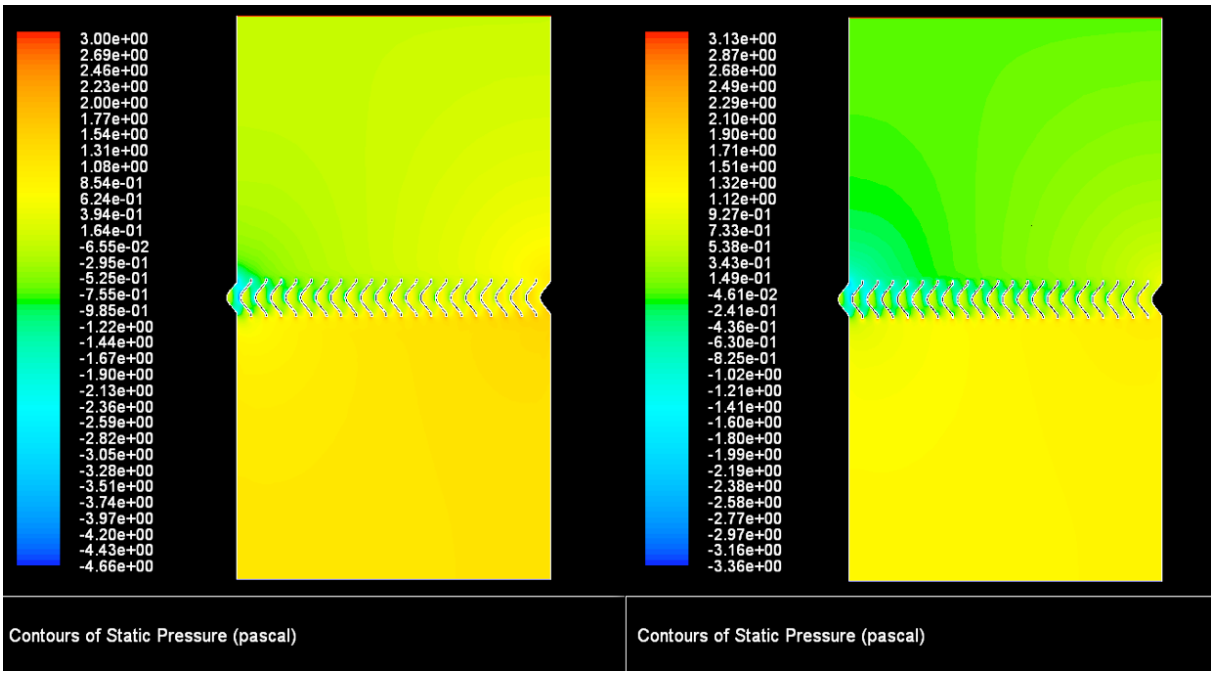

Figure 7.32: Comparison of the pressure field of the fine and coarse grids for the wooden lath eliminator for a velocity of 0,91 m s^{-1} (left: fine, right: coarse)

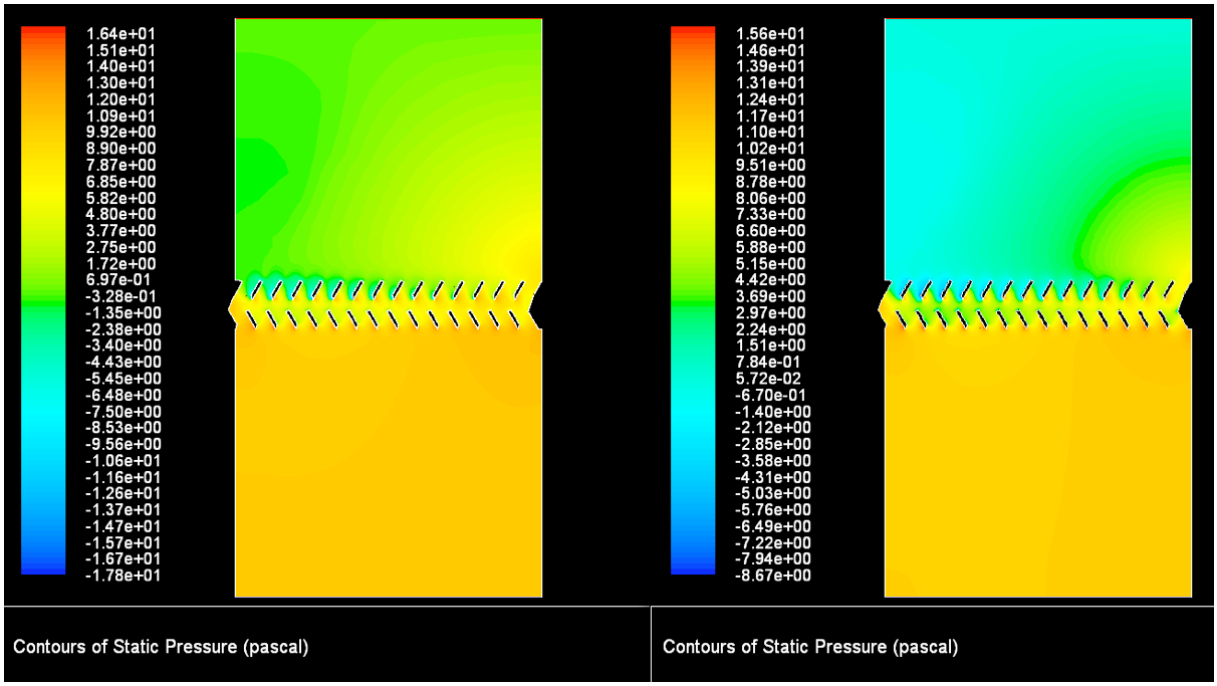

Figure 7.33: Comparison of the pressure field of the fine and coarse grids for the wooden lath eliminator for a velocity of 2,13 m s^{-1} (left: fine, right: coarse)

As well as for a velocity of 1, 52 m s^{-1} for the other two velocities it can be seen that the coarse grid calculates the pressure higher than the fine one.

7.4.2 Asbesto- cement eliminator

Now, the results for the asbesto- cement eliminator for the coarse and fine grids are compared.

Figure 7.34 displays the comparison of the pressure fields for the two grids for an inlet air velocity of 1,58 m s^{-1}. On the left side the result for the fine grid is shown. The right side shows the results for the coarse grid.

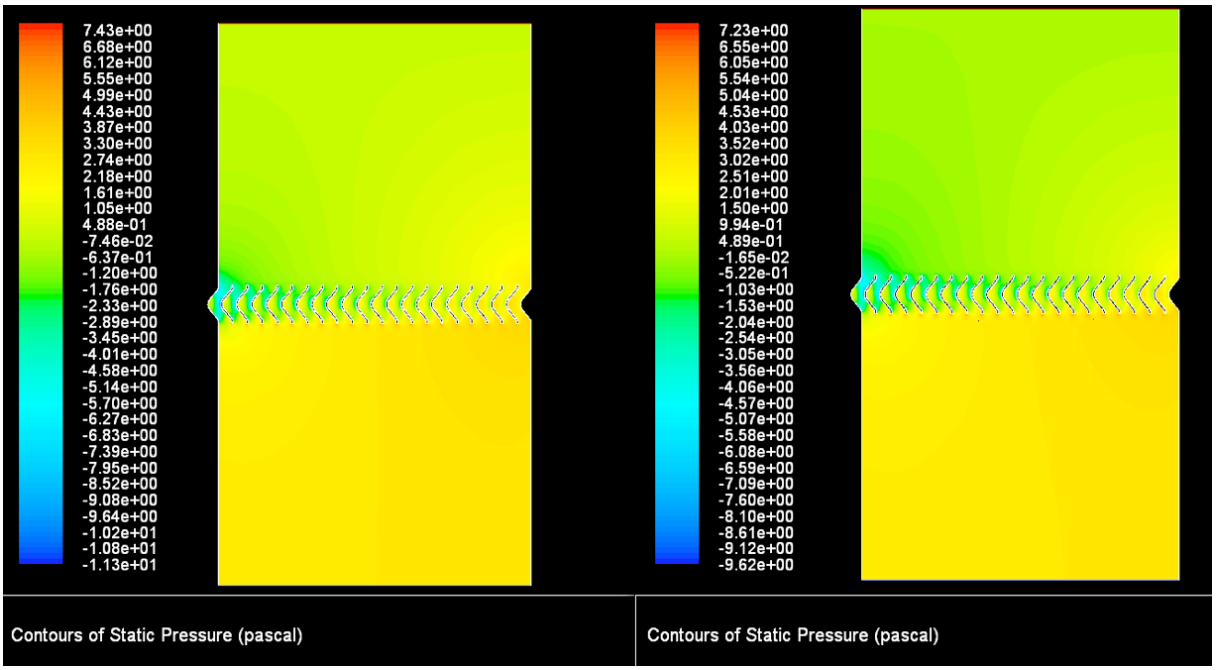

Figure 7.34: Comparison of the pressure field of the fine and coarse grids for the asbesto-cement eliminator for a velocity of 1,58 m s^{-1} (left: fine, right: coarse)

Since the difference for the inlet surfaces calculated in chapter 5 (average inlet pressure fine grid: 2,7513 Pa, average inlet pressure coarse grid: 2,9938 Pa) is not as big as for the wooden lath eliminator, the pressure distributions are almost equal.

Figure 7.35 displays the comparison for the velocity fields and the same velocity.

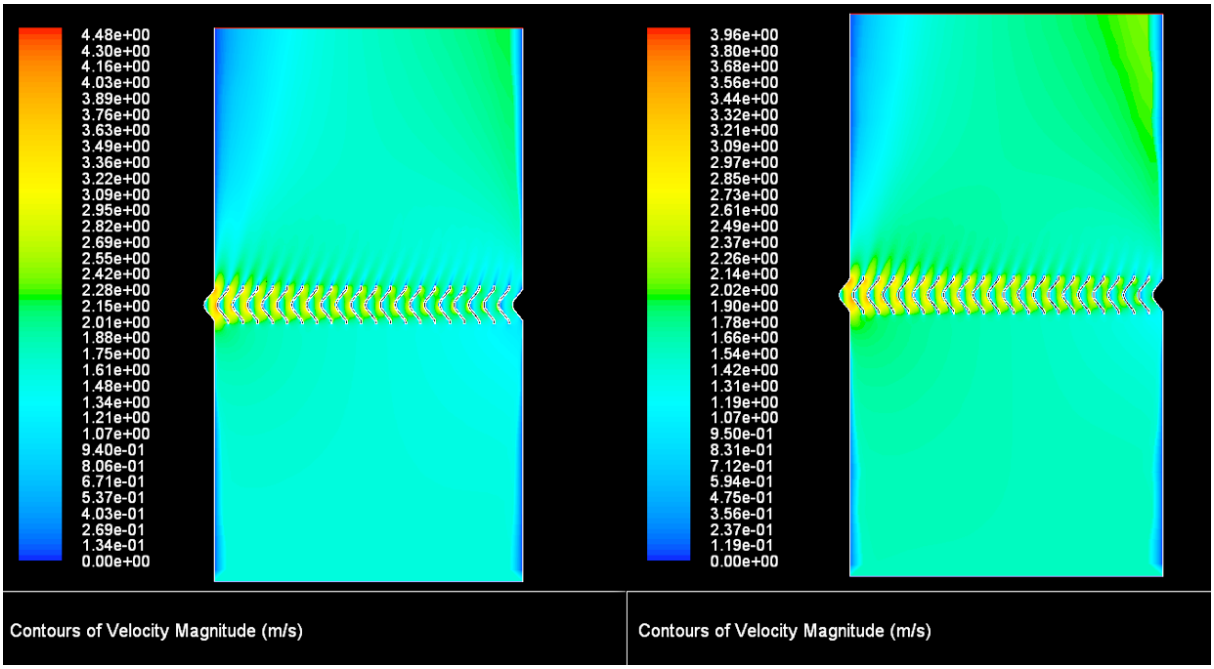

Figure 7.35: Comparison of the velocity field of the fine and coarse grids for the asbesto-cement eliminator for a velocity of 1,58 m s^{-1} (left: fine, right: coarse)

For the two velocity fields almost no difference can be seen. The only thing is that the coarse grid seems to calculate the velocity on the left side lower and on the right side higher than the fine grid. But the difference is very small and can be disregarded.

Figures 7.36 and 7.37 display the pressure fields for the two other velocities regarded. As well as for the wooden lath eliminator, the velocity distributions are not displayed.

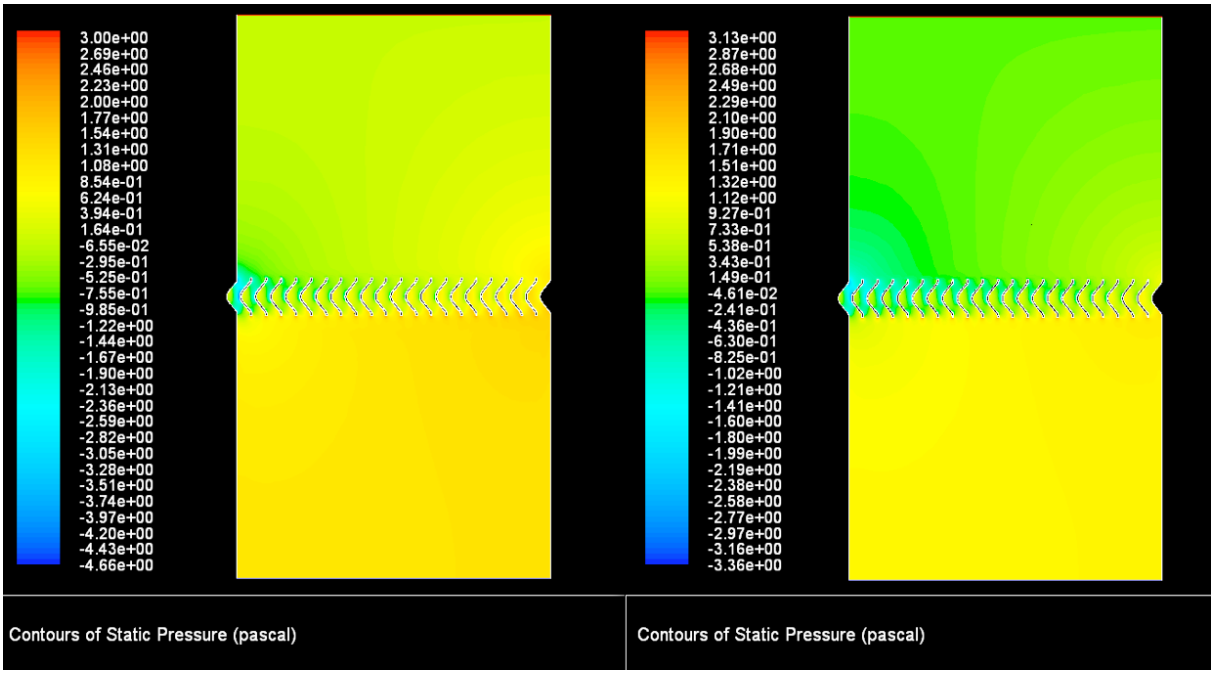

Figure 7.36: Comparison of the pressure field of the fine and coarse grids for the asbesto-cement eliminator for a velocity of 0,94 m s^{-1} (left: fine, right: coarse)

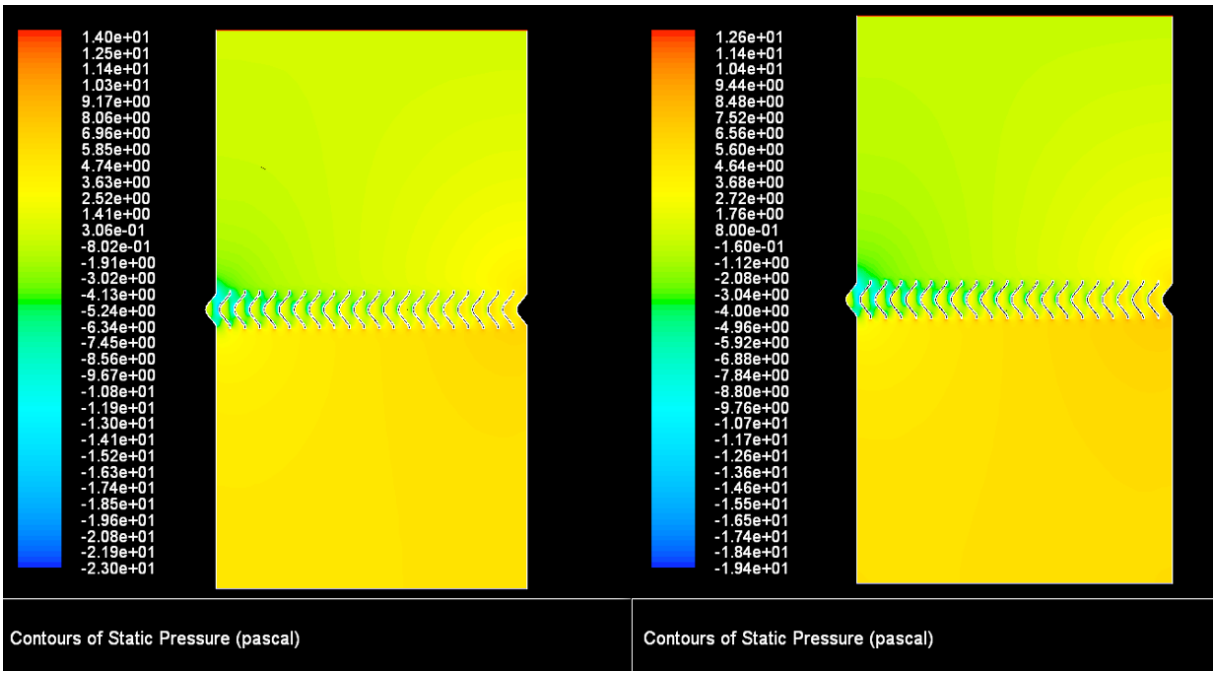

Figure 7.37: Comparison of the pressure field of the fine and coarse grids for the asbesto-cement eliminator for a velocity of 2,23 m s^{-1} (left: fine, right: coarse)

For a velocity of 2,23 m s^{-1} the pressure fields for the two grids do not show much difference. However, for a velocity of 0,94 m s^{-1} the calculation for the coarse grid appears to be pretty different from the one for the fine grid. But this difference results from the varying colour code.

7.5 Drag coefficients

Now, as a result of the numerical simulation the drag coefficient for the two different geometries is calculated. The drag coefficient is a dimensionless quantity that describes a characteristic amount of aerodynamic drag caused by fluid flow. In the present case it is a quantity for the aerodynamic resistance of the drift eliminators. It is defined as follows:

$$c_D = \frac{\Delta P}{\frac{1}{2}\rho A v^2} \tag{7.1}$$

where ΔP is the pressure drop, A is the reference area, v is the velocity, and ρ is the density of the flow.

In this case the reference area is the width of the computational domain multiplied by the depth of 1 m. The width of the computational domain for the wooden lath eliminator is 1,15 m and for the asbesto- cement eliminator 1,19 m, see 3.2.2. Therefore the reference area for

the wooden lath eliminator is 1,15 m^2 and 1,19 m^2 in the case of the asbesto- cement eliminator.

The used pressure drops for the calculation of the drag coefficients are the same pressure drops as stated in chapter 6.

Also, it is possible to calculate *Reynold*s numbers using the widths of the computational domains as characteristic length. Table 7.1 shows the calculated drag coefficients, the *Reynold*s numbers for the according velocities and pressure drops for the wooden lath eliminator. The columns “fine“ and “coarse“ display which grids are used for the calculation. Table 7.2 shows the values for the asbesto- cement eliminator.

Table 7.1: Drag coefficients and *Reynold*s numbers for the wooden lath eliminator

Velocity, v [m s^{-1}]	*Reynold*s number, *Re* [-]	Pressure drop, ΔP [Pa]		Drag coefficient, c_D [-]	
-	-	fine	coarse	fine	coarse
0,91	69300	1,5033	1,6812	2,62	2,93
1,52	116000	4,1225	4,4826	2,57	2,80
2,13	162000	8,0473	8,4982	2,56	2,70

Table 7.2: Drag coefficients and *Reynold*s numbers for the asbesto- cement eliminator

Velocity, v [m s^{-1}]	*Reynold*s number, *Re* [-]	Pressure drop, ΔP [Pa]		Drag coefficient, c_D [-]	
-	-	fine	coarse	fine	coarse
0,94	71500	1,0124	1,1245	1,65	1,84
1,58	120000	2,6191	2,7206	1,51	1,57
2,23	170000	4,9106	4,8987	1,42	1,42

The Figure 7.38 shows the diagram for the *Reynold*s number and the drag coefficient for the wooden lath eliminator, and Figure 7.39 for the asbesto- cement eliminator.

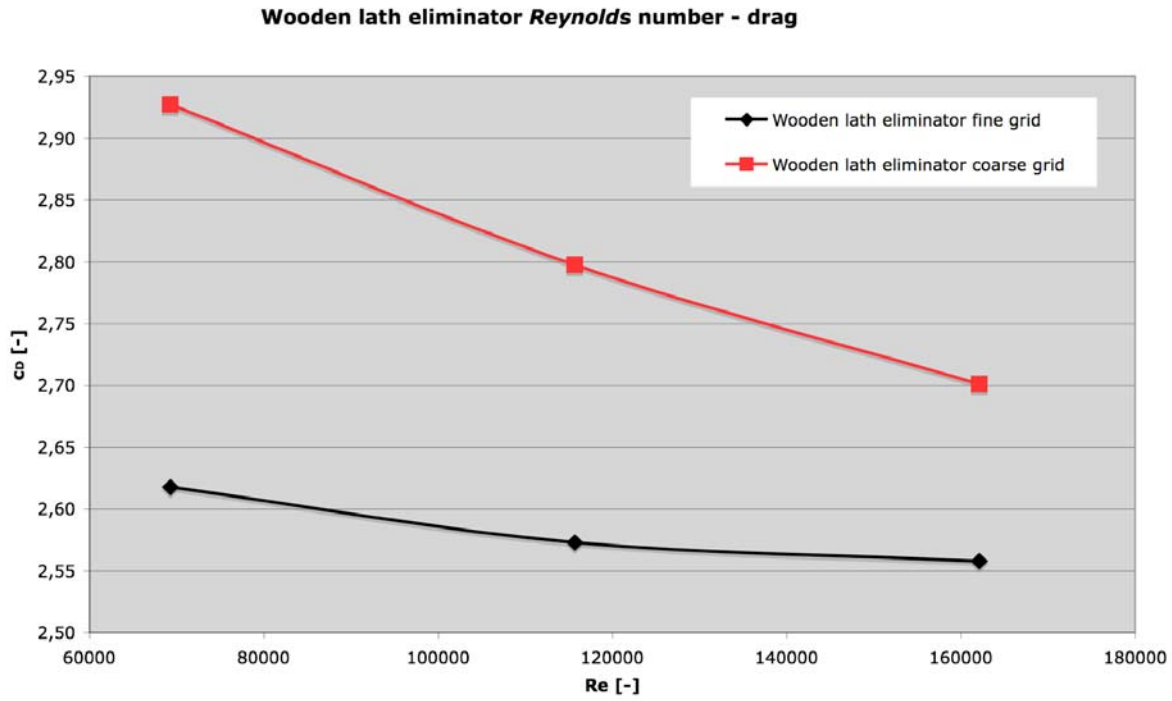

Figure 7.38: *Reynold*s number – drag coefficient diagram for the wooden lath eliminator

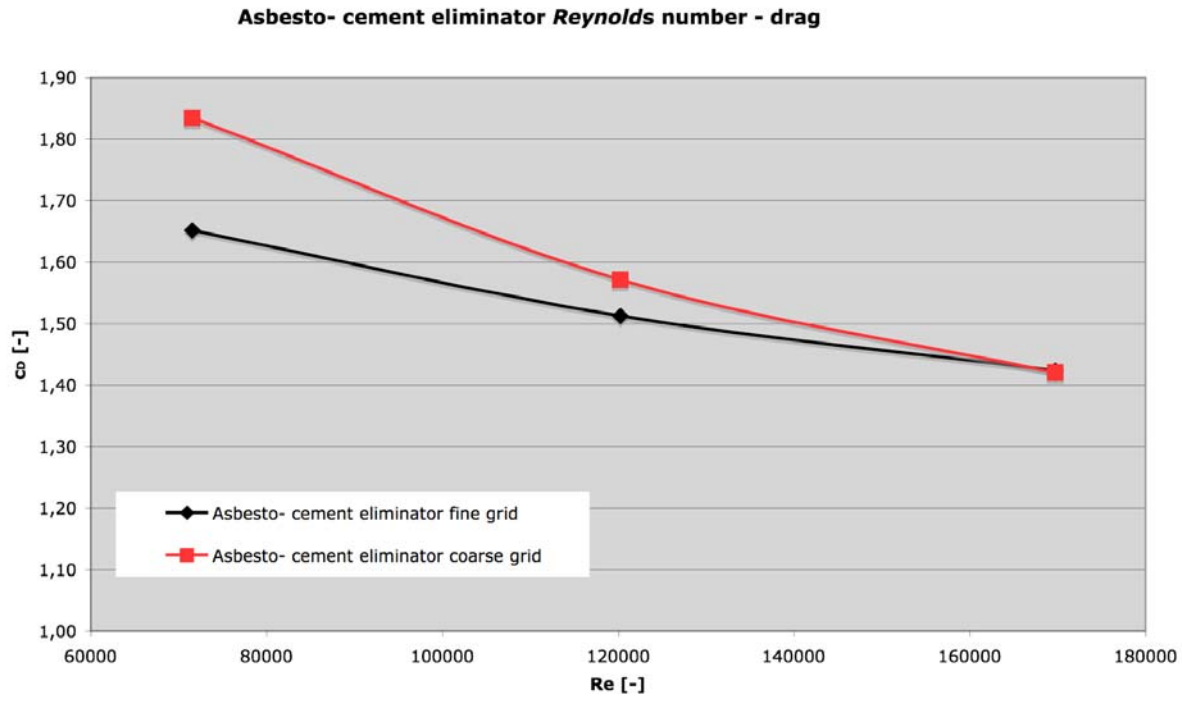

Figure 7.39: *Reynold*s number – drag coefficient diagram for the asbesto- cement eliminator

For the fine grid of the wooden lath eliminator the drag coefficient is almost constant and around a value of 2,6. The values for the coarse grid are all higher and for a higher *Reynold*s number the values decrease.

In the case of the asbesto- cement eliminator the deviation between the values for the two grids is not as big as for the wooden lath eliminator. For the highest *Reynold*s number the drag coefficients are equal. For an increasing *Reynold*s number the drag coefficient decreases.

8 Conclusion

8.1 Conclusion of the working procedure

In the present work the behaviour of an air flow passing through eliminators of a cooling tower has been examined numerically. The main focus was laid on the pressure drop. Two different types of eliminators have been considered. The wooden lath eliminator and the asbesto- cement eliminator. For the numerical simulation the software of FLUENT was used.

For the examination literary sources have been analysed. From these sources a two-dimensional computational domain has been built for each eliminator type. In these domains grids with different cell numbers were introduced to examine the behaviour of the solution depending on the grid size. Therefore an uncertainty methodology was introduced and applied with several sets of grids. In doing so, different approaches were taken. First, only the interesting eliminator area was examined using fine grids and enhanced wall treatment. Second, only the first rows of the grids next to the eliminator walls using enhanced wall treatment were regarded, too. And in the end, considering coarse meshes using wall function as near- wall approach. For all three studies a satisfying small value for the Grid Convergence Index, *GCI*, was calculated.

Another study to determine the dependence of the solution from the grid size was also introduced. This study dealt with the value of y^+. For both geometries a value of y^+ could be found for which the solution stabilised.

Based on the study of the value of y^+ a fine grid was chosen and several simulations were run, introducing the different air velocities found in the literature to the computational domain. The results of these simulations were presented and compared with the results of the literature. Also, a coarse mesh was chosen for each geometry depending on the uncertainty study. As well as for the fine grid, simulations with the velocities found in the literature were run and the results compared.

8.2 Conclusion of results

The results shown for both geometries that on one side of the computational domain the velocity was much higher than on the other side. The pressure behaves contrarily. That is to say, on the side where the velocity was relatively high the pressure was relatively low. This was probably caused by the geometries of the eliminators. Both geometries were curved, so it appeared that the flow was conducted to one side. The influence of the geometry was bigger for the wooden lath eliminator than for the asbesto- cement eliminator.

For each geometry the pressure drop for three different velocities was determined. The numerical results for the wooden lath eliminator agreed with a deviation between 1 and 2% with the experimental ones using a fine mesh and till 10% using a coarse one. However, in the case of the asbesto- cement eliminator the deviation of the numerical and experimental results was up to 50% for a fine mesh as well as for a coarse one. Why the results were so different was and is still not clear. There can be various reasons taken into account.

- First: The computational model was not chosen appropriately, for example, the k- ε turbulence model may not fit the requirements to model the flow correctly.
- Second: Another reason may also be that the calculations were performed as steady ones. Perhaps in an unsteady consideration periodic vortexes are formed and influence the pressure drop.
- Third: Only an air flow was considered, but in a real cooling tower and in the experimental source this air flow bears water droplets. These water droplets may cause an increase of the pressure drop.
- Fourth: Thus, the literary sources were mixed to get all magnitudes needed to define the computational domain and the boundary conditions, the behaviour of flow may be changed by the “new“ environment.
- Fifth: The experimental data was simply wrong.

However, the good results for the wooden lath eliminator disagree with the first five assumptions.

8.3 Outlook

The object of the present work was to create a computational model of eliminators of a cooling tower to be able to optimise the shapes of these eliminators. For the optimization process two magnitudes are of interest: the pressure drop of the eliminators and the rejection of water droplets. In this work only the pressure drop was examined. It could be reasoned that for a grid with a value of y^+ of around 5 the numerical solution is constant.

The next step would be to introduce drops into the computational domain and examine how the flow behaves and if the results agree with the experimental ones. But, there can be found the same problem as for this work now: the literary sources are scarce.

If it is necessary to expand the computational domain to simulate more parts of a cooling tower or to add a third dimension to the domain, it is strongly recommended to use very coarse grids with a value of y^+ of around 30. As examined in this work, the numerical results for such coarse grids differ from the ones for fine grids, but for both geometries the maxima deviation between both results was about 5%. However, the computational effort decreases enormously by using coarse grids.

9 Bibliography

[1] S. R. HANNA AND S. D. SWISHER: A method of calculating the size of cooling tower plumes, *Atmospheric Environment*, Vol 6 (1972), pp. 587- 588

[2] M. W. GOLAY, W. J. GLANTSCHIG AND F. R. BEST: Comparision of methods for measurement of cooling tower drift, *Atmospheric Environment* Vol. 20 No. 2 (1986), pp. 269- 291

[3] K. E. HAMAN AND S. P. MALINOWSKI: Observations of cooling tower and stack plumes and their comparision with plume model "Alina", *Atmospheric Environment* Vol. 23 (1989), No. 6, pp. 1223- 1234

[4] A. K. M. MOHIUDDIN AND K. KANT: Knowledge base for the systematic design of wet cooling towers. Part II: Fill and other design parameters, *International Journal of Refrigeration* Vol. 19 (1996), No. 1, pp.52- 60

[5] T. MICHIOKA, A. SATO, T. KANZAKI AND K. SADA: Wind tunnel experiment for predicting a visible plume region from a wet cooling tower, *Journal of Wind Engineering and Industrial Aerodynamics* Vol. 95, Issue 8 (2006), pp. 741- 754

[6] A. MARTIN AND F. R. BARBER: Some water droplet measurements inside cooling towers, *Atmospheric Environment*, Vol 8 (1974), pp. 325- 336

[7] P. M. FOSTER, M. I. WILLIAMS AND R. J. WINTER: Droplet behaviour and collection by counterflow cooling towers eliminators, *Atmospheric Environment*, Vol. 8 (1974), pp. 349- 360

[8] J. CHAN AND M. W. GOLAY: Comparative performance evaluation of current design evaporative cooling tower drift eliminators, *Atmospheric Environment*, Vol. 11 (1977), pp. 775- 781

[9] B. R. GARDNER AND H. J. LOWE: The research and development background to the environmental problems of natural draught cooling towers, *Atmospheric environment*, Vol. 8 (1974), pp. 313- 320

[10] A. K. M. MOHIUDDIN: Experimental study in a spray filled tower for flow visualization and drift eliminators characteristics, *Journal of Applied Sciences*, Vol. 5 (2005), pp. 284- 291

[11] R. AL- WAKED AND M. BEHNIA: Enhancing performance of wet cooling towers, *Energy Conservation & Management*, Vol. 48, Issue 10 (2007), pp. 2638- 2648

[12] M. R. MOKHTARZDEH- DEHGHAN, C. S. KÖNIG AND A. G. ROBINS: Numerical study of single and two interacting turbulent plumes in atmospheric cross flow, *Atmospheric Environment*, Vol. 40 (2006), pp. 3909- 3923

[13] R. N. MERONEY: CFD prediction of cooling tower drift, *Journal of Wind Engineering and Industrial Aerodynamics*, Vol. 94 (2006), pp. 463- 490

[14] S. P. FISENKO, A. I. PETRUCHIK AND A. D. SOLODUKHIN: Evaporative cooling of water in a natural draft cooling tower, *International Journal of Heat and Mass Transfer*, Vol. 45 (2002), pp. 4683- 4694

[15] C. J. FREITAS: The issue of numerical uncertainty, *Applied Mathematical Modelling*, Vol 26, Issue 2 (1999), pp. 237- 248

[16] FLUENT INC.: FlUENT 6.3 User's guide, (2006)

[17] C. J. FREITAS, U.GHIA, I. CELIK, P. ROACHE AND P.RAAD: ASME's quest to quantify numerical uncertainty, *AIAA*

Reduced Spanish version / *Versión española reducida*

Estudio numérico de la influenciade diferentes tipos de separadores en la emisión de gotas y en la pérdida de carga establecida en una torre de refrigeración

Proyecto fin de carrera

De

Ulrich Kling

Director: Dr. Antonio Sánchez Kaiser

Codirector: Dr. Blas Zamora Parra

Departamiento de Ingeniería Térmica y de Fluidos

Universidad Politécnica de Cartagena

Abril 2008

für meine Eltern | para mis padres | for my parents

Agradecimientos

A *Prf. Dr. Eberhard Göde* de la Universidad de Stuttgart, Alemania, ante todo por la formación académica que he gozado en “su“ departamento y el entusiasmo por las turbinas hidráulicas que me ha transmitido. También por dejarme venir a España para realizar mi proyecto.

A mi director *Dr. Antonio Sánchez Kaiser* de la Universidad Politécnica de Cartagena, España, por la introdución al mundo de la mecánica de fluidos computacional, por su apoyo, animación, interés en mi trabajo, y por su paciencia con mi español “teutónico“. Pero sobre todo por las múltiples posibilidades ofrecidas.

A mi codirector *Dr. Blas Zamora Parra* de la Universidad Politécnica de Cartagena, España, quien siempre tenía tiempo para mí, mis preguntas y dudas, por su ayuda y por sorportar mi español. También por la posibilidad de hacer mi proyecto fin de carrera en Cartagena.

Índice

Índice de figuras

Índice de tablas

Lista de símbolos

Latín

A	Área
e_a	Error relativo aproximado
e_{ext}	Error relativo estimado extrapolado
G_k	Término de la producción de energia turbulenta
h	Celda representativa de la malla
k	Kinetica energia turbulenta
l	Longitud
p	Presión estática
p	Orden del método
r	Factor del refinamiento de la malla
Re	Número de Reynolds
S_M	Termino de fuente en la ecuación de la cantidad de movimiento
U	Velocidad media del flujo
u	Componente de la velocidad según x
u_τ	Velocidad de fricción, $(\tau_\omega/\rho)^{1/2}$
u^+	Velocidad cerca de la pared, adimensional, U/u_τ
v	Componente de la velocidad según y
V_C	Volume de control
x, y	Coordinadas cartesianas
y^+	Distancia de la pared, adimensional, $\rho u_\tau y/\mu$

Griego

δ_{ij}	Delta de Kronecker
ε	Ratio de disipación
μ	Viscosidad dinámica
μ_t	Viscosidad dinámica turbulenta
ν	Viscosidad kinematica
ρ	Densidad de aire
τ_{ij}	Tensor de esfuerzo cortante

Subíndices

i, j	Componentes de un vector o una matriz

1 Introducción

Uno de los sistemas más empleados en la industria para enfriar agua lo consituyen los torres de refrigeración. Este enfriamiento se consigue estableciendo en su interior un flujo cruzao entre una corrente de aire ascendente (introducida por un sistema de ventilación) y un flujo de agua pulverizada en sentido contrario. Parte del agua pulverizada se evapora absorbiendo energía para ello y reduciendo de este modo la temperatura de la misma.

El aire se lleva pequeñas gotas de agua al exterior. Las gotas causan varios problemas. Pueden mojar los alrededores de la torre lo cual puede ser peligroso en el invierno en países del norte de Europa (formación de hielo, etc.). Pero también en países del sur, como España, lo mal puede ser peligroso. A través del agua se pueden extender agentes patógenos (Legionella pneumophila, causa la enfermedad del legionario).

En Murcia, España, hubo una epidemia de la enfermedad de legionelosis con más de 800 personas infectadas. La epidemia fue causada por una torre de refrigeración situada encima de un hospital en una zona urbana (2001).

Para reducir la emisión de gotas de agua a la atmósfera se colocen separadores en el interior de la torre. Los separadores están situados encima de las planchistas que pulverizan el agua. Tienen una forma especial que fuerza la corriente de aire a cambiar la dirección. Por ese cambio rápido las gotas no pueden seguir el flujo e impactan contra los separadores, y caen al suelo de la torre.

No es sólo importante para el ambiente que no salga agua de la torre sino también para el funcionamiento de la torre misma. Todo el agua que sale de la torre tiene que ser reemplazada, para l buen funcionamiento de la misma.

Pero la instalación de los separadores aumenta la pérdida de presión. Esa pérdida influye en el funcionamiento de la torre, porque hace que baje la corriente de aire en torres de tiro natural o hay que aumentar el redimiento del ventilador (torres de tiro mecánico).

Este trabajo se centra en el estudio de la influencia de los separadores sobre el flujo en el interior de la torre. Se eximinarán dos tipos de separadores con la ayuda de simulaciones numéricas. Especialmente se centra la atención en la pérdida de presión de los diferentes tipos de separadores. Los resultados de las simulaciones se compararán con resultados experimentales encontrados en la biliografía.

1.1 Antecedentes

El parlamento y consejo de la Union Europea establece en su directiva 2002/91/EC de diciembre de 2002 que el sector de la construcción consume 40% de la energía de la UE y continua en expansión. Eso lleva a un consumo de energía aún más alto y más emisiones de dióxido de carbono.

Los sistemas de refrigeración que utilizan agua como refrigerante consumen menos energía que aquellos sistemas con aire como refrigerante sin pérdida de rendimiento por la presión de condensación más baja. De acuerdo con lo establecido por la ley española (Código Técnico de la Edificación HS4) los sistemas de refrigeración enfriados por agua deben tener instalaciones de recuperación. La instalación mas comun es la torre de refrigeración.

Después de varias epidemias de la enfemedad de legionelosis, veáse arriba, algunos gobiernos regionales de España límitan el uso de las torres de refrigeración y muchas de ellas han sido reemplazadas por otras tecnologías, que no emiten gotas de agua a la atmósfera pero que suponen un mayor consumo energético. Este aumento del consumo energético produce de igual modo un aumento de las emisiones de dioxido de carbono.

Por eso el gobierno de España requiere estudios comparativos del sistema del aire acondicionado para ciertos nuevos edificios incluyendo sistemas de rechazo de calor.

Este proyecto forma parte del trabajo de colaboración establecida entre la Universidad Politécnica de Cartagena (UPCT), España, y la Universidad de Miguel Hernández de Elche (UMH), España, bajo el Proyecto de Investigación del Plan Nacional “Estudio energético de sistemas de evacuación de calor en instalaciones centralizadas de aire acondicionado y de su impacto en el entorno“.

1.2 Objetivos

El objetivo del presente trabajo es una simulación numérica de un flujo dentro de una torre de refrigeración, en particular el flujo de aire a través de los separadores. La pérdida de presión introducida por los separadores es la variable que se evalurará, junto con los cambios en el comportamiento del flujo. La simulación se aplicará con el programa de FLUENT, un código comercial que usa el método de los volúmenes finitos.

El proyecto consiste en diferentes pasos que se pueden resumir del modo siguente:

- Estudio de la bibliografía con respecto a datos experimentales de los separadores de una torre de refrigeración, recabando información sobre la forma de los separadores, velocidad del aire introducido, valores de la pérdida de presión, una descripción de la configuración de ensayo.
- En la segunda fase del proyecto se construirá el dominio computacional con la forma de los separadores encontrados en la bibliografía para aplicar la malla para la simulación numérica. Se llevará a cabo un estudio de la incertidumbre

de la malla con el fin de encontrar una solución que no dependa del número de las celdas de la malla.

- Introducción de flujo del aire al dominio computacional y análisis del flujo mismo y su comportamiento a través de los separadores. Se registrará la pérdida de presión.
- Comparación de los resultados con los datos encontrados en la bibliografía con respecto a la pérdida de presión.

Finalmente, el presente trabajo se utilizará como punto de partida para la optimización de los separadores. El trabajo debe crear un modelo basado en los estudios hechos para que sea posible utilizar el modelo para la optimización.

1.3 Fases

En la primera fase del proyecto se revisará la bibliografía que trata de torres de refrigeración. Se buscarán especialmente artículos sobre ensayos con separadores. Con la información encontrada se creará un dominio computacional con la geometría encontrada de los separadores. Después se aplicarán diferentes mallas al dominio con el objetivo de encontrar una solución que no dependa del número de celdas de la malla. Mediante ese proceso se determinará la incertidumbre del mallado.

Por medio del estudio de la malla se elegirá una de ellas para introducir diferentes velocidades del aire y examinar el flujo por los separadores.

Se puede dividir el proyecto en diferentes fases:

1. Revisión de la bibliografía que trata sobre torres de refrigeración
2. Creación de un modelo computacional de los datos encontrados
3. Creación de diferentes mallas
4. Estudio de la incertidumbre de las diferentes mallas y la dependecia de las soluciones de las mallas
5. Introducción de diferentes velocidades de aire al modelo virtual
6. Estudio de los resultados y del flujo mismo
7. Interpretación y demostración de los resultados
8. Comparación de los resultados numéricos con los datos de la bibliografía

2 Modelo general analizado

2.1 Seleción de la geometría a estudiar

En la bibliografía se puede encontrar varios autores que se dedican a las torres de refrigeración. Hay artículos sobre las torres en general, pero también algunos especialmente sobre los separadores de una torre de refrigeración. La información obtenida resultó bastante espersa por lo que para la obtención para un modelo completo (geometría, modelo analítico y validación experimental) ha sido necesario un trabajo de recopilación de información basada principalmente en cinco publicaciones ([6], [7], [8], [9], [10]). La Tabla 2.1 muestra la información necesaria y en qué artículo fue encontrada.

Tabla 2.1: Información encontrada en la bibliografía (< **X** > existente y usada, < **O** > existente pero no usada, < **-** > no existente)

Fuente bibliográfica	**[6]**	**[7]**	**[8]**	**[9]**	**[10]**
Geometría del separador	**-**	**X**	**-**	**X**	**-**
Pérdida de la presión	**-**	**-**	**O**	**X**	**O**
Velocidad	**-**	**O**	**O**	**X**	**O**
Densidad	**-**	**-**	**X**	**-**	**-**
Configuración de ensayo	**-**	**X**	**O**	**O**	**O**

Ee la tabla 2.1 se puede ver que la información sobre la geometría se ha obtenido de dos diferentes artículos. Eso es porque los dos artículos tratan de las mismas geometrías. Toda la información importante fue obtenida de los artículos [7] y [8]. Los dos artículos hablan de dos diferentes tipos de geometrías: el “wooden lath eliminator“ y el “asbesto- cement eliminator“. A partir de estas dos geometrías se construirán los modelos analizados numéricamente en este trabajo.

Solo la densidad se obtuvo de otro artículo. La razón por la cual se tomó la densidad es que en [9] la pérdida de presión está escrito en “units of velocity heads“ (*uvh*) y definida como:

$$uvh = \frac{\Delta P}{\frac{1}{2}\rho V^2} \tag{2.1}$$

Donde ΔP es la pérdida de presión, ρ la densidad y v es la velocidad. Sin saber la densidad no se puede calcular la pérdida de presión en Pascal. Para coger un valor típico de la densidad de un flujo de aire dentro de una torre de refrigeración, se cogió el valor de la densidad de [8].

2.2 Creación del modelo virtual por medio de GAMBIT

Para una simulación numérica se necesita un dominio computacional que contenga la malla a la que se puede aplicar las ecuaciones que gobiernan el problema dado. La malla se creó con el software GAMBIT, el generador de mallas de FLUENT.

La Figura 2.1 muestra el dominio computacional para el wooden lath eliminator y la Figura 2.2 el detalle de un separador. Las Figuras 2.3 y 2.4 muestran el dominio computacional y la geometría para el separador asbesto- cement.

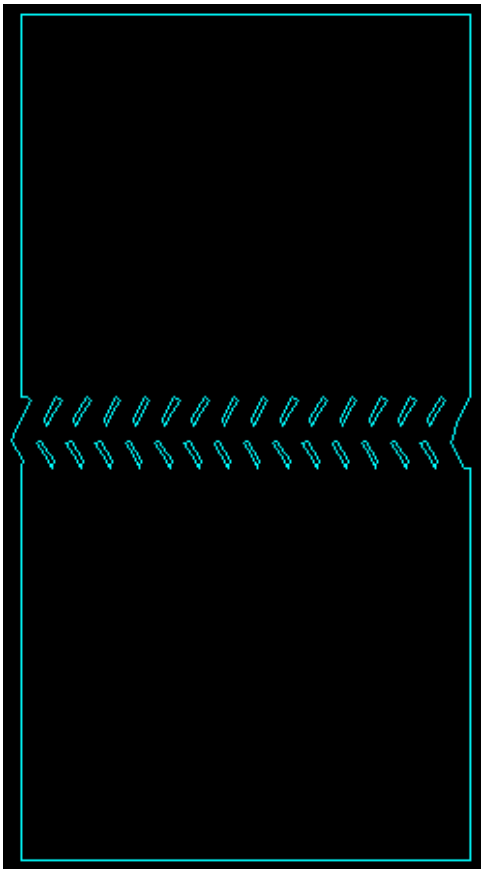

Figura 2.1: Dominio computacional para el separador del tipo wooden lath

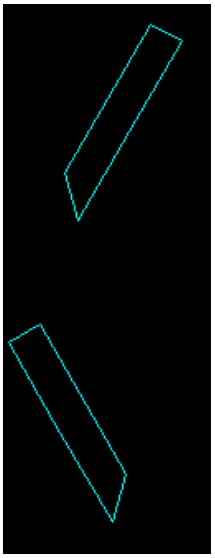

Figura 2.2: Amplificación de la geometría del wooden lath eliminator

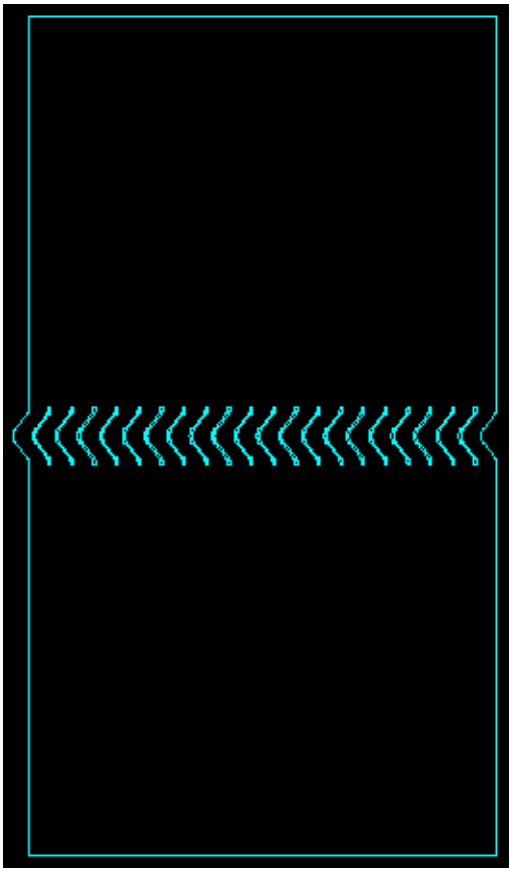

Figura 2.3: Dominio computacional para el separador del tipo asbesto- cement

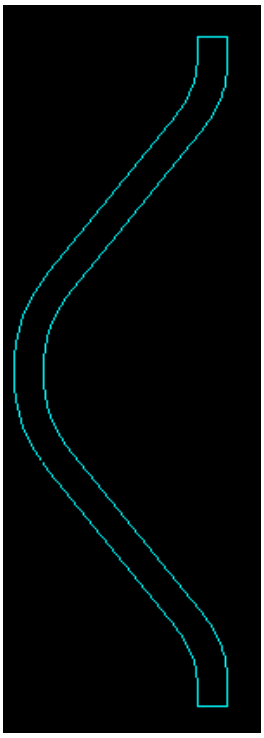

Figura 2.4: Amplificación de la geometría del asbesto- cement eliminator

3 Modelo matemático para la simulación numérica

3.1 Modelos para el flujo

3.1.1 Ecuaciones de *Navier- Stokes* y turbulencia

A continuación, se exponen las ecuaciones que gobiernan el comportamiento de un flujo bidimesional.

- Ecuación de la continuidad

$$\frac{\partial \rho}{\partial t} + \nabla\left(\rho \vec{u}\right) = 0 \tag{3.1}$$

- Ecuación de cantidad de movimiento

$$\rho \frac{Du}{Dt} = -\frac{\partial p}{\partial x} + \nabla\left(\mu \nabla u\right) + S_{Mx} \tag{3.2}$$

$$\rho \frac{Dv}{Dt} = -\frac{\partial p}{\partial y} + \nabla\left(\mu \nabla v\right) + S_{My} \tag{3.3}$$

Por el número de Reynolds calculado se considera el flujo como turbulento. Para calcular un flujo turbulento hace falta introducir las ecuaciones promediadas de Reynolds. A continuación se muestran la ecuaciones en forma cartesiana y como tensor.

$$\frac{\partial}{\partial x_i}\left(\rho u_i\right) = 0 \tag{3.4}$$

$$\frac{\partial}{\partial x_j}\left(\rho u_i u_j\right) = -\frac{\partial p}{\partial x_i} + \frac{\partial}{\partial x_j}\left[\mu\left(\frac{\partial u_i}{\partial x_j} + \frac{\partial u_j}{\partial x_i} - \frac{2}{3}\delta_{ij}\frac{\partial u}{\partial x}\right)\right] + \frac{\partial}{\partial x_j}\left(-\rho\overline{u_i' u_j'}\right) \tag{3.5}$$

Para resolver estas ecuaciones se necesitan modelos de turbulencia. En este trabajo se utiliza el modelo de turbulencia k- ε. Este modelo consite en dos ecuaciones, una para k, que es la energía cinética turbulenta, y otra para ε, que es la disipación turbulenta.

$$\frac{\partial}{\partial x_i}(\rho k u_i) = \frac{\partial}{\partial x_j}\left[\left(\mu + \frac{\mu_t}{\sigma_k}\right)\frac{\partial k}{\partial x_j}\right] + G_k - \rho\varepsilon \tag{3.6}$$

$$\frac{\partial}{\partial x_i}(\rho\varepsilon u_i) = \frac{\partial}{\partial x_j}\left[\left(\mu + \frac{\mu_t}{\sigma_\varepsilon}\right)\frac{\partial \varepsilon}{\partial x_j}\right] + C_{1\varepsilon}\frac{\varepsilon}{k}G_k - C_{2\varepsilon}\rho\frac{\varepsilon^2}{k} \tag{3.7}$$

3.1.2 Tratamiento de las paredes

En el presente trabajo las capas límites en las paredes de los separadores parciales se consideran como mayor fuente de la pérdida de presión de flujo. Por eso es muy importante modelar las capas límites correctamente. En FLUENT el tratamiento de las paredes depende mucho del tamaño de las celdas. En este trabajo se utiliza el modelo de *k*- para la turbulencia, con dicho modelo se puede elegir dos diferentes tratamientos de las paredes, uno para mallas con celdas grandes (wall functions) y otro para mallas con celdas pequeñas (enhanced wall treatment). El valor por medio del que se elige el tratamiento de las paredes es el valor de y^+.

$$y^+ \equiv \frac{\rho u_\tau y}{\mu} \tag{3.8}$$

donde ρ es la densidad, u es la velocidad de la fricción y μ es la viscosidad dinámica.

Para un valor de y^+ más pequeño que 1 (si no puede ser por lo menos un valor más pequeño que 5) se utiliza el “enhanced wall treatment”. Para valores de y^+ entre 30 y 500 se utlizan las “wall functions”.

Las wall functions calculan las capas límites simplemente con ecuaciones empíricas. El otro método de enhanced wall treatment intenta resolver la zona cerca a la pared.

3.2 Simulación

3.2.1 Solver

En FLUENT existe la posibilidad de eligir entre dos solvers. El solver segregado y el solver acoplado. En este trabajo solo se usa el solver segregado. Este solver resuelve las ecuaciones de gobierno de forma secuencial. Dado que las ecuaciones de gobierno son acopladas se necisita un proceso iterativo para poder resolverlas. La Figura 3.1 muestra como funciona el proceso del solver segregado.

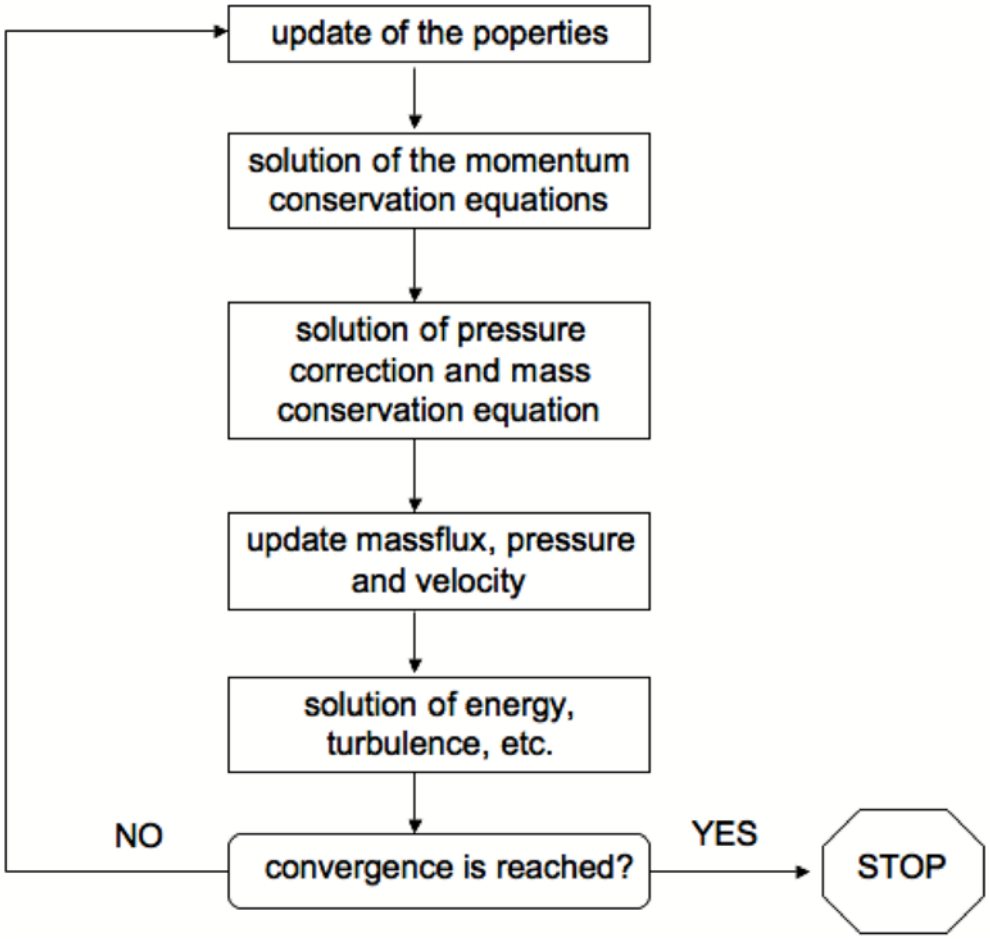

Figura 3.1: Proceso de cálculo del solver segregado

3.3 Condiciones del contorno

En FLUENT se pueden eligir entre muchas condiciones del contorno , pero en el presente trabajo sólo se usan tres diferentes tipos:

- *Velocity inlet*: Esta opción se usa para definir la velocidad, u otras propiedades scalares, en la zona de la entrada del flujo. En est trabajo se introducjeron varias velocidades al dominio computacional por el *velocity inlet*.
- *Pressure outlet*: Se usa para definir la presión estática del flujo a la salida del dominio computacional. En este trabajo se definió como 0 Pa en todas las simulaciones.
- *Wall*: La condición del contorno *wall* (pared) se aplica para introducir una superficie solida o una pared al dominio computacional. Es posible especificar las propiedades como por ejemplo transmisión de calor. En este proyecto se trabajó con los valores estándard de esta condición del contorno.

3.4 Enfoques para la simulación en FLUENT

En este párrafo se introducen de forma resumida por medio de tablas los métodos utilizados por FLUENT para realizar una simulación numérica. La Tabla 3.1 muestra las propiedades del solver aplicado, la Tabla 3.2 los esquemas de la interpolación y discretización.

Tabla 3.1: Propiedades del solver aplicado

Solver	Segregado
Formulación	Implícita
Evaluación del gradiente	Basada en la celda
Formulación de la velocidad	Absolut
Dimensión del dominio	Bidimensional
Dependencia del tiempo	Estacionario

Tabla 3.2: Esquemas de interpolación y discretizacion utilizadas

Presión	Upwind segundo orden
Acoplamiento presión – velocidad	SIMPLE
Cantidad de movimiento	Upwind segundo orden
Energia kinéica del la turbulencia	Upwind segundo orden
Ratio de la disipación de la turbulencia	Upwind segundo orden

Tabla 3.3: Factores de subrelajación

Presión	0,3
Densidad	1
Fuerzas sobre el cuerpo	1
Cantidad de movimiento	0,7
Energia kinetica de la turbulencia	0,8
Ratio de la disipación de la turbulencia	0,8
Viscosidad turbulenta	1

3.5 Criterios de convergencia

No existe un criterio universal para evaluar la convergencia de un código de CFD. En este trabajo se utilizó un conjunto de tres criterios para considerar una simulación convergida:

- *Residuos escalados*: El criterio estandard de convergencia utilizado por FLUENT para los residuos escalados es apropiado para muchos problemas. Para satisfacerlo los residuos escalados deben ir decreciendo con el número de iteraciones hasta alcanzar valores del orden 10^{-3} para todas las ecuaciones.
- *Magnitudes fluidas*: Debe observarse la estabilización y convergencia de todas las magnitudes fluidas monitorizadas durante el proceso de cálculo. En este trabajo se monitorizó como la magnitud fluida la presión en un punto justo encima de los separadores.
- *Balance de masa global*: Debe cumplirse con un error del orden de 10^{-16} kg/s al final del proceso iterativo de cálculo.

4 Error e incertidumbre

Es conocido que las simulaciones numéricas llevan una incertidumbre. Por eso son necesarios métodos para evaluar esa incertidumbre. En este capítulo se presentará un estudio para determinar la incerticumbre de una simulación numérica y otro estudio basado en el valor de y^+. Los dos estudios sirven para encontrar una simulación numérica que no dependa de la malla, o mejor dicho del tamaño de las celdas de la malla.

4.1 Métodología para evaluar la incertidumbre numérica

4.1.1 Introducción

Antes de aplicar la métodología hace falta completar algunas actividades. Se necesita un código capaz de resolver un sistema de ecuaciones no- lineal y acoplado de ecuaciones en derivadas parciales con unas condiciones iniciales y/o de contorno determinadas, consiguiendo aproximar la solución exacta de estas ecuaciones cuando se emplea una malla de resolución suficiente. Antes de realizar ninguna estimación del error de discretización debe asegurarse que la convergencia iterativa se consigua con al menos tres órdenes de magnitud sobre los residuos normalizados de cada ecuación resuelta. Este será uno de los aspectos que se analizarán con FLUENT y se encuentra recogido en el siguiente capítulo.

A continuación, se expone una métodología para la estimación de la incertidumbre numérica. Este procedimiento consta de cinco pasos y está basado en la extrapolación de Richardson mejorada con el Índice de Convergencia de la Malla de Roache (*Gird Convergente Index, GCI*). Este procedimiento es el propuesto por el *Computational Fluid Dynamics Technical Committee* de la *American Society of Mechanical Engineers* (ASME) y por el *American Institute of Aeronautics* (AIAA) para cuantificar la incertidumbre numérica asociada a una simulación por ordenador.

- Paso 1

  Se define un tamaño de celda o celda representativa *h*. El siguiente es definido para mallas tridimensionales, estrucutradas y geométricamente similares:

$$h = (\Delta x_{\max} \cdot \Delta y_{\max} \cdot \Delta z_{\max})^{1/3} \tag{4.1}$$

  para mallas noestrucutradas:

$$h = \left(\frac{1}{N} \sum_{i=1}^{N} \Delta V_i \right)^{1/3} \tag{4.2}$$

  donde:

  x_{max} es la distancia máxima de la celda representativa en dirección del eje *x*

y_{max} es la distancia máxima de la celda representativa en dirección del eje *y*
z_{max} es la distancia máxima de la celda representativa en dirección del eje *z*
V_i es el volumen de la celda *i*- ésima
N es el número total de celdas del dominio computacional

- Paso 2

Se seleccionan tres tamaños de resolución de malla y se realiza una serie de simulaciones numéricas con cada una para determinar los valores de una variable "testigo" ϕ, la cual debe ser una variable importante del estudio a realizar. Es aconsejable que el factor de refinamiento de la malla r sea mayor o igual a 1.3. Este es un valor basado en experiencia y, por tanto, no se puede demostrar mediante un procedimiento formal.

$$r = h_{grosero} / h_{fino} \tag{4.3}$$

El proceso de refinamiento tiene que ser realizado sistemáticamente y con celdas geométricamente similares.

- Paso 3

De aquí en adelante se hará referencia a las tres mallas mediante los subíndices 1, 2 y 3. Estando éstos asociados a las mallas finas, normal y basta o gruesa, repectivamente. De lo anterior se deduce que $h_1 < h_2 < h_3$. Los factores de refinamiento entre las mallas se pueden obtener como:

$$r_{21} = \frac{h_2}{h_1} \quad \text{(conecta la malla fina con la del centro)} \tag{4.4}$$

$$r_{32} = \frac{h_3}{h_2} \quad \text{(conecta la malla del centro con la malla gruesa)} \tag{4.5}$$

Con estos factores se puede calcular el orden aparente (u observado) del método *p* a patir de las siguientes expresiones:

$$p = \frac{1}{\ln r_{21}} \cdot \left(\ln \left| \frac{\varepsilon 32}{\varepsilon 21} \right| + q(p) \right) \tag{5.6}$$

$$q(p) = \ln \left(\frac{r_{21}^p - s}{r_{32}^p - s} \right) \tag{5.7}$$

$$s = 1 \cdot sign \left(\frac{\varepsilon_{32}}{\varepsilon_{21}} \right) \tag{5.8}$$

donde $\varepsilon_{32} = \phi_3 - \phi_2$ y $\varepsilon_{21} = \phi_2 - \phi_1$, y ϕ_k denota el valor de la variable testigo en la malla *k*. Para obtener el orden aparente del método hay que resolver el sistema formado por las tres ecuaciones anteriores. Para ello, se puede emplear el algoritmo del punto- fijo partiendo de la condición inicial $q = 0$.

Se requieren como mínimo cuatro mallas para demostrar que el orden p es constante para un conjunto de simulaciones. Si los valores de la variable testigo se encuentran en la zona asintótica para al menos dos de las mallas estudiadas, es decir, en la zona donde la influencia de la malla sobre los resultados numéricos es pequeña o prácticamente despreciable, sólo se necesitarán tres tamaños de la malla distintos. Aunque, de hecho, se requieren más de tres mallas para demostrar que estamos dentro de la región asintótica, posiblemente cinco o seis mallas de diferente resolución.

- Paso 4

  Se calculan los valores extrapolados a partir de las siguientes expresiones:

$$\phi_{ext}^{21} = \frac{\left(r_{21}^{p}\phi_1 - \phi_2\right)}{\left(r_{21}^{p} - 1\right)} \tag{4.9}$$

$$\phi_{ext}^{32} = \frac{\left(r_{32}^{p}\phi_2 - \phi_3\right)}{\left(r_{32}^{p} - 1\right)} \tag{4.10}$$

- Paso 5

  Se calculan los siguientes errores estimados a partir del orden aparente del método *p* obtenido en el paso 3 y empleando los valores extrapolados del paso 4.

  Error relativo aproximado:

$$e_a^{21} = \left|\frac{\phi_1 - \phi_2}{\phi_1}\right| \tag{4.11}$$

$$e_a^{32} = \left|\frac{\phi_2 - \phi_3}{\phi_2}\right| \tag{4.12}$$

  Error relativo estimado extrapolado:

$$e_{ext}^{21} = \left|\frac{\phi_{ext}^{21} - \phi_1}{\phi_{ext}^{21}}\right| \tag{4.13}$$

$$e_{ext}^{32} = \left| \frac{\phi_{ext}^{32} - \phi_2}{\phi_{ext}^{32}} \right| \tag{4.14}$$

Haciendo uso de los parámetros obtenidos anteriormente se define el *Grid Convergence Index, GCI* o ìndice de convergencia de la malla según:

$$GCI_{fino} = \frac{Fs \cdot e_a^{21}}{r_{21}^p - 1} \tag{4.15}$$

$$GCI_{grosero} = \frac{Fs \cdot e_a^{32}}{r_{32}^p - 1} \tag{4.16}$$

donde *Fs* es un factor de seguridad al cual Roache asignó en un principio un valor de 3 (1993). Posteriormente, Roache (1998) recomendó un valor menos conservador de 1,25, que se puede aplicar cuando se emplean tres mallas en el estudio y se hace uso del orden aparente *p*. Roache obtuvo este coeficiente a través de estudios empíricos. Éste valor está fuertemente correlacionado con la definición de incertidumbre *U* usada por Coleman y Stern (1997) y pone de manifiesto que usando un valor de 1,25 se obtienen resultados del *GCI* con un intervalo de confianza del 95%. Por tanto, éste sera el valor de Fs que se utilizará para el calculao del *GCI*.

Si el orden aparente del método p obtenido es menor que 1 se puede dar un intervalo de error obteniendo los valores del GCI para $p = 1$. Sin embargo, esto no es necesario, ya que el valor obtenido para $p < 1$ es más conservador que el que se obtiene para un orden $p = 1$.

4.1.2 Estudio de la sensibilidad de la malla

El objetivo del estudio de la sensibilidad de la malla es determinar la influencia del tamaño de las celdas en la solución de la simulación. De este manera se puede evaluar la exactidud de los resultados calculados con una cierta malla y al mismo tiempo tener en cuenta el tamaño de la malla y el gasto computacional.

Para realizar el estudio es necesario elegir la zona o zonas dentro del dominio computacional que tiene(n) la influencia más grande sobre el flujo. En esta(s) zona(s) se tiene que realizar el estudio.

El análisis del flujo pasando por los separadores es el principal objetivo de este trabajo, por eso se elige la zona donde están situados los separadores para aplicar el estudio de la sensibilidad de la malla.

Se aplica el estudio tres veces diferentes. Cada vez con diferentes consideraciones. La primera vez se considera a los separadores como mayor fuente de pérdida de presión. Se utilizan mallas con celdas muy pequeñas con valores de y^+ cerca a 1.

La Figura 4.1 muestra el dominio computacional del wooden lath eliminator con la zona de los separadores marcada y una amplicación de un sólo separador. La Figura 5.2 muestra lo mismo para el asbesto- cement eliminator.

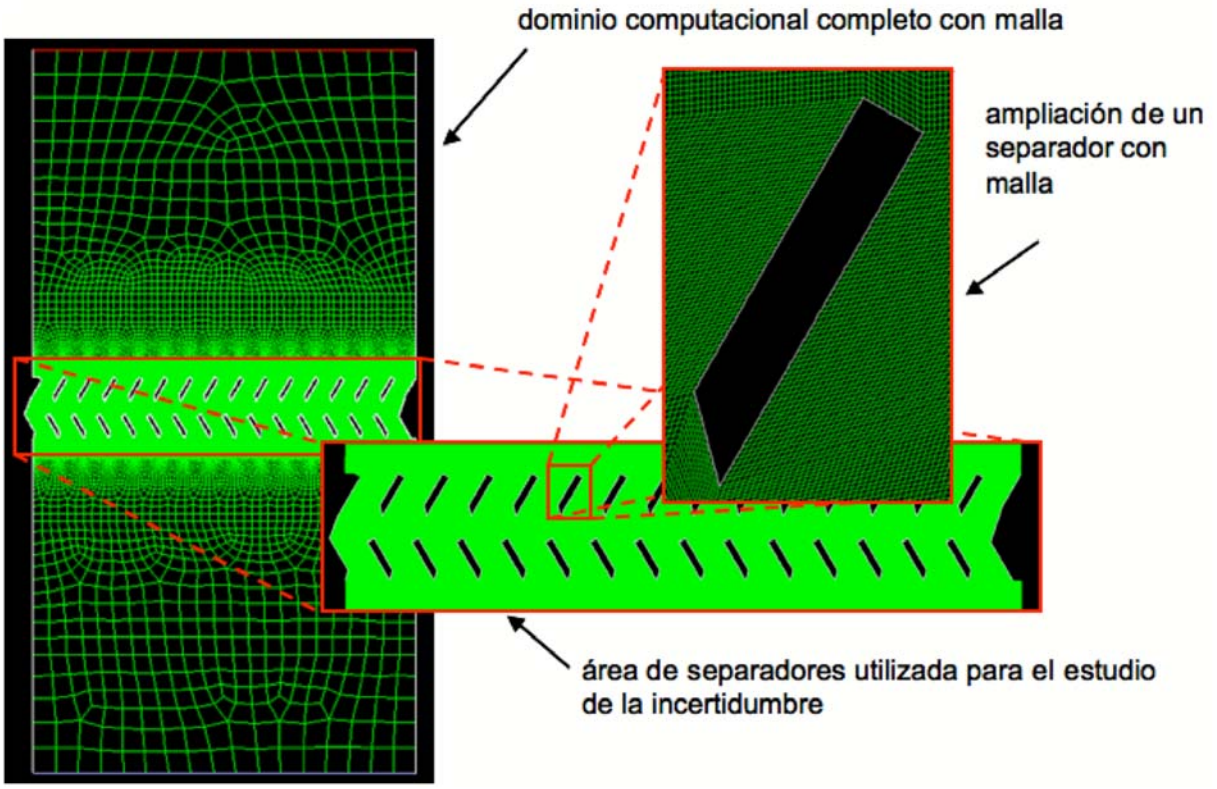

Figura 4.1: Dominio computacional del wooden lath eliminator con zona de los separadores marcada

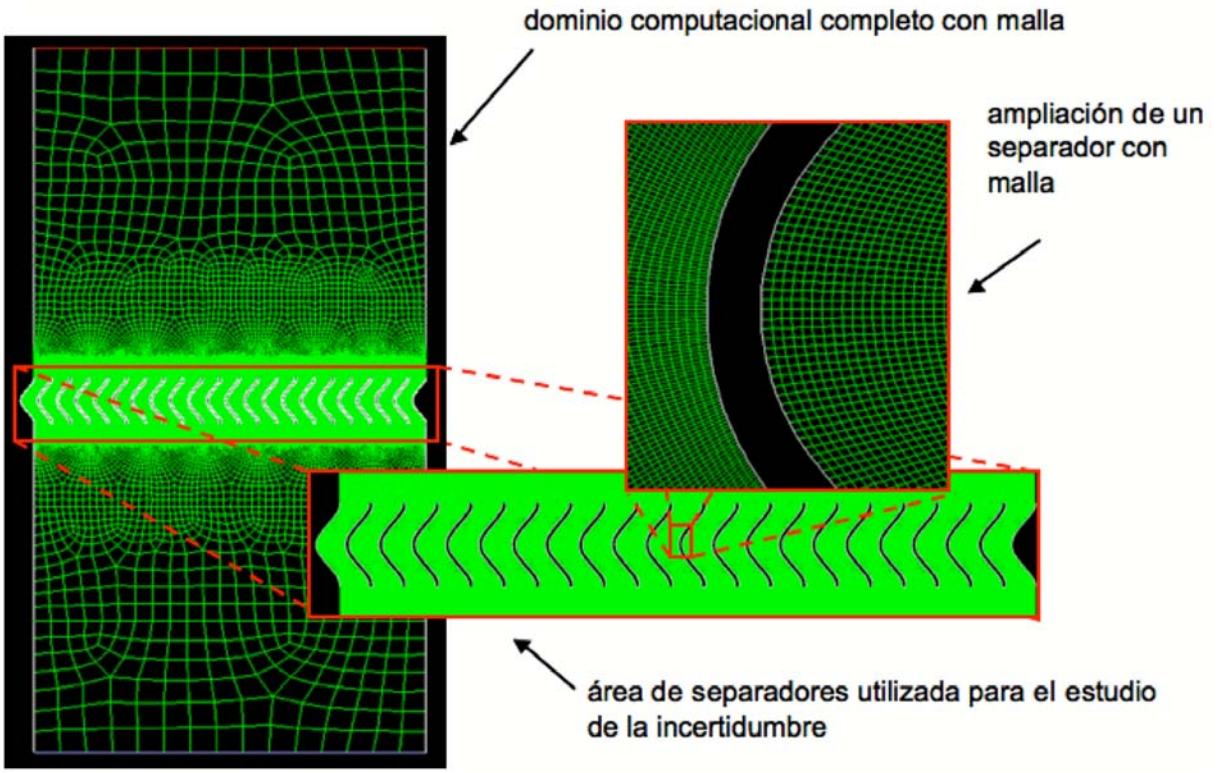

Figura 4.2: Dominio computacional del asbesto- cement eliminator con zona de los separadores marcada

La segunda vez el estudio se aplica a las celdas próximas a la pared, a las celdas dentro de una distancia de 0,5 cm de las paredes de los separadores. Eso es motivado por la consideración de que no son los separadores los que introducen la pérdida de presión sino las capas límites de las paredes de ellos. En este caso también “enhanced wall treatment“ se usa como la aproximación cerca de la pared.

Las celdas cerca de la pared se muestra en la Figura 4.3 para el wooden lath eliminator y en la Figura 4.4 para el asbesto- cement eliminator. Las celdas están marcadas en rojo.

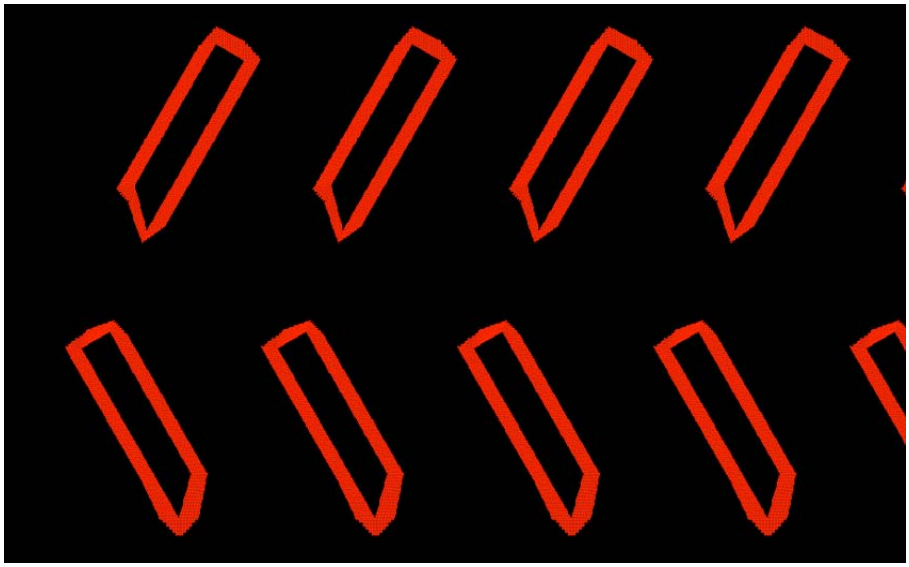

Figura 4.3: Celdas próximas a la pared utilizadas para el estudio de la sensibilidad para el wooden lath eliminator

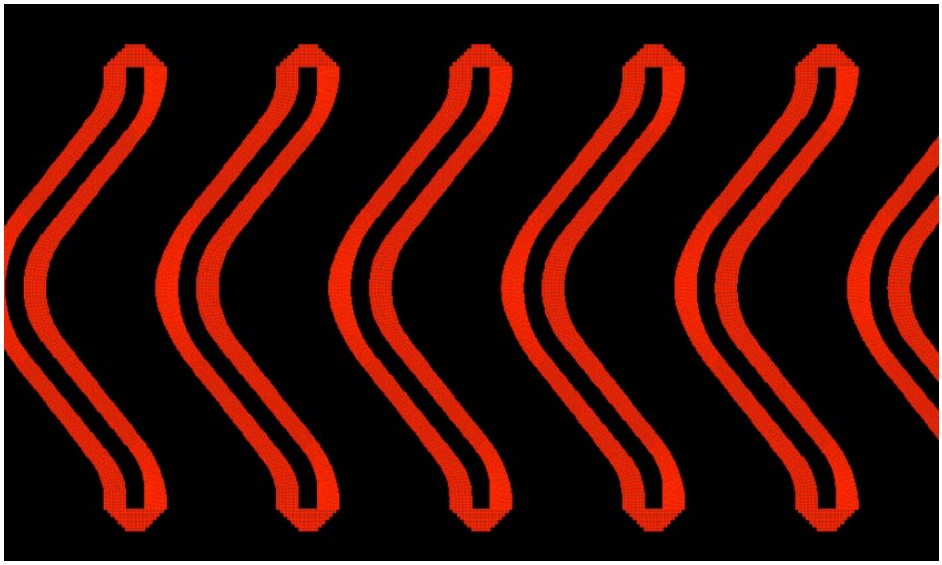

Figura 4.4: Celdas próximas a la pared utilizadas para el estudio de la sensibilidad para el asbesto- cement eliminator

Se aplica la métodología por una úlitma vez para las dos geometrías de los dos separadores. Esta vez con mallas con celdas grandes. Las celdas grandes resultan en valores de y^+ más grandes. Por eso como aproximación del compotamiento del flujo próxima a la pared se utilizan “wall functions“. Con las mallas gruesas se intenta bajar el número de celdas para reducir el gasto computacional.

Se consideró las dos geometrías de los separadores como referencias para el estudio de la sensibilidad de la malla. Para el wooden lath eliminator se introdujó una velocidad inicial de 1,52 m s-1 y para el asbesto- cement eliminator 1,58 m s-1. La pérdida de la presión introducida por los separadores se tomó como variable de testigo para analizar los resultados

del estudio. Para evaluar se tomó el valor de la presión a la entrada, pero se tuvo en cuenta que en la salida se habia puesto una presión de valor de 0 Pa como condición de contorno.

4.1.2.1 Estudio de la sensibilidad de la malla en la zona de los separadores con enhanced wall treatment

4.1.2.1.1 Wooden lath eliminator

Con el fin de poder conseguir un *GCI* satisfactoria, se aplicó un refinamiento sucesivo y se ejecutó el estudio. Se crearon seis mallas con un número de celdas desde 85269 hasta 1486781. El número de celdas es solo el número en la zona de los separadores. Las características de las mallas se pueden ver en la Tabla 4.1 y la Tabla 4.2 muestra los resultados de los estudios.

Tabla 4.1: Propiedades de las mallas para el wooden lath eliminator

Número de la malla [-]	Número de celdas [-]	Media área de celda [m^2]	Tamaño de la celda representativa *h* [-]	Media presión a la entrada [Pa]
6	85269	3,48E-06	0,001865747	5,5264
5	152589	1,95E-06	0,001394856	5,4769
4	280341	1,06E-06	0,001028854	5,4214
3	496734	5,97E-07	0,00077287	5,3734
2	866069	3,43E-07	0,000585303	5,3184
1	1486781	2,00E-07	0,000446699	5,3060

Tabla 4.2: Resultados del estudio de la incertidumbre para el wooden lath eliminator con la zona de los separadores y enhanced wall treatment

Mallas	6 – 5 – 4	5 – 4 – 3	4 – 3 – 2	3 – 2 – 1
$r_{grueso/centro}$ [-]	1,34	1,36	1,33	1,32
$r_{centro/fino}$ [-]	1,36	1,33	1,32	1,31
$\varepsilon_{grueso/centro}$ [-]	0,0496	0,0555	0,0480	0,0550
$\varepsilon_{centro/fino}$ [-]	0,0555	0,0480	0,0550	0,0124
p	-0,23	0,28	-0,58	5,31
$e_a^{centro/fino}$ [%]	1,02	0,89	1,03	0,87
$GCI_{centro/fino}$ [%]	-19,28	13,50	-8,67	0,09

Se puede ver que algunos de los valores de p son negativos. Por eso la Tabla 4.3 muestra los resultados de los estudios donde p < 1 con un valor de p =1. Este procedimiento esta descrito en la etapa 4.1.1.

Tabla 4.3: Resultados del estudio de la incertidumbre para el wooden lath eliminator con la zona de los separadores y enhanced wall treatment, p = 1

Mallas	6 – 5 – 4	5 – 4 – 3	4 – 3 – 2
p	1,00	1,00	1,00
$e_a^{centro/fino}$ [%]	1,02	0,89	1,03
$GCI_{centro/fino}$ [%]	3,59	3,37	4,03

4.1.2.1.2 Asbesto- cement eliminator

La Tabla 4.4 muestra las propiedades de las mallas utilizadas para el estudio. La Tabla 4.5 los resultados.

Tabla 4.4: Propiedades de las mallas para el asbesto- cement eliminator

Número de la malla [-]	Número de celdas [-]	Media área de celda [m^2]	Tamaño de la celda representativa *h* [-]	Media presión a la entrada [Pa]
5	90000	3,12E-06	0,001765203	2,8142
4	152000	1,62E-06	0,001273513	2,7708
3	257000	9,53E-07	0,000976189	2,9214
2	476000	5,50E-07	0,00074162	3,1072
1	844000	3,22E-07	0,000567222	3,0169

Tabla 4.5: Resultados del estudio de la incertidumbre para el asbesto- cement eliminator con la zona de los separadores y enhanced wall treatment

Mallas	5 – 4 – 3	4 – 3 – 2	3 – 2 – 1
$r_{grueso/centro}$ [-]	1,37	1,30	1,32
$r_{centro/fino}$ [-]	1,30	1,32	1,31
$\varepsilon_{grueso/centro}$ [-]	0,043	-0,151	-0,186
$\varepsilon_{centro/fino}$ [-]	-0,151	-0,186	0,090
p	-4,46	-0,65	2,65
$e_a^{centro/fino}$ [%]	5,15	5,97	2,99
$GCI_{centro/fino}$ [%]	-9,27	-45,39	3,62

La Tabla 4.6 muestra otra vez los resultados para los estudios donde $p < 1$ con un valor de $p = 1$.

Tabla 4.6: Resultados del estudio de la incertidumbre para el asbesto- cement eliminator con la zona de los separadores y enhanced wall treatment, p =1

Mallas	5 – 4 – 3	4 – 3 – 2
p	1,00	1,00
$e_a^{centro/\,fino}$ [%]	5,15	5,97
$GCI_{centro/fino}$ [%]	21,16	23,63

4.1.2.2 Estudio de la sensibilidad de la malla en las celdas próximas a la pared

En FLUENT existe la posibilidad de adaptar mallas. Se puede elegir un valor, por ejemplo el valor de y^+ y adaptar la malla o una cierta zona para que las celdas elegidas tengan el valor de y^+ requerido. Esta posibildad se utiliza ahora para adapatar todas las celdas dentro de una distancia de 0,5 cm a las paredes de los separadores. El procedimiento de adaptación divide una celda en cuatro más pequeñas, veáse Figura 4.5.

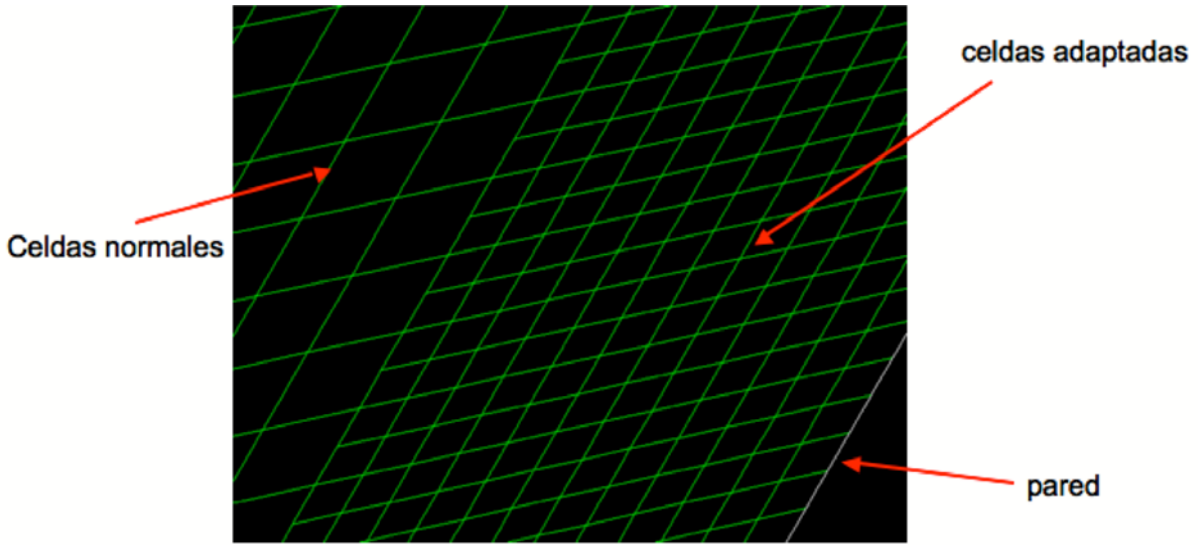

Figure 4.1: Grid adaption in FLUENT

Las mallas utilizadas son por un lado las mismas mallas que en el párrafo anterior y por otro lado mallas adaptadas basadas en esas mallas.

4.1.2.2.1 Wooden lath eliminator

La Tabla 4.7 muestra las propiedades de las mallas. El número de la malla se refiere al párrafo anterior para que se pueda ver cuales son las mismas mallas. Algunos números llevan la letra “a“ así se pueden conocer las mallas adaptadas. En la Tabla 4.8 los resultados de los estudios

están esritos. La última malla (malla número 1) está marcada en gris porque no se utilizó para el estudio por los factores de refinamiento que se entrecruzan con los factores de las mallas adaptadas. Es decir, que entre la malla 1 y las mallas 3a y 4a el criterio de la métodología ($r_{grueso/fino} > 1{,}3$) no está satisfecho.

Tabla 4.7: Propiedades de las mallas y mallas adaptadas para el wooden lath eliminator

Número de la malla [-]	Número de celdas [-]	Número de celdas en las primeras filas [-]	Media área de celda [m^2]	Tamaño de la celda representativa *h* [-]	Media presión a la entrada [Pa]
6	85269	10814	3,20E-06	0,001788854	5,5264
5	152589	18382	1,80E-06	0,001341641	5,4769
4	280341	29420	9,67E-07	0,000983362	5,4214
4a	368601	118398	2,42E-07	0,000491681	5,3785
3	496734	52266	5,48E-07	0,00074027	5,3734
3a	653532	210022	1,37E-07	0,000370135	5,2843
2	866069	96758	3,18E-07	0,000563915	5,3184
1	1486781	161828	1,84E-07	0,00042945	5,3649

Tabla 4.8: Resultados del estudio de la incertidumbre para el wooden lath eliminator con las celdas dentro de una distancia de 0,5 cm a la pared y con enhanced wall treatment

Mallas	6 – 5 – 4	5 – 4 – 3	4 – 3 – 2	4 – 3 – 4a	3 – 2 – 3a
$r_{grueso/centro}$ [-]	1,33	1,36	1,33	1,33	1,31
$r_{centro/fino}$ [-]	1,36	1,33	1,31	1,51	1,52
$\varepsilon_{grueso/centro}$ [-]	0,0496	0,0555	0,0480	0,0480	0,0549
$\varepsilon_{centro/fino}$ [-]	0,0555	0,0480	0,0550	-0,0051	0,0341
p	-0,12	0,18	-0,64	7,68	1,64
$e_a^{centro/fino}$ [%]	1,02	0,89	1,03	0,09	0,65
$GCI_{centro/fino}$ [%]	-35,43	21,12	-8,09	0,01	0,81

La Tabla 4.9 muestra otra vez los resultados para los estudios donde $p < 1$, pero ahor con $p = 1$.

Tabla 4.9: Resultados del estudio de la incertidumbre para el wooden lath eliminator con las celdas dentro de una distancia de 0,5 cm a la pared y con enhanced wall treatment, $p = 1$

Mallas	6 – 5 – 4	5 – 4 – 3	4 – 3 – 2
p	1,00	1,00	1,00
$e_a^{centro/fino}$ [%]	1,02	0,89	1,03
$GCI_{centro/fino}$ [%]	3,51	3,40	4,13

4.1.2.2.2 Asbesto- cement eliminator

Para el asbesto- cement eliminator las mallas on iguales que antes, pero también hay dos nuevas que son adaptaciones de mallas ya utilizadas. La Tabla 4.10 muestra las propiedades de las mallas y la Tabla 4.11 los resultados de los estudios.

Tabla 4.10: Propiedades de las mallas y mallas adaptadas para el asbesto- cement eliminator

Número de la malla [-]	Número de celdas [-]	Media área de celda [m^2]	Tamaño de la celda representativa h [-]	Media presión a la entrada [Pa]	Número de la malla [-]
5	88032	21304	2,96E-06	0,001788854	2,8142
4	168729	29680	1,57E-06	0,001341641	2,7708
3	286681	48450	9,22E-07	0,000983362	2,9214
3a	432031	194220	2,31E-07	0,000480104	3,1065
2	494480	88396	5,22E-07	0,00074027	3,1072
2a	759668	354172	1,31E-07	0,000361248	2,8664
1	846855	148014	3,08E-07	0,000554977	3,0169

Tabla 4.11: Resultados del estudio de la incertidumbre para el asbesto- cement eliminator con las celdas dentro de una distancia de 0,5 cm a la pared y con enhanced wall treatment

Mallas	5 – 4 – 3	4 – 3 – 2	3 – 2 – 3a	2 – 1 – 2a
$r_{grueso/centro}$ [-]	1,37	1,30	1,33	1,30
$r_{centro/fino}$ [-]	1,30	1,33	1,50	1,54
$\varepsilon_{grueso/centro}$ [-]	0,0434	-0,1506	-0,1858	0,0903
$\varepsilon_{centro/fino}$ [-]	-0,1506	-0,1858	0,0007	0,1588
p	-4,49	-0,52	19,61	-0,19
$e_a^{centro/fino}$ [%]	5,15	5,97	0,02	5,56
$GCI_{centro/fino}$ [%]	-9,24	-54,25	9,31E-06	-87,95

Otra vez algunos valores de p son menores a 1. La Tabla 4.12 muestra los resultados para p = 1.

Tabla 4.12: Resultados del estudio de la incertidumbre para el asbesto- cement eliminator con las celdas dentro de una distancia de 0,5 cm a la pared y con enhanced wall treatment, p = 1

Mallas	5 – 4 – 3	4 – 3 – 2	2 – 1 – 2a
p	1,00	1,00	1,00
$e_a^{centro/fino}$ [%]	5,15	5,97	5,56
$GCI_{centro/fino}$ [%]	21,13	22,72	12,95

4.1.2.3 Estudio de la sensibilidad de la malla con wall functions

A continuación se aplica el estudio a mallas gruesas. En este caso no se puede utilizar el enhanced walll treatment por los valores de y^+ más grandes. Por eso se utiliza las wall functions. Las mallas se construyeron de manera que los valores de y^+ mas pequeños son aproximadamente de treinta.

La razón para utilizar mallas gruesas es la reducción del gasto computacional. Como se puede ver en los párrafos anteriores, para conseguir un *GCI* muy bajo hay que aumentar el número de celdas.

Como en los estudios de primer caso se considera la zona de los separadores para aplicar la metodología.

4.1.2.3.1 Wooden lath eliminator

La Tabla 4.13 muestra las propiedades de las mallas gruesas. La numeración se orienta a la numeración del los párrafos anteriores. Ahora la malla más fina tiene el número 7, antes la malla más gruesa era la malla con el número 6. La Tabla 4.14 muestra los resultados de los estudios.

Tabla 4.13: Propiedades de las mallas gruesas para el wooden lath eliminator

Número de la malla [-]	Número de celdas [-]	Media área de celda [m^2]	Tamaño de la celda representativa *h* [-]	Media presión a la entrada [Pa]
10	1444	2,05E-04	0,014317821	5,5985
9	6616	4,50E-05	0,006708204	6,1393
8	11405	2,61E-05	0,005107935	5,9968
7	35400	8,39E-06	0,002896550	5,7125

Tabla 4.14: Resultados del estudio de la incertidumbre para el wooden lath eliminator con la zona de los separadores y con wall functions

Mallas	10 – 9 – 8	9 – 8 – 7
$r_{grueso/centro}$ [-]	2,12	1,31
$r_{centro/fino}$ [-]	1,31	1,76
$\varepsilon_{grueso/centro}$ [-]	-0,5408	0,1426
$\varepsilon_{centro/fino}$ [-]	0,1426	0,2843
p	2,10	0,10
$e_a^{centro/fino}$ [%]	2,38	4,98
$GCI_{centro/fino}$ [%]	3,84	103,38

La Tabla 4.15 muestra los resultados cambiando los valores de *p* que son menores a 1.

Tabla 4.15: Resultados del estudio de la incertidumbre para el wooden lath eliminator con wall functions, $p = 1$

Mallas	9 – 8 – 7
p	1,00
$e_a^{centro/fino}$ [%]	4,98
$GCI_{centro/fino}$ [%]	8,15

4.1.2.3.2 Asbesto- cement eliminator

En Tabla 4.16 están descritas las propiedades de las mallas gruesas para el asbesto- cement eliminator. La Tabla 4.17 muestra los resultados para el estudio de la sensibilidad.

Tabla 4.16: Propiedades de las mallas gruesas para el asbesto- cement eliminator

Número de la malla [-]	Número de celdas [-]	Media área de celda [m^2]	Tamaño de la celda representativa h [-]	Media presión a la entrada [Pa]
9	4176	6,69E-05	0,008179242	3,7202
8	12496	2,22E-05	0,004711688	3,4258
7	33847	8,16E-06	0,002856326	3,0161
6	78340	3,49E-06	0,001868154	2,9938

Tabla 4.17: Resultados del estudio de la incertidumbre para el asbesto- cement eliminator con la zona de los separadores y con wall functions

Mallas	9 – 8 – 7	8 – 7 – 6
$r_{grueso/centro}$ [-]	1,74	1,65
$r_{centro/fino}$ [-]	1,65	1,53
$\varepsilon_{grueso/centro}$ [-]	0,2944	0,4097
$\varepsilon_{centro/fino}$ [-]	0,4097	0,0223
p	-0,82	5,74
$e_a^{centro/fino}$ [%]	13,58	0,75
$GCI_{centro/fino}$ [%]	-50,68	0,09

Otra vez un valor de p es menor que uno. En la Tabla 4.18 se muestra el resultado del estudio para un valor de $p = 1$.

Tabla 4.18: Resultados del estudio de la incertidumbre para el asbesto- cement eliminator con wall functions, $p = 1$

Mallas	9 – 8 – 7
p	1,00
$e_a^{centro/fino}$ [%]	13,58
$GCI_{centro/fino}$ [%]	26,14

4.2 Estudio de las mallas por medio del valor y^+

Este estudio intenta conectar los valores de y^+ de las diferentes mallas con las soluciones calculadas. Como ya se ha mencionado las capas límites estan consideradas como una gran fuente para la pérdida de presión. Para diferentes mallas finas FLUENT recomienda el uso de las aproximaciónes del flujo cerca de las paredes: Enhanced wall treatment para mallas finas y wall functions para mallas gruesas. Un pequeño valor de y^+ se conecta con una malla fina, ya que el valor de y^+ depende mucho del tamaño de las celdas.

El estudio intenta por refinamiento de la malla encontrar una solución de las calculaciones que no dependa del valor de y^+. Es decir, se supone que desde un cierto valor de y^+ las soluciones calculadas no cambian.

Para el estudio se utlizan las mismas mallas que antes y algunas nuevas. En las tablas siguientes se muestra un número de malla que se refiere a los estudios de la incertidumbre de los párrafos anteriores. Las mallas marcada con una "X" son mallas nuevas.

Aunque las mallas gruesas tienen un valor de y^+ mucho mas grande que el valor recomendable ($y^+ \approx 1$) se aplicaron para todas las mallas el enhanced wall treatment para usar siempre la misma aproximación del flujo cerca de la pared.

4.2.1 Estudio del valor de y^+ para el wooden lath eliminator

En la Tabla 4.19 se muestran todas las propiedades de las mallas utilizadas. Con el valor de y^+ como eje en dirección x y con los valores de la presión a la entrada como eje en direción y se puede realizar un diagrama, veáse la Figura 4.6.

Tabla 4.19: Propiedades de las mallas para el estudio del valor de y^+ del wooden lath eliminator con enhanced wall treatment

Número de celdas [-]	Número de malla en estudio de incertidumbre [-]	Valor de y^+ [-]	Media presión a la entrada [Pa]
1444	10	80,38	5,5985
6616	9	46,82	6,1393
11405	8	27,99	5,9968
35400	7	20,94	5,7125
85269	6	9,98	5,5264
152589	5	7,82	5,4769
280341	4	5,98	5,4214
320670	X3	4,07	5,3256
368601	4a	3,12	5,3785
378330	X2	3,03	5,3297
471400	X1	2,00	5,2784
496734	3	4,61	5,3734
653532	3a	2,37	5,2843
866069	2	3,61	5,3184
1486781	1	2,78	5,3060

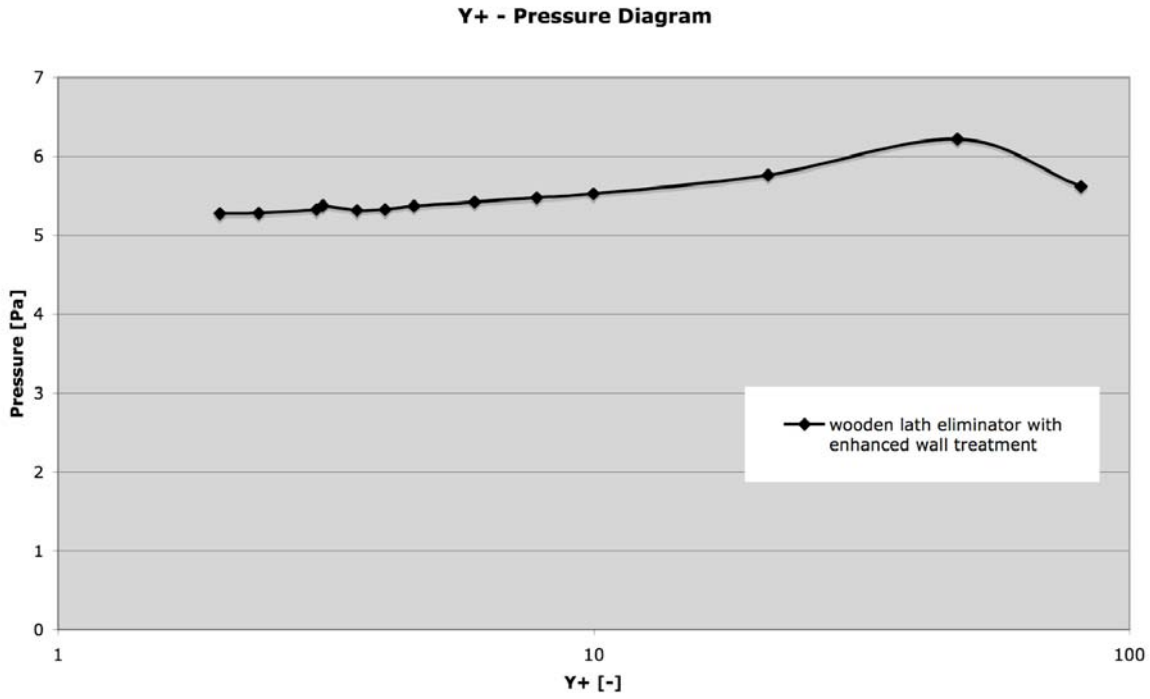

Figura 4.2: diagrama de y^+ - presión para el wooden lath eliminator con enhanced wall treatment

4.2.2 Estudio del valor de y^+ para el asbesto- cement eliminator

En la Tabla 4.20 se muestran las propiedades de las mallas para el estudio del valor de y^+ para el asbesto- cement eliminator. La figura 4.7 muestra el diagrama de y^+ - presión para los valores dados.

Tabla 4.20: Propiedades de las mallas para el estudio del valor de y^+ del asbesto- cement eliminator con enhanced wall treatment

Número de celdas [-]	Número de malla en estudio de incertidumbre [-]	Valor de y^+ [-]	Media presión a la entrada [Pa]
4176	9	80,77	3,7202
12496	8	41,66	3,4258
33847	7	25,50	3,0161
78340	6	25,74	2,9938
88032	5	13,99	2,8142
168729	4	10,29	2,7708
257920	X3	5,38	3,1979
286681	3	7,83	2,9214
322432	X2	2,94	2,9447
394880	X1	2,75	2,7513
432031	3a	3,73	3,1065
494480	2	5,76	3,1072
759668	2a	2,84	2,8581
846855	1	4,36	3,0169

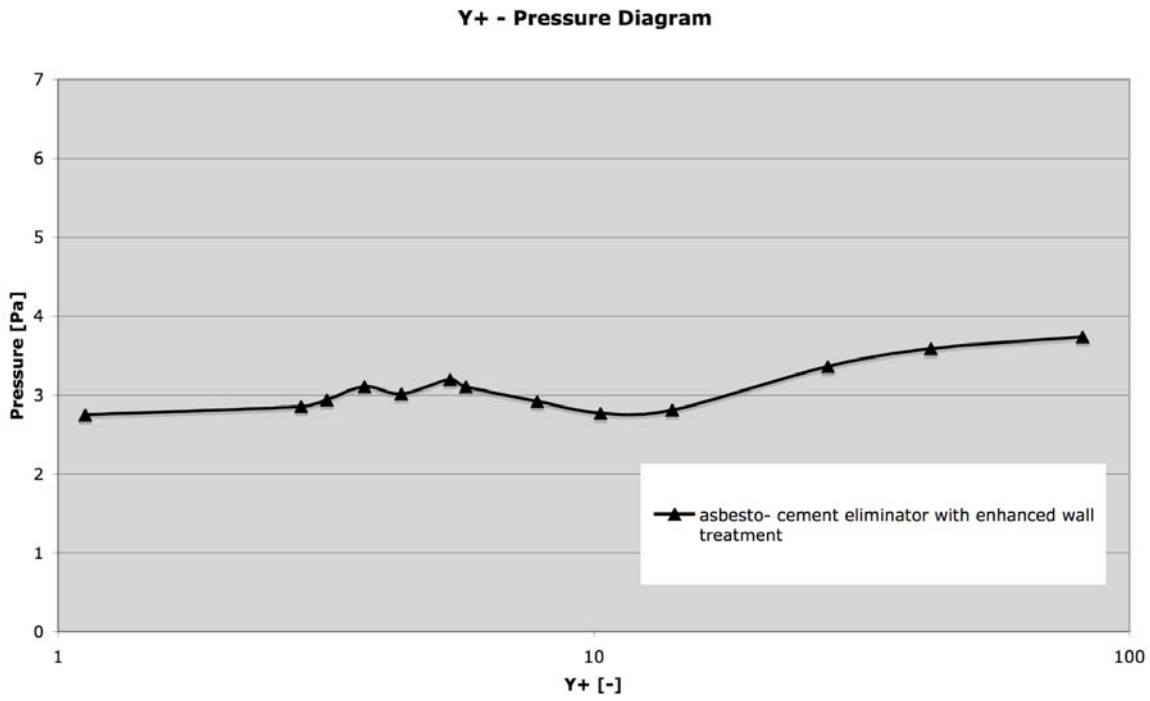

Figura 4.3: y^+ - pressure diagram for asbesto- cement eliminator using enhanced wall treatment

4.3 Discusión

En este párrafo se discuten los resultados de los diferentes estudios y se elige una malla fina para cada geometría para hacer más cálculos con otras velocidades y para tener una solución mas detallada. Pero también se elige una malla gruesa para cada geomtría para los siguientes cálculos. La malla gruesa se elige con la intención de si hay que extender el dominio computacional para simular mas partes de una torre de refrigeración. Con las mallas finas el gasto computacional es exesivo.

4.3.1 Wooden lath eliminator

Para cada uno de los cuatro estudios de las mallas se ha elegido una que se considera la mejor. La Tabla 4. muestra la mallas elegidas para el wooden lath eliminator.

Tabla 4.21: Mallas elegidas para cada tipo de estudio, wooden lath eliminator

Tipo de estudio	Número de la malla [-]	Número de celdas [-]	*GCI* [%]	Valor de y^+ [-]	Media presión a la entrada [Pa]
Área de los separadores, enhanced wall treatment	3	496734	13,50 *(3,37 for p = 1)*	4,61	5,3734
Primeras filas de celdas, enhanced wall treatment	4a	368601	0,01	3,12	5,3785
Área de los separadores, wall functions	6	11405	3,84	27,99	5,9968
Estudio de y^+	X1	471400	-	2,00	5,2784

Para los tres diferentes estudios de incertidumbre se pudieron calcular valores de *GCI* bastante satisfactorios. Pero para conseguir un valor tan bajo hacía falta crear mallas que necesitaran gastos computacionales enormes, la malla más fina casi tiene un número de celdas de 1500000. En el primer caso de los estudios se pudo calcular con una malla con un número de celdas más o menos de 500000 (malla número 3) un valor de *GCI* de 13,50%, que está bien en comparación con el gasto computacional.

En el estudio que sólo consideró las primeras filas de las celdas también fue posible calcular un *GCI* muy bajo. Pero también aquí el gasto computacional creció y no queda claro si los resultados son tan satisfactorios por la consideración de que las capas límites son la influencia más grande sobre el flujo o porque sólo cambiar las celdas en las primeras filas no afecta mucho en la malla entera. Como se puede ver en la Tabla 4.21 los dos estudios con enhanced wall treatment calculan la presión casi igual. Pero en el estudio con las primeras filas el valor del *GCI* es mucho más bajo. Probalemente la razon es que no es suficiente considerar solo las primeras filas, porque solo una pequña parte de la malla cambia pero para el cálculo del *GCI* los factores de refinamiento cambian mucho.

Con mallas gruesas también hay un valor de *GCI* que es bastante satifactorio. Sin embargo, si se comparan los resultados para la presión a la entrada de las mallas gruesas con las de mallas finas, se puede ver que los valores de las mallas finas son mucho mas bajos que los de las mallas gruesas.

En el estudio del valor de y^+ se puede ver que desde un cierto valor de y^+ ($y^+ \approx 7$) la presión a la entrada no cambia (mucho) y la solución se estabiliza. En comparación con los estudios de la incertidumbre se puede decir que, en general, con valores bajos de y^+ de mallas se consigue un valor bajo de *GCI*. Pero también parece que la métodología de la incertidumbre no es muy indicada para este dominio computacional. En nigún caso la orden *p* resultó constante y los valores de *GCI* cambian mucho en cada uno de los tres casos considerados. La razón puede ser que las mallas tienen que ser muy similares para los estudios, pero aquí, puesto que son muchas celdas en las mallas, a lo mejor ya las mallas cambian demasiado.

Por eso se elige una malla fina del estudio del valor de y^+ para las siguientes calculaciones. La malla con el número "X1" de la tabla 4.19 tiene el valor de y^+ más bajo y por eso se elige esta malla. Como malla gruesa se elige la malla con el número 8 por el valor de *GCI*.

4.3.2 Asbesto- cement eliminator

La Tabla 4.22 muestra las propiedades de las mallas elegidas de cada uno de los estudios.

Tabla 4.22: Mallas elegidas para cada tipo de estudio, asbesto- cement eliminator

Tipo de estudio	Número de la malla [-]	Número de celdas [-]	*GCI* [%]	Valor de y^+ [-]	Media presión a la entrada [Pa]
Área de los separadores, enhanced wall treatment	2	496734	-45,39 *(23,63 for p = 1)*	5,76	3,1072
Primeras filas de celdas, enhanced wall treatment	3a	432032	9,31E-06	3,73	3,1065
Área de los separadores, wall functions	8	78340	0,09	41,66	2,9938
Estudio de y^+	X1	394880	-	2,75	2,7513

Para el asbesto- cement eliminator se aplica lo mismo que para el wooden lath eliminator: se pudieron calcular bajos valores del *GCI* para cada caso de los estudios de la incertidumbre. Sin embargo, los diferentes resultados son muy distintos y los valores del *GCI* cambian mucho. En el primer caso con la zona de los separadores y con enhanced wall treatment solo para el ultimo conjunto de mallas el valor del *GCI* fue calculado bajo, y ya con un gasto computacional muy grande.

En el caso de las primeras filas los resultados son muy contradictorios. Para un conjunto de mallas (3 – 2 – 3a) un valor del GCI es casi zero, pero para otro conjunto con mallas mas finas (2 – 1 – 2a) es casi -87%. Sin embargo, pasa lo mismo que en el caso de wooden lath eliminator. Los resultados para la presión para los estudions con enhanced wall treatment son casi iguales, pero los valores del *GCI* son muy diferentes. Por lo tanto solo considerar las primeras filas no parece suficiente.

En caso de mallas gruesas se pudo calcular un *GCI* bajo pero los resultados de la presión a la entrada, en comparación con los resultados para mallas finas, son mucho más altos.

El estudio del valor de y^+ resulta también en un estabilización de la solución en un cierto valor ($y^+ \approx 7$).

Como para el wooden lath eliminator se puede decir que la métodología de la incertidumbre no parece muy apropiada aquí. En nigún caso la orden p resultó constante y los valores del *GCI* son generalmente muy altos, negativos, o las dos cosas. Por eso aquí también se elige una malla por medio del estudio de valor de y^+. La malla tiene el número „“X1“ y es otra vez la malla con el valor de y^+ más bajo.

Como malla gruesa se elige la malla número 6 por el valor de *GCI*.

5 Comparación con datos experimentales

En este capítulo se comparan los resultados de las simulaciones numéricas de las dos mallas, gruesa y fina, para las dos geometrías con los datos encontrados en la bibliografía.

Para la comparación con los datos encontrados en la bibliografía se toman los medios valores de la presión de una superficie encima y otro debajo de los separadores. La diferencia entre los dos valores de las superficies se considera como la pérdida de presión introducida por los separadores. La Figura 5.1 muestra el dominio computacional para el wooden lath eliminator con las dos superficies y Figura 5.2 para el asbesto- cement eliminator. Las superficies están marcodas en rojo.

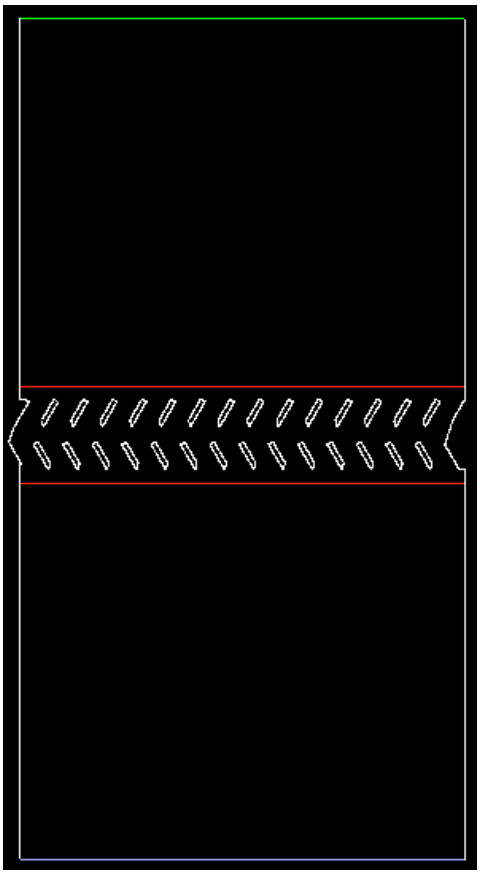

Figura 5.1: Dominio computacional para el wooden lath eliminator con superficies

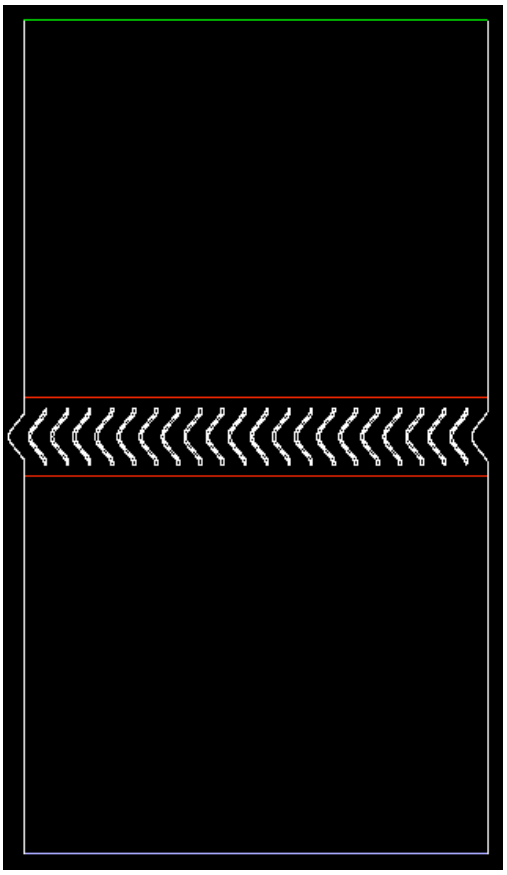

Figura 5.2: Dominio computacional para el asbesto- cement eliminator con superficies

La Tabla 5.1 muestra los valores de la presión encontrados en la bibliografía, la pérdida de presión para las dos mallas consideradas con las velocidades conformes para el wooden lath eliminator. Tabla 5.2 muestra lo mismo para el asbesto – cement eliminator. Asi se puede compara los valores de los experimentos con los valores calculados por la simulación numérica.

Tabla 5.1: Valores de presión para el wooden lath eliminator

Velocidad del aire introducido [m s^{-1}]	Pérdida de presión, Δp, malla fina [Pa]	Pérdida de presión, Δp, malla gruesa [Pa]	Presión encontrada en la bibliografía, p_{bib} [Pa]
0,91	1,5033	1,6812	1,463
1,52	4,1225	4,4826	4,063
2,13	8,0473	8,4982	7,963

Tabla 5.2: Valores de presión para el asbesto- cement eliminator

Velocidad del aire introducido [m s^{-1}]	Pérdida de presión, Δp, malla fina [Pa]	Pérdida de presión, Δp, malla gruesa [Pa]	Presión encontrada en la bibliografía, p_{bib} [Pa]
0,94	1,0124	1,1245	1,831
1,58	2,6191	2,7206	5,120
2,23	4,9106	4,8987	10,153

Las Figuras 5.3 y 5.4 muestran diagramas con los valores de presión calculados y encontrados en la bibliografía sobre la velocidad. Realmente es lo mismo que las tablas arriba, pero en forma gráfica.

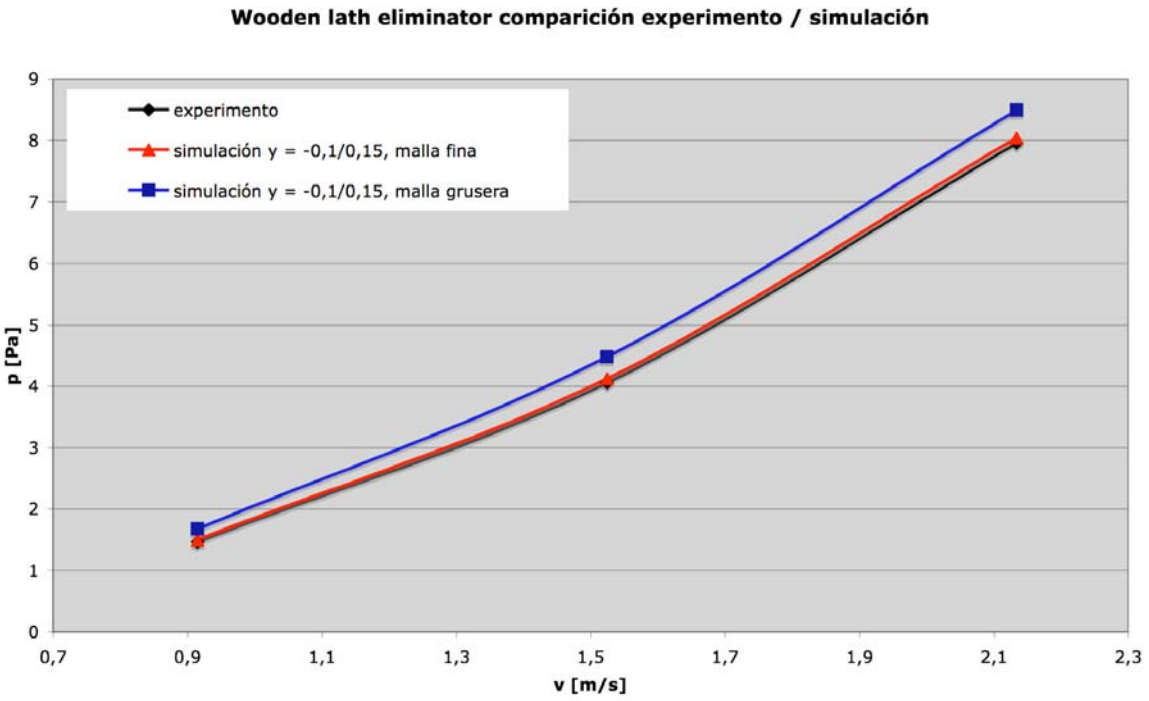

Figura 5.3: Comparación ensayo / simulación para la presión para el wooden lath eliminator

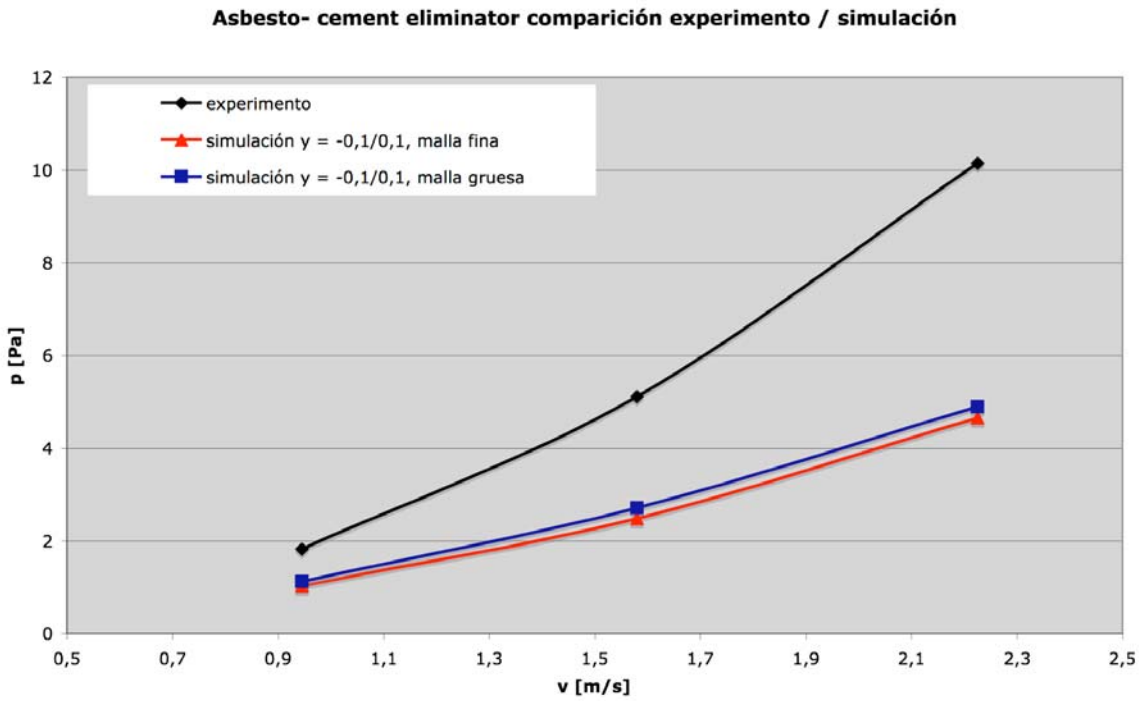

Figura 5.4: Comparación ensayo / simulación para la presión para asbesto- cement eliminator

Se puede ver que para el wooden lath eliminator los resultados de las simulaciones coinciden con los valores del experimento. Hay una diferencia mínima de 1,05% de los dos valores para una velocidad de 2,13 m s^{-1} para la malla fina. Para una velocidad de 0,91 m s^{-1} la diferencia es 2,68% y para una velocidad de 1,52 m s^{-1} la diferencia es 1,44%. Para la malla gruesa las deviaciones son: 14,91% (0,91 m s^{-1}), 10,33% (1,52 m s^{-1}) y 6,72% (2,12 m s^{-1}). En los dos casos la deviación decae con el aumento de la velocidad.

Sin embargo para el asbesto- cement eliminator los resultados numéricos no coinciden con los valores experimentales. Para la malla fina la diferencia mínima entre dos valores es 44,71% para una velocidad de 0,94 m s^{-1}. Las otras desviaciones son 48,85% (1,58 m s^{-1}) y 51,63% (2,23 m s^{-1}). Para la malla gruesa las deviaciones decaen un poco y son: 38,59% (0,94 m s^{-1}), 46,86% (1,58 m s^{-1}) y 51,75 (2,23 m s^{-1}). Para los dos casos las deviaciones son muy grandes en comparación con el wooden lath eliminator y tampoco decaen con el aumento de velocidad.

6 Resultados numéricos

En este capítulo se presentan los resultados numéricos para las dos diferentes geometrías. Se consideran los campos de presión y de velocidad para diferentes velocidades.

Las velocidades elegidas son las velocidades de la bibliografía. Para el wooden lath eliminator las velocidades son: 0,91 m s^{-1}, 1,52 m s^{-1} y 2,13 m s^{-1}. Para el asbesto- cement eliminator: 0,94 m s^{-1}, 1,58 m s^{-1} y 2,23 m s^{-1}.

Los resultados para las mallas finas se considera mas detallados puesto que la malla tiene mucho mas celdas y se puede ver el flujo mas detallado. En el párrafo 5.3 se comparan los resultados de las mallas finas con los de las mallas gruesas para las dos geometrías.

6.1 Wooden lath eliminator

En general se puede decir que para las tres diferentes velocidades el comportamiento del flujo no cambia mucho. La Figura 6.1 muestra el campo de presión y la Figura 6.2 el campo de velocidad para el dominio computacional para la velocidad de 1,52 m s^{-1}, que es la velocidad de los estudios de incertidumbre y del valor de y^+.

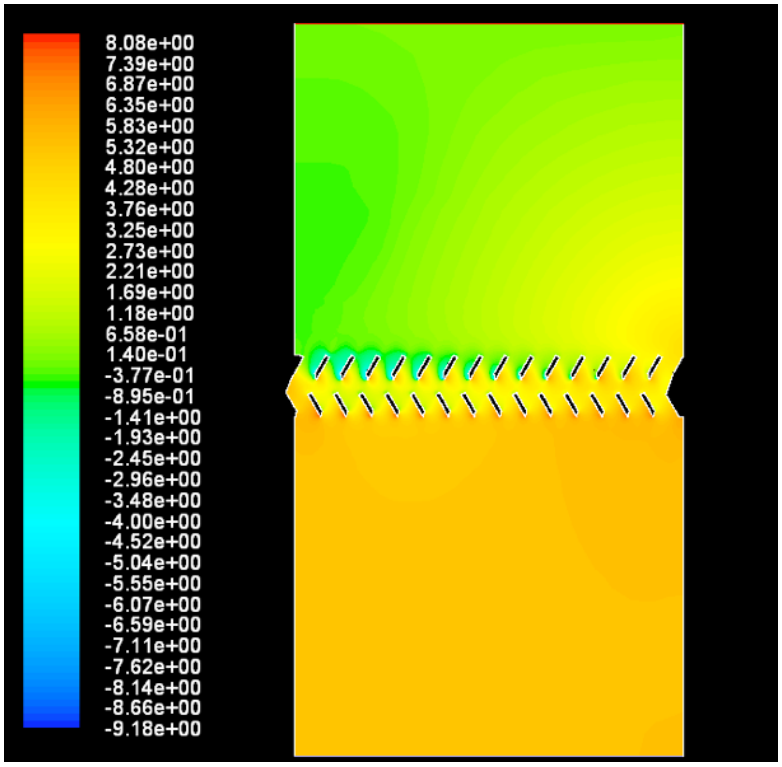

Figura 6.1: Campo de presión estática para el wooden lath eliminator para una velocidad de 1,52 m s^{-1} (Pa)

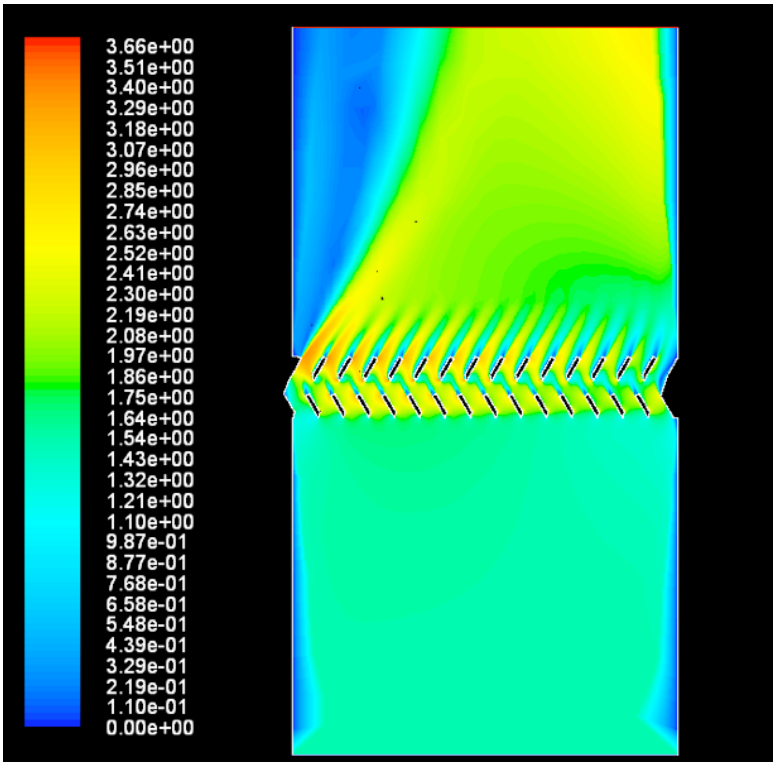

Figura 6.2: Campo de velocidad para el wooden lath eliminator para una velocidad de 1,52 m s^{-1} (m s^{-1})

Se puede ver que al lado izquierdo la presión está mucho más baja que a la derecha. Viceversa la velocidad está mas alta al lado izquierdo que a la derecha. La razón es probablemente la forma de los separadores, que es como una curva a la derecha, por eso el flujo se acelera a la izquierda.

Al lado de la aceleración del flujo a la izquierda sólo llama la ateción la influencia de la pared a la izquierda que se ve en el campo de la velocidad. La influencia viene del dominio computacional. Para que quepan los separadores la pared al nivel de los separadores está adaptada a la forma de ellos. Por eso en una parte del área encima de los separadores la velocidad está más baja que a la derecha de la misma área.

Se puede ver cómo encima de los separadores la presión está más baja que debajo de ellos. Eso es la pérdida de presión que introducen los separadores.

Las siguientes figuras muestran los campos de presión y de velocidad para las otras velocidades. La Figura 6.3 el campo de presión y la Figura 6.4 el campo de velocidad para una velocidad de 0,91 m s^{-1}. La Figura 6.5 el campo de presión y Figura 6.6 el campo de velocidad para una velocidad de 2,13 m s^{-1}.

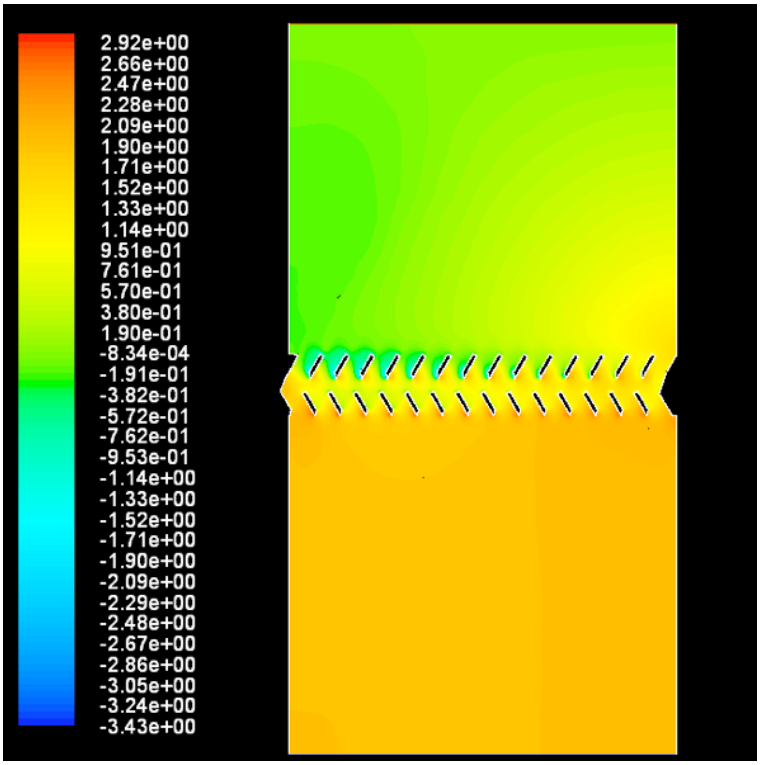

Figura 6.3: Campo de presión estatica para el wooden lath eliminator para una velocidad de 0,91 m s^{-1} (Pa)

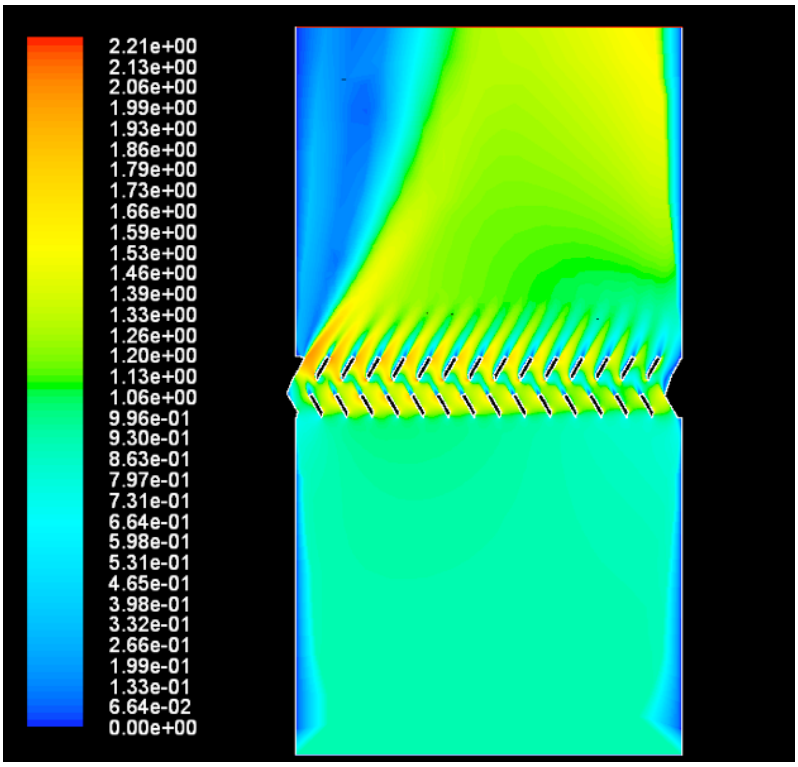

Figura 6.4: Campo de velocidad para el wooden lath eliminator para una velocidad de 0,91 m s^{-1} (Pa)

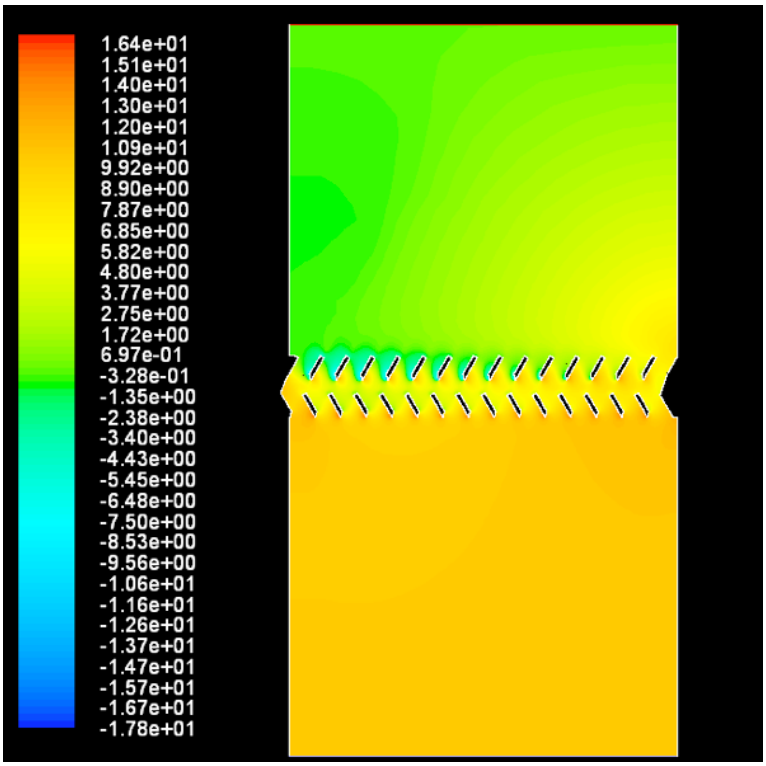

Figura 6.5: Campo de presión estatica para el wooden lath eliminator para una velocidad de 2,13 m s^{-1} (Pa)

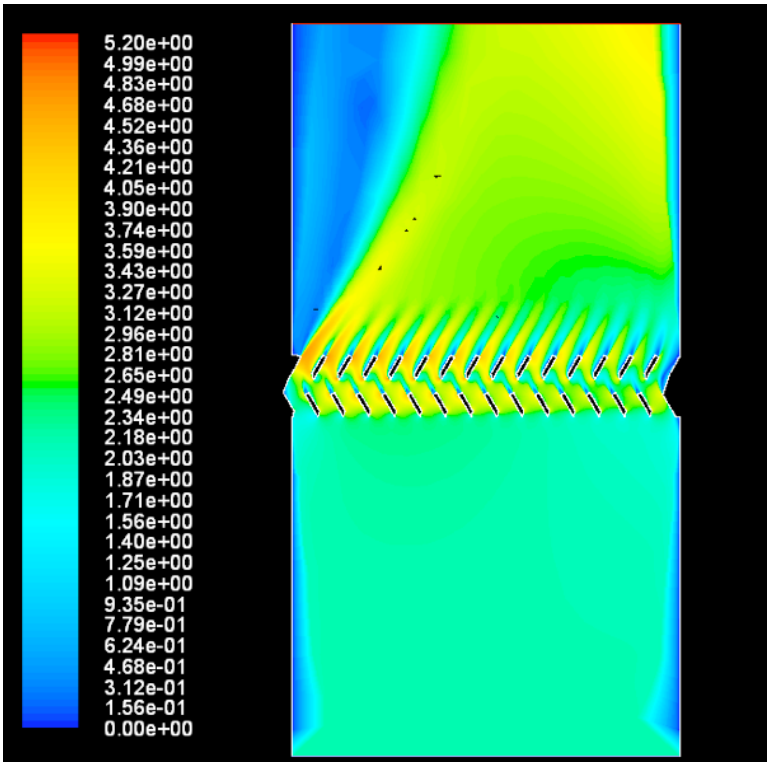

Figura 6.6: Campo de velocidad para el wooden lath eliminator para una velocidad de 2,13 m s^{-1} (Pa)

Si se comparan las diferentes imágenes de los campos se puede ver que el comportamiento del flujo no cambia mucho entre las velocidades. Esto quiere decir que no aparecen nuevos fenómenos con el cambio de la velocidad.

6.2 Asbesto- cement eliminator

Para el asbesto- cement eliminator se aplica lo mismo que para el wooden lath eliminator. El comportamiento del flujo no cambia mucho entre las tres velocidades. La Figura 6.7 muestra el campo de la presión y la Figura 6.7 el campo de la velocidad para una velocidad de 1,58 m s^{-1}. Está es la velocidad con la cual se ejecutaron los estudios de la incertidumbre y del valor de y^+.

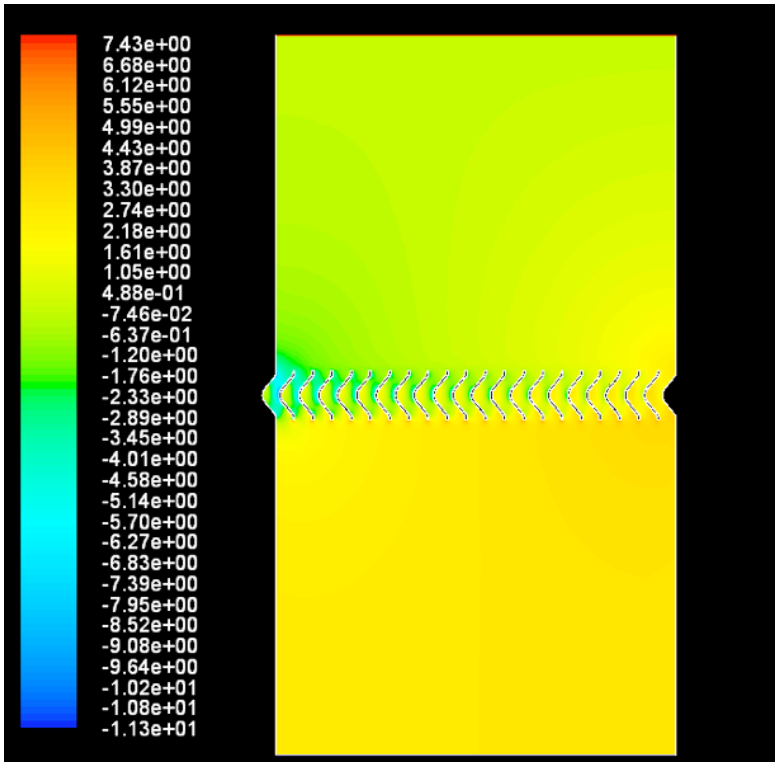

Figura 6.7: Campo de presión estática para el asbesto- cement eliminator para una velocidad de 1,58 m s^{-1} (Pa)

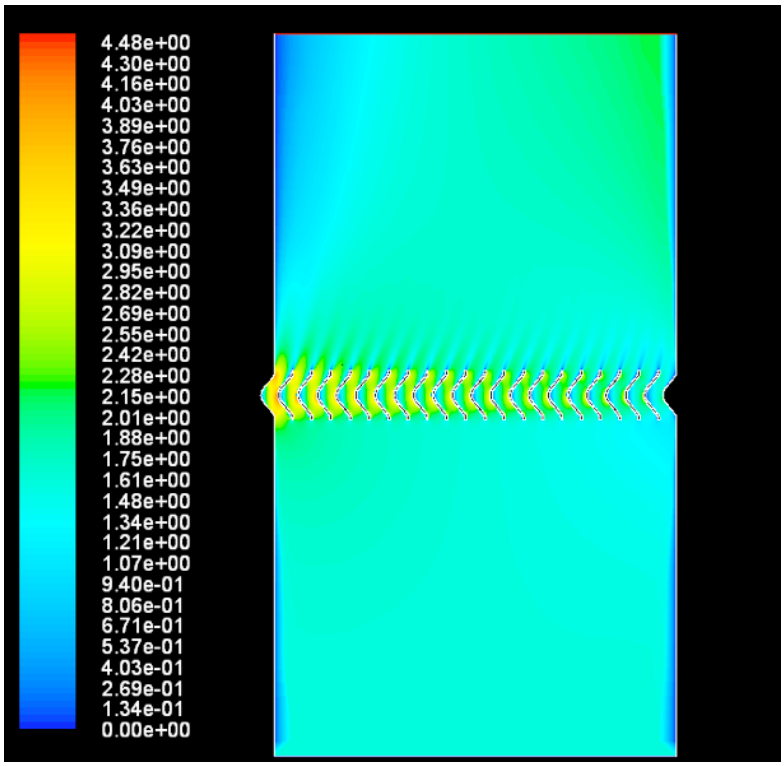

Figura 6.8: Campo de velocidad para el asbesto- cement eliminator para una velocidad de 1,58 m s^{-1} (Pa)

Lo que llama la atención aquí también es la aceleración del flujo a la izquierda del dominio computacional. Otra vez obviamente introducida por la forma de los separadores que curva a la derecha. Sin embargo, la aceleración no es tan grande y sólo dentro de los separadores más a la izquierda.

También la diferencia entre la presión encima de los separadores y debajo de ellos no es tan obvia como en el caso del wooden lath eliminator.

La Figura 6.9 muestra el campo de la presión y la Figura 6.10 el campo de velocidad para una velocidad de 0,94 m s^{-1}. La Figura 5.11 muestra el campo de la presión y la Figura 6.11 el campo de velocidad para una velocidad de 2,23 m s^{-1}.

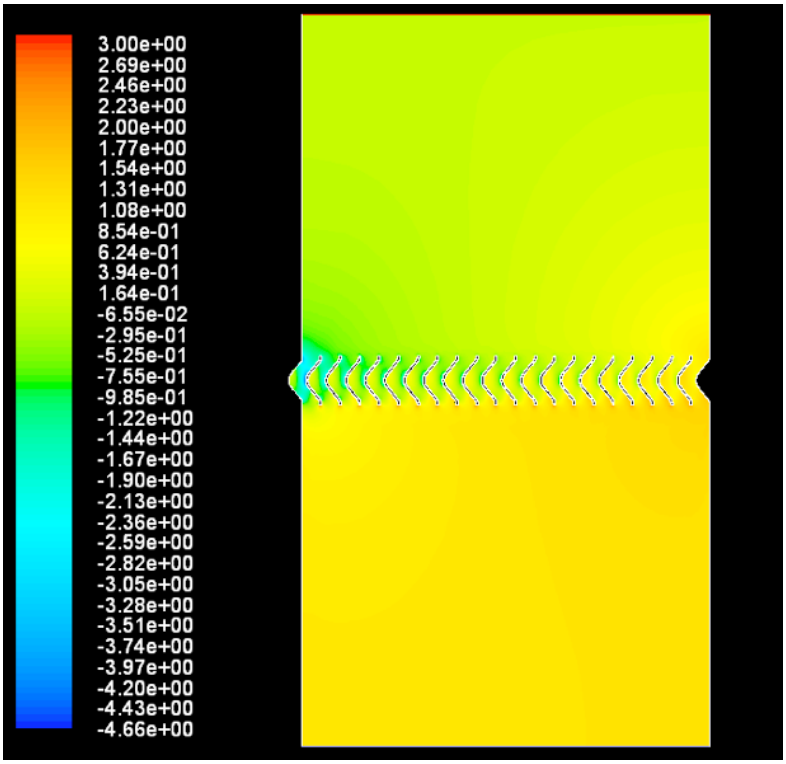

Figura 6.9: Campo de presión estática para el asbesto- cement eliminator para una velocidad de 0,94 m s^{-1} (Pa)

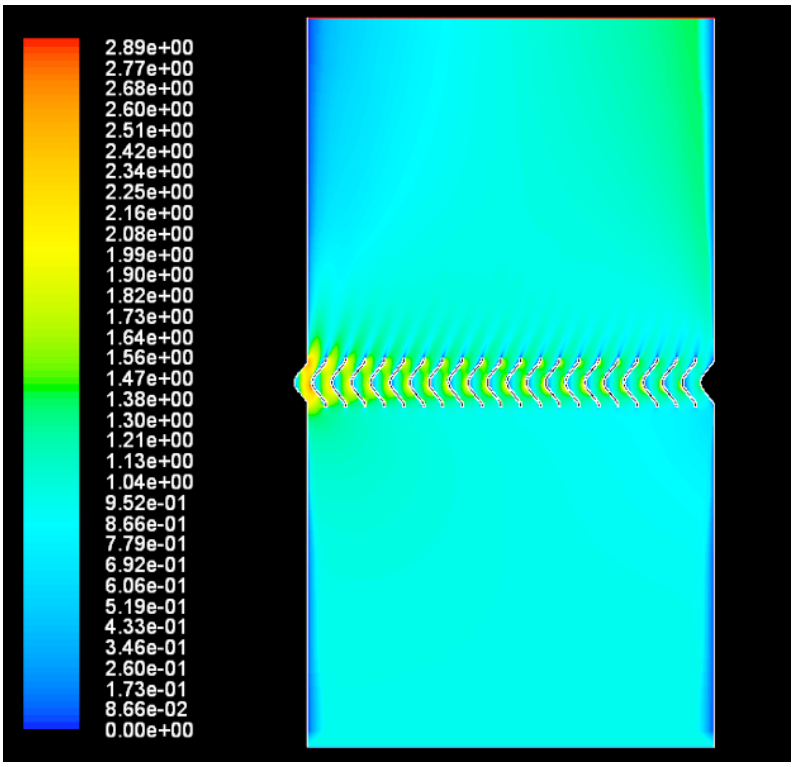

Figura 6.10: Campo de velocidad para el asbesto- cement eliminator para una velocidad de 0,94 m s^{-1} (Pa)

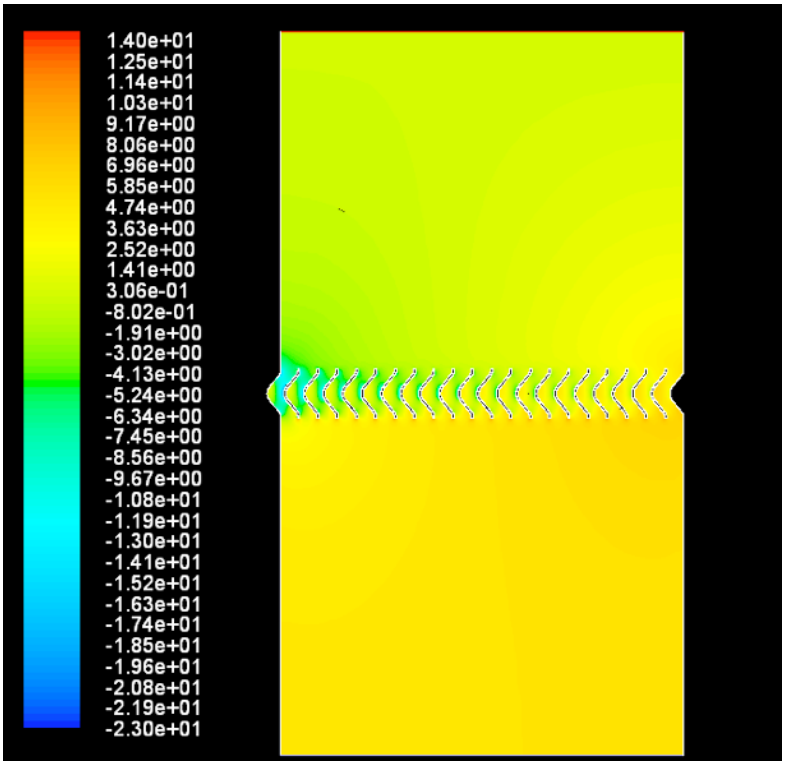

Figura 6.11: Campo de presión estática para el asbesto- cement eliminator para una velocidad de 2,23 m s^{-1} (Pa)

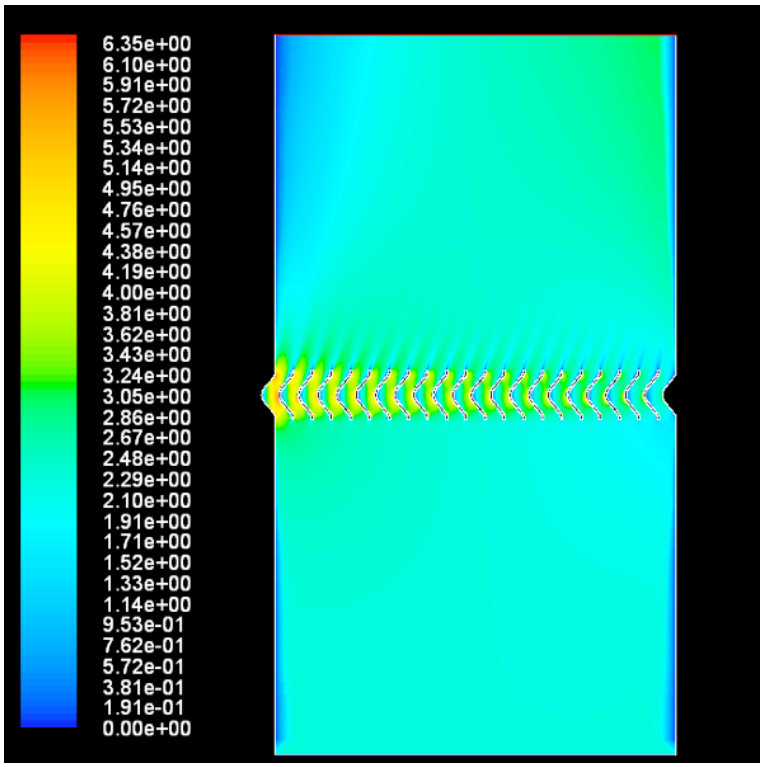

Figura 6.12: Campo de velocidad para el asbesto- cement eliminator para una velocidad de 2,23 m s^{-1} (Pa)

6.3 Comparación de los resultados de las mallas finas y gruesas

En este sección se comparan los resultados para las mallas finas y gruesas. Se pude decir que no aparecer nuevos fenomenos y el compartamiento del flujo se queda igual en las dos geometrías.

6.3.1 Wooden lath eliminator

Figura 6.13 muestra el campo de la presión para las dos mallas. A la izquierda se ve el resultado para la malla fina y a la derecha para la malla gruesa.

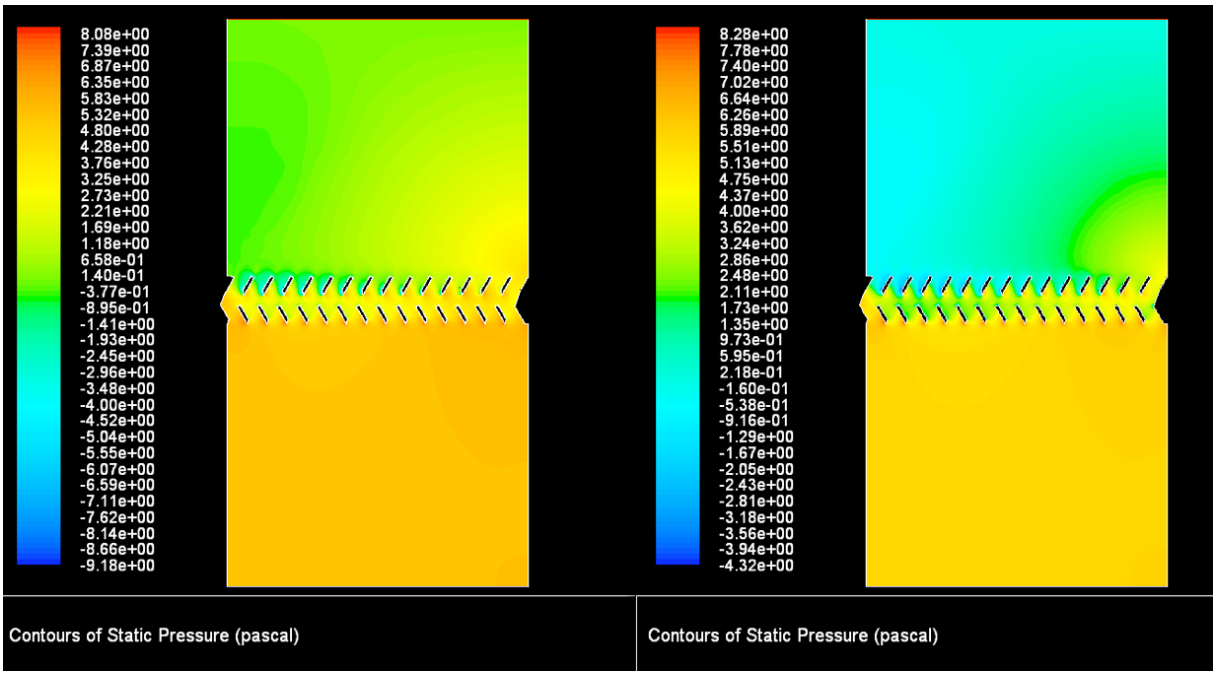

Figura 6.13: Comparación de los campos de presión de la fina y gruesa malla para el wooden lath eliminator para una velocidad de 1,52 m s^{-1} (izquierda: fina, derecha: gruesa)

Como se pudo ver en capítulo 4 la malla gruesa calcula la presión mas alta que la malla fina para la superficie de la entrada. Por eso también el campo de presión se calucla mas alta para la malla gruesa. Por los diferentes colores la diferencia entre los dos resultados parece mucho. Pero mirando al codigo de los números y colores se puede ver que la diferencia es la misma que entre los resultados para las entradas calculados en el capítulo anterior.

Figura 6.14 muestra el campo de velocidad para la misma velocidad de 1,52 m s^{-1}.

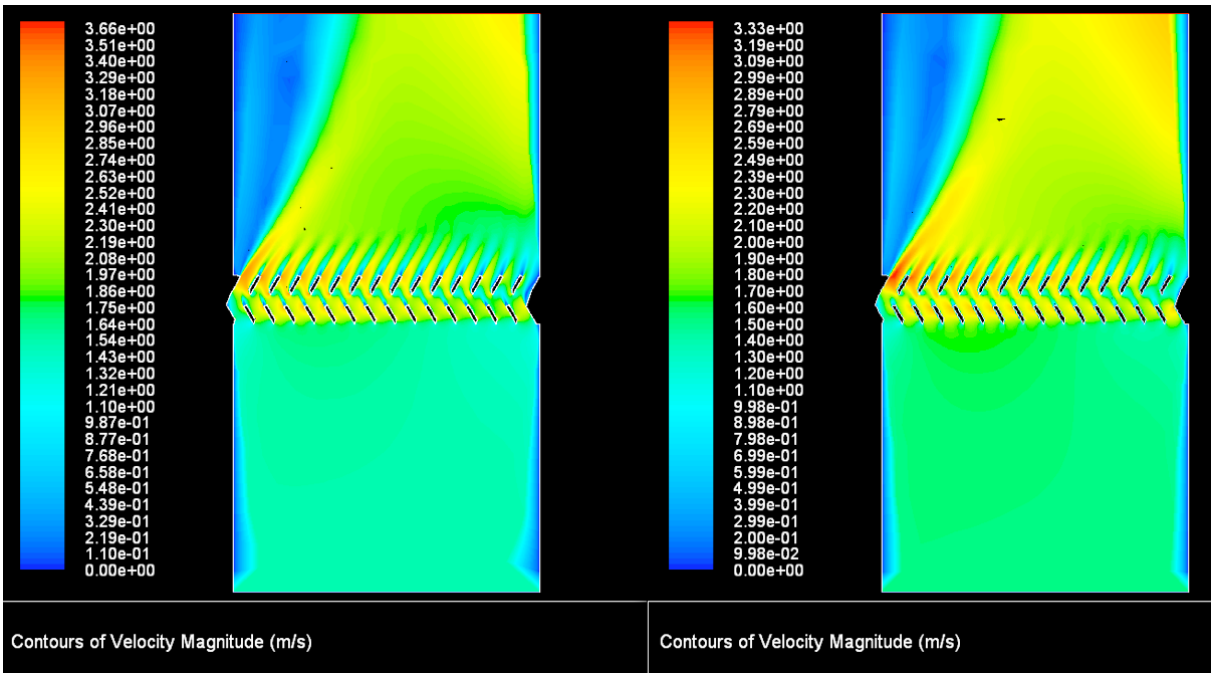

Figura 6.14: Comparación de los campos de velocidad de la fina y gruesa malla para el wooden lath eliminator para una velocidad de 1,52 m s^{-1} (izquierda: fina, derecha: gruesa)

Los campos de velocidad son muy similares, pero eso fue esperado por la ecuación de continuidad.

Las figuras 6.15 y 6.16 demuestran las comparaciones de las distrubuciones de la presión para las otras dos velocidades. Se renuncia de mostrar las comparaciones de los campos de velocidad para las otras velocidades de entrada porque no hay diferencia entre las dos mallas.

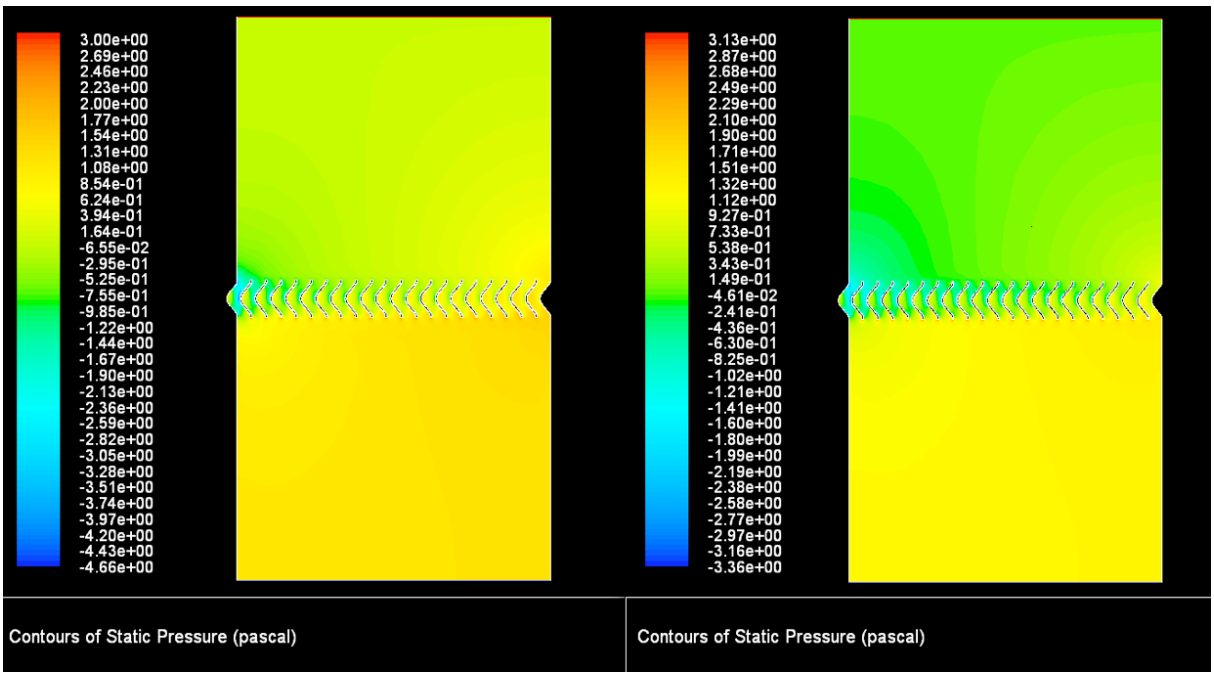

Figura 6.15: Comparación de los campos de presión de la fina y gruesa malla para el wooden lath eliminator para una velocidad de 0,91 m s^{-1} (izquierda: fina, derecha: gruesa)

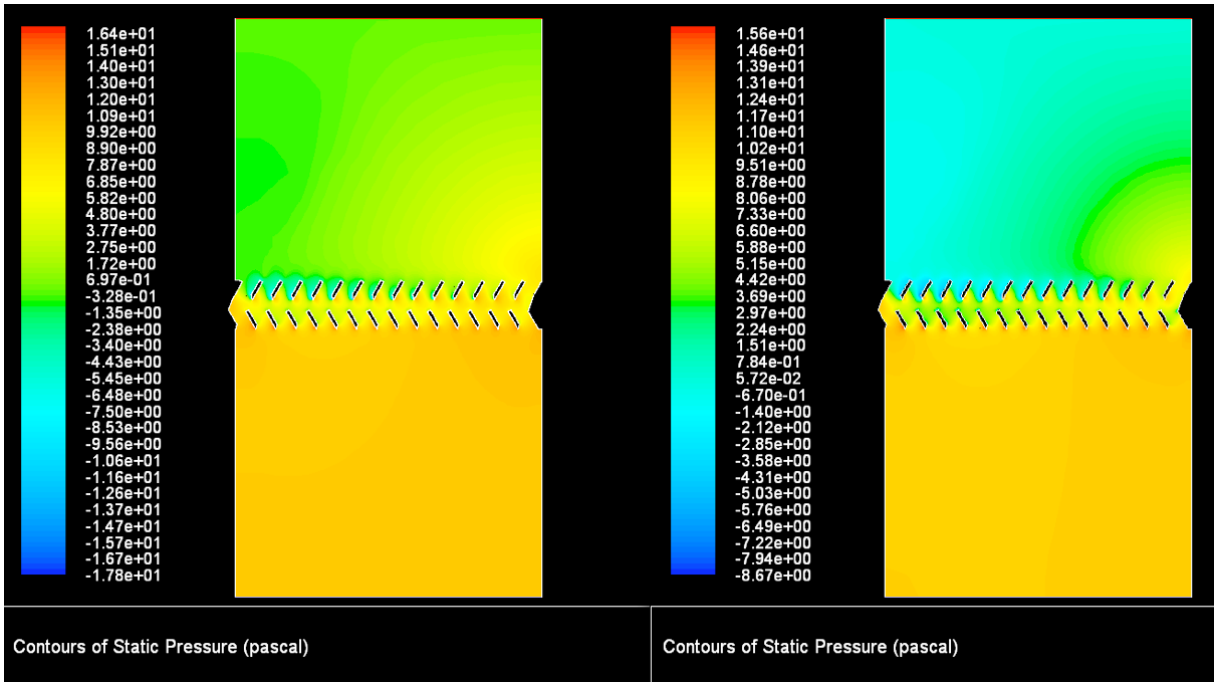

Figura 6.16: Comparación de los campos de presión de la fina y gruesa malla para el wooden lath eliminator para una velocidad de 2,13 m s^{-1} (izquierda: fina, derecha: gruesa)

Como para una velocidad de 1, 52 m s^{-1} la malla gruesa calcula la presión mas alta para las otras velocidades.

6.3.2 Asbesto- cement eliminator

Ahora se comparan los resultados para el asbesto- cement eliminator para la malla fina y gruesa.

Figura 6.17 demuestra la comparación de los campos de presión para las dos mallas para una velocidad de entrada de aire de 1,58 m s^{-1}. A la izquierda se puede ver el resultado para la malla fina y a la derecha para la malla gruesa.

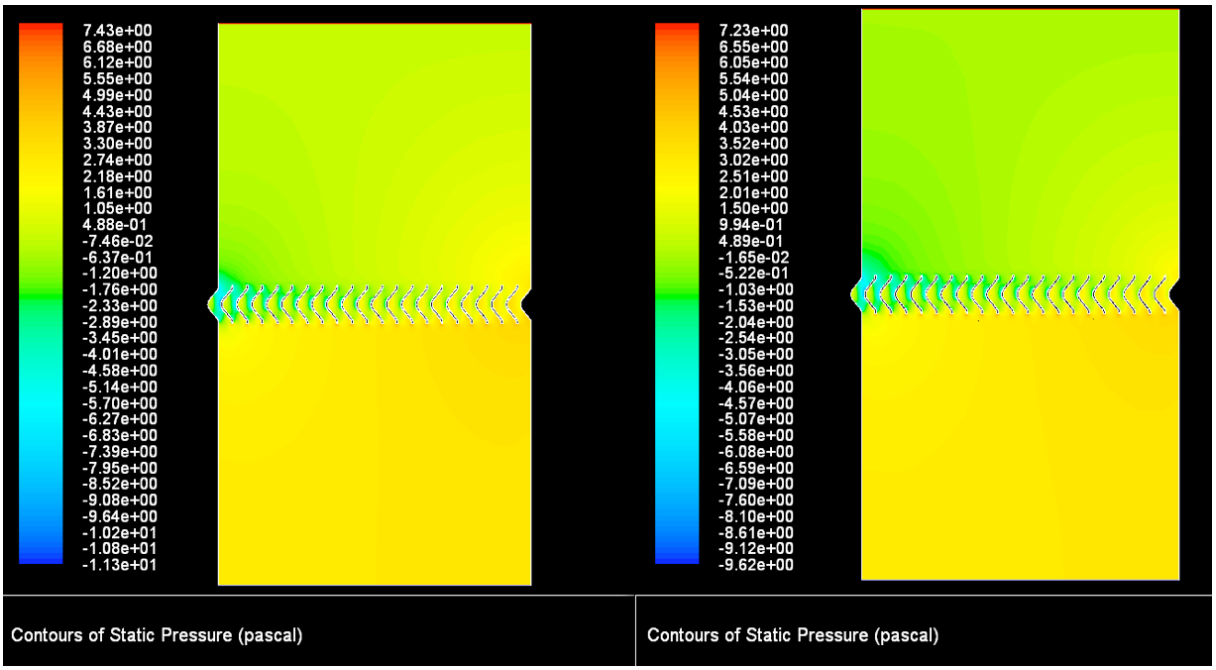

Figura 6.17: Comparación de los campos de presión de la fina y gruesa malla para el asbesto-cement eliminator para una velocidad de 1,58 m s^{-1} (izquierda: fina, derecha: gruesa)

Como se puede ver las distribuciones de la presión son casi iguales.

Figura 6.18 muestra la comparación para los campos de velocidad para la misma velocidad de entrada.

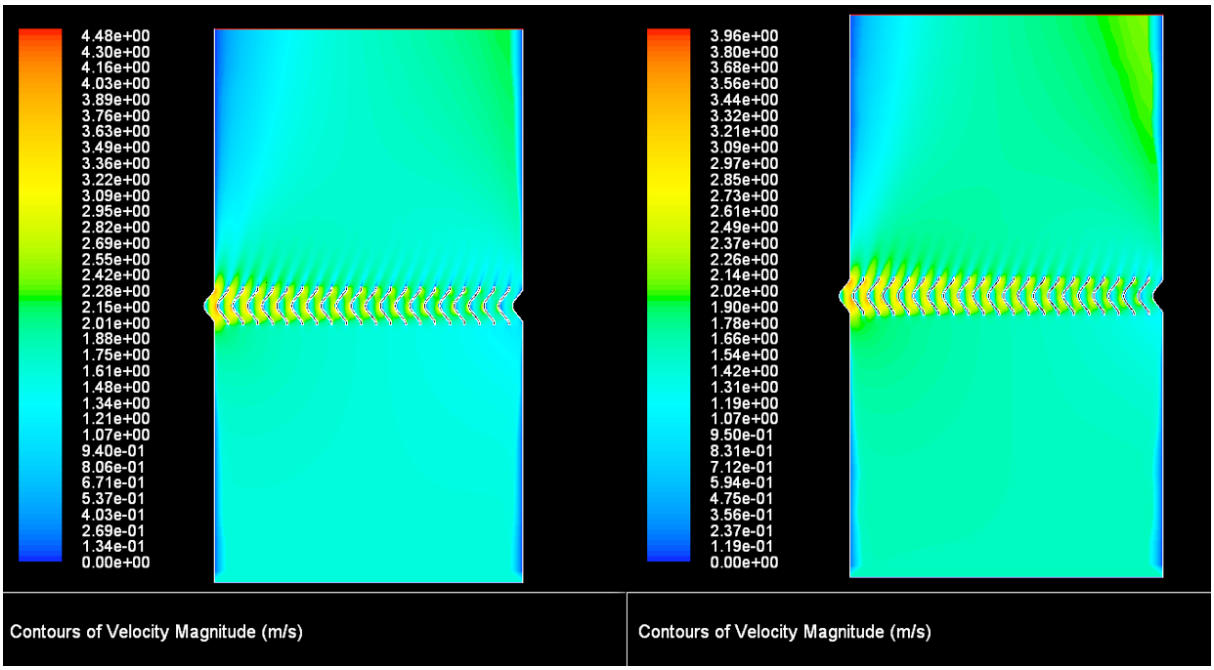

Figura 6.18: Comparación de los campos de velocidad de la fina y gruesa malla para el asbesto- cement eliminator para una velocidad de 1,58 m s^{-1} (izquierda: fina, derecha: gruesa)

Casi no se puede ver una diferencia entre los dos campos. La unica cosa es que la malla gruesa calcula la velocidad a la izquierda un poco mas baja y a la derecha un poco mas alta que la malla fina. Pero la diferencia es minimal.

Las figuras 6.19 y 6.20 muestran los campos de presión para las otras dos velocidades de entrada, 0,94 m s^{-1} y 2,23 m s^{-1}. Se renuncia de mostrar los campos de velocidad por la diferencia minima entre las dos mallas.

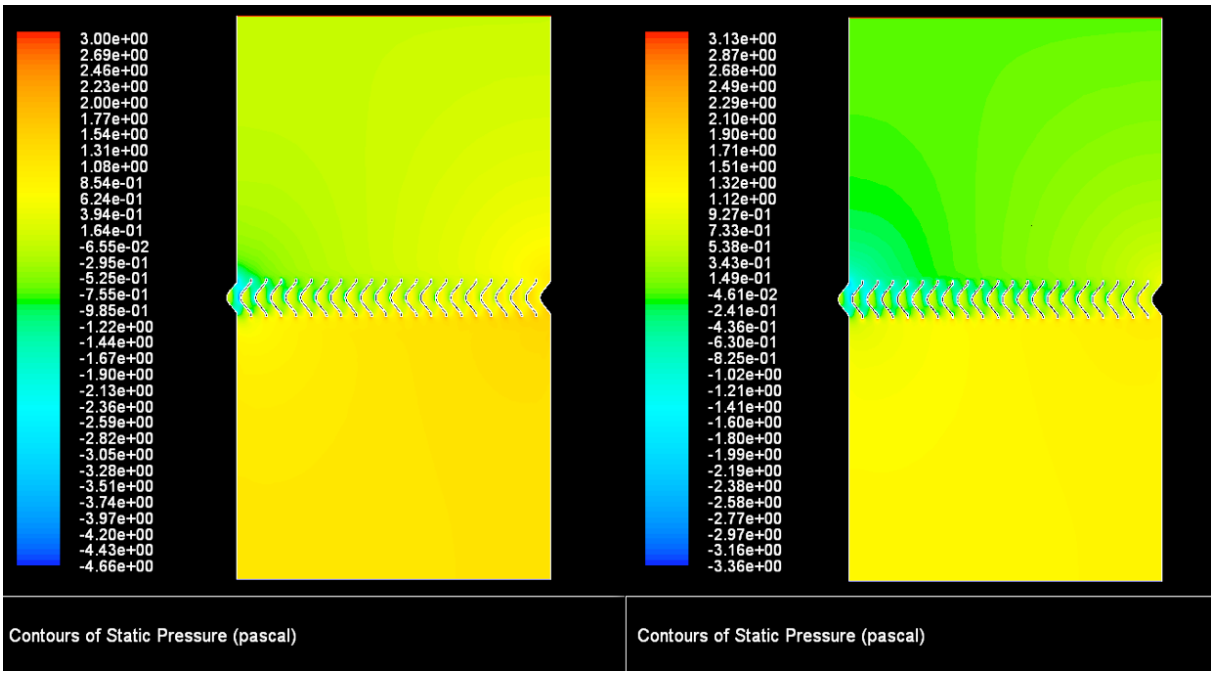

Figura 6.19: Comparación de los campos de presión de la fina y gruesa malla para el asbesto-cement eliminator para una velocidad de 0,94 m s^{-1} (izquierda: fina, derecha: gruesa)

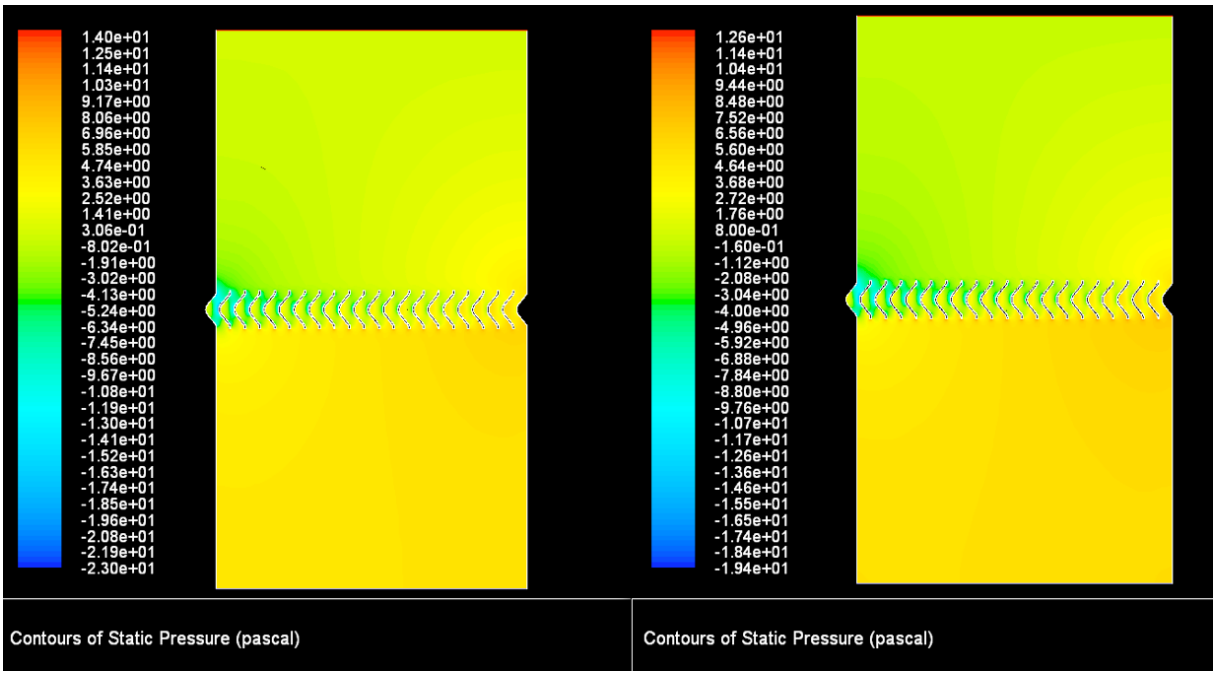

Figura 6.20: Comparación de los campos de presión de la fina y gruesa malla para el asbesto-cement eliminator para una velocidad de 2,23 m s^{-1} (izquierda: fina, derecha: gruesa)

Para las dos diferentes velocidad los campos de velocidad se parecen mucho. Por los colores parecen muy diferentes pero si se considera el codigo de colores se puede ver que los campos son casi iguales.

6.4 Coeficientes de retardo

Con los resultados de las simulaciones se puede calcular los coeficientes de retardo para cada geometría. El coeficiente de retardo es un valor adimensional que describe la resitencia aerodinámica de un flujo. En el presente trabajo es un valor que describe la resitencia de los separadores. El coeficiente de retardo es definido:

$$c_D = \frac{\Delta P}{\frac{1}{2}\rho A v^2} \tag{6.1}$$

donde ΔP is la pérdia de presión, A es la área de referencia, v es la velocidad, y ρ es la densidad del flujo de aire.

En este caso la área de referencia es el ancho del dominio computacional multiplicado por una profundidad de un metro. El ancho del dominio computacional para el wooden lath eliminator es 1,15 m y 1,19 m para el asbesto- cement eliminator. Por lo tanto la área de referencia en caso del wooden lath eliminator es 1,15 m^2 y en caso del asbesto- cement eliminator 1,19 m^2.

Las pérdidas de cargas utilizadas para los cálculos de los coeficientes de retardo son las mismas como calculadas en el capítulo 5.

También es posible calcular números de *Reynold*s con el ancho de los diminios computacionales como longitud característica. La Tabla 6.1 muestra los coeficientes de retardo y números de *Reynold*s para el wooden lath eliminator y la Tabla 6.2 para el asbesto-cement eliminator. Las columnas “fina“ y “gruesa“ demuestran los diferentes resultados para las mallas finas y gruesas.

Tabla 6.1: Coeficientes de retardo y números de *Reynold*s para el wooden lath eliminator

Velocidad, v [m s^{-1}]	Número de *Reynold*s, *Re* [-]	Pérdida de carga, ΔP [Pa]		Coeficiente de retardo, c_D [-]	
-	-	fina	gruesa	fina	gruesa
0,91	69300	1,5033	1,6812	2,62	2,93
1,52	116000	4,1225	4,4826	2,57	2,80
2,13	162000	8,0473	8,4982	2,56	2,70

Tabla 6.2: Coeficientes de retardo y números de *Reynold*s para el asbesto- cement eliminator

Velocidad, v [m s^{-1}]	Número de *Reynold*s, *Re* [-]	Pérdida de carga, ΔP [Pa]		Coeficiente de retardo, c_D [-]	
-	-	fina	gruesa	fina	gruesa
0,94	71500	1,0124	1,1245	1,65	1,84
1,58	120000	2,6191	2,7206	1,51	1,57
2,23	170000	4,9106	4,8987	1,42	1,42

La Figura 6.21 muestra el diagrama del número de *Reynold*s y del coeficiente de retardo para el wooden lath eliminator y la Figura 6.22 para el asbesto- cement eliminator.

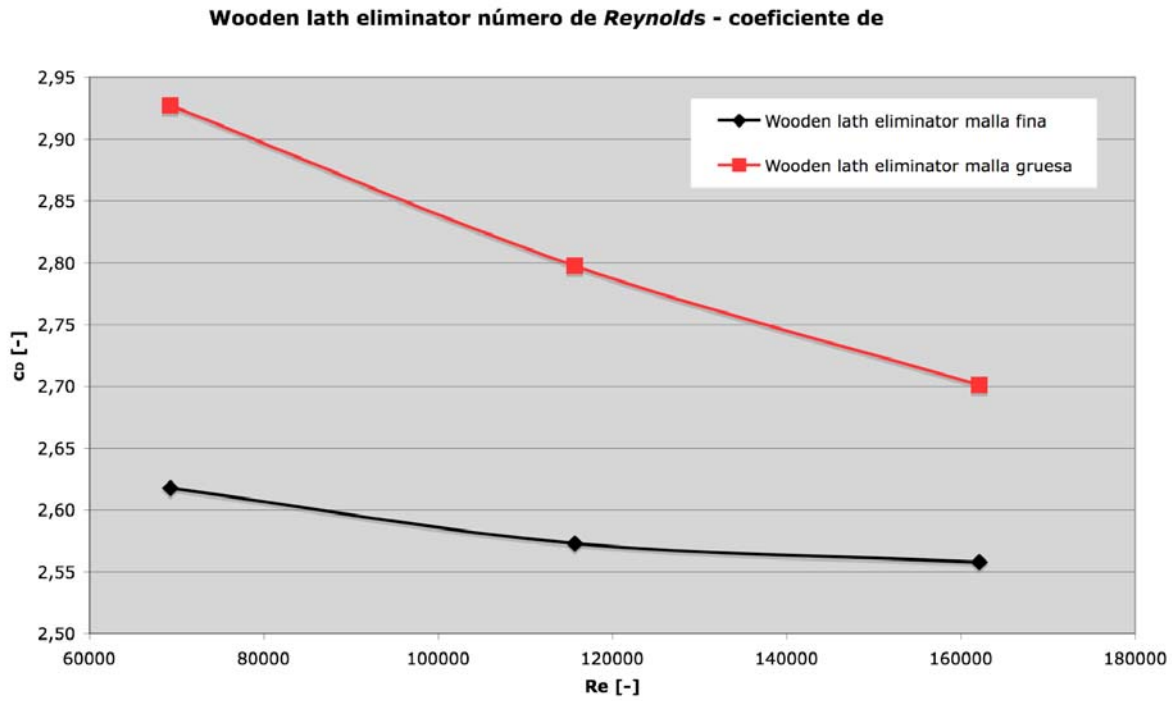

Figura 6.21: Diagrama número de *Reynold*s – coeficiente de retardo para el wooden lath eliminator

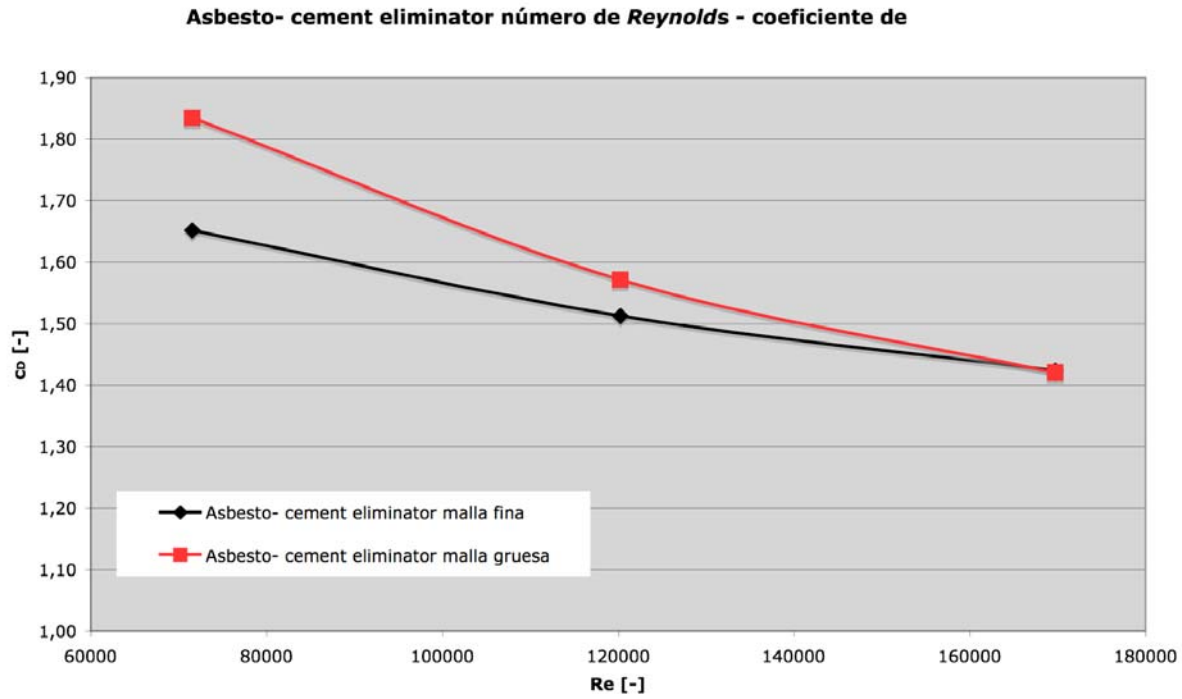

Figura 6.22: Diagrama número de *Reynold*s – coeficiente de retardo para el asbesto- cement eliminator

Para la malla fina del wooden lath eliminator el coeficiente de retardo es casi constante y aproximadamente 2,6. Los valores para la malla gruesa son todos más altos y para números de *Reynold*s más altos los valores bajan.

En caso del asbesto- cement eliminator la deviación entre los valores de las diferentes mallas no es tan grande como para el caso del wooden lath eliminator. Para el número de Reynolds más alto el coeficiente de retardo son igulas. También se puede ver que para un número de *Reynold*s creciente el coeficiente de retardo decae.

7 Conclusiones

7.1 Conclusión general

En el presente trabajo se ha eximinado el flujo de aire dentro de una torre de refrigeración y la pérdida de presión resultante. Para eso se ha revisado la bibliografía para encontrar datos experimentales sobre los separadores que están situados dentro de una torre para evitar que salgan gotas de agua de ella. Se han encontrado dos diferentes geometrías de los separadores. Para las geometrías se ha construido un dominio computacional para cada una. Con los dos dominios se han realizado varias simulaciones numéricas para determinar la pérdida de presión.

7.2 Conclusión de los resultados

Para las dos geometrías se han ejecutado diferentes estudios para determinar la incertidumbre de la solución numérica. Sin embargo la métodología utilizada ha resultado muy apropiada para los dos casos de este trabajo. Los resultados no son conluyentes. Por eso se ha utilizado un estudio de valor de y^+ para encontrar una solución numérica que no dependa de la malla.

En comparación con los datos de la bibliografía se puede decir que para una geometría (wooden lath eliminator) los valores numéricos coinciden casi perfectamente con ellos. Sin embargo, para la otra geometría (asbesto- cement eliminator) no es así. La diferencia entre los datos experimentales y numéricos es muy grande. Las razones de la gran diferencia no están claras. Al caso viene diferentes posibildades, por ejemplo: el modelo de turbulencia no es adecuado, el caso calculado es estacionario, falta las gotas de agua, y la fuente de la bibliografía puede ser falsa. Todas las posiblidades excepto la última contradicen el satisfactorio resultado para el wooden lath eliminator.

Como este trabajo quiere ser la base para el proceso de optimización de la forma de los separadores se puede decir que se ha encontrado un modelo que usa el valor de y^+. Esto Quiere decir que un modelo numérico que respeta el valor de y^+, que la malla se construirá con un valor de y^+ sobre aproximadamente 5, se puede usar para encontrar la mejor forma de los separadores. Por lo menos optimizada en la pérdida de presión, porque falta el paso de introducir gotas al dominio computacional.

Sin embargo, si se quiere extender el dominio computacional hay que utilizar mallas gruesas con funciones de pared para que el gasto computacional no sea demasiado grande para manejarlo. Es mostrado en capítulo 5 las diferncias entre mallas gruesas y finas no son muy grandes.

8 Bibliografía

[1] S. R. HANNA, S. D. SWISHER: A method of calculating the size of cooling tower plumes, *Atmospheric Environment*, Vol 6 (1972), pp. 587- 588

[2] M. W. GOLAY, W. J. GLANTSCHIG, F. R. BEST: Comparision of methods for measurement of cooling tower drift, *Atmospheric Environment* Vol. 20 No. 2 (1986), pp. 269- 291

[3] K. E. HAMAN, S. P. MALINOWSKI: Observations of cooling tower and stack plumes and their comparision with plume model "Alina", *Atmospheric Environment* Vol. 23 (1989), No. 6, pp. 1223- 1234

[4] A. K. M. MOHIUDDIN, K. KANT: Knowledge base for the systematic design of wet cooling towers. Part II: Fill and other design parameters, *International Journal of Refrigeration* Vol. 19 (1996), No. 1, pp.52- 60

[5] T. MICHIOKA, A. SATO, T. KANZAKI AND K. SADA: Wind tunnel experiment for predicting a visible plume region from a wet cooling tower, *Journal of Wind Engineering and Industrial Aerodynamics* Vol. 95, Issue 8 (2006), pp. 741- 754

[6] A. MARTIN, F. R. BARBER: Some water droplet measurements inside cooling towers, *Atmospheric Environment*, Vol 8 (1974), pp. 325- 336

[7] P. M. FOSTER, M. I. WILLIAMS, R. J. WINTER: Droplet behaviour and collection by counterflow cooling towers eliminators, *Atmospheric Environment*, Vol. 8 (1974), pp. 349- 360

[8] J. CHAN, M. W. GOLAY: Comparative performance evaluation of current design evaporative cooling tower drift eliminators, *Atmospheric Environment*, Vol. 11 (1977), pp. 775- 781

[9] B. R. GARDNER, H. J. LOWE: The research and development background to the environmental problems of natural draught cooling towers, *Atmospheric environment*, Vol. 8 (1974), pp. 313- 320

[10] A. K. M. MOHIUDDIN: Experimental study in a spray filled tower for flow visualization and drift eliminators characteristics, *Journal of Applied Sciences*, Vol. 5 (2005), pp. 284- 291

[11] R. AL- WAKED, M. BEHNIA: Enhancing performance of wet cooling towers, *Energy Conservation & Management*, Vol. 48, Issue 10 (2007), pp. 2638- 2648

[12] M. R. MOKHTARZDEH- DEHGHAN, C. S. KÖNIG, A. G. ROBINS: Numerical study of single and two interacting turbulent plumes in atmospheric cross flow, *Atmospheric Environment*, Vol. 40 (2006), pp. 3909- 3923

[13] R. N. MERONEY: CFD prediction of cooling tower drift, *Journal of Wind Engineering and Industrial Aerodynamics*, Vol. 94 (2006), pp. 463- 490

[14] S. P. FISENKO, A. I. PETRUCHIK, A. D. SOLODUKHIN: Evaporative cooling of water in a natural draft cooling tower, *International Journal of Heat and Mass Transfer*, Vol. 45 (2002), pp. 4683- 4694

[15] C. J. FREITAS: The issue of numerical uncertainty, *Applied Mathematical Modelling*, Vol 26, Issue 2 (1999), pp. 237- 248

[16] FLUENT INC.: FlUENT 6.3 User's guide, (2006)

[17] C. J. FREITAS, U.GHIA, I. CELIK, P. ROACHE, P.RAAD: ASME's quest to quantify numerical uncertainty, *AIAA*